

Theory of Nonlinear Polarization Spectroscopy in the Frequency Domain (NLPF) with Applications to Photosynthetic Antennae

D I S S E R T A T I O N

zur Erlangung des akademischen Grades

doctor rerum naturalium

(dr. rer. nat.)

im Fach Mathematik

eingereicht an der

Mathematisch-Naturwissenschaftlichen Fakultät I

Humboldt-Universität zu Berlin

von

Herr Dipl.-Phys., Dipl.-Wirtsch.-Phys. Wichard Johann Daniel Beenken

geboren am 14.10.1964 in München

Präsident der Humboldt-Universität zu Berlin:

Prof. Dr. Jürgen Miynek

Dekan der Mathematisch-Naturwissenschaftlichen Fakultät I:

Prof. Dr. Michael Linscheid

Gutachter:

1. Dr. habil. Volkhard May
2. Prof. Dr. Thomas Elsässer
3. Prof. Dr. Villy Sundström

eingereicht am: 15. Juli 2003

Tag der mündlichen Prüfung: 21. November 2003

Abstract

In the work be presented a standard theory of non-linear polarization spectroscopy in the frequency domain (NLPF) will be established. The NLPF technique based on anisotropy induced in a dye-solution, which is isotropic elsewhere, by a polarized monochromatic pump laser field. This is probed by a second laser field, which polarization direction is turned of 45 degree in respect to that of the pump. From the fundamental equations describing the non-linear response of molecular systems on electromagnetic fields, the two-dimensional NLPF spectrum is deduced for arbitrary pump-intensities. At low pump-intensities a subband analysis by NLPF has been established. This allows one to study the term scheme and energy relaxation path of molecular and supra-molecular systems by their NLPF-spectra. This includes the determination of transition-frequencies and -dipole orientations, homogeneous and inhomogeneous linewidths, as well as energy relaxation rates. Furthermore, using a self-consistent approach, the pump-field dependence of the NLPF-spectrum has been deduced for the two-level system in general and also for specific multi-level systems. This method allows one to determine the oscillator strength without knowledge of the concentration, what is quite useful for studying molecular aggregates. Applications are presented to the peripheral light harvesting antenna LH2 of purple bacteria and the light harvesting complexes LHC II and CP 29 of higher plants.

Keywords:

optical Kerr effect, non-linear response, dissipative quantum dynamics, photosynthesis

Zusammenfassung

In der vorliegenden Arbeit wird eine einheitliche und allumfassende Theorie der Nichtlinearen Polarisationspektroskopie in der Frequenzdomäne (NLPF) aufgestellt. Diese Methode basiert auf der in einer isotropen Farbstofflösung durch ein polarisiertes, monochromatisches Laserfeldes (pump) erzeugten Anisotropie, die mittels eines weiteren monochromatischen Laserfeldes (probe) mit einer um 45° gegenüber dem Pumpfeld gedrehten Polarisationsrichtung geprobt wird.

Ausgehend von den grundlegenden Gleichungen für den nichtlinearen Respons molekularer Systeme auf elektromagnetische Felder wird das zweidimensional NLPF-spektrum hergeleitet, und zwar sowohl in der niedrigsten Ordnung Störungstheorie als auch unter Verwendung eines selbstkonsistenten Ansatzes für beliebige Pumpfeldstärken. In der niedrigsten Ordnung Störungstheorie können drei in ihrer Frequenzabhängigkeit sich unterscheidende Arten von Ausdrücke explizit angegeben werden. Diese sind drei Arten von Peaks im NLPF-spektrum zuzuordnen: Den T_2 -peaks, dem T_1 -peaks und den Zweiphotonen-peaks. Letztere sind unter Normalbedingungen im allgemeinen nicht beobachtbar und wurden daher nicht weiter behandelt.

Die in dieser Arbeit erstmals gelungene, allgemeine und einheitliche theoretische Beschreibung der T_1 - und T_2 -peaks in NLPF-spektren von Mehrniveausystemen stellt einen Durchbruch hin zu einer allumfassenden Subbandenanalyse mittels NLPF dar. Durch Einbeziehung der teilweise bereits bekannten Auswirkungen homogener und inhomogener Linienverbreiterung und spektraler Diffusion auf NLPF-spektren, sowie deren Verallgemeinerung im Rahmen der Theorie nichtmarkowscher Dissipationsprozesse, konnte eine Methodik entwickelt werden, die es erlaubt, NLPF-spektren molekularer und supramolekularer Systeme in Bezug auf das ihnen zugrundeliegende Termschema mit Übergangsfrequenzen und -dipolen, die homogenen und inhomogenen Linienbreiten, sowie dem zugeordneten Energierelaxations- und -transferpfad mitsamt zugehörigen Raten zu analysieren.

Die in dieser Arbeit vorgestellte und über frühere rudimentäre Ansätze weit hinausgehende Theorie der NLPF bei starken Pumpfeldern, die auf einem selbstkonsistenten Ansatz für den Fourier-transformierten statistischen Operator beruhen, eröffnet ein komplett neues Feld von Anwendungen der NLPF. Für Zweiniveausysteme konnten die selbstkonsistenten Gleichung vollständig analytisch gelöst werden. Dabei konnten die Querverbindungen zur nichtlinearen Absorption und zum optischen Starkeffekt aufgezeigt werden. Die resultierende Sättigungskurve

für das NLPF-signal kann unter Heranziehen der aus Analyse des T_1 -peaks bei niedrigen Intensitäten gewonnenen Energielaxationsrate und der analog aus T_2 -peakanalyse erhaltenen homogenen Linienbreite zur Bestimmung der Dipolstärke des Übergangs ohne Bestimmung der Farbstoffkonzentration verwendet werden. Durch Abbildung auf das gelöste Zweiniveauprobem konnte die Methodik auch auf spezielle Mehrniveausysteme übertragen werden.

Beide oben beschriebenen Methoden, Subbandanalyse bei niedrigen und Bestimmung der Übergangsdipolstärke bei hohen Pumpintensitäten, wurden in der vorliegenden Arbeit zur Untersuchung der Natur der angeregten Zustände in photosynthetischen Antennen von Purpurbakterien (LH2) und höheren Pflanzen (LHC II und CP29) eingesetzt, insbesondere zum Auffinden delokalierter Ekzitonenzustände.

Schlagwörter:

Optischer Kerreffekt, Nichtlineare Respons, Dissipative Quantendynamik, Photosynthese

Dedication

For Lilian, though she won't understand it.

Acknowledgements

The author of the present work wants to express his gratitude to all colleagues of the group of Dr. sc. Dieter Leupold at Max-Born-Institute and of the group of Dr. habil. Volkhard May at the chair of Halbleitertheorie of the Humboldt University (both Berlin) for the fruitful cooperation. In particular he want to thank Dr. Bernd Voigt, Dr. Frank R. Nowak, and Axel Schubert, whose question initiate new theoretical ideas and who were always open to adapt the theoretical results for new experiments, as well as to Dr. Jürgen Ehlert, who checked the theoretical calculations and implemented them into his fitting software. For support regarding theoretical methodic special thanks to Dr. habil. Volkhard May, Dr. Thomas Renger, and Dr. Dirk H. Schirrmeister, as well as Prof. Dr. Arvi Freiberg, for his suggestion to study non-Markovian line shapes in NLPF. The biological parts of this work would not have been possible without the help of Dr. Heiko Lokstein and Dr. Ute Hansen (Humboldt University Berlin), Dr. Beate Ücker and Prof. Hugo Scheer (both University Munich). The financial support by Deutsche Forschungs Gemeinschaft may be acknowledged, too. Last but not least the author wants to express his best gratitude to associate professor Tõnu Pullerits for his patience, whenever the author spent his time with the work be presented instead of his present work. Thanks also to all the other colleagues from Lund, who brought me back to the joyful side of science.

Contents

1	Introduction	1
I	Theory of NLPF	4
2	Principles of NLPF	5
2.1	The NLPF-line-shape function	6
2.1.1	External fields and polarization	6
2.1.2	Phase-matching condition	7
2.1.3	Signal generation and reabsorption: the NLPF-line-shape function	8
2.2	Molecular response to the external fields	10
2.3	Components of NLPF-spectra	12
2.3.1	T ₂ -peaks	12
2.3.2	T ₁ -peak	14
2.3.3	Two-photon-peaks	16
2.4	Orientational averaging	17
2.5	Summary	19
2.6	Supplement: Time-domain description of NLPF-spectra	20
3	NLPF-spectra for dissipative systems	23
3.1	General description of dissipative quantum systems	24
3.1.1	Reduced density matrix	25
3.1.2	Secular approximation	26
3.1.3	Markov approximation and reorganization	28
3.2	Harmonic oscillator model	30
3.2.1	Harmonic oscillator approximation	31
3.2.2	Correlation function and spectral density	33

3.2.3	Frequency dependent dephasing and energy relaxation rates	35
3.2.4	Debye spectral density	38
3.3	NLPF-spectrum of a dissipative two-level system	39
3.3.1	T_1 -peak of a dissipative two-level system	40
3.3.2	Non-Markovian T_2 -peak in the high temperature limit	41
3.3.3	T_2 -peak at low temperatures	43
3.4	Summary	45
3.5	Supplement: Cumulant expansion	47
3.5.1	Cumulant expansion of the Greens function	47
3.5.2	Cumulant expansion for the NLPF-line-shape function	49
4	NLPF-spectra of multi-level systems	51
4.1	Discrete spectral structures	52
4.1.1	Heterogeneous substructure	55
4.1.2	Incoherent excitation energy transfer	59
4.1.3	Homogeneous substructure	63
4.1.4	Excited-state absorption and stimulated emission	67
4.2	Mixed discrete substructures	71
4.3	Ground state progression	72
4.3.1	The Λ -system	72
4.3.2	‘Raman’-peaks	75
4.4	Summary	76
4.5	Supplement: Applicaton of NLPF to subband analysis in praxi	77
5	Inhomogeneously broadened NLPF-spectra	80
5.1	Inhomogeneous broadening	81
5.2	Förster transfer for inhomogeneously broadened donors and acceptors	83
5.3	Spectral diffusion	87
5.4	Orientalional relaxation	90
5.5	Summary	91
6	Strong field theory of NLPF	94
6.1	General description of the NLPF-signal at high pump intensities	95
6.1.1	Self-consistent equation for occupation	95
6.1.2	Two-level system	96
6.2	Multi-level systems at high pump intensities	100

Contents

6.2.1	Fast intra- and inter-band relaxation	100
6.2.2	Fast energy transfer and excitation annihilation	103
6.3	Summary	106
II	Application of NLPF to photosynthetic antennae	108
7	Short introduction to photosynthesis	109
8	The B850-band of the peripheral light harvesting antenna (LH2) of purple bacteria	112
8.1	Structure and absorption spectrum of LH2	112
8.2	Theoretical model for the B850 band	114
8.3	Low-intensity NLPF-spectra of the B850-band	118
8.3.1	T ₂ -peaks	118
8.3.2	T ₁ -peak	121
8.4	Pump-intensity dependence of the NLPF-signal in the B850 band	122
8.4.1	Delocalization length of an assumed B850-exciton	123
8.4.2	Fast hopping transfer	126
8.5	Summary	127
8.6	Supplement: Orientation-averaging for the circular B850-aggregate	128
9	Excitonic coupling of chlorophylls in the light-harvesting complex II of higher plants	131
9.1	Structure of LHC II	131
9.2	Excitonic coupling in LHC II	133
9.2.1	Excitonic coupling for the Chl a ₂ /b ₂ dimer	134
9.2.2	Alternative arrangements	135
9.2.3	Limitation of delocalization by exciton-phonon coupling	136
9.2.4	Experimental tests for spectral shifts and redistribution of oscillator strength in LHC II	137
9.2.5	Homogeneous substructure for excitonically coupled Chl a/b dimers	139
9.3	Pump-intensity-dependent NLPF-spectra for LHC II	140
9.3.1	ξ-spectrum of trimeric LHC II	140
9.3.2	Decomposition of the fluorescence band	144
9.4	Summary	147
9.5	Supplement: Calculation of excitonic coupling in the Chl a ₂ /b ₂ dimer	147

10 Spectral substructure and excitonic interactions in the minor Photosystem II antenna complex CP29	149
10.1 T ₂ -peak analysis within the Q _y -band of CP29	151
10.2 T ₂ -peaks of CP29 for pumping the Q _y -band and probing the Soret	152
10.3 Summary	153
11 Conclusion	158

List of Figures

2.1	NLPF-Setup	6
2.2	T ₂ -peak of a two-level system	14
2.3	NLPF-spectra of a two level system	16
2.4	Illustration of the two Euler angles θ and ϕ as described in the text	18
2.5	Feynman graphs relevant for NLPF	22
3.1	Sections $U_{\mu\mu}(\omega_\xi)$ and $U_{\nu\nu}(\omega_\xi)$ through the potential surfaces	33
3.2	Coupling function $K_{\mu\nu}(\omega)$ for a Debye spectral density	39
3.3	Nonmarkovian pump and probe frequency dependences of the T ₂ peak in the high temperature limit	42
3.4	Non-Markovian T ₂ -peak of a two-level system at low temperature	43
3.5	Nonmarkovian pump and probe frequency dependences of the T ₂ peak at different temperatures	44
3.6	Nonmarkovian T ₂ peak for $T \rightarrow 0\text{K}$	45
4.1	Term-schemes for different types of discrete spectral	55
4.2	T ₂ -peaks for a heterogeneous substructure	57
4.3	T ₁ -peak for two independent two level systems (heterogeneous substructure)	58
4.4	T ₂ -peaks for donor acceptor pair with an excitation energy transfer	61
4.5	T ₁ -peak for donor acceptor pair	63
4.6	T ₂ -peaks for a homogeneous substructure	65
4.7	T ₁ -peak for homogeneous substructure	66
4.8	Chemical structure of the xanthophyll lutein	67
4.9	T ₂ -peaks for a three level system in the case $\omega_{21} \sim \omega_{10}$	68
4.10	Probe-frequency dependence of the T ₂ -peaks of different three-level	69
4.11	Probe-frequency dependence of the T ₂ -peaks of a three-level system pumped at $\omega_p = \omega_{20}$ for $r = 1$ (solid line), $r = 0$ (dot), $r = 0.5$ (dash), and $r = 2$ (dash-dot) where μ_{10}/γ_1 has been fixed. Other parameters and axis as in Fig. 4.9.	70

4.12	T ₂ -peaks for a Λ -system in the ‘hole-burning’ limit	74
4.13	T ₁ -peaks for Λ -systems with different energy relaxation	75
4.14	NLPF-spectrum with T ₁ -peak (center) and two ‘Raman’-peaks	76
4.15	Structure formula of the pinacyanol (kation)	78
4.16	NLPF spectra of pinacyanol	79
5.1	T ₂ -peak for a inhomogeneous broadened two-level system	82
5.2	T ₂ -peaks for a donor acceptor pair with $\omega_{da} = 0$	85
5.3	T ₂ -peaks for the same donor-acceptor pair as in Fig. 5.2 but different energy relaxation	86
5.4	T ₂ -peaks for the same donor-acceptor pair as in Fig. 5.3 but with $\omega_{da} = -\Delta$	87
5.5	T ₂ -peak for spectral diffusion	89
5.6	Scheme for different kinds of broadening at high temperatures	92
6.1	Saturation function $F[x]$ according to Eq. 6.6.	97
6.2	NLPF-spectra of a two-level system at different pump intensities	99
6.3	Probe dependency of the NLPF-spectrum for $I_p = 50I_s$ at $\omega_p = \omega_t$	100
6.4	Term scheme for the model system containing fast intra- and inter-band relaxation	102
6.5	Scheme of the annihilation process	104
7.1	Structure formulas of chlorophyll a and b (Chl a, Chl b) as well as of bacteriochlorophyll a (Bchl a)	110
7.2	Artistic illustration of the thylakoid membrane with embedded photosystems PS I and PS II, associated antennae complexes, cytochrome-b6f complex and ATPase	111
8.1	Artistic illustration of the photosynthetic reaction center (RC), the core antenna (LH1) and several peripheral antennae (LH2) of the purple bacterium <i>Rhodospirillum (Rs.) molischianum</i>	113
8.2	Arrangement of the Bchls in the peripheral antenna complex LH2 of <i>Rps. acidophila</i>	114
8.3	Absorption spectrum for the peripheral light harvesting antenna (LH2) of <i>Rs. molischianum</i>	115
8.4	NIR-absorption spectra for the peripheral light harvesting antennae (LH2) of <i>Rb. spheroides</i> and <i>Rps. acidophila</i>	116
8.5	Theoretically predicted exciton bands for the LH2 of <i>Rb. molischianum</i>	117

List of Figures

8.6	Fitted NLPF-spectra (B850-band) of the light harvesting antenna LH2 of the purple bacteria <i>Rs. molischianum</i> , <i>Rps. acidophila</i> , and <i>Rb. sphaeroides</i> at room temperature	120
8.7	Room-temperature absorption spectrum of the LH2 of <i>Rb. sphaeroides</i>	121
8.8	T_1 -peak for LH2 of <i>Rs. molischianum</i>	122
8.9	Pump-intensity dependence of the NLPF signal for LH2 of <i>Rs. molischianum</i> pumped at 850 nm and probed at 840 nm	123
8.10	Transient absorption spectrum of the for <i>Rb. sphaeroides</i> with decomposition	125
9.1	Structure of the trimeric LHC II according to electron crystallography data	132
9.2	Absorption and fluorescence spectrum of trimeric LHCII	133
9.3	NLPF spectra of trimeric LHC II for different pump intensities	141
9.4	Pump-intensity dependence of the NLPF-signal probed and pumped at 685 nm and 678 nm, respectively	142
9.5	ξ -spectrum of the Q_y -band of trimeric LHC II	143
9.6	Decomposition of the measured fluorescence spectrum of LHCII	145
10.1	Absorption spectrum of CP29 (solid line) and LHC II	150
10.2	NLPF spectra for CP29 probed and pumped in the Q_y -band	155
10.3	Term scheme for the Chl a/b dimer with excitonic coupling	156
10.4	NLPF spectra for CP29 probed in the Soret region for pumping the Q_y -band	157

Chapter 1

Introduction

The subject of the work to be presented, is the theory of **Non-Linear Polarization spectroscopy in the Frequency domain** (NLPF), a spectroscopic method quite powerful for the analysis of molecular and supra-molecular aggregates, e.g. photosynthetic aggregates. In some way it represents a complementary method to time-resolved spectroscopy by being able to reveal energy relaxation and dephasing processes, as well. As the name already suggests, NLPF is a combination of *polarization spectroscopy* and *non-linear* optics. Classical polarization spectroscopy has been introduced by M. Mitscherlich 1835 measuring the optical activity of tartrate and boron acid [Biot, 1844]. His method is still in use, e.g. in viticulture for determination of the sucrose content of grapes, and his principle setup with the sample located between two crossed polarizers is used in NLPF as well. That optical activity and birefringence can be induced in elsewhere isotropic media by magnetic and electric fields has been found by M. Faraday (1845) and Kerr (1875), respectively. In the present context the latter is of particular interest. In principle the setup used in NLPF represents a Kerr-cell where the static electric field is replaced by an optical electromagnetic field (cf. Fig. 2.1). The effect NLPF based on is the optical Kerr-effect [Ogawa et al., 2002], which represents a specific component of the non-linear optical response on two different electromagnetic fields, here named as probe and pump field. Simply spoken, the NLPF signal represents the turn of the polarization plane of the probe by an optical anisotropy induced by the pump in an elsewhere isotropic sample. For both fields being monochromatic the experiment is performed *in the frequency domain*.

At first NLPF has been used in the gas phase as a Doppler-free method [Wieman and Hänsch, 1976]. It was Song, Lee, and Levenson, who applied this technique to molecular systems diluted in condensed phase media, in order to separate homogeneous and inhomogeneous broadening and determine energy relaxation rates [Song et al., 1978]. In the following years several studies to different kinds of dye-molecules have been accomplished [Andrews and

Hochstrasser, 1980, Saikan and Sei, 1983a, Garcia-Golding, 1983, Marcano O et al., 1990]. Not much later first attempts towards an analysis of supra-molecular aggregates, in particular photosynthetic antennae were made [Leupold et al., 1993, Leupold et al., 1994]. With the coming up of fs-pump-probe spectroscopy the optical Kerr-effect has been used in numbers of time resolved measurements, in particular as a tool for analyzing ultra-short laser pulses by frequency resolved optical gating (FROG) [Kane and Trebino, 1993, Trebino et al., 1996, DeLong and Trebino, 1994, Trebino et al., 1997]. NLPF as a complementary method in the frequency domain has been nearly forgotten.

One of the reasons for the stagnation of NLPF as spectroscopic method may have been the lack of an all-appropriate theory. Though all theoretical approaches based on the same fundamental principles shown in the present work, they have been almost related only to the specific problem. This was mainly the original problem of the relation between homogeneous and inhomogeneous broadening, the latter with an extension to spectral diffusion [Garcia-Golding, 1983, Neef and Mory, 1991]. Simplifying, in the most cases the dye molecule has been described by a two-level system. Only exceptionally the models has been extended to molecular multi-level systems, which, however, were limited to maximum four levels [Andrews and Hochstrasser, 1980, Saikan and Sei, 1983a, Saikan and Sei, 1983b].

By the work be presented here a consistent all-purpose theory of NLPF will be achieved, which is applicable to a wide field of problems concerning the spectroscopic properties of molecules and supra-molecular aggregates. In the first part a general ansatz for the description of non-linear spectroscopy in the frequency domain will be broken down to the specific features of NLPF-spectra. Thereby the consistent model for NLPF-spectra of nearly all kinds of multi-level systems and aggregates takes the center stage. Additionally the models for homogeneous and inhomogeneous broadening will be extended by spectral diffusion but also to the general case of non-Markovian excitation energy dissipation. On the basis of the theoretical NLPF-line-shape functions for different kinds of substructure a standard method for global subband analysis using NLPF-spectra will be deduced which enables one to determine the term scheme with transition frequencies and dipoles, homogeneous and inhomogeneous line widths, as well as the associated energy-relaxation path with respective rates to a large extent. Concluding the first part, the strong-field theory of NLPF will be made up, which exists previously only in rudiments [Marcano O and Garcia-Golding, 1985, Marcano O et al., 1986]. In the framework of a self-consistent approach, the NLPF-spectra of the two-level system will be deduced as being exact for arbitrary pump intensities not ionizing or dissociating the molecule. Subsequently, a mapping of specific multi-level systems to the previous case will be established. This will enable one to determine the absolute values for the cross-section of ground- as well as excited-state absorption and stimulated emission, without knowing the dye concentrations.

The second part presents applications of the theoretical models as developed in the first part to three photosynthetic antennae, namely the peripheral light harvesting antenna of purple bacteria LH2, the bulk light harvesting complex II (LHC II) of higher plants, and the minor photosystem II antenna complex CP29 of photosystem II in higher plants. In all three cases the subject of interest is possible excitonic coupling between the light absorbing pigments. About the nature of the excitonic state in the B850-aggregate of the bacterial antenna LH2 there exists a long-standing debate [Sundström et al., 1999, van Amerongen et al., 2000, Dahlbom et al., 2001]. In the present work the exciton delocalization on B850 will be studied by means of subband analysis and pump-intensity-dependent NLPF. For trimeric LHC II only the latter method will be used. By the contribution of emission to the pump-intensity dependence of the NLPF-spectra excitonic coupling may be detected for a chlorophyll dimer acting as terminal emitter at the end of the energy transfer chain in LHC II. An attempt for detecting excitonic coupling between chlorophyll a and chlorophyll b in CP29 by only using subband analysis concludes the second part.

Part I

Theory of NLPF

Chapter 2

Principles of NLPF

This chapter shall provide a very general deduction of the NLPF-spectrum from first principles, which will be further specified in the subsequent chapters. In order to measure the NLPF-signal a classical polarimeter (see Fig. 2.1), which consist of two crossed linear polarizers (polarizer and analyzer), is passed by probe laser beam (index t for test).¹ The sample is located between polarizer and analyzer, where a further laser (index p for pump) intersects the pathway of the probe laser beam. Usually the probe field is much weaker than the pump field. The important feature of the NLPF setup is that the polarization of the pump-laser field \mathbf{E}_p is approximately turned about 45° to that of the probe-laser field \mathbf{E}_t , in order to obtain maximum effect on the probe field by a pump-induced optical anisotropy. Other than in classical polarization spectroscopy in NLPF the sample is ought to be isotropic, i.e. free of circular dichroism (CD) and birefringence (LD). Thus the probing light can pass the analyzer only for an optical anisotropy created by the pump laser field. The NLPF-signal to be measured \mathbf{E}_s is just this pump-induced component which has passed the analyzer, with polarization plane perpendicular to \mathbf{E}_t . Since it has been blocked by the analyzer the incident probe field do not mix, with signal, i.e. the detection is homodyn, though both fields propagate in the same direction, i.e. the wave-vectors \mathbf{k}_s and \mathbf{k}_t are parallel.. Problems can only occur if the signal is contaminated by scattered pump light. This disturbing effect can be reduced by choosing the propagation vector \mathbf{k}_p of the pump laser perpendicular to that of the probe laser \mathbf{k}_t . That one can do so results from the special phase-matching condition for NLPF, which will be shown below. Beside the reduction of scattering, orthogonal propagation of the probe and pump field (see Fig. 2.1) provides furthermore a homogeneous illumination by the pump beam. For the same purpose the pump beam is spread along the probe-pathway by using a set of cylindric lenses.

¹It has to be mentioned that there also versions of NLPF one using circularly and elliptically polarized laser fields [Wieman and Hänsch, 1976, Song et al., 1978]. The present work will only deal with linear polarizations.

2.1. The NLPF-line-shape function

The advantages of this specific setup, reduced scattering and homogeneous illumination, have been proven experimentally [Voigt et al., 1999].

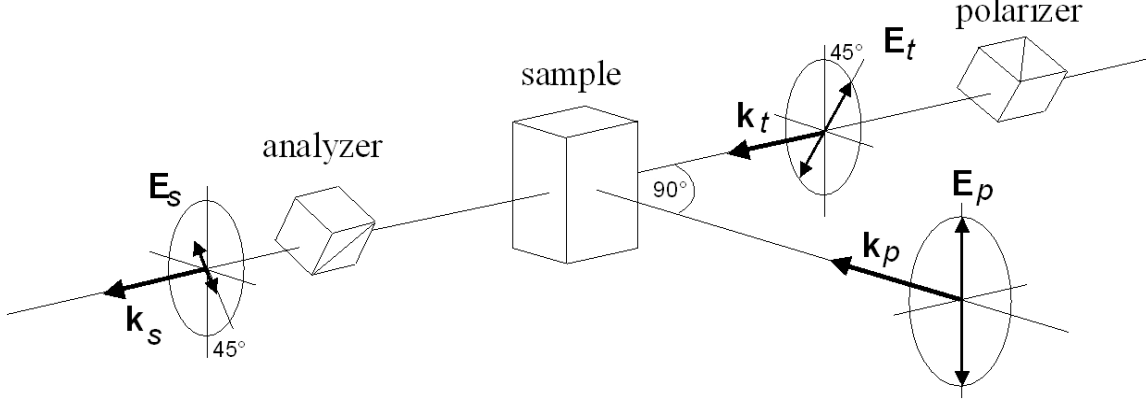


Figure 2.1: NLPF-Setup by [Voigt et al., 1999]: The sample is located between two crossed polarizers which are passed by the probe beam (wavevector \mathbf{k}_t , field \mathbf{E}_t). The pump beam (wavevector \mathbf{k}_p , field \mathbf{E}_p) intersects the probe beam under 90° inside the sample. The polarization of the polarization vectors of pump (\mathbf{E}_p) and probe (\mathbf{E}_t) are turned about 45° to each other. The signal (wavevector \mathbf{k}_s , field \mathbf{E}_s) is detected in the direction of the probe beam ($\mathbf{k}_s \parallel \mathbf{k}_t$) behind the analyzer, i.e. for the polarization perpendicular to the probe ($\mathbf{E}_s \perp \mathbf{E}_t$).

2.1 The NLPF-line-shape function

The aim of the present section is to give a general formula for the NLPF-signal as result of the non-linear response of the sample to the external fields. Thereby the interaction between electromagnetic fields and dye molecules of the sample will be described in the semi-classical approach [Haken, 1989, Mukamel, 1995]. This means that a quantum-mechanical model will be applied to the dye molecule, while the electromagnetic fields will be not quantized but treated as in classical electrodynamics.

2.1.1 External fields and polarization

For frequency domain the probe and the pump laser field will be both approximated by plane monochromatic continuous waves. Thus the total external electromagnetic field acting on the dye molecule is given by

$$\mathbf{E}(t, \mathbf{r}) = \mathbf{E}_p \exp[-i(\omega_p t - \mathbf{k}_p \mathbf{r})] + \mathbf{E}_t(t, \mathbf{r}) \exp[-i(\omega_t t - \mathbf{k}_t \mathbf{r})] + c.c., \quad (2.1)$$

where ω_p is the pump frequency and ω_t is the probe frequency. The wave-vectors of the pump and the probe beam \mathbf{k}_p and \mathbf{k}_t , respectively are arbitrary as one will see below. Nevertheless, as mentioned above a perpendicular intersection of the pump and probe beam is to prefer in order to get a constant amplitude of the pump field \mathbf{E}_p along the propagation path of the probe beam through the sample. Furthermore, the diameter of the probe beam is to be kept much smaller than the absorption length of the sample. Note, however, that the diffraction of the probe beam shall be negligible due to the plane wave approximation in Eq. 2.1. This results in a lower limit for the diameter of the probe beam.²

Using the dipole approximation, which is valid for dye molecules being small compared to the used wavelengths [Cohen-Tannoudji et al., 1977], the time dependent macroscopic polarization $\mathbf{P}(t, \mathbf{r})$ (linear and non-linear) is microscopically given by the expectation value of the oscillating transition dipoles $\langle \mu(t, \mathbf{r}) \rangle$ (the permanent dipole moments μ are supposed to be zero). For the statistical operator $\rho(t, \mathbf{r})$ describing the time evolution of pure as well as mixed quantum state of the dye molecules in Schrödinger representation one obtains

$$\mathbf{P}(t, \mathbf{r}) = \langle \mu(t, \mathbf{r}) \rangle = \frac{1}{8\pi} \int \text{tr} \{ \mu \rho(t, \mathbf{r}) \} d\Theta. \quad (2.2)$$

The integral $\int \dots d\Theta$ provides the average over the different orientations of the molecules in the sample. For samples used in NLPF this average it is zero when all fields are switched off due to the precondition that the sample is isotropic. For fields switched on the statistical operator $\rho(t, \mathbf{r})$ will depend on the external fields for the electromagnetic interaction given by $\mu \mathbf{E}(t, \mathbf{r})$. Therefore, the orientational averaging acts also on $\rho(t, \mathbf{r})$ and will result in a non-vanishing NLPF-signal as will be demonstrated in. section 2.4. As will be shown below, for a constant pump field amplitude \mathbf{E}_p the non-linear polarization $\mathbf{P}(t, \mathbf{r})$ follows the probe field $\mathbf{E}_t(t, \mathbf{r})$ in respect of the dependency on \mathbf{r} and t , though not in respect of phase and polarization.

2.1.2 Phase-matching condition

For a sample that consists of homogeneously diluted dye molecules which are much smaller than the occurring wavelengths and are not interacting to each other the statistical operator $\rho(t, \mathbf{r})$ follows locally the external fields $\mathbf{E}(t, \mathbf{r})$. In frequency domain, for the periodic external field, i.e. constant amplitudes \mathbf{E}_p and \mathbf{E}_t (the latter assumed as a slowly varying amplitude) one can expand the statistical operator $\rho(t, \mathbf{r})$ into Fourier-series of the carrier-waves as

$$\rho(t, \mathbf{r}) = \sum_{n_p, n_t} \rho^{(n_p, n_t)} \exp [i (n_p (\omega_p t - \mathbf{k}_p \mathbf{r}) + n_t (\omega_t t - \mathbf{k}_t \mathbf{r}))]. \quad (2.3)$$

²Note, however, that the diffraction of the probe beam shall be neglectable in order to the approximative use of Eq. 2.1. This results in a lower limit for the diameter of the probe beam.

2.1. The NLPF-line-shape function

Here the Fourier components $\rho^{(n_p, n_t)}$ are constant but complex. By inserting $\rho(t, \mathbf{r})$ as given in 2.3 into the Fourier-transformed expression for the polarization (cf. Eq. 2.2) one obtains the Fourier transformed polarization as

$$\begin{aligned}
 P_s(\omega_s, \mathbf{k}_s) &= \frac{N}{128\pi^5} \sum_{n_p, n_t} \int \text{tr} \{ \mu_s \rho^{(n_p, n_t)} \} d\Theta \\
 &\times \int_{-\infty}^{\infty} \exp[-i(\omega_s - n_p \omega_p - n_t \omega_t)t] dt \\
 &\times \int_V \exp[i(\mathbf{k}_s - n_p \mathbf{k}_p - n_t \mathbf{k}_t) \mathbf{r}] d^3r
 \end{aligned} \tag{2.4}$$

where μ_s is the component of the dipole operator μ parallel to \mathbf{E}_s , i.e. to the polarization plane of the analyzer. The Fourier integral in time results in frequency constriction

$$\omega_s = n_p \omega_p + n_t \omega_t \tag{2.5}$$

and for macroscopic volumes V of the sample the evaluation of the space integrals results in likewise in the phase-matching condition

$$\mathbf{k}_s = n_p \mathbf{k}_p + n_t \mathbf{k}_t. \tag{2.6}$$

Both together can be only fulfilled for

$$n_p = 0, n_t = 1, \tag{2.7}$$

since harmonic generation by the probe are to exclude for its weakness. This means that the pump-wave-vectors \mathbf{k}_p can be arbitrarily oriented, particularly it may be perpendicular to the probe-wave-vector \mathbf{k}_t as shown in Fig. 2.1, and the probe light is monochromatic at the same frequency as the probe³. Thus the NLPF signal is generated only by the component of polarization

$$P_s(\omega_t, \mathbf{k}_t) = \frac{N}{8\pi^2} \int \text{tr} \{ \mu_s \rho^{(0,1)} \} d\Theta. \tag{2.8}$$

2.1.3 Signal generation and reabsorption: the NLPF-line-shape function

As mentioned above, the pump field (\mathbf{E}_p) can be set approximately constant by experimental dispositions. However, the amplitude of the NLPF-signal, will depend only on the generation by

³Nevertheless, in praxi one will use a monochromator after the analyzer in order to detect a NLPF signal being free of e.g. scattered pump light.

the nonlinear polarization but also on the linear absorption and reabsorption of probe and signal, respectively, during their way through the sample. Splitting off the linear (re)absorption for \mathbf{E}_s and \mathbf{E}_t , which for both is given by the same optical density $OD(\omega_t)$ (cf. Eq. 2.5), the NLPF-signal after passing the sample can be calculated in slowly varying amplitude approximation to

$$\mathbf{E}_s(\omega_t) = \frac{i\omega_t}{nc\varepsilon_0} \mathbf{P}_s(\omega_t, \mathbf{k}_t) \times OD(\omega_t) \exp[-OD(\omega_t)]. \quad (2.9)$$

Here $\mathbf{P}_s(t, r_t)$ is the vector component of the non-linear polarization perpendicular to \mathbf{E}_t , According to the homodyn detection, the NLPF signal is given by the intensity of the signal⁴ as $I_s(\omega_t) \propto |\mathbf{E}_s(\omega_t)|^2$. From Eqs. 2.9 follows that for optimal signal intensity the optical density of the sample should be chosen as $OD(\lambda_t) \approx 2$. This value can be adjusted either by the concentration of dye molecules (N) or the path length through the sample (D). Note, however, that long pathways of the probe beam through the sample make the homogeneous illumination by the pump beam more difficult, but high optical densities may influences the pump-frequency dependence of the NLPF-spectrum by non-uniformly absorption of the pump. The latter effect can be reduced by locating the probe beam near to the incident face for the pump beam. Otherwise, the NLPF-signal is also to be corrected by the respective effective pump intensity. This leads already to the definition of the NLPF-line-shape function as given by

$$S(\omega_t, \omega_p, I_p) = \frac{E_s(\omega_t, D)}{E_t(\omega_t, D)} \xrightarrow{I_p \rightarrow 0} s(\omega_t, \omega_p) I_p. \quad (2.10)$$

The pump-intensity independent function $s(\omega_t, \omega_p)$ represents the NLPF-line-shape function in third order perturbation theory for low pump intensities, while $S(\omega_t, \omega_p, I_p)$ is to use for arbitrary pump intensities (cf. chapter 6).

At last it has to be noted, that a weak linear circular dichroism (CD) will not distort the NLPF-measurements in principle. In this case the analyzer is only to be adjusted in such a way, that (for pump beam switched off) the probe field $\mathbf{E}_t(t, \mathbf{r})$ turned by the CD is blocked as well. Since CD is a linear effect, the polarization plane of the signal $\mathbf{E}_s(t, \mathbf{r})$ turns just the same amount as $\mathbf{E}_t(t, \mathbf{r})$. Therefore the fundamental condition for NLPF, that probe and signal field are always perpendicular, will hold also in the presence of an weak CD as long as the turn of the polarization planes is significantly less than 45° . Otherwise, the pump-field-induced anisotropy would not be able to turn the probe polarization in an unambiguous way. In case of doubt one should simply shorten the optical path length for the probe beam.

⁴In the present work intensities are all given in photons $\text{cm}^{-2}\text{s}^{-1}$.

2.2 Molecular response to the external fields

According to Eq. 2.8 the Fourier component $\rho^{(0,1)}$ of the statistical operator $\rho(t)$, describing the non-linear response of the molecular system primarily relevant for generation of the NLPF signal. however, this Fourier component must also depend on the pump field. Otherwise, the response would be only linear and blocked by the analyzer.

In general the time evolution of the statistical operator $\rho(t)$ used in Eq. 2.2 is ruled by the Liouville-von-Neumann equation

$$\frac{\partial}{\partial t}\rho(t) = -i\mathcal{L}(t)\rho(t) \quad (2.11)$$

with the Liouville super-operator $\mathcal{L}(t)$ given by the commutator

$$\mathcal{L}(t)\dots = \frac{1}{\hbar}[H(t),\dots], \quad (2.12)$$

for the Hamiltonian

$$H(t) = H_{mol} - \mu\mathbf{E}(t, \mathbf{r}). \quad (2.13)$$

consisting of the molecular Hamiltonian H_{mol} and the interaction of the molecular dipole operator μ with the external electromagnetic field $\mathbf{E}(t, \mathbf{r})$ as defined in Eq. 2.1. According to the semi-classical approach (see above) the latter will be treated as a classical field [Haken, 1994, Mukamel, 1995].

In order to determine the Fourier components $\rho^{(n_p, n_i)}$ in terms of a response of the molecular system on the external fields, it is useful to introduce the Fourier-transformed Greens-function $\mathcal{G}(\omega)$ for the Liouville-von-Neumann equation Eq. 2.11 as given by by the equation

$$i(\omega + \mathcal{L}_0)\mathcal{G}(\omega) = 1. \quad (2.14)$$

In principle $\mathcal{G}(\omega)$ solves the quantum-mechanical problem for the molecular response exactly. In praxi, however, such a proceeding is impossible due to the enormous degree of freedom for the molecular system, in particular for dye molecules being embedded in a matrix of condensed matter, liquid or glass. Therefore, one has to reduce the statistical operator $\rho(t)$, and consequently $\mathcal{G}(\omega)$, in order to obtain an equation analogues to Eqs. 2.11 and 2.14 but containing an effective Liouville operator \mathcal{L}_0 for the molecular system with much lower rank. In chapter 3 it will be shown, how this can be done for molecular systems with dissipative surrounding, resulting in a superoperator \mathcal{L}_0 which contains imaginary relaxation terms. For the time being, let us assume that \mathcal{L}_0 is known. Unfortunately, Eq. 2.14 is not invertible, because even the effective Liouville operator \mathcal{L}_0 is singular (cf. chapter 3). Hence, one needs additionally the

constrictions

$$\text{tr} \{ \mathcal{G}(\omega) \} = 0 \quad (2.15)$$

$$\mathcal{G}^\dagger(\omega) = \mathcal{G}(-\omega). \quad (2.16)$$

The first constriction guarantees the fundamental property of any statistical operator

$$\text{tr} \{ \rho \} = 1, \quad (2.17)$$

meaning that the probability to find the system in any state is certain. The second constriction means the hermitism of the statistical operator, i.e. $\rho^\dagger(t) = \rho(t)$. From the general solution of Eq. 2.14 one obtains resonances of $\mathcal{G}(\omega)$ at the eigen-frequencies $\omega_{\mu\nu}$ of the Liouville operator \mathcal{L}_0 .

Using the Fourier-transformed Greens-functions $\mathcal{G}(\omega)$, the Fourier-components $\rho^{(n_p, n_t)}$ of the statistical operator can be determined in response to the external fields \mathbf{E}_p and \mathbf{E}_t by the recursive formula

$$\begin{aligned} \rho^{(n_p, n_t)} &= \rho^{eq} \delta_{n_p, 0} \delta_{n_t, 0} + \mathcal{G}(n_p \omega_p + n_t \omega_t) \\ &\times \left\{ [\mu, \mathbf{E}_p \rho^{(n_p-1, n_t)}] + [\mu, \mathbf{E}_p^*, \rho^{(n_p+1, n_t)}] \right. \\ &\quad \left. + [\mu, \mathbf{E}_t \rho^{(n_p, n_t-1)}] + [\mu \mathbf{E}_t^*, \rho^{(n_p, n_t+1)}] \right\}. \end{aligned} \quad (2.18)$$

This recursive approach is very useful for perturbation theory, but also to find a self consistent equation for strong pump fields. Note that the recursions break off for ρ^{eq} , which is the solution of the stationary Liouville-von-Neumann equation $\mathcal{L}_0 \rho^{eq} = 0$ constricted by Eq. 2.17.

Finally a simple, more empirical model of a dissipative two-level system shall be demonstrated (cf. chapter 3). In this model the Liouville operator \mathcal{L}_0 is given by the matrix elements

$$[\mathcal{L}_0]_{1010} = -[\mathcal{L}_0]_{0101}^* = \omega_{10} + i\Gamma \text{ and } [\mathcal{L}_0]_{0011} = i\gamma. \quad (2.19)$$

According to Eq. 2.11, the off-diagonal matrix element $\rho_{10}(t)$ describes a oscillation with the frequency ω_{10} damped by the dephasing rate Γ . The diagonal matrix element $\rho_{11}(t)$ represents the excited state population, which decays with the energy relaxation rate γ . The ground-state occupation, yields as $\rho_{00}(t) = 1 - \rho_{11}(t)$. The corresponding Fourier-transformed Greens function (cf. Eq. 2.14) consists only of the matrix elements

$$\mathcal{G}_{1010}(\omega) = -\mathcal{G}_{0101}^*(-\omega) = \frac{1}{i\omega + i\omega_{10} + \Gamma}, \quad (2.20)$$

$$\mathcal{G}_{0011}(\omega) = -\mathcal{G}_{1111}(\omega) = \frac{1}{i\omega + \gamma}. \quad (2.21)$$

In the next section, it will be demonstrated that these two groups of Greens functions correspond to two kinds of peaks in the NLPF-spectrum, which are quite different in respect of their dependences on the pump and probe frequency. All other matrix elements of $\mathcal{G}(\omega)$ are zero.

2.3 Components of NLPF-spectra

The NLPF-signal can be deduced in any order of the external fields by using a self-consistent solution of Eq. 2.18. Nevertheless, it is useful to constrain the calculation to the first order of \mathbf{E}_t , according to the weakness of a typical probe field. This means namely to neglect all terms $\rho^{(n_p, n_t)}$ for $|n_t| > 1$. Thus the last term in Eq. 2.18 vanishes for $\rho^{(0,1)}$ and one obtains the NLPF-line-shape function (cf. Eqs. 2.10, 2.9, and 2.8) as

$$S(\omega_t, \omega_p, I_p) = \frac{1}{8\pi^2 (\hbar\varepsilon_0 n c)^3} \int \text{tr} \left\{ \mu_s \mathcal{G}(\omega_t) \left([\mu_t, \rho^{(0,0)}] + [\mu_p, \rho^{(-1,1)}] \frac{E_p}{E_t} + [\mu_p, \rho^{(1,1)}] \frac{E_p^*}{E_t} \right) \right\} d\Theta, \quad (2.22)$$

where μ_p and μ_t are the components of the dipole operator μ parallel to \mathbf{E}_p and \mathbf{E}_t , respectively. In what follows the three commutators occurring in NLPF-line-shape function will be discussed separately. due to the different indices for the Fourier components $\rho^{(0,0)}$, $\rho^{(-1,1)}$, and $\rho^{(1,1)}$ the normalized NLPF-spectra as given by $|S(\omega_t, \omega_p, I_p)|^2$ shows quite different spectral features, distinguishable by their dependence on the probe and pump frequency. For reasons explained in what follows, these will be called the T_2 -, T_1 - and two-photon-peaks, respectively.

2.3.1 T_2 -peaks

According to Eq. 2.18 the Fourier component $\rho^{(0,0)}$ is given by

$$\rho^{(0,0)} = \rho^{eq} + \mathcal{G}(0) [\mu_p, \mathcal{G}(\omega) [\mu_p, (|E_p|^2 \rho^{(0,0)} + E_p^2 \rho^{(-2,0)})] - h.c.]. \quad (2.23)$$

It has to be noted that for the constriction to first order in \mathbf{E}_t any Fourier component $\rho^{(n_p, 0)}$ can only be recurred to components with $n_t = 0$. Therefore $\rho^{(0,0)}$ does not depend on the probe frequency ω_t . Furthermore, it depends only on powers of the pump intensity.⁵ This property is quite useful for the calculation of the NLPF-line-shape function $S(\omega_t, \omega_p, I_p)$ for higher pump intensities I_p , as performed in chapter 6. For low pump intensity one obtains approximately

$$\rho^{(0,0)} = \rho^{eq} + i\mathcal{G}(0) \sigma(\omega_p, \omega_p) \rho^{eq} I_p + O(I_p^2). \quad (2.24)$$

Here the operator for the generalized cross-sections of pumping has been introduced by

$$\sigma^{(x,y)}(\omega, \omega') \rho^{eq} = \frac{-i\omega'}{\hbar\varepsilon_0 n c} \{ [\mu_x, \mathcal{G}(\omega) [\mu_y, \rho^{eq}]] + [\mu_y, \mathcal{G}(-\omega') [\mu_x, \rho^{eq}]] \}. \quad (2.25)$$

⁵The reason for this behavior is, that by the subsequent recursions of the term $\rho^{(-2,0)} E_p^2$ in Eq.2.23 one obtains terms proportional to $|E_p|^2 \rho^{(0,0)}$ and to $E_p^4 \rho^{(-4,0)}$. The latter has to be recurred again. Since all recursions breaks only for $\rho^{(0,0)} = \rho^{eq} + \dots$, the right side of the equality in Eq. 2.23 represents a series in terms of $|E_p|^{2n} \rho^{eq} \propto I_p^n \rho^{eq}$.

As one will see below, it is useful to allow different indices for the arguments of the external fields on frequencies and dipoles. The cross-section of pumping with indices $x = y$ and arguments $\omega = \omega'$ is directly related to the total cross-section of absorption $\sigma_{abs}(\omega)$ by

$$\sigma_{abs}(\omega) = \frac{1}{8\pi^2} \int \text{tr} \{ \sigma^{(x,x)}(\omega, \omega) \rho^{eq} \} d\Theta. \quad (2.26)$$

Inserting Eq. 2.24 in Eq. 2.22 results in the first term of the NLPF-line-shape function at low intensities as

$$s(\omega_t, \omega_p) = \frac{1}{8\pi^2} \int \text{tr} \{ \zeta^{(s,t)}(\omega_t) \mathcal{G}(0) \sigma^{(p,p)}(\omega_p, \omega_p) \rho^{eq} \} d\Theta I_p E_t + \dots \quad (2.27)$$

using the probing function

$$\zeta^{(s,t)}(\omega) \dots = \frac{i\omega}{\hbar \varepsilon_0 n c} \mu_s \mathcal{G}(\omega) [\mu_t, \dots]. \quad (2.28)$$

For the example model of a dissipative two-level system (cf. Eqs. 2.20 and 2.21) the orientational averaging results in an factor 1/15 (cf. section 2.4). Neglecting terms containing $(\omega_{p,t} + \omega_{10})^2$ in the denominator (rotating wave approximation), the remaining cross-section of pumping needed in Eq. 2.27 is given by

$$\sigma_{10}(\omega_p, \omega_p) = \frac{\mu_{10}^2}{\hbar \varepsilon_0 n c} \frac{2\Gamma \omega_p}{(\omega_p - \omega_{10})^2 + \Gamma^2}. \quad (2.29)$$

Note that in this model $\rho_{11}^{eq} = 0$ and $\rho_{00}^{eq} = 1$. The probing functions yield as

$$\zeta_{10}(\omega_t) = \zeta_{01}(\omega_t) = \frac{\mu_{10}^2}{\hbar \varepsilon_0 n c} \frac{\omega_t}{\omega_t - \omega_{10} + i\Gamma} \quad (2.30)$$

in rotating wave approximation. The central Greens-function $\mathcal{G}(0)$ in Eq. 2.27 reduces to a constant γ^{-1} , which represents the effective lifetime of the excited state. Thus the first contribution to the NLPF-line-shape function of the two level system at low pump-intensities is given by

$$s(\omega_t, \omega_p) = \frac{1}{15} \frac{\mu_{10}^4}{(\hbar \varepsilon_0 n c)^2} \frac{\omega_t}{\omega_t - \omega_{10} + i\Gamma} \frac{1}{\gamma} \frac{2\Gamma \omega_p}{(\omega_p - \omega_{10})^2 + \Gamma^2} + \dots \quad (2.31)$$

as previously obtained e.g. by Neef and Mori [Neef and Mory, 1991]. The corresponding spectral feature in the two-dimensional NLPF-spectrum is a single peak centered at $\omega_t, \omega_p = \omega_{10}$ as shown in Fig. 2.2. This peak will be called T₂-peak in what follows since its widths in probe- and pump-frequency dependence, respectively are determined by dephasing rate Γ which corresponds to the inverse of the transversal relaxation time T₂. The line shape of T₂-peak

2.3. Components of NLPF-spectra

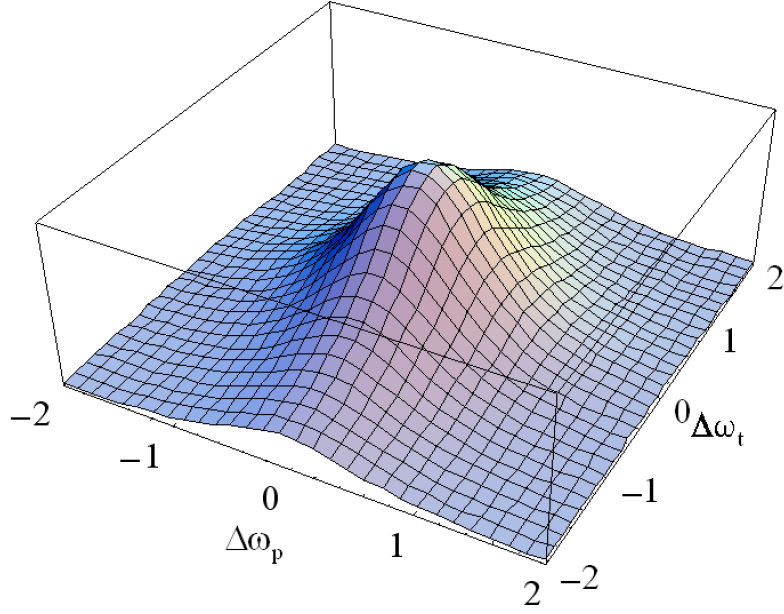


Figure 2.2: T_2 -peak of a two-level system. Axes labeled by $\Delta\omega_{p,t} = (\omega_p - \omega_{10})/\Gamma$. NLPF-signal in arbitrary units.

in respect of the probe-frequency dependence is despite of the factor ω_p in Eq. 2.31 in good approximation a Lorentzian with width $FWHM = 2\Gamma$, while in respect of the probe-frequency dependence the Lorentzian is squared and consequently $FWQM = 2\Gamma$ ($FWHM$: full width at half maximum; $FWQM$: full width at quarter maximum).

For multi-level systems more resonances for a higher dimensional matrix $\mathcal{G}(\pm\omega)$ will occur. For the additional resonances at different eigen-frequencies of the Liouville operator several T_2 -peaks will appear in the NLPF-spectrum. These are correlated in respect of their probe- and pump-frequency dependence by the matrix $\mathcal{G}(0)$. A detailed discussion of the resulting patterns of T_2 -peaks will be presented in the chapter 4. Analysis of these patterns will allow one to determine the term scheme and the associated energy relaxation path to quite large extend.

2.3.2 T_1 -peak

According to Eq. 2.18 the Fourier component $\rho^{(-1,1)}$ is given by the recursion

$$\rho^{(-1,1)} = \mathcal{G}(\omega_t - \omega_p) \{ [\mu_t, \rho^{(-1,0)}] E_t + [\mu_p, \rho^{(0,1)}] E_p^* + [\mu_p, \rho^{(-2,1)}] E_p \}. \quad (2.32)$$

For the weakness of the probe field, the subsequent recursions can do the step from $n_t = 1$ to $n_t = 0$ only once. The step back to $n_t = 1$ is forbidden. Since the break off is reached only for

the term $\rho^{eq}\delta_{n_p,0}\delta_{n_t,0}$ in Eq. 2.18, the second term of $S(\omega_t, \omega_p, I_p)$ will be finally recurred to the self-consistent solution for $\rho^{(0,0)}$ (see above) as will be explicitly demonstrated in chapter 6.

The last term in Eq. 2.32 is at least of the order I_p^2 . Therefore it is to neglect in NLPF-line-shape function $s(\omega_t, \omega_p)$ at low intensities, which second term of yields as

$$s(\omega_t, \omega_p) = \dots + \frac{1}{8\pi^2} \int \text{tr} \{ \zeta^{(s,p)}(\omega_t) \mathcal{G}(\omega_t - \omega_p) \sigma^{(t,p)}(\omega_t, \omega_p) \rho^{eq} \} d\Theta + \dots \quad (2.33)$$

The probing functions $\zeta^{(s,p)}(\omega_t)$ and cross-sections of pumping $\sigma^{(t,p)}(\omega_t, \omega_p)$ are given by Eqs. 2.28 and 2.25, respectively. Note the different indices on the arguments for the cross-section of pumping $\sigma_{tp}(\omega_t, \omega_p)$. These give rise to usually minor corrections in the line shape. The main spectral feature results from the central Greens function $\mathcal{G}(\omega_t - \omega_p)$, which depends now on the detuning between pump and probe frequency. In the case of the exemplary two-level system Eq. 2.33 results in

$$s(\omega_t, \omega_p) = \dots + \frac{1}{15} \frac{\mu_{10}^4}{(\hbar\varepsilon_0 n c)^2} \frac{\omega_t}{\omega_t - \omega_{10} + i\Gamma} \frac{1}{\gamma + i(\omega_t - \omega_p)} \times \left(\frac{\omega_p}{\Gamma + i(\omega_t - \omega_{10})} + \frac{\omega_p}{\Gamma - i(\omega_p - \omega_{10})} \right) \quad (2.34)$$

for rotating wave approximation (cf. [Neef and Mory, 1991]). For $\gamma \ll \Gamma$ this term means a single narrow peak in the NLPF-spectrum with maximum at $\omega_p = \omega_t$. In respect of its dependence on the detuning $\omega_t - \omega_p$ it represents at least in the upper part an Lorentzian with line width $FWHM = 2\gamma$. Because γ equals the inverse longitudinal relaxation time T_1 , this peak has been named by the author the T_1 -peak [Voigt et al., 1999]. Thus it has been often used in order to determine the energy relaxation rates (but see below).

For the two-level system, the sum of the two terms given by Eqs. 2.31 and 2.34 represents already the complete NLPF-line shape function. Fig. 2.3 shows an exemplary NLPF-spectra of a two-level system scanned over the pump frequency ω_p for three different probe frequencies ω_t . For each spectrum one can recognize both, the broad T_2 -peak centered at $\omega_p = \omega_0$ and the narrow T_1 -peak at $\omega_p \approx \omega_t$, which reflects exactly the behavior mentioned above.

For multi-level systems the T_1 -peak shows usually a complex substructure, as will be demonstrated in chapter 4. This may complicate the determination of the relaxation time by the T_1 -peak. Furthermore, for multi-level systems $\mathcal{G}(\omega_t - \omega_p)$ possess more than one resonance in the spectrum dependent on the detuning $(\omega_t - \omega_p)$. These so-called tunneling terms [Chachisvilis and Sundström, 1996] result in additional side-peaks apart from the central T_1 -peak at $\omega_t = \omega_p$. They do not concern the energy relaxation but are connected with coherence between two excited states close to each other. As related to the molecular Raman effect, they may be called ‘Raman’ peaks, which will be discussed in a special case in chapter 4 (cf. section 4.3.2).

2.3. Components of NLPF-spectra

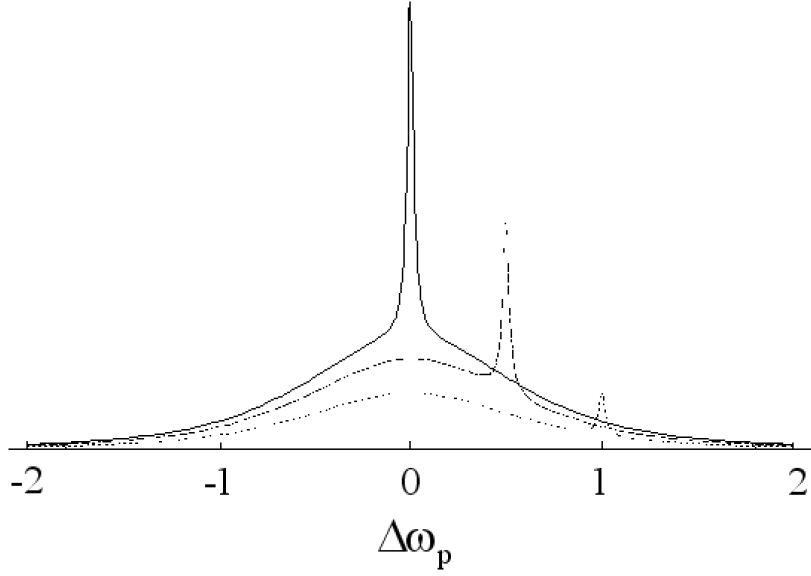


Figure 2.3: NLPF-spectra of a two level system with $\gamma = 0.1\Gamma$ for probe frequencies $\omega_t = \omega_0$ (solid line), $\omega_0 + 0.5\Gamma$ (dashes), and $\omega_0 + 1\Gamma$ (dots) recorded over $\Delta\omega_p = (\omega_p - \omega_0) / \Gamma$.

The mentioned tunneling terms occur also for $\mathcal{G}(0)$ in the T_2 -peak. There, however, they represent only minor corrections to the line shape of the T_2 -peak, which can be estimated to be less than 10 % even for dephasing and energy relaxation rates of the same order of magnitude. In the present work effects by these tunneling terms will not be studied any further.

2.3.3 Two-photon-peaks

The last term in Eq. 2.22 can be also recurred according to Eq. 2.18, what results in

$$\rho^{(1,1)} = \mathcal{G}(\omega_t + \omega_p) \{ [\mu_t, \rho^{(1,0)}] E_t + [\mu_p, \rho^{(0,1)}] E_p + [\mu_p, \rho^{(2,1)}] E_p^* \}. \quad (2.35)$$

Though this equation seems to be quite similar to Eq. 2.32, due to the different sign of ω_p in the argument of $\mathcal{G}(\omega_t + \omega_p)$ and $\mathcal{G}(\omega_t - \omega_p)$, respectively, the resulting spectral features are completely different. Firstly, the relevant resonances for $\mathcal{G}(\omega_t + \omega_p)$ are definitely not related to energy relaxation but to doubly excited states. Secondly, $\rho^{(1,1)}$ represents a direct two photon absorption. However, in contrast to Fourier components $\rho^{(2,0)}$ and $\rho^{(-2,0)}$ here an probe and pump photon are to absorb simultaneously, i.e. within the dephasing time between the ground- and the doubly excited state. For this specificity $\rho^{(1,1)}$ contributes to the NLPF-line-shape function even at lowest pump intensities by the term

$$s(\omega_t, \omega_p) = \dots + \frac{1}{8\pi^2} \int \text{tr} \{ \zeta^{(s,p)}(\omega_t) \mathcal{G}(\omega_t + \omega_p) \sigma^{(p,t)}(\omega_t, -\omega_p) \rho^{eq} \} d\Theta I_p E_t. \quad (2.36)$$

According to resonance frequencies $\omega_{\mu\nu}$ of the Greens function $\mathcal{G}(\omega)$ in the NLPF-spectrum two-photon peaks will appear at the sum frequencies $\omega_t + \omega_p = \omega_i \gg 0$. In what follows the two-photon peak will be also ignored. Thus, the following statements may be sufficient: (i) The widths of the two-photon-peaks are not related to dephasing rates. The reason is, that the energy relaxation is strictly connected to the resonance maximum of $\mathcal{G}(\omega)$ at $\omega \approx 0$, as one will see in chapter 3. (ii) For a two-level system the two-photon peaks is neglected in rotating wave approximation, because either $\mathcal{G}(\omega_t + \omega_p)$ or $\sigma^{(p,t)}(\omega_t, -\omega_p)$ have to be extremely off-resonant. (iii) For multi-level systems where all transitions are allowed at least one two-photon peak interfere with one of the T_2 -peaks. This results from the fact, that the term $\mathcal{G}(\omega_t + \omega_p) \sigma_{pt}(\omega_t, -\omega_p)$ contains necessarily a common resonance with $\sigma_{pp}(\omega_p, \omega_p)$. (v) For dephasing much faster than the energy relaxation the two-photon peak can be neglected compared the T_2 -peak. The same holds for contributions by two-photon processes, which are related to the Fourier components $\rho^{(2,0)}$ and $\rho^{(-2,0)}$, for NLPF-spectra at high pump intensities.

2.4 Orientational averaging

The probing functions as well as the cross-sections of pumping (cf. Eqs. 2.28 and 2.25, respectively) depends on the orientation of the transition dipoles μ relative to the external fields \mathbf{E}_p , \mathbf{E}_t , and the signal polarization \mathbf{E}_s as the superscripts in the Eqs. 2.24, 2.33, and 2.36 assign. Therefore, the integrals $\int \dots d\Theta$ for the averaging over isotropic oriented molecules acts not only on the component of the transition dipole moment μ_s parallel to \mathbf{E}_s but also on the scalar products $\mu \mathbf{E}_t = \mu_t E_t$ and $\mu \mathbf{E}_p = \mu_p E_p$, as mentioned above. Here, the averaging will be shown for probed and pumped transition dipoles being parallel, what is trivially fulfilled for the two level system.

In this case two Euler angles describe the relevant orientation of the molecule (cf. Fig. 2.4): θ which is defined as the angle between the dipole operator μ and the probe wave-vector \mathbf{k}_t ; and ϕ which is the angle between the pump field \mathbf{E}_p and the projection of the transition dipole μ into the plane perpendicular to \mathbf{k}_t , and which is counted from the direction of \mathbf{E}_p towards that of \mathbf{E}_t . A third Euler angle ψ , describing rotations of the molecule around the transition dipole μ is not required. With this choice of angles describing the molecular orientation one obtains

$$\mu_p = |\mu| \sin \theta \cos \phi, \quad \mu_t = |\mu| \sin \theta \cos \left(\phi + \frac{\pi}{4} \right), \quad \text{and} \quad \mu_s = |\mu| \sin \theta \cos \left(\phi - \frac{\pi}{4} \right). \quad (2.37)$$

Thus for low intensities the averaging integral is given by

$$\frac{1}{4\pi} \int_0^\pi \sin^5 \theta d\theta \int_0^{2\pi} \cos \left(\phi - \frac{\pi}{4} \right) \cos \left(\phi + \frac{\pi}{4} \right) \cos^2 \phi d\phi = \frac{1}{15} \quad (2.38)$$

2.4. Orientational averaging

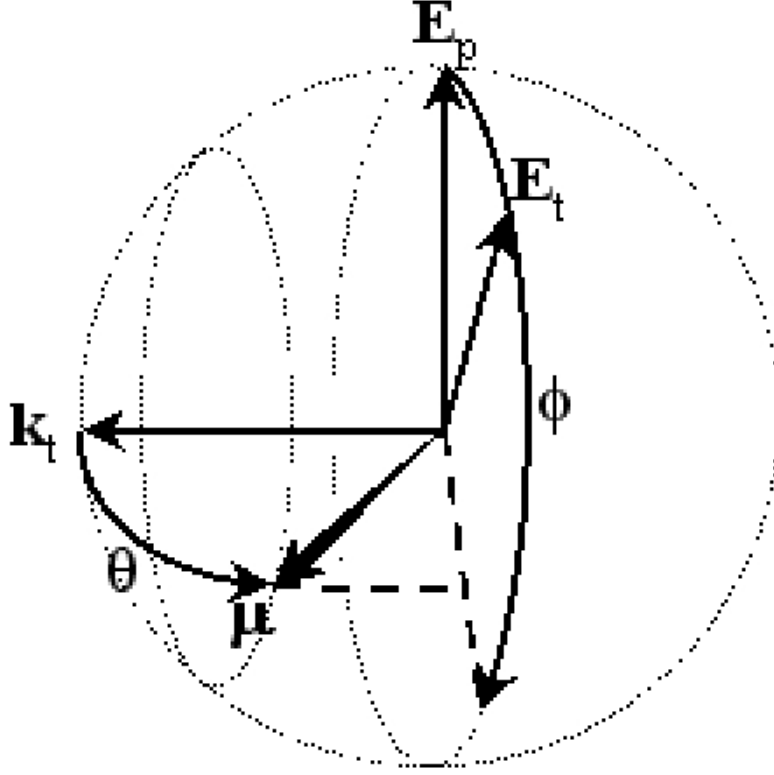


Figure 2.4: Illustration of the two Euler angles θ and ϕ as described in the text. \mathbf{E}_p and \mathbf{E}_t are the pump and probe field, respectively. \mathbf{k}_t the wavevector of the probe. μ is the transition dipole vector, which is to average over the whole sphere.

and the NLPF-line-shape function turns finally out as

$$s(\omega_t, \omega_p) = \frac{1}{15} \text{tr} \{ \zeta(\omega_t) [\mathcal{G}(0) \sigma(\omega_p, \omega_p) + \mathcal{G}(\omega_t - \omega_p) \sigma(\omega_t, \omega_p) + \mathcal{G}(\omega_t + \omega_p) \sigma(\omega_t, -\omega_p)] \rho^{eq} \}, \quad (2.39)$$

where the probing function and the cross-section of pumping are defined as in Eqs. 2.28 and 2.25 but using $\mu = |\mu|$ instead of different μ_x and μ_y . Analogously, for the cross-section of linear absorption the orientational averaging yields

$$\sigma(\omega) = \frac{1}{3} \text{tr} \{ \sigma(\omega, \omega) \rho^{eq} \}. \quad (2.40)$$

For the multilevel-system the averaging may be complicated by a possible angle between the transition dipole moment probed and that pumped. For non-parallel transition dipoles one can expect that the averaging for the three addends of the NLPF-line-shape function, given by Eqs. 2.24, 2.33, and 2.36, results in different prefactors depending on this angle. Nevertheless,

this averaging can be performed in a similar way as will be demonstrated in section 4.1. More intricate is the orientational averaging at high intensities, since from solving the self-consistent equations one obtains denominators which depends on the angles θ and ϕ . As shown in chapter 6 this difficulty have been be overcome only for specific multi-level systems with parallel dipole moments yet.

2.5 Summary

Above the NLPF-spectrum has been deduced from a microscopic model for the nonlinear polarization by using Fourier-transformed Greens-function $\mathcal{G}(\omega)$ related to the statistical operator $\rho(t)$, which describes the coherent as well as the incoherent quantum dynamics of the dye molecules to be studied, particularly, energy relaxation and dephasing. The external fields has been treated classically. This results in a NLPF-line-shape function $s(\omega_t, \omega_p)$, the square module of represents the normalized two-dimensional NLPF-spectrum (cf. Eq. 2.10). For the two-level system (cf. Eq. 2.24 and 2.33) the NLPF-line-shape function at low pump intensity yields as

$$s(\omega_t, \omega_p) = \frac{1}{15} \frac{|\mu_{10}|^4}{(\hbar \varepsilon_0 n c)^2} \frac{\omega_t}{\omega_t - \omega_{10} + i\Gamma} \left\{ \frac{1}{\gamma (\omega_p - \omega_{10})^2 + \Gamma^2} + \frac{\omega_t}{\omega_t - \omega_p + i\gamma} \left(\frac{\omega_p}{\omega_t - \omega_{10} + i\Gamma} - \frac{\omega_p}{\omega_p - \omega_{10} - i\Gamma} \right) \right\} \quad (2.41)$$

where ω_{10} , μ_{10} , Γ , and γ represent transition frequency, transition dipole, dephasing rate and energy relaxation rate, respectively.

In general, for low pump intensities kinds of peaks are apparent in a NLPF-spectrum according to the different terms of the NLPF-line-shape function $s(\omega_t, \omega_p)$. Due to their different dependence on pump and probe frequency, as well as for their different widths, they have been classified as T_2 -, T_1 - and two-photon-peaks. The T_2 -peaks indicate the spectral positions of the transitions and the corresponding widths give the dephasing rates (cf. Fig. 2.3). The T_1 -peak depends on the detuning between probe and pump frequency and for the simples case of a two-level system its width give the energy relaxation rate γ . For multi-level systems it will be structured and probably ‘Raman’-peaks will appear as side bands. The two-photon peaks only appears in multi-level systems, where doubly excitation by two-photon processes is possible. It depends on the sum-frequency of pump and probe. As exceptional cases which appears only for dephasing rates smaller or equal the energy relaxation, ‘Raman’ and two-photon-peaks will be not discussed any further. The pattern and structures of T_2 - and T_1 -peaks, however, will be discussed in the three following chapters comprehensively.

2.6. Supplement: Time-domain description of NLPF-spectra

Last but not least it has been shown that in principle the NLPF-signal can be deduced in any order of the pump field strength by a system of self-consistent equations. In detail this will be demonstrated for the two-level system and special cases of multi-level systems in chapter 6.

2.6 Supplement: Time-domain description of NLPF-spectra

Beside the frequency domain techniques using the Fourier-components $\rho^{(n_p, n_t)}$, the NLPF-line-shape function can be also deduced by calculating the time dependent nonlinear response of the system on the external fields (cf. Eq. 2.1). According to the Liouville-von-Neumann equation (see Eq. 2.11) in the time domain the Greens function reads formally as

$$\mathcal{G}(t) = \exp[-i\mathcal{L}_0 t]. \quad (2.42)$$

Then the NLPF line-shape function for low pump intensity can be constituted by a multiple Fourier transformation as

$$s(\omega_t, \omega_p) = \frac{\omega_p \omega_t}{8\pi^3} \iiint_0^\infty S(t_1, t_2, t_3) F(\omega_t, \omega_p; t_1, t_2, t_3) dt_1 dt_2 dt_3 \quad (2.43)$$

using the third-order response function of the molecular system as given in the eigen-basis $\{\mu\}$ of the Hamilton operator H_0 by

$$\begin{aligned} S(t_1, t_2, t_3) = & \frac{1}{15(\hbar\varepsilon_0 n c)^2} \sum_{\mu\nu\kappa\lambda} \mu_{\mu\nu} \mu_{\lambda\kappa} \mathcal{G}_{\mu\nu, \mu\nu}(t_3) \\ & \{ [\mu_{\mu\lambda} \mu_{\kappa\nu} \mathcal{G}_{\mu\kappa, \mu\kappa}(t_2) + \mu_{\nu\mu} \mu_{\kappa\lambda} \mathcal{G}_{\mu\mu, \kappa\kappa}(t_2)] \\ & \times [\mathcal{G}_{\kappa\lambda, \kappa\lambda}(t_1)(n_\kappa - n_\lambda) + \mathcal{G}_{\mu\lambda, \mu\lambda}(t_1)(n_\mu - n_\lambda)] \\ & + [\mu_{\mu\lambda} \mu_{\kappa\nu} \mathcal{G}_{\lambda\nu, \lambda\nu}(t_2) + \mu_{\nu\mu} \mu_{\kappa\lambda} \mathcal{G}_{\nu\nu, \lambda\lambda}(t_2)] \\ & \times [\mathcal{G}_{\kappa\nu, \kappa\nu}(t_1)(n_\nu - n_\kappa) + \mathcal{G}_{\lambda\kappa, \lambda\kappa}(t_1)(n_\kappa - n_\lambda)] \}, \end{aligned} \quad (2.44)$$

and the time-propagation of the monochromatic external fields given by

$$\begin{aligned} F(\omega_t, \omega_p; t_1, t_2, t_3) = & \exp[i\omega_p(t_3 + t_2 + t_1) - i\omega_p(t_3 + t_2) + \omega_t t_3] \\ & + \exp[-i\omega_p(t_3 + t_2 + t_1) + i\omega_p(t_3 + t_2) + \omega_t t_3] \\ & + \exp[i\omega_p(t_3 + t_2 + t_1) + i\omega_t(t_3 + t_2) - \omega_p t_3] \\ & + \exp[i\omega_t(t_3 + t_2 + t_1) - i\omega_p(t_3 + t_2) + \omega_p t_3] \\ & + \exp[-i\omega_p(t_3 + t_2 + t_1) + i\omega_t(t_3 + t_2) + \omega_p t_3] \\ & + \exp[i\omega_t(t_3 + t_2 + t_1) + i\omega_p(t_3 + t_2) - \omega_p t_3], \end{aligned} \quad (2.45)$$

for interactions at times $t - t_3 - t_2 - t_1$, $t - t_3 - t_2$, and $t - t_3$. Note that for sake of causality the three time intervals t_1 , t_2 , and t_3 have to be positive. The function $F(\omega_t, \omega_p; t_1, t_2, t_3)$ shows explicitly the time order of interactions as they result from the Feynman graphs relevant for NLPF as shown in Fig. 2.5. Each of two subsequent terms in Eq. 2.45 corresponds to the frequency dependence of the T_2 -, T_1 - and two-photon-peaks.⁶ The main differences between T_2 -, T_1 -, and two-photon-peak is the time order of the interactions with pump and probe field: For the T_2 -peak initially the pump interacts twice (ω_p and $-\omega_p$) with a time gap t_1 in between. Subsequently the molecular system developed freely during a time t_2 , before the probe (ω_t) acts on the system followed by the generation of the NLPF-signal (ω_s) after the lapse of time t_3 . The graphs belonging to the T_1 -peak are distinguished from those for the T_2 -peak by an exchange the time order between pump (ω_p) and probe (ω_t) interaction. The two-photon peaks are like the right bottom graphs for T_2 - and T_1 -peaks. They differ by the fact that the initial interacting probe and pump field have the same sign of frequency. Consequently during the time t_2 the system evolves according to the Greens function $\mathcal{G}(t) \exp[i(\omega_p + \omega_t)t_2]$, which corresponds in frequency space to $\mathcal{G}(\omega_p + \omega_t)$ (cf. Eq. 2.36)

Note that for $|\omega - \omega_{\mu\nu}| \gtrsim |\omega|$ fast oscillating terms $\mathcal{G}(t) \exp[i\omega t]$ corresponds to small values of $\mathcal{G}(\omega)$ in frequency domain. Assuming that they cancel out, in rotating wave approximation (RWA) they will be neglected. This has been partially considered in Fig. 2.5 by using only such graphs where the initial interacting field from the left has negative frequency, while that from the right has positive frequency. For the two-photon processes this means, furthermore, that there must exist a higher excited state with $\omega_{\mu 0} \sim \omega_p + \omega_t$. Hence two-photon-peaks do not appear in NLPF-spectra of two-level systems, as mentioned above.

Using the phenomenological model for the two-level system with dephasing and energy relaxation the time-dependent Greens functions reads as

$$\mathcal{G}_{1010}(t) = \mathcal{G}_{0101}^*(t) = \exp[-i\omega_{10}t - \Gamma t] \quad (2.46)$$

$$\mathcal{G}_{0011}(t) = -\mathcal{G}_{1100}(t) = \exp[-\gamma t] \quad (2.47)$$

and one obtains the third-order response function as

$$S(t_1, t_2, t_3) = \frac{4|\mu_{10}|^4}{15(\hbar\varepsilon_0 n c)^2} \exp[(\omega_t - i\omega_{10} - \Gamma)t_3 - \gamma t_2 - \Gamma t_1] \cos[\omega_{10}t_1] (n_1 - n_0). \quad (2.48)$$

⁶This is easily understood after simplifying and factorizing the exponentials, what results in

$$\begin{aligned} F(\omega_t, \omega_p; t_1, t_2, t_3) = & \exp[\omega_t t_3] \{2 \cos[\omega_p t_1] \\ & + \exp[i(\omega_t - \omega_p)t_2] (\exp[i\omega_t t_1] + \exp[-i\omega_p t_1]) \\ & + \exp[i(\omega_t + \omega_p)t_2] (\exp[i\omega_t t_1] + \exp[i\omega_p t_1])\}, \end{aligned}$$

2.6. Supplement: Time-domain description of NLPF-spectra

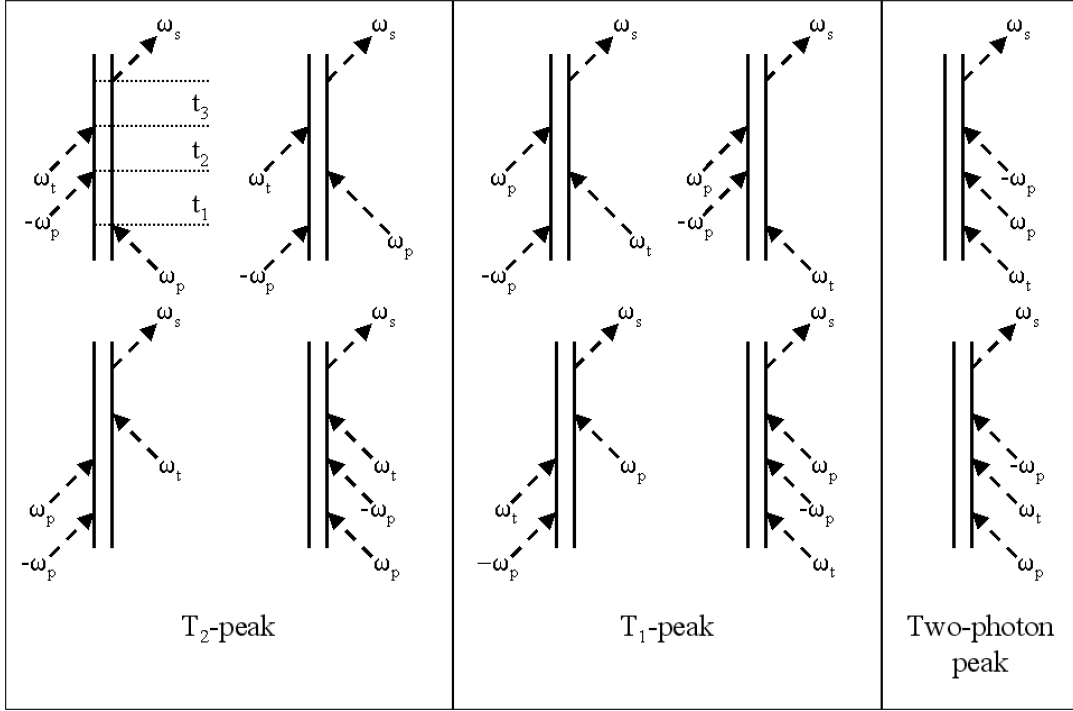


Figure 2.5: Feynman graphs relevant for NLPF (in RWA). The vertical double line represents the statistical operator $\rho(t)$ (left line ket $|\psi\rangle$, right line bra $\langle\psi|$) the dashed arrows the external fields acting on it. The time runs from bottom to top. For the first graph the time intervals t_1 , t_2 , and t_3 between the interactions are shown.

Inserted in Eq. 2.43 this results in the same NLPF-line-shape function as shown in Eq. 2.41. The time-domain description of the NLPF-line-shape function will be important for the cumulant expansion in supplement 3.5.

Chapter 3

NLPF-spectra for dissipative systems

In this chapter a model more substantiated than the phenomenological one used in the previous chapter will be deduced. This shall describe the NLPF-spectra of dye molecules diluted in a solvent dissipating the excitation energy. Thereby, the electromagnetic interaction shall be treated as hitherto classically. This proceeding will result in a NLPF-line-shape function $s(\omega_t, \omega_p)$ as given by Eq. 2.39 in terms of the Fourier transformed Greens function $\mathcal{G}(\omega)$. At this point the problem comes up that it is impossible to list the matrix elements $\mathcal{G}_{\mu\nu\kappa\lambda}(\omega)$ for $|\mu\rangle$, $|\nu\rangle$, etc. representing eigen-states of the total Hamiltonian of a molecule embedded in a dissipative surrounding. The reason is the high degree of freedom of the problem, which results mainly from the huge amount of surrounding solvent molecules but also from internal vibrational modes for even not very large dye molecules. Hence, a reduction of the degree of freedom is indispensable for calculation of a manageable Greens function $\mathcal{G}(\omega)$, though this is connected with a lost of (usually experimentally redundant) information. In order to reduce the degrees of freedom, the total system of dye molecules and solvent is to separate into a relevant system, which intrinsic properties are taken into account exactly, and a reservoir, which will be treated by quantum statistical methods (cf. [Blum, 1981, Weiss, 1999, May and Kühn, 2000]). This separation is rather crucial. Particularly, one has to take care that the coupling to the electromagnetic field is implied in the relevant system as far as possible. In order to obtain an simplified description of a dye-molecule in solution, it will be assumed that the relevant system is given by the electronic system of the dye-molecule. The reservoir will be treated as a bath of harmonic oscillators (modes) representing the molecular vibrations and the dye-solvent interactions.

Using a diabatic basis set the coupling between the relevant electronic system and the reservoir will be described by diagonal and off-diagonal ‘displacements’ between the harmonic

3.1. General description of dissipative quantum systems

potential surface for the excited state relative to the ground state¹. These ‘displacements’ will be assumed to be stochastically distributed for different modes and small in order to apply perturbation theory for the system–reservoir interaction. One will see that in second order perturbation theory the system–reservoir interaction results directly in the dephasing and energy relaxation rates as empirically introduced in chapter 2. Here, however they are complex and frequency dependent. This leads to a significant deviation of the T_2 -peak from the shape shown in Fig. 2.2, while the T_1 -peak changes merely his width. The deviation, depends on two factors: the distribution of the variance of the displacements in respect of the mode frequencies, which will be represented by the spectral density and on the the thermal occupation of the reservoir modes given by the Bose-Einstein distribution. For high-temperatures and an ohmic spectral density one obtains the Markov limit of frequency independent dephasing rates, as used in the phenomenological model. For the energy-relaxation in a two-level system this limit is reached already due to the high optical excitation energy, as one will see. For low temperatures, the T_2 -peak will get quite different. Particularly, for the probe frequency dependence it will split into two, one representing the absorption and the other the stimulated emission with maxima separated by a Stokes-shift. Furthermore, this chapter will provide several useful relations between the different rates, e.g. the detailed balance. These will be of special use for the description of multi-level systems in general.

3.1 General description of dissipative quantum systems

In order to reduce the degree of freedom one separates the complete quantum-mechanical system, e.g. the dye molecule and all solvent molecules, into a relevant system with a degree of freedom that allows one to solve the Schrödinger equation exactly, and into a reservoir, which will be treated by quantum statistics. Corresponding to that, the Hamiltonian H will be split into three terms: for the relevant system H_S , for the reservoir H_R , and the interaction between both H_{SR} . The latter is to be small compared to H_S for applying perturbation theory. For determining optical properties it is further necessary, that the relevant system contains the interaction with the external electromagnetic fields $\mathbf{E}(t)$. The separation of the Hamilto-

¹The use of a diabatic basis set, has two advantages: (i) the couplings between different electronic states, which result in the energy relaxation, can be treated as off-diagonal displacements of the reservoir modes, while in the adiabatic basis set the non-adiabatic matrix elements would be connected with displacements in the momentum coordinates; (ii) diabatic eigenstates fulfill the Condon approximation trivially, since the electronic wavefunctions do not depend on the actual reaction coordinate. Due to the smallness of the displacements, the deviation between the diabatic and the adiabatic (non-pathologic) potential surfaces can be assumed to be small.

nian alone, however, will not make any advantage, since the three parts all are still acting on the complete statistical operator $\rho(t)$ for the complete system in the Liouville-von-Neumann equation. This needs further treatments.

3.1.1 Reduced density matrix

The next step in lowering the degree of freedom of a dissipative quantum-mechanical system is to reduce the statistical operator $\rho(t)$ to a matrix, which is defined only on the eigen-states $|\mu\rangle$ for the Hamiltonian of the relevant system H_S . This results in the reduced density matrix

$$\rho_{\mu\nu}(t) = \langle \mu | \text{tr}_R \{ \rho(t) \} | \nu \rangle, \quad (3.1)$$

where $\text{tr}_R \{ \dots \}$ means the trace over all reservoir states. From the Liouville-von-Neumann equation (see Eq. 2.11) one obtains the equation of motion for the reduced density matrix in the field-free case as

$$\frac{\partial}{\partial t} \rho_{\mu\nu}(t) = -i \langle \mu | \text{tr}_R \{ (\mathcal{L}_S + \mathcal{L}_R + \mathcal{L}_{SR}) \rho(t) \} | \nu \rangle, \quad (3.2)$$

where \mathcal{L}_S , \mathcal{L}_R , and \mathcal{L}_{SR} , are the Liouville operators corresponding to the Hamiltonians H_S , H_R , and H_{SR} defined as in Eq. 2.12. In order to transform Eq. 3.2 into a form equivalent to a Liouville-von-Neumann equation with an effective Liouville operator \mathcal{L}_{eff} , one uses the Projection operator method [Feshbach, 1962, Mower, 1966, Blum, 1981, May and Kühn, 2000] by introducing the projection $\mathcal{P}\rho(t) = \sum_{\mu\nu} \rho_{\mu\nu}(t) |\mu\rangle \langle \nu| \otimes \rho_R(t)$, which factorize the statistical operator of the complete system into one for the reservoir degrees of freedom $\rho_R(t)$ and the reduced density matrix for the relevant system. The complementary projector is defined as $\mathcal{Q} = 1 - \mathcal{P}$. Now one can separate Eq. 2.11 into a system of equations as

$$\begin{aligned} \frac{\partial}{\partial t} \mathcal{P}\rho(t) &= i\mathcal{P}(\mathcal{L}_S + \mathcal{L}_R + \mathcal{L}_{SR})\mathcal{P}\rho_S(t) + i\mathcal{P}\mathcal{L}_{SR}\mathcal{Q}\rho(t) \\ \frac{\partial}{\partial t} \mathcal{Q}\rho(t) &= i(1 - \mathcal{P})(\mathcal{L}_S + \mathcal{L}_R + \mathcal{L}_{SR})\mathcal{Q}\rho(t) + i(1 - \mathcal{P})\mathcal{L}_{SR}\mathcal{P}\rho_S(t) \end{aligned} \quad (3.3)$$

Eliminating the second equation results in the well known Nakajima–Zwanzig Equation [Nakajima, 1958, Zwanzig, 1961]. In the present context, using perturbation theory only the solution up to second order in \mathcal{L}_{SR} shall be considered. Thence the equation of motion for the reduced density matrix yields as

$$\frac{\partial}{\partial t} \rho_{\mu\nu}(t) = -i\omega_{\mu\nu}\rho_{\mu\nu}(t) - \sum_{\kappa,\lambda} \int_0^\infty \mathcal{R}_{\mu\nu\kappa\lambda}(\tau) \rho_{\kappa\lambda}(t - \tau) d\tau \quad (3.4)$$

with frequencies $\omega_{\mu\nu}$ given by the eigenvalues of the relevant system as

$$\langle \mu | \text{tr}_R \{ \mathcal{L}_S \rho(t) \} | \nu \rangle = \omega_{\mu\nu} \rho_{\mu\nu}(t) \quad (3.5)$$

3.1. General description of dissipative quantum systems

and the relaxation operator $\mathcal{R}(\tau)$ has been introduced as

$$\mathcal{R}(\tau) = i \langle \mathcal{L}_{SR} \rangle_R \delta(\tau) + \{ \langle \mathcal{L}_{SR}(\tau) \mathcal{L}_{SR}(0) \rangle_R - \langle \mathcal{L}_{SR} \rangle_R^2 \}. \quad (3.6)$$

The abbreviation $\langle \dots \rangle_R$ means averaging over the reservoir by $\text{tr}_R \{ \dots \rho_R \}$. Here $\mathcal{L}_{SR}(\tau)$ is represented in the interaction picture and consequently time dependent. In principle, one can use the Eq. 3.4 directly to determine the matrix elements $\mathcal{G}_{\mu\nu\kappa\lambda}(\omega)$, which represent the Fourier transformed Greens-function in the reduced basis set of the relevant system, using the system of equations

$$\sum_{\kappa,\lambda} \{ i(\omega + \omega_{\mu\nu}) \delta_{\mu\kappa} \delta_{\nu\lambda} + \mathcal{R}_{\mu\nu\kappa\lambda}(\omega) \} \mathcal{G}_{\kappa\lambda\mu'\nu'}(\omega) = \delta_{\mu\mu'} \delta_{\nu\nu'}. \quad (3.7)$$

where

$$\mathcal{R}_{\mu\nu\kappa\lambda}(\omega) = \int_0^\infty \mathcal{R}_{\mu\nu\kappa\lambda}(\tau) \exp[i\omega\tau] d\tau. \quad (3.8)$$

For practical calculations, however, the relaxation matrix $\mathcal{R}_{\mu\nu\kappa\lambda}(\omega)$ as given by Eq. 3.8 is still bulky. Hence it is useful to simplify this matrix by applying further approximations, namely the secular and the Markov approximation.

3.1.2 Secular approximation

First the secular approximation shall be demonstrated and justified. If one iterates the equation Eq. 3.7 for the specific matrix element $\mathcal{G}_{\mu\nu\mu\nu}(\omega)$, one obtains the series

$$\begin{aligned} \mathcal{G}_{\mu\nu\mu\nu}(\omega) &= \frac{1}{i\omega + i\omega_{\mu\nu} + \Gamma_{\mu\nu}(\omega)} \\ &+ \sum_{\kappa,\lambda \neq \mu,\nu} \frac{\mathcal{R}_{\mu\nu\kappa\lambda}(\omega)}{(i\omega + i\omega_{\mu\nu} + \Gamma_{\mu\nu}(\omega))(i\omega + i\omega_{\kappa\lambda} - \Gamma_{\kappa\lambda}(\omega))} + \dots, \end{aligned} \quad (3.9)$$

where the complex frequency dependent dephasing rate has been introduced as $\Gamma_{\mu\nu}(\omega) = \mathcal{R}_{\mu\nu\mu\nu}(\omega)$. Since $\mathcal{R}_{\mu\nu\kappa\lambda}(\omega)$ has to be small compared to $\omega_{\mu\nu}$ according to the smallness of the perturbation \mathcal{L}_{SR} , the second term in Eq. 3.9 is only important for $|\omega - \omega_{\mu\nu}| \lesssim |\Gamma_{\mu\nu}(\omega)|$ and $|\omega - \omega_{\kappa\lambda}| \lesssim |\Gamma_{\kappa\lambda}(\omega)|$. This means that the transitions $\mu \rightarrow \nu$ and $\kappa \rightarrow \lambda$ (not identical because of $\kappa \neq \mu$ and $\lambda \neq \nu$) have to be nearly degenerate. Considering only the first term in Eq. 3.9 means the first part of the secular approximation and is valid for degeneration-free systems.

In the same way one can justify to neglect all matrix elements $\mathcal{G}_{\mu\nu\kappa\lambda}(\omega)$ for $\kappa \neq \mu$ or $\lambda \neq \nu$ but one: The matrix elements $\mathcal{G}_{\mu\mu\kappa\kappa}(\omega)$ can be not neglected, since here the Eq. 3.7 reduces only to

$$\sum_{\kappa} (i\omega \delta_{\nu\mu} + \gamma_{\nu\mu}(\omega)) \mathcal{G}_{\mu\mu\kappa\kappa}(\omega) = \delta_{\nu\kappa}. \quad (3.10)$$

The rates $\gamma_{\nu\mu}(\omega)$ have been introduced as abbreviation for $\mathcal{R}_{\mu\mu\nu\nu}(\omega)$. While the matrix elements $\mathcal{G}_{\mu\nu\kappa\lambda}(\omega)$ for $\mu \neq \nu$ or $\kappa \neq \lambda$ can be neglected due to an expansion similar to Eq. 3.9, the matrix elements $\mathcal{G}_{\mu\mu\kappa\kappa}(\omega)$ are all of the same order of magnitude for comparable $\gamma_{\nu\mu}(\omega)$ and the common frequency term $i\omega\delta_{\nu\mu}$ in Eq. 3.10. Therefore, one has to invert the whole system of equation. As one will see below, this is not simply possible, because the matrix $\gamma_{\nu\mu}(\omega)$ becomes singular for $\omega \rightarrow 0$. This problem can be circumvent by using the general property of any statistical operator $tr \{\rho(t)\} = 1$ to add constrictions on the $\mathcal{G}_{\mu\mu\kappa\kappa}(\omega)$ given by

$$\sum_{\mu} \mathcal{G}_{\mu\mu\kappa\kappa}(\omega) = \delta(\omega). \quad (3.11)$$

For details see chapter 4. Thus secular approximation means limitation to the elements $\mathcal{G}_{\mu\nu\mu\nu}(\omega)$ and $\mathcal{G}_{\mu\mu\kappa\kappa}(\omega)$. This is equivalent to approximate the relaxation matrix $\mathcal{R}_{\mu\nu\kappa\lambda}(\omega)$ by

$$\mathcal{R}_{\mu\nu\kappa\lambda}(\omega) = \gamma_{\mu\kappa}(\omega)\delta_{\mu\nu}\delta_{\kappa\lambda} + \Gamma_{\mu\nu}(\omega)\delta_{\mu\kappa}\delta_{\nu\lambda}(1 - \delta_{\mu\nu}). \quad (3.12)$$

In some cases (one will be shown below) the relaxation matrix yields exactly this form ab-initio

The function $\Gamma_{\mu\nu}(\omega)$ has been assigned as the complex, frequency-dependent dephasing rate due to the fact that in time-domain its real part is related to a decay of the density matrix elements $\rho_{\mu\nu}(t)$, which describe the coherence between the states $|\mu\rangle$ and $|\nu\rangle$. This coherence is destroyed by destruction of the phase relation between the two states with the rate $\Gamma_{\mu\nu}(\omega)$. Analogously, the real part of $\gamma_{\mu\kappa}(\omega)$ is related to a decay of the reduced density matrix element $\rho_{\kappa\kappa}(t)$, which represents the occupation of the state $|\kappa\rangle$. The loss of occupation in the state $|\kappa\rangle$ (which is transferred to the state $|\mu\rangle$) is connected to a change of the system energy by $(\varepsilon_{\kappa} - \varepsilon_{\mu})\gamma_{\mu\kappa}(0)$. Therefore, $\gamma_{\mu\kappa}(\omega)$ has been named the complex, frequency-dependent energy relaxation rate. Note that for $\rho_{\mu\mu}$ being necessarily real and semi-positivedefinit the static rate $\gamma_{\nu\mu}(0)$ needs to be real. Concerning the exact meaning of the imaginary parts of $\Gamma_{\mu\nu}(\omega)$ and $\gamma_{\nu\mu}(\omega)$ see below (section 3.2.3). The secular approximation is assumed to be valid in all what follows, last but not least because it is crucial in order to assign the different spectral features occurring in NLPF-spectra to processes on and properties of the molecular system in condensed phase to be studied.²

²It shall be mentioned that secular approximation according to the expansion in Eq. 3.9 is already justified by the limitation of the present theory for dissipation to second order of the system bath coupling \mathcal{L}_{SR} , as shown above. Only for nearly degenerate eigen-frequencies of \mathcal{L}_S it fails. In this case, however, one can usually transform the sub-eigen-basis set $\{\mu, \nu, \kappa, \lambda\}$ of the degenerate states in order to find an equivalent basis set $\{\mu', \nu', \kappa', \lambda'\}$ where the relaxation operator $\mathcal{R}(\omega)$ has a suitable form for applying the secular approximation.

3.1. General description of dissipative quantum systems

3.1.3 Markov approximation and reorganization

In order to determine the relaxation operator $\mathcal{R}(\tau)$ in Eq. 3.6 one has to average over the reservoir state by $\langle \dots \rangle_R \hat{=} \text{tr}_R \{ \dots \rho_R \}$. Thereby a complication occurs because the dynamics of the statistical operator of the reservoir ρ_R are not known in detail. In what follows two limits are important for the reservoir dynamics: The equilibration of the reservoir can be extremely slow or extremely fast compared to the dynamics of the relevant system.

In the latter case, when the reservoir dynamics are ultrafast, the reservoir equilibrates immediately and one obtains $\mathcal{R}(\tau) = \mathcal{R}(0) \delta(\tau)$. In this case the relaxation term in Eq. 3.4 depends only on the instantaneous value of the matrix elements $\rho_{\kappa\lambda}(t)$, which corresponds to a Markovian process. In frequency domain the Markov approximation means that the Fourier-transformed relaxation operator $\mathcal{R}(\omega)$ is independent of frequency and almost real.

Usually, the Markov approximation is not necessarily valid on arbitrary time scales. Therefore, the reservoir dynamics shall be separately studied on the different time scales of the relevant system for (i) the electromagnetic interaction, (ii) the dephasing process, and (iii) the energy relaxation. For the fast electromagnetic interaction, the Condon approximation is most probably valid, i.e. during this process the state of the reservoir is not changed. Hence the subsequent dephasing and energy relaxation process starts with the reservoir state

$$\rho_R^{(\nu)} = \frac{\langle \nu | \exp \left[\frac{H_R + H_{SR}}{kT} \right] | \nu \rangle}{\text{tr} \left\{ \exp \left[\frac{H_R + H_{SR}}{kT} \right] \right\}}. \quad (3.13)$$

held before the external fields act. For the cross-section of pumping as given by the function $\sigma_{\mu 0}(\omega, \omega')$ (cf. Eqs. 2.40 and 2.24, respectively) this is the equilibrated ground state given by the statistical operator $\rho_R^{(0)}$. Thus the cross-section of pumping for a dissipative two-level system yields as

$$\sigma_{10}(\omega, \omega') = \frac{|\mu_{10}|^2}{\hbar \varepsilon_0 n c} \left(\frac{\omega'}{i\omega - i\omega_{10} - \Gamma_{10}^{(0)}(\omega)} + \frac{\omega'}{i\omega_{10} - i\omega' - \Gamma_{01}^{(0)}(-\omega')} \right). \quad (3.14)$$

Here and in what follows, the dependence of the dephasing on the initial statistical operators $\rho_R^{(\nu)}$ (cf. $\langle \dots \rangle_R$ in Eq. 3.6) will be assigned by a superscript as $\Gamma_{\mu\nu}^{(\nu)}(\omega)$.

In the original basis set the relaxation matrix is given by

$$\mathcal{R}_{\mu\nu\kappa\lambda}(\omega) = \sum_{\mu'\nu'} \{ T_{\mu\mu'} T_{\nu\nu'} T_{\kappa\nu'} T_{\lambda\nu'} \gamma_{\mu'\nu'}(\omega) + T_{\mu\mu'} T_{\nu\nu'} T_{\kappa\mu'} T_{\lambda\nu'} \Gamma_{\mu'\nu'}(\omega) \}$$

where $T_{\mu\mu'}$ are the basis-transformation matrix elements. Like a secular approximated relaxation matrix the transformed matrix $\mathcal{R}_{\mu\nu\kappa\lambda}(\omega)$ has the same property to keep the density matrix $\rho_{\mu\nu}$ semi-positv definit, means $\rho_{\mu\mu} \geq 0$, what is necessary for populations. For arbitrary relaxation matrices $\mathcal{R}_{\mu\nu\kappa\lambda}(\omega)$ this condition is usually not fulfilled [Seke, 1991a]. Thus secular approximation has a deeper meaning than to be only a simplification of the relaxation operator.

For the probe frequency dependence one has to consider that one probes different states $|\nu\rangle$ of the relevant system, which developed from the energy relaxation process. During the energy relaxation of the relevant system also the reservoir will be reorganized. Only if the former process is much slower than the latter, i.e.

$$|\gamma_{\nu\nu}(\omega)| \ll \tau_R^{-1}, \quad (3.15)$$

where τ_R is the characteristic reorganization time, the reservoir can be assumed to be equilibrated instantaneously. Furthermore, for the dephasing process the initial state of the reservoir is represented by a statistic operator $\rho_R^{(\nu)}$ (as given by Eq. 3.13) where $|\nu\rangle$ is the state being probed. Thus the functions for probing the bleaching and the stimulated emission of a dissipative two-level system are different and yield as

$$\begin{aligned} \zeta_{10}(\omega_t) &= \frac{|\mu_{10}|^2}{\hbar\varepsilon_0 n c} \frac{\omega_t}{i\omega_t - i\omega_{10} - \Gamma_{10}^{(0)}(\omega_t)} \\ \zeta_{01}(\omega_t) &= \frac{|\mu_{10}|^2}{\hbar\varepsilon_0 n c} \frac{\omega_t}{i\omega_t - i\omega_{10} - \Gamma_{10}^{(1)}(\omega_t)}, \end{aligned} \quad (3.16)$$

respectively. The NLPF-spectrum of the dissipative two-level system results from the line-shape function

$$s(\omega_t, \omega_p) = \frac{\zeta_{10}(\omega_t) + \zeta_{01}(\omega_t)}{15} \left(\frac{\sigma_{10}(\omega_p, \omega_p)}{\tilde{\gamma}_{01}(0)} + \frac{\sigma_{10}(\omega_t, \omega_p)}{\tilde{\gamma}_{01}(\omega_t - \omega_p) + i\omega_p - i\omega_t} \right), \quad (3.17)$$

with $\tilde{\gamma}_{01}(\omega) = \gamma_{01}(\omega) + \gamma_{10}(\omega)$ (cf. Eq. 4.13). For the Markov approximation being valid the NLPF-spectrum of the dissipative two-level system is given by the same NLPF-line-shape function $s(\omega_t, \omega_p)$ as defined in Eq. 2.41 for the empirical model. One has only to set $\gamma := \tilde{\gamma}_{01}$ and $\Gamma := \Gamma_{10}^{(0)}(\omega_{10}) = \Gamma_{10}^{(1)}(\omega_{10})$.

In the opposite extreme case where the reservoir reorganization is very slow compared to the energy relaxation, i.e. $|\gamma_{\nu\nu}(\omega)| \gg \tau_R^{-1}$, one obtains $\rho_R(\tau) \approx \rho_R(0)$ for all relevant time-scales. Consequently, the averaging over the reservoir degrees of freedom is not to be carried out for the relaxation operator $\mathcal{R}(\tau)$ but for the NLPF line-shape function as a whole, i.e.

$$s(\omega_t, \omega_p) = \frac{1}{15} \left\langle (\zeta_{10}(\omega_t) + \zeta_{01}(\omega_t)) \left(\frac{\sigma_{10}(\omega_p, \omega_p)}{\tilde{\gamma}_{01}} + \frac{\sigma_{10}(\omega_t, \omega_p)}{\tilde{\gamma}_{01} + i\omega_p - i\omega_t} \right) \right\rangle_R. \quad (3.18)$$

This represents the inhomogeneous limit. Note that, if the reservoir does not equilibrate during the process, the effective transition frequencies $\omega_{\mu\nu} = [\mathcal{L}_S + \mathcal{L}_{SR}]_{\mu\nu}$ are stochastically distributed, i.e. the transition is inhomogeneously broadened (cf. chapter 5). More generally the reservoir dynamics is to be split into a fast and a slowly reorganizing part R_F and R_S , respectively. The averaging over the fast part $\langle \dots \rangle_{R_F}$ yields homogeneously broadened line shapes

3.2. Harmonic oscillator model

as given by the functions $\zeta_{10}(\omega)$, $\zeta_{01}(\omega)$, and $\sigma_{10}(\omega, \omega')$ (cf. Eqs. 3.14 and 3.16), while that over the slow part $\langle \dots \rangle_{RS}$ has to be carried out over the line-shape function as a whole (cf. Eq. 3.18) resulting in the inhomogeneous broadening, i.e. stochastically distributed transition frequencies

$$\omega_{10} = [\langle \mathcal{L}_S + \mathcal{L}_{SR_S} \rangle_{R_F}]_{1010}. \quad (3.19)$$

For the combinations and intermediate cases of both types of broadening in a NLPF-spectrum see supplement 3.5 and chapter 5.

3.2 Harmonic oscillator model

In order to determine the properties, particularly the frequency dependence and relation between real and imaginary part of $\Gamma_{\mu\nu}(\omega)$ and $\gamma_{\mu\nu}(\omega)$, first of all it is necessary to find a microscopic model for the relevant system and the reservoir in terms of quantities, which can be treated by statistical methods in order to evaluate Eq. 3.6. In this section a simplified model for the dissipative dynamics of very diluted dye-molecules in a condensed non-crystal solvent (liquid or glass) will be developed.

For the electromagnetic coupling primarily the electronic system of the dye-molecule is responsible. Therefore a separation of the motion of the electrons of the dye molecule from that of its nuclei as well as of the surrounding solvent molecules is advisable. This means Born-Oppenheimer approximation. The total Hamiltonian of the molecular system is given by

$$H_{mol} = \sum_{el} \sum_{nuc} \left(V(\mathbf{r}_{el}, \mathbf{r}_{nuc}) - \frac{\hbar^2}{2m_{el}} \nabla_{el}^2 - \frac{\hbar^2}{2M_{nuc}} \nabla_{nuc}^2 \right) \quad (3.20)$$

where the index *el* assigns electronic and the index *nuc* nuclear coordinates. Thereby it shall be not important whether \mathbf{r}_{nuc} and ∇_{nuc} refer to the nuclei of the dye-molecule or to the position of complete solvent molecules, while \mathbf{r}_{el} and ∇_{el} are to refer only to the dye-molecule, which will represent the relevant system. According to the Born-Oppenheimer separation, firstly one determines the eigen-states $|\mu\rangle$ of the electronic Hamiltonian

$$H_{el} = \sum_{el} \left(V(\mathbf{r}_{el}, \mathbf{r}_{nuc}^0) - \frac{\hbar^2}{2m_{el}} \nabla_{el}^2 \right) \quad (3.21)$$

for a given conformation \mathbf{r}_{nuc}^0 . In what follows, the eigen-states $|\mu\rangle$ will refer only to this configuration (diabatic basis). Nevertheless, one can determine the matrix elements of the

electronic Hamiltonian $\langle \mu | H_{el} | \nu \rangle$ for each conformation \mathbf{r}_{nuc} by

$$\begin{aligned} U_{\mu\nu}(\mathbf{r}_{nuc}) &= \langle \mu | \{ V(\mathbf{r}_{el}, \mathbf{r}_{nuc}) - V(\mathbf{r}_{el}, \mathbf{r}_{nuc}^0) \} | \nu \rangle \\ &= \int \{ V(\mathbf{r}_{el}, \mathbf{r}_{nuc}) - V(\mathbf{r}_{el}, \mathbf{r}_{nuc}^0) \} \tilde{\rho}_{\mu\nu}(\mathbf{r}_{el}) d^3r. \end{aligned} \quad (3.22)$$

Here, the diagonal matrix element $\tilde{\rho}_{\mu\mu}(\mathbf{r}_{el})$ represents the electron density for the state $|\mu\rangle$ and correspondingly $U_{\mu\mu}(\mathbf{r}_{nuc})$ the diabatic potential surfaces for the nuclear motion if the electronic system is in the state $|\mu\rangle$. The off-diagonal matrix element $\tilde{\rho}_{\mu\nu}(\mathbf{r}_{el})$ represents an electronic transition density and consequently $U_{\mu\nu}(\mathbf{r}_{nuc})$ for $\mu \neq \nu$ describes not a potential but the coupling between the two different electronic states $|\mu\rangle$ and $|\nu\rangle$. For the nuclear conformation \mathbf{r}_{nuc}^0 , which has been used for determination of the orthonormal diabatic basis set, the coupling must trivially vanish, i.e. $U_{\mu\nu}(\mathbf{r}_{nuc}^0) = \varepsilon_\mu \delta_{\mu\nu}$. Concluding the diabatic Hamiltonian for the nuclear motion has the form

$$H_{\mu\nu} = \left(\varepsilon_\mu - \sum_{nuc} \frac{\hbar^2}{2M_{nuc}} \nabla_{nuc}^2 \right) \delta_{\mu\nu} + U_{\mu\nu}(\mathbf{r}_{nuc}). \quad (3.23)$$

It has to be noted, that there exists some freedom in the choice of the nuclear conformation \mathbf{r}_{nuc}^0 used for the determination of the diabatic basis-set. The most useful choice of \mathbf{r}_{nuc}^0 , however, is a global stationary point for the nuclear motion (supposed it exist), since with $\text{tr}_R \{ \mathbf{r}_{nuc} \rho_R^{(0)} \} \rightarrow \mathbf{r}_{nuc}^0$ for $T \rightarrow 0\text{K}$ (cf. Eq. 3.13), the following calculations will be a little bit simpler.

3.2.1 Harmonic oscillator approximation

The diabatic potential surface of the electronic ground state $U_{00}(\mathbf{r}_{nuc})$ can be expanded into a power series around its minimum as

$$U_{00}(\dots Q_\xi \dots) = \frac{1}{2} \sum_{\xi} \hbar \omega_{\xi} Q_{\xi}^2 + \dots, \quad (3.24)$$

by using dimensionless normal mode coordinates Q_{ξ} and the oscillator frequencies ω_{ξ} . Expanded in the same coordinate system the diabatic potential surfaces for the other electronic states reads as

$$U_{\mu\nu}(\dots Q_{\xi} \dots) = \sum_{\xi} \hbar \omega_{\xi} q_{\xi\mu\nu} Q_{\xi} + \sum_{\xi, \xi'} \hbar \omega_{\xi} W_{\xi\xi'\mu\nu} Q_{\xi} Q_{\xi'} + \dots, \quad (3.25)$$

with the dimensionless gradients

$$q_{\xi\mu\nu} = \frac{1}{\hbar \omega_{\xi}} \left. \frac{\partial U_{\mu\nu}(\dots Q_{\xi} \dots)}{\partial Q_{\xi}} \right|_{Q_{\xi}=0}, \quad (3.26)$$

3.2. Harmonic oscillator model

and Hessian elements

$$W_{\xi\xi'\mu\nu} = \frac{1}{2\hbar\omega_\xi} \left. \frac{\partial^2 U_{\mu\nu}(\dots Q_\xi \dots)}{\partial Q_\xi \partial Q_{\xi'}} \right|_{Q_\xi=Q_{\xi'}=0}. \quad (3.27)$$

Neglecting higher orders in Q_ξ than second, for $W_{\xi\xi'\mu\nu} > 0$ the potential surfaces $U_{\mu\mu}(\dots Q_\xi \dots)$ represent harmonic oscillator potentials. The displacement of their minimum versus the ground-state minimum is given by the gradients $q_{\xi\mu\mu}$, while the Hessian elements $W_{\xi\xi'\mu\mu}$ take into account that the oscillator frequencies of the excited-state potential surfaces may be different from ω_ξ , but also that the normal coordinate system may be rotated. Using $q_{\xi\mu\nu}$ and $W_{\xi\xi'\mu\nu}$ one can specify the criterion for a mode ξ allowed to be treated as a reservoir mode: Since the nuclear motion belonging to such a mode may affect only small perturbations of the potential surface of the excited states compared to that of the ground state, one needs the condition

$$q_{\xi\mu\nu} \ll 1 \text{ and } W_{\xi\xi'\mu\nu} \approx \delta_{\xi\xi'} \delta_{\mu\nu} \quad (3.28)$$

to be fulfilled. In what follows all terms of higher than second order in Q_ξ shall be negligible³. Furthermore, for sake of simplicity it will be assumed that $W_{\xi\xi'\mu\nu} = \delta_{\xi\xi'} \delta_{\mu\nu}$. Fig. 3.1 shows a section through the diabatic potential surfaces $U_{\mu\mu}(Q_\xi)$, $U_{\nu\nu}(Q_\xi)$, and $U_{\mu\nu}(Q_\xi)$, respectively, for one normal mode coordinate Q_ξ . Note that in the shown scheme the values for the displacements $q_{\xi,\mu\nu}$, $q_{\xi,\mu\mu}$, and $q_{\xi,\nu\nu}$ are definitely too large for a reservoir mode according to Eq. 3.28, while the second condition $W_{\xi\xi'\mu\nu} = \delta_{\xi\xi'} \delta_{\mu\nu}$ is fulfilled.

Represented in dimensionless coordinates Q_ξ and momenta $P_\xi = \partial/\partial Q_\xi$, the Hamiltonian for the nuclear motion of the reservoir modes reads as

$$H_{\mu\nu} \approx \hbar\omega_{\mu 0} \delta_{\mu\nu} + \frac{1}{2} \sum_{\xi} \hbar\omega_{\xi} (P_{\xi}^2 + Q_{\xi}^2) \delta_{\mu\nu} - \sum_{\xi} \hbar\omega_{\xi} q_{\xi\mu\nu} Q_{\xi}, \quad (3.29)$$

For applying the reduced density matrix method as described above, the Hamiltonian in Eq. 3.29 is to split into three terms: The relevant system Hamiltonian

$$H_S = \sum_{\mu} \hbar\omega_{\mu 0} |\mu\rangle \langle \mu|, \quad (3.30)$$

the reservoir Hamiltonian

$$H_R = \frac{1}{2} \sum_{\xi} \hbar\omega_{\xi} (P_{\xi}^2 + Q_{\xi}^2), \quad (3.31)$$

³A mode ξ^* which do not fulfil these criteria, has to be treated as part of the system Hamiltonian H_S . The resulting eigenstates $|\mu M\rangle$ represent product states of electronic wavefunction $\phi_{\mu}(\mathbf{r}_{el})$ and the vibrational wavefunction $\Phi_{\mu M}(Q_{\xi^*})$ (see chapter ??).

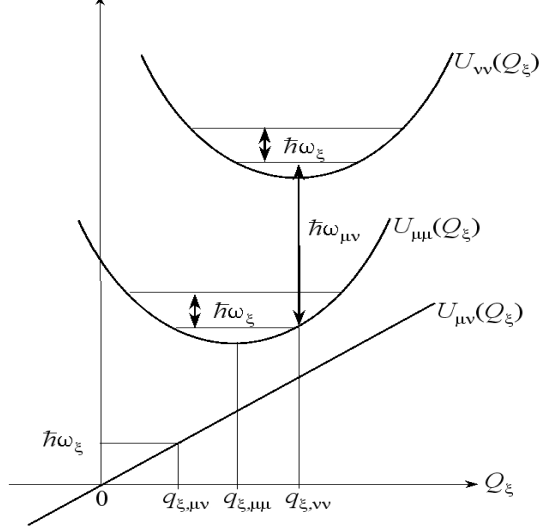


Figure 3.1: Sections $U_{\mu\mu}(\omega_\xi)$ and $U_{\nu\nu}(\omega_\xi)$ through the potential surfaces of two electronic states $|\mu\rangle$ and $|\nu\rangle$ for the dimensionless normal mode coordinate Q_ξ (simplified model for Hamiltonian according to Eq. 3.29). The electronic transition frequency is $\omega_{\nu\mu}$, the vibrational frequency ω_ξ . The displacements are given as $q_{\xi,\mu\mu}$ and $q_{\xi,\nu\nu}$, respectively.

and last but not least the system-reservoir interaction

$$H_{SR} = \sum_{\mu,\nu} \sum_{\xi} \hbar\omega_\xi q_{\xi\mu\nu} \delta_{\xi\xi'} Q_\xi |\mu\rangle \langle\nu|. \quad (3.32)$$

The three Liouville operators \mathcal{L}_S , \mathcal{L}_R and \mathcal{L}_{SR} corresponding to H_S , H_R , and H_{SR} will be used for the determination of the relaxation operator $\mathcal{R}(\omega)$ according to Eqs. 3.6 and 3.8.

3.2.2 Correlation function and spectral density

Since for harmonic oscillators in thermal equilibrium (remember that above $\rho_R^{(0)}$ has been supposed to represent the equilibrium state of the reservoir if the relevant system is in the ground state) the average $\langle Q_\xi \rangle_R$ vanishes as the first term $\langle \mathcal{L}_{SR} \rangle_R$ in Eq. 3.6. Thus for determination of $\mathcal{R}(\omega)$ only the time-dependent term $\langle \mathcal{L}_{SR}(t+\tau) \mathcal{L}_{SR}(t) \rangle_R$ has to be evaluated. By separating the propagation of the system and the reservoir one can introduce the time-correlation functions of the reservoir as

$$C_{\xi\xi'}(\tau) = 4\omega_\xi\omega_{\xi'} \langle Q_\xi(\tau) Q_{\xi'}(0) \rangle_R = \omega_\xi^2 \{n_\xi \exp[i\omega_\xi\tau] + (n_\xi + 1) \exp[-i\omega_\xi\tau]\} \delta_{\xi\xi'}. \quad (3.33)$$

3.2. Harmonic oscillator model

For a thermally equilibrated reservoir the occupations are given by $n_\xi = n(\omega_\xi)$ using the Bose-Einstein distribution

$$n(\omega) = \frac{1}{\exp[\hbar\omega/kT] - 1}. \quad (3.34)$$

Using the half-sided Fourier transformed of $C_{\xi\xi}(\tau)$ given as

$$C_\xi(\omega) = \int_0^\infty C_{\xi\xi}(\tau) \exp[i\omega\tau] d\tau, \quad (3.35)$$

one can express the frequency dependent relaxation matrix $\mathcal{R}_{\mu\nu\kappa\lambda}(\omega)$ (see Eqs. 3.6 and 3.8) as

$$\begin{aligned} \mathcal{R}_{\mu\nu\kappa\lambda}(\omega) &= \sum_{\xi, \mu'} (\delta_{\nu\lambda} q_{\xi\mu\mu'} q_{\xi\mu'\kappa} C_\xi(\omega_{\mu'\nu} - \omega) + \delta_{\mu\kappa} q_{\xi\lambda\mu'} q_{\xi\mu'\nu} C_\xi^*(\omega_{\mu'\kappa} + \omega)) \\ &- q_{\xi\mu\kappa} q_{\xi\lambda\nu} (C_\xi(\omega_{\mu\lambda} - \omega) + C_\xi^*(\omega_{\nu\kappa} + \omega)). \end{aligned} \quad (3.36)$$

This formula contains still a nearly infinite number of parameters $q_{\xi\mu\nu}$ and correlation functions $C_\xi(\omega)$. Therefore, a statistical model is to apply, which enables one to carry out the summation over the modes ξ . The basis for such a statistical model is the assumption that the displacements $q_{\xi\mu\nu}$ representing the system-reservoir coupling are stochastically distributed and statistical independent to each other. This means one can substitute

$$\sum_{\xi} q_{\xi\mu\nu} q_{\xi\kappa\lambda} \dots \rightarrow \delta_{\mu\lambda} \delta_{\nu\kappa} \frac{1}{\pi} \int_{-\infty}^{\infty} \dots J_{\mu\nu}(\omega) d\omega', \quad (3.37)$$

introducing the spectral density $J_{\mu\nu}(\omega)$ as

$$J_{\mu\nu}(\omega) = \sum_{\xi} q_{\xi\mu\nu}^2 \delta(\omega_\xi - \omega). \quad (3.38)$$

The spectral density is directly related to the variances of the displacements for a certain interval of mode frequencies. There exists several spectroscopic methods, e.g. by site-directed fluorescence spectroscopy [Peterman et al., 1997, Pullerits et al., 1995], which have been applied in order to determine $J_{\mu\nu}(\omega)$ for certain kinds of transitions experimentally. For practical purposes, however, one will be described the $J_{\mu\nu}(\omega)$ by a theoretical continuous model function.

Now one will summarize the correlation functions and displacements for a given transition $\mu \leftrightarrow \nu$ to a single coupling function

$$K_{\mu\nu}(\omega) = \sum_{\xi} q_{\xi\mu\nu}^2 C_\xi(\omega), \quad (3.39)$$

which in the continuous limit (cf. Eq. 3.37) yields as

$$\begin{aligned} K_{\mu\nu}(\omega) &= \{J_{\mu\nu}(\omega)(n(\omega) + 1) + J_{\mu\nu}(-\omega)n(-\omega)\} \omega^2 \\ &+ \frac{i}{2} \text{PV} \int_{-\infty}^{\infty} \frac{J_{\mu\nu}(\omega)(n(\omega) + 1) + J_{\mu\nu}(-\omega)n(-\omega)}{\omega - \omega'} \omega'^2 d\omega'. \end{aligned} \quad (3.40)$$

Note that $\Im K_{\mu\nu}(\omega)$ is correlated to $\Re K_{\mu\nu}(\omega)$ by a Kramers-Kronig relation (PV stands for principal value), which is expression of the analyticity of the complex coupling function $K_{\mu\nu}(\omega)$ [Jänich, 1983]. This relation is rather important, since it means that the imaginary part of $K_{\mu\nu}(\omega)$ can only exist if the real part is frequency dependent.

3.2.3 Frequency dependent dephasing and energy relaxation rates

By applying Eq. 3.37 on Eq. 3.36 one obtains the astonishing result that the frequency dependent relaxation matrix $\mathcal{R}_{\mu\nu\kappa\lambda}(\omega)$ decomposes directly into the frequency dependent energy relaxation rates, which are given by

$$\gamma_{\mu\nu}(\omega) = K_{\mu\nu}(\omega_{\nu\mu} + \omega) + K_{\mu\nu}^*(\omega_{\nu\mu} - \omega) \text{ for } \mu \neq \nu \quad (3.41)$$

$$\gamma_{\mu\mu}(\omega) = - \sum_{\kappa \neq \mu} (K_{\kappa\mu}(\omega_{\kappa\mu} + \omega) + K_{\kappa\mu}^*(\omega_{\kappa\mu} - \omega)). \quad (3.42)$$

and the frequency dependent dephasing rates given by

$$\Gamma_{\mu\nu}(\omega) = \sum_{\kappa} K_{\mu\kappa}(\omega_{\kappa\nu} - \omega) + \sum_{\kappa} K_{\nu\kappa}^*(\omega_{\kappa\mu} + \omega), \quad (3.43)$$

as if one would have applied the secular approximation (cf. Eq. 3.12).

The static energy relaxation rate $\gamma_{\mu\nu}(0) = \Re K_{\mu\nu}(\omega_{\nu\mu})$ is real and represents the non-oscillating transfer of occupation from the diabatic electronic state $|\nu\rangle$ to the state $|\mu\rangle$. The transfer vice versa happens with the rate $\gamma_{\nu\mu}(0)$ is connected to $\gamma_{\mu\nu}(0)$ by the detailed balance, which generalized to the frequency dependent energy relaxation rates $\gamma_{\mu\nu}(\omega)$ yields as

$$\frac{\Re \gamma_{\mu\nu}(\omega)}{\Re \gamma_{\nu\mu}(\omega)} = \exp \left[- \frac{\hbar}{kT} (\omega_{\mu\nu} + \omega) \right]. \quad (3.44)$$

Note that due to the construction of the diagonal elements $\gamma_{\mu\mu}(\omega) = - \sum_{\kappa \neq \mu} \gamma_{\kappa\mu}(\omega)$ (cf. Eqs. 3.41 and 3.42) for $\omega = 0$ the whole energy relaxation matrix $\gamma(0)$ becomes singular. This makes a special treatment for the determination of the diagonal matrix elements of the Greens function $\mathcal{G}_{\mu\mu\kappa\kappa}(\omega)$ necessary, as mentioned above (cf. Eq. 3.11) and will be demonstrated in chapter 4.

The dephasing rate $\Gamma_{\mu\nu}(\omega)$ as given in Eq. 3.43 contains contributions from both, off-diagonal coupling functions $K_{\mu\nu}(\omega)$, which occur also in Eq. 3.41 for the energy relaxation rate, and the diagonal coupling functions $K_{\mu\mu}(\omega)$ and $K_{\nu\nu}^*(\omega)$. For the absorption spectrum as well as for the pump-dependence of the T_2 -peak of a two-level system the dephasing rate $\Gamma_{10}^{(0)}(\omega)$ in the vicinity of the transition frequency ω_{10} is of special interest. The superscript (0) means that the reservoir is initially equilibrated for the ground state $|0\rangle$ (cf. Eq. 3.13) where

3.2. Harmonic oscillator model

also the diabatic basis set is defined on, i.e. $q_{\xi,00} = 0$ (see above). According to Eq. 3.40 for $\omega \rightarrow \omega_{10}$ one obtains the real part of the dephasing rate at ω_{10} , as

$$\Re\Gamma_{10}^{(0)}(\omega_{10}) = \left| \frac{\gamma_{11}(0) + \gamma_{00}(0)}{2} \right| + \frac{kT}{\hbar} \lim_{\omega \rightarrow 0} [\omega J_{11}(\omega)]. \quad (3.45)$$

For the dephasing rate being constant (Markov limit) $2\Re\Gamma_{10}^{(0)}(\omega_{10})$ represents the homogeneous line width of the absorption spectrum (FWHM) as well as that of the T_2 -peak in respect of the pump-frequency dependence (FWQM; cf. Eq. 3.14). The first term in Eq. 3.45 represents the dephasing caused by the finite lifetimes of the involved electronic states, as caused by the energy relaxation. The second term represents the pure dephasing, which describes the desynchronization for the nuclear motion on two different multi-dimensional potential surfaces due to the different displacements $q_{\xi,11}$ for the different modes ξ (note that for $q_{\xi,00} = 0 \Rightarrow J_{00}(\omega) = 0$). The obtained linear temperature dependence of the pure dephasing term is directly related to a line-broadening of the absorption band as well as of the T_2 -peaks with increasing temperature (see Eq. 3.14). For the occurrence of pure dephasing, however, one has to suppose that the spectral density show an asymptotic as ω^{-1} for $\omega \rightarrow 0$, i.e. asymptotically ohmic [May and Kühn, 2000]. This is not a problem at all, since it has been shown that a reservoir, where certain modes, which are directly coupled to the relevant system, are damped by the others, e.g. in the Brownian oscillator model [Mukamel, 1995], can with certain reservations be mapped to an asymptotically ohmic spectral density $J_{\mu\nu}(\omega)$ of uncoupled modes⁴.

The imaginary part of the dephasing rate at $\omega = \omega_{10}$ is given by

$$\Im\Gamma_{10}^{(0)}(\omega_{10}) = \Delta\omega_{10} + \frac{S_{11}}{2}, \quad (3.47)$$

where the Stokes-shift of the transition has been introduced as

$$S_{11} = \int_0^\infty \omega' J_{11}(\omega') d\omega'. \quad (3.48)$$

⁴In general pure dephasing can occur also without the constriction to asymptotically ohmic spectral densities $J_{\mu\mu}(\omega)$. If beside the displacements $q_{\xi\mu\mu}$ (bilinear coupling) also Hessians $W_{\xi\xi'\mu\mu} \neq \delta_{\xi\xi'}$ (linear-quadratic coupling) are to consider, one obtains a second spectral density which is given as

$$J_{\mu\mu}^{(2)}(\omega, \omega') = \sum_{\xi, \xi' \neq \xi} W_{\xi\xi'\mu\mu}^2 \delta(\omega - \omega_\xi) (\delta(\omega' - \omega_{\xi'}) + \delta(\omega' + \omega_{\xi'})),$$

and provides a coupling function $K_{\mu\mu}^{(2)}(\omega)$ analogous to that used in Eq. 3.43. The real part of $K_{\mu\mu}^{(2)}(\omega)$ yields as

$$\Re K_{\mu\mu}^{(2)}(\omega) = - \int_{-\infty}^{\infty} \omega'^2 J_{\mu\mu}^{(2)}(\omega', \omega' + \omega) n(\omega') (n(\omega' + \omega) + 1) d\omega', \quad (3.46)$$

which can be non-zero for all ω , even though $J_{\mu\mu}^{(2)}(\omega', \omega'')$ is finite for $\omega', \omega'' \rightarrow 0$. This extension of the model, however, provides a non-linear temperature dependence of the homogeneous line width in general.

The first terms in Eq. 3.47 given by

$$\Delta\omega_{10} = \Im\{K_{10}(\omega_{10})\} - \Im\{K_{01}(\omega_{01})\} \quad (3.49)$$

represent the second order corrections to the eigen-frequencies ω_{10} of the relevant system by the off-diagonal system-reservoir coupling between them⁵. The imaginary part of an otherwise constant dephasing rate (what, however, is only approximately possible due to the Kramers-Kronig relations for Eq. 3.40) would result simply in a shift of the T_2 -peak (pump-frequency dependence) from the transition frequency ω_{10} to $\omega_{10} + \Im\Gamma_{10}^{(0)}(\omega_{10})$ (cf. Eqs. 3.14 and 3.16, respectively). The probe-frequency dependence of the T_2 -peak is different, since for the probing function $\zeta_{01}(\omega)$ as defined in Eq. 3.16 one needs the dephasing rate $\Gamma_{10}^{(1)}(\omega)$. This can be obtained from Eq. 3.43 simply by exchanging $J_{11}(\omega)$ and $J_{00}(\omega)$, what results in

$$\Gamma_{10}^{(1)}(\omega) = \Gamma_{01}^{(0)}(-\omega) = \left[\Gamma_{10}^{(0)}(\omega)\right]^* . \quad (3.50)$$

Consequently, the line-shape of $\zeta_{01}(\omega)$, which represents the probed emission, is the image mirrored at the axis $\omega = \omega_{10}$ of the line-shape of $\zeta_{10}(\omega)$, which represents the bleached absorption. In the case $\Gamma_{10}^{(0)}(\omega) \approx \Gamma_{10}^{(0)}(\omega_{10}) \neq \Gamma_{10}^{(1)}(\omega_{10})$ (cf. above), the probe-frequency dependence of the T_2 -peak is the superposition of two complex Lorentzians (cf. Eq. 3.17) with maxima approximately separated by the ‘effective’ Stokes-shift $S_{11} + 2(\Delta\varepsilon_1 - \Delta\varepsilon_0)$. Unfortunately, the ‘pure’ Stokes-shift S_{11} can not be extracted from the ‘effective Stokes-shift, since a independent determination of the term $2(\Delta\varepsilon_1 - \Delta\varepsilon_0)$ e.g. by the complex energy relaxation rate $\gamma_{01}(\omega_t - \omega_p)$ via the T_1 -peak (cf. Eq. 3.17) is not possible. According to Eq. 3.41 for $\Im\gamma_{01}(0) = \Im\gamma_{10}(0) = 0$ the interesting terms cancel out. In the case of non-Markovian T_2 -peaks it becomes even more difficult to extract the parameters $\Delta\varepsilon_1$, $\Delta\varepsilon_0$, and S_{11} from the ‘effective’ Stokes-shift as measured by NLPF (cf. Fig. 3.5).

⁵Interpreting the imaginary parts of the first terms in Eq. 3.43 as shifts of the eigen-energies ε_μ for the relevant system by the system bath coupling one obtains

$$\Delta\omega_{\mu 0} \xrightarrow{T \rightarrow 0K} \frac{1}{2} \sum_{\kappa \neq \mu} \sum_{\xi} \frac{|\omega_\xi q_{\xi\mu\kappa}|^2}{\omega_{\mu 0} - \omega_\xi} .$$

according to Eq.3.39. For $\omega_{\mu 0} \gg \omega_\xi$ this expression is quite similar to

$$\Delta\varepsilon_\mu^{(2)} = \frac{1}{2} \sum_{\kappa \neq \mu} \frac{|H'_{\mu\kappa}|^2}{\varepsilon_\mu - \varepsilon_\kappa} ,$$

which one obtains from second order Rayleigh-Schrödinger perturbation theory using the perturbation hamiltonian

$$H'_{\mu\kappa} = \sum_{\xi} \hbar\omega_\xi q_{\xi\mu\kappa} Q_\xi$$

for statistically independent coupling constants $q_{\xi\mu\kappa}$ and $\langle Q_\xi^2 \rangle = 1$ in the vibrational ground state.

3.2. Harmonic oscillator model

3.2.4 Debye spectral density

In order to analyze NLPF-spectra in the non-Markovian case of complex, frequency dependent relaxation rates, the spectral density $J_{\mu\nu}(\omega)$ is to be represented by a smooth model function with as few parameters as possible instead of using Eq. 3.38, which picks out a infinite number of single modes from the reservoir by δ -functions. Last but not least this is necessary for the mapped the spectral densities $J_{\mu\mu}(\omega)$ being asymptotically ohmic, as mentioned above (cf. Eq. 3.45). Beside of the asymptotic ω^{-1} for $\omega \rightarrow 0$ the used function $J_{\mu\mu}(\omega)$ has to be limited for $\omega \rightarrow \infty$. Otherwise, one will not obtain a finite Stokes-shift $S_{\mu\mu}$ (cf. Eq. 3.48).

An example for a smooth function, which fulfills both requirements to the spectral density, is the so-called Debye spectral density [Mukamel, 1995, May and Kühn, 2000], which is given as

$$J_{\mu\nu}(\omega) = \frac{S_{\mu\nu}}{\pi\omega} \frac{\omega_D}{\omega^2 + \omega_D^2}, \quad (3.51)$$

with a characteristic frequency ω_D , called the Debye frequency. Here, it has been assumed that the spectral density $J_{\mu\nu}(\omega)$ is independent of the states $|\mu\rangle$ and $|\nu\rangle$, except for the parameter $S_{\mu\nu}$. It should be mentioned that the Debye spectral density represents the simple case of an reservoir represented by a single overdamped Brownian oscillator [Mukamel, 1995].

Inserting Eq. 3.51 in Eq. 3.40 one obtains immediately the real part of the function $K_{\mu\nu}(\omega)$ as

$$\Re K_{\mu\nu}(\omega) = S_{\mu\nu} \frac{\omega_D \omega}{\omega^2 + \omega_D^2} \frac{1}{1 - \exp[-\hbar\omega/kT]}. \quad (3.52)$$

After a bit more complicated calculation, the imaginary part of the function $K_{\mu\nu}(\omega)$ turns out to be

$$\Im K_{\mu\nu}(\omega) = S_{\mu\nu} \frac{\omega_D \omega}{\omega^2 + \omega_D^2} \left(\frac{\omega_D}{2\omega} + \frac{kT}{\hbar\omega_D} + \frac{1}{\pi} \psi \left[\frac{\hbar\omega_D}{2\pi kT} \right] - \frac{1}{\pi} \Re \psi \left[i \frac{\hbar\omega}{2\pi kT} \right] \right), \quad (3.53)$$

where $\psi[x]$ represents the Digamma function [Abramowitz and Stegun, 1972]. In Fig. 3.2 the function $K_{\mu\nu}(\omega)$ is shown for different temperatures. Note that $\Re K_{\mu\nu}(0) = S_{\mu\nu} kT / \hbar\omega_D$ and $\Im K_{\mu\nu}(0) = S_{\mu\nu} / 2$ is valid at any temperature in correspondence to Eqs. 3.45 and 3.47, respectively.

In the high temperature limit, i.e. $kT \gg \hbar\omega_D$, one obtains

$$K_{\mu\nu}(\omega) \xrightarrow{kT \gg \hbar\omega_D} S_{\mu\nu} \frac{kT}{\hbar(\omega_D - i\omega)}, \quad (3.54)$$

It is worth to be noted that the Fourier transformed of $K_{\mu\nu}(\omega)$ represents an exponential decay with a time constant $\tau_R = \omega_D^{-1}$ (cf. supplement 3.5). This express clearly the fact that the Debye spectral density represents an overdamped reservoir dynamics (cf. [Mukamel, 1995]). The

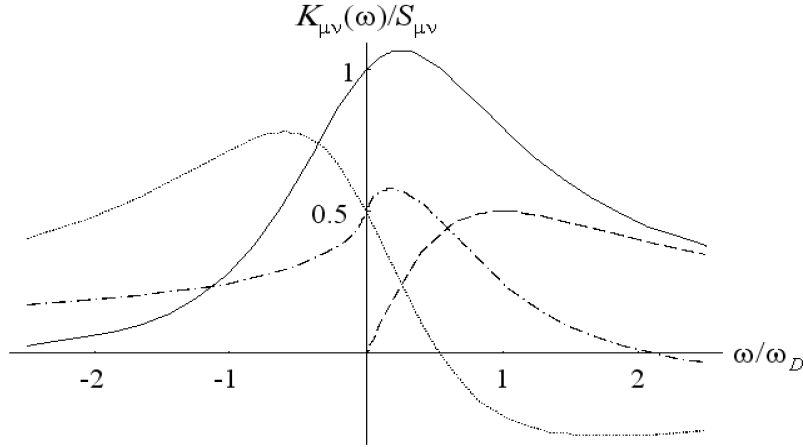


Figure 3.2: Coupling function $K_{\mu\nu}(\omega)$ for a Debye spectral density at $T = \hbar\omega_D/k$ (solid line: $\Re K_{\mu\nu}(\omega)$; dots: $\Im K_{\mu\nu}(\omega)$) and for $T \rightarrow 0\text{K}$ (dashes: $\Re K_{\mu\nu}(\omega)$; dash-dots: $\Im K_{\mu\nu}(\omega)$).

Markov-limit is obtained for $\omega_D \gg |\omega|$, where according to Eq. 3.54 the functions $K_{\mu\nu}(\omega)$ and subsequently the relaxation rates are approximately real and frequency independent. In time domain this means $\tau_R \rightarrow 0$, with other words there exists no memory for the system-reservoir interaction (cf. section 3.1.3).

In the low temperature limit ($\omega_D \gg kT/\hbar$) from Eqs. 3.52 and 3.53 one obtains

$$K_{\mu\nu}(\omega) \xrightarrow{\hbar\omega_D \gg kT} S_{\mu\nu} \frac{\omega_D \omega}{\omega^2 + \omega_D^2} \left(\Theta[\omega] + \frac{i}{2} \frac{\omega_D}{\omega} + \frac{i}{\pi} \ln \left| \frac{\omega_D}{\omega} \right| \right). \quad (3.55)$$

The unit-step function $\Theta[\omega]$ express the fact that for $T \rightarrow 0\text{K}$ thermal activated energy fluctuations of the reservoir ($\omega < 0$) are not available but only dissipation of the excess energy ($\omega > 0$) from the relevant system into the reservoir.

3.3 NLPF-spectrum of a dissipative two-level system

The NLPF-spectrum of a dissipative two-level system with probably non-Markovian reservoir dynamics is given by the line-shape function in Eq. 3.17 for $\omega_D \gg \gamma_{01}(\omega)$ (cf. Eq. 3.15). The latter condition calls for studying the frequency dependent energy relaxation rate first, which also determines the T_1 -peak, .

3.3. NLPF-spectrum of a dissipative two-level system

3.3.1 T₁-peak of a dissipative two-level system

Since the optical transition the frequency ω_{10} is much larger than the detuning $\omega_t - \omega_p$ the T₁-peak depends on (cf. Eq. 3.17), it is useful to expand $\gamma_{01}(\omega_t - \omega_p)$ into a Taylor series for the small parameter $(\omega_t - \omega_p)/\omega_{10}$ as

$$\tilde{\gamma}_{01}(\omega) \approx \tilde{\gamma}_{01} + \tilde{\gamma}'_{01} \frac{\omega}{\omega_{10}} + \dots \quad (3.56)$$

Here γ_{01} represents the static energy relaxation rate given by

$$\tilde{\gamma}_{01} = \gamma_{01}(0) \approx S_{10} \frac{2\omega_D \omega_{10}}{\omega_{10}^2 + \omega_D^2}. \quad (3.57)$$

Due to the detailed balance (cf. Eq. 3.44) for $\hbar\omega_{10} \gg kT$ the corresponding static uphill energy relaxation rate is negligible, i.e. $\gamma_{10}(0) \approx 0$. Note that inter alia the static rate $\tilde{\gamma}_{01}$ determines the height of the T₂-peak (cf. Eq. 3.17). Using Eq. 3.57 one can also check the time-scale of the energy relaxation in comparison to that of the reservoir reorganization, which is given by $\tau_R = \omega_D^{-1}$ (see above and supplement 3.5). Thus the condition $\omega_D \gg \tilde{\gamma}_{01}(0)$ corresponds to Eq. 3.15 and is certainly fulfilled for $S_{10} \ll \omega_{10}$. Hence, for the present case, where the Debye spectral density given in Eq. 3.51 is the same for dephasing and energy relaxation, one can usually assume that the reservoir is equilibrated before the excited state is probed⁶. Therefore, in what follows the line-shape function as given in Eq. 3.17 shall be used in order to analyze the NLPF-spectrum of a dissipative two-level system the case of the two-level system at sufficient high temperature.

The linear term of Eq. 3.56 is purely imaginary with the coefficient $\tilde{\gamma}'_{01}$ given as

$$\tilde{\gamma}'_{01} \approx i \frac{2}{\pi} \tilde{\gamma}_{01} \frac{\omega_{10}^2 - \omega_D^2}{\omega_{10}^2 + \omega_D^2} \left(\psi \left(\frac{\hbar\omega_D}{2\pi kT} \right) + \frac{\pi kT}{\hbar\omega_D} - 1 \right) \quad (3.58)$$

The non-linear terms of the Taylor series are absolutely much smaller than $|\tilde{\gamma}_{01} + \tilde{\gamma}'_{01} \frac{\omega}{\omega_{10}}|$. Even if the linear term is the dominant one, the T₁-peak will be still a Lorentzian, however, then with a line width given as

$$FWHM \approx 2 \tilde{\gamma}_{01} \left(1 + \frac{\tilde{\gamma}'_{01}}{i\omega_{10}} \right)^{-1}. \quad (3.59)$$

Usually $|\tilde{\gamma}'_{01}| \ll \omega_{10}$ is valid for a wide range of Debye frequencies ω_D . Even for $\omega_D \sim \omega_{10}$ (but $\omega_D \neq \omega_{10}$) the maximum corrections are of the order $S_{10}/\omega_{10} \ll 1$. Thus in order to determine the T₁-peak one can usually set $\tilde{\gamma}_{01}(\omega) \approx \tilde{\gamma}_{01}$ as in Markov approximation.

⁶In the case of inhomogeneous broadening (cf. supplement 3.5 and section 5) the constriction to a unique Debye spectral density seems obviously to be wrong.

3.3.2 Non-Markovian T_2 -peak in the high temperature limit

As mentioned above for the two-level system the frequency dependence of the energy relaxation rate γ_{01} is usually negligible. Therefore, it is the pure-dephasing part in Eq. 3.43 which may causes a deviation of the shape of the T_2 -peak from the (quadratic) Lorentzian shape shown in Fig. 2.3, due to a non-Markovian dynamics. Both dependences, that on probe as well as that on pump frequency are affected, since the complex and frequency dependent dephasing rate $\Gamma_{10}^{(0)}(\omega)$ occur in the cross-section of pumping $\sigma_{10}(\omega_p, \omega_p)$ and as well as in the combined probing functions $\zeta_{10}(\omega_t) + \zeta_{01}(\omega_t)$ (cf. Eqs. 3.14, 3.16, and 3.17; for $\zeta_{01}(\omega_t)$ see below).

In the high temperature limit $kT \gg \hbar\omega_D$ according to Eqs. 3.54 the frequency dependence of the dephasing rate is given by

$$\Gamma_{10}^{(0)}(\omega) = \Gamma_{10}^{(1)}(\omega) = \frac{\gamma_{01}}{2} + \bar{\Gamma}_{10} \frac{\omega_D}{\omega_D - i(\omega - \omega_{10})}. \quad (3.60)$$

using the ‘Markovian’ pure-dephasing rate

$$\bar{\Gamma}_{10} = S_{11} \frac{2kT}{\hbar\omega_D}. \quad (3.61)$$

Note that in the high temperature limit the Stokes-shift is negligible for $\bar{\Gamma}_{10} \gg S_{11}$.

The Markov limit is obtained for the relevant frequency range if $\bar{\Gamma}_{10} \ll \omega_D$, which means an extremely small Stokes-shift S_{11} – more precisely

$$S_{11} \ll \frac{\hbar\omega_D^2}{2kT} \ll \omega_D. \quad (3.62)$$

Note that this condition is more constrictive than the initial one that the displacements $q_{\xi,11}$ have to be small for application of perturbation theory in the system-reservoir interaction.

Nevertheless, for $\bar{\Gamma}_{10} \gtrsim \omega_D$ the second order perturbation theory as used above fails. Thence, one has to apply other methods like the cumulant expansion (see supplement 3.5). In the extreme case $\gamma_{01} \ll \omega_D \ll \bar{\Gamma}_{10}$, which represents the inhomogeneous dephasing limit⁷, one obtains the probing functions (cf. Eqs. 3.80-3.83) as

$$\zeta_{10}(\omega) = \zeta_{01}(\omega) \approx \frac{|\mu_{\mu\nu}|^2}{\hbar\varepsilon_0 n c} \frac{\omega}{\sqrt{2\pi\bar{\Gamma}_{10}\omega_D}} \int_{-\infty}^{\infty} \frac{\exp\left[-\frac{\omega'^2}{2\bar{\Gamma}_{10}\omega_D}\right]}{\gamma_{01} + i(\omega - \omega' - \omega_{10} - S_{11})} d\omega'. \quad (3.63)$$

Thus the square module $|2\zeta_{10}(\omega_t)|^2$ describes the complete probe-frequency dependence of the T_2 -peak. The cross-section of pumping $\sigma_{10}(\omega, \omega) = 2\Re\{\zeta_{10}(\omega)\}$ represents a Voigt-profile

⁷The author prefer to call the limit $\bar{\Gamma}_{01} \gg \omega_D$ the inhomogeneous dephasing limit (cf. [Mukamel, 1995]). With regard to the specifics of the two-dimensional NLPF-spectrum (cf. section 5) the name inhomogeneous limit shall be reserved for the limit $\gamma_{01} \gg \omega_D$.

3.3. NLPF-spectrum of a dissipative two-level system

with a Gaussian width (FWHM) of $2\sqrt{\ln 2 \bar{\Gamma}_{10} \omega_D}$ and a Lorentzian width of $2\gamma_{01}$. In order to obtain the pump-frequency dependence of the T_2 -peak this has to be only squared. Both frequency dependences are not really correlated to each other according to Eq. 3.17. In section 5.3 one will see that the same result can be obtained more easily by using the energy transfer model which represents the spectral diffusion within a inhomogeneously broadened spectrum (cf. Fig. 5.5).

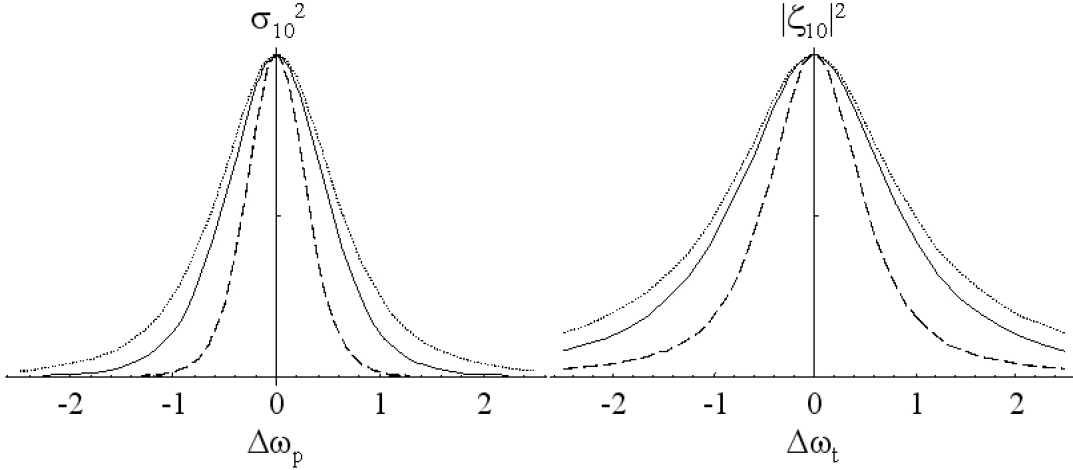


Figure 3.3: Nonmarkovian pump and probe frequency dependences of the T_2 peak ($\sigma_{10}(\omega_p, \omega_p)^2$ and $|\zeta_{10}(\omega_t)|^2$, respectively) in the high temperature limit ($kT \gg \hbar\omega_D$), for $\bar{\Gamma}_{10}/\omega_D = 0.1$ (dots), 1 (solid line), and 10 (dashes). Calculation according to section 3.5.1. All functions are normalized for maximum. Axes label as $\Delta\omega_{p,t} = (\omega_{p,t} - \omega_{10})/\omega_D$.

In Fig. 3.3 the probe- and the pump-frequency dependences of the T_2 -peaks at high temperature are shown. Thereby, the Stokes-shift S_{11} and energy relaxation rate γ_{01} have been assumed to be negligibly small (cf. above). For increasing ratios $\bar{\Gamma}_{10}/\omega_D$ the line shapes demonstrate the transition from the Markov-limit (Lorentzian) to the inhomogeneous dephasing limit (Gaussian). Interesting the intermediate case $\bar{\Gamma}_{10} = \omega_D$ seems to interpolate between the line shapes of the two extreme cases. While the central part looks like the (quadratic) Lorentzian obtained in the Markovian-limit, the outer wings decline more like those of a Gaussian. Another interesting fact is that in the intermediate case the widths of the T_2 -peak in respect of the probe- and the pump-frequency dependences ($FWHM$ and $FWQM$, respectively) do not correspond anymore (cf. Fig. 3.4), since the $FWHM$ of $|2\zeta_{10}(\omega_t)|^2$ is slightly larger than the $FWQM$ of $|\sigma_{10}(\omega_p, \omega_p)|$. Beside, the significant decline of the wings, which may be difficult to identify, this may be the only hint to a non-Markovian pure dephasing process that one can find in a NLPF-spectrum of a two-level system at high temperature.

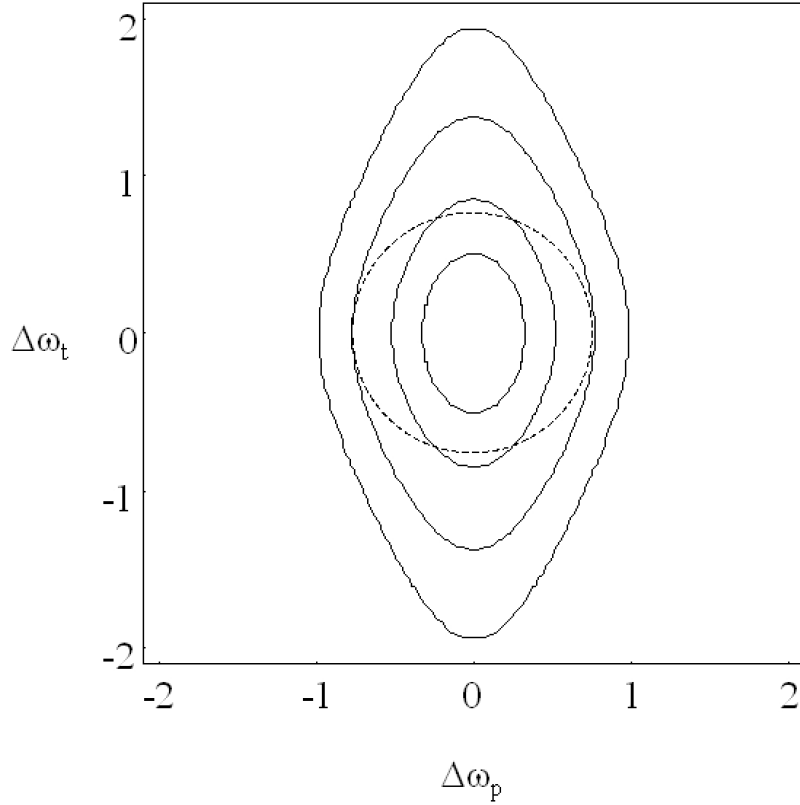


Figure 3.4: Non-Markovian T_2 -peak of a two-level system for $\bar{\Gamma}_{10} = \omega_D \gg \gamma_{01}, kT/\hbar$. Isolines are drawn at 0.125, 0.25, 0.5, 0.75 of the maximum value. The dashed circle represents the $FWQM$ in respect of the pump-frequency dependence. Axes labels as in Fig. 3.3.

In the ‘real’ inhomogeneous limit ($\omega_D \ll \gamma_{01}, \bar{\Gamma}_{10}$) the cumulant expansion fails (by reasons given in the supplement 3.5). Therefore, an alternative method for calculating the inhomogeneous broadening, which will be demonstrated in chapter 5, is to prefer. In this limit, the probe and pump frequency dependences are extremely correlated to each other (cf. Eq. 3.78), i.e. the position of the probe frequency dependence of the T_2 -peak maximum shifts to higher frequencies for increasing pump frequency (cf. Fig. 5.1). For the intermediate case $\bar{\Gamma}_{10} \gtrsim \omega_D \gtrsim \gamma_{01}$, between homogeneous and inhomogeneous broadening, the cumulant expansion (cf. supplement 3.5) is the favorable method.

3.3.3 T_2 -peak at low temperatures

At lower temperatures, where $kT \lesssim \hbar\omega_D$ (but still $\gamma_{01} \ll \omega_D$) the NLPF-spectrum of the two-level system results from the NLPF-line-shape function as given by Eq. 3.17. This means

3.3. NLPF-spectrum of a dissipative two-level system

again that the pump and probe frequency dependences of the T_2 -peak are not correlated to each other. The cross-section of pumping and the probing function however given by Eqs. 3.14 and 3.16 may be quite different to those obtained in the high temperature limit.

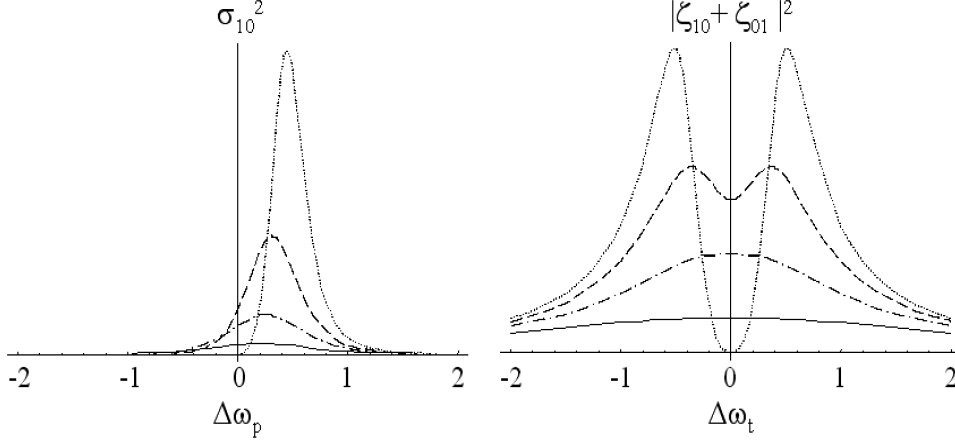


Figure 3.5: Nonmarkovian pump and probe frequency dependences of the T_2 peak ($\sigma_{10}(\omega_p, \omega_p)^2$ and $|\zeta_{10}(\omega_t) + \zeta_{01}(\omega_t)|^2$, respectively) for Stokes shift $S_{11} = \omega_D$ at temperatures $T \rightarrow 0\text{K}$ (dots), $T = 0.5 T_D$ (dashes) $T = T_D$ (dash dots) and $T = 2T_D$ (solid line) with $T_D = \hbar\omega_D/k$. Axes label as $\Delta\omega_{p,t} = (\omega_{p,t} - \omega_{10})/\omega_D$.

For lowering the temperature the T_2 -peaks show specific features resulting⁸ (cf. Fig. 3.5). The pump frequency dependence $\sigma_{10}(\omega_p, \omega_p)^2$ gets an asymmetric line-shape. Finally, at $T \rightarrow 0\text{K}$ it vanishes completely for $\omega_p < \omega_{10}$ and the maximum is shifted to $\omega_{10} + S_{11}/2$. The probe frequency dependence $|\zeta_{10}(\omega_t) + \zeta_{01}(\omega_t)|^2$, however, split into two peaks for $T \rightarrow 0\text{K}$: One with maximum at $\omega_t > \omega_{10}$ represents the probing of the bleaching (cf. $\zeta_{10}(\omega_t)$), the other with maximum at $\omega_t < \omega_{10}$ that of the stimulated emission (cf. $\zeta_{01}(\omega_t)$), respectively. Due to the complex superposition of the probe spectrum in NLPF at $T \rightarrow 0\text{K}$ the distance between the two peak-maxima is slightly larger than the Stokes-shift (S_{11}) as obtained from the corresponding absorption and fluorescence spectra. All these effects are related to the frequency-dependent dephasing rate, which at low temperatures is necessarily asymmetric at least due to the Bose-Einstein factor in Eq. 3.52 (cf. Fig. 3.2). The symmetry of the probing function $\zeta_{10}(\omega_t) + \zeta_{01}(\omega_t)$ in respect of the axis $\omega_t = \omega_{10}$ results from the general relation between the dephasing rates $\Gamma_{10}^{(0)}(\omega)$ and $\Gamma_{01}^{(1)}(-\omega)$ as given by Eq. 3.50. Fig. 3.6 illustrates the two-dimensional shape of the T_2 -peak at $T \rightarrow 0\text{K}$.

⁸It will be assumed that the dephasing related to the energy relaxation, i.e. γ_{11} as well as $\Delta\varepsilon_1 - \Delta\varepsilon_0$ (cf. Eqs. 3.45 and 3.47) are negligible even for $T \rightarrow 0\text{K}$.

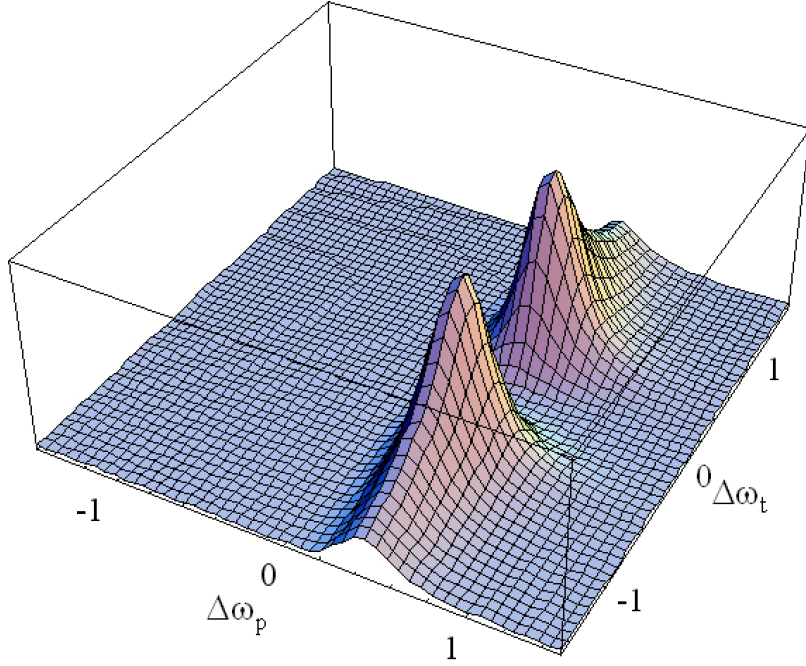


Figure 3.6: Nonmarkovian T_2 peak for $T \rightarrow 0\text{K}$. For other parameters and axes see Fig. 3.5.

At his point, however, two reservations have to be made: (i) for extreme low temperatures, the reservoir dynamics may freeze out. This means that $\tau_R \gg \omega_D^{-1}$. In this case the condition for thermalization of the reservoir before probing as given by Eq. 3.15 may not be fulfilled anymore. In the extreme case this results in the inhomogeneous limit mentioned above (cf. section 3.1.3 and chapter 5); (ii) for $S_{11} \gg \omega_D$ or kT/\hbar one obtains a cross-section of pumping which almost represents a Lorentzian like that obtained in the Markov limit. The different probe frequency dependence with two peaks, both almost Lorentzians, which are well separated by the Stokes shift, only seems to clarify the different situation. In fact a similar pattern of T_2 -peaks appears also for a multi-level system with e.g. excited state absorption (cf. section 4.1.4) which is completely Markovian in all other respects.

3.4 Summary

In order to explain the homogeneous line shapes of the T_1 - and T_2 -peaks appearing in the NLPF-spectrum of a dye diluted in a dissipative solvent a model has been developed – following an approach only slightly different from the standard way [Blum, 1981, Mukamel, 1995, May and Kühn, 2000]. Based on the separation of the problem into a relevant system and a reservoir, the degrees of freedom were reduced to a reasonable number. The relevant system has been

3.4. Summary

described quantum–mechanically in a diabatic basis set. The remains of the reservoir after the reduction were complex relaxation terms (see Eq. 3.36) in the effective equation of motion for the relevant system. For the model of stochastically displaced harmonic oscillators these terms reduce automatically to only two kinds of frequency dependent and complex relaxation rates: the dephasing rate $\Gamma_{\mu\nu}(\omega)$ and the energy relaxation rates $\gamma_{\mu\kappa}(\omega)$. Thus one obtained the same result as for applying the secular approximation. At this point the author would like to admit that the featured methods to describe dissipation are still in general discussion, particularly the Redfield approach if the secular approximation is not valid (cf. [Seke, 1991b]).

It turned out that the frequency dependence of the energy relaxation rates is only a minor effect, which does not force the T_1 -peak to deviate from a Lorentzian (cf. the phenomenological model in chapter 2) Whereas the frequency dependences of the dephasing rates are decisive for the shapes of the T_2 -peaks, which may deviate from the (quadratic) Lorentzians in Fig. 2.3 extremely and particularly differently for the probe- and the pump-dependency (cf. Figs. 3.4 and 3.6). Only in the Markov-limit, when the reservoir reacts instantaneously, the T_2 -peak results exactly as shown in Fig. 2.2.

These deviations have been studied in the work be presented for describing the reservoir by the quite common Debye spectral density [Blum, 1981, Mukamel, 1995, May and Kühn, 2000] in certain limits. Thereby, it turns out that the second order perturbation theory for the system–reservoir interaction is not always sufficient. For such cases it fails, the cumulant expansion provides the exact result in the present model (see supplement 3.5). Unfortunately this approach needs a lot more computational effort in order to analyzing measured NLPF-spectra. Therefore, in mainly two different limits will be used in what follows: (i) the Markov-limit, with frequency-independent relaxation rates $\Gamma_{\mu\nu}$ and $\gamma_{\mu\nu}$ resulting in (quadratic) Lorentzian line shapes, as already mentioned, and (ii) the inhomogeneous dephasing limit which results in Gaussian line shapes or Voigt-profiles, respectively. The Markov-approximation representing the homogeneous broadening will be implied for the discussion of multi-level systems in the following chapter 4. The transition to the corresponding non-Markovian but not inhomogeneously broadened case (e.g. the inhomogeneous dephasing limit) is simply to perform by substituting the respective constant rates by the frequency-dependent relaxation rates $\Gamma_{\mu\nu}^{(\nu)}(\omega)$ in the respective NLPF-line-shape function. Note that in doing so one has to take care that emission and absorption processes are treated separately. The special case of the inhomogeneous broadening, which results from a non-Markovian energy relaxation due to an extreme slow reorganization of the reservoir, will be treated in chapter 5. As mentioned above, in this case a strong correlation between pump and probe frequency dependence of the T_2 -peak occurs (cf. fig. 5.1).

Further results, well-known but important in what follows, of this chapter are: (i) the detailed balance between up- and downhill energy relaxation rates (cf. Eq. 3.44); (iii) the

limitation of the total dephasing rate at low temperature by the energy relaxation (cf. Eq. 3.45), which means that the T_1 -peak can not be significantly broader than the T_2 -peak; (ii) the linear temperature dependence of the pure dephasing rate, which suggests that for room temperature the dephasing rate will mostly be much larger than the energy relaxation what limits tunneling terms (cf. section 2.3.2) and two-photon peaks (cf. section 2.3.3); and (iv) the occurrence of an Stokes-shift between probing the bleaching and the stimulated emission.

3.5 Supplement: Cumulant expansion

For the applicability of perturbation theory initially it has to be assumed that the system-reservoir interaction given by H_{SR} is small. For the harmonic oscillator model this limitation can be overcome by using the cumulant expansion [Mukamel, 1995].

3.5.1 Cumulant expansion of the Greens function

In order to propagate the reduced density matrix $\rho_{\mu\nu}(t)$ in time-domain one needs the Greens function

$$\tilde{\mathcal{G}}(t) = \langle \mathcal{G}(t) \rangle_R = \langle \exp [i (\mathcal{L}_S + \mathcal{L}_R + \mathcal{L}_{SR}) t] \rangle_R. \quad (3.64)$$

Expanding the exponential function $\exp [\mathcal{L}_{SR} t]$ in the interaction picture the reduced into a power series and carrying out the averages over the reservoir degrees of freedom for each addend separately, the Greens function yields as

$$\tilde{\mathcal{G}}(t) = 1 + \sum_{n=1}^{\infty} i^n \int_0^t \cdots \int_0^{\tau_{n-1}} \langle \mathcal{L}_{SR}(\tau_n) \cdots \mathcal{L}_{SR}(\tau_1) \rangle_R d\tau_n \cdots d\tau_1. \quad (3.65)$$

using the interaction picture for the time dependent operator $\mathcal{L}_{SR}(t)$. In the framework of the harmonic oscillator model used above one obtains cumulants $\langle \mathcal{L}_{SR}(\tau_n) \cdots \mathcal{L}_{SR}(\tau_1) \rangle_R$ which all can be expressed in terms of $\mathcal{R}(\tau)$ as given by Eq. 3.6. Thus the time-dependent Greens-function for the reduced density operator reads as

$$\tilde{\mathcal{G}}(t) = \exp \left[i \mathcal{L}_S t - \int_0^t \int_0^{\tau'} \mathcal{R}(\tau) d\tau d\tau' \right]. \quad (3.66)$$

In secular approximation the matrix elements of $\tilde{\mathcal{G}}(t)$ which propagate the off-diagonal reduced density matrix elements $\rho_{\mu\nu}(t)$ for $t \geq 0$ are given as

$$\tilde{\mathcal{G}}_{\mu\nu,\mu\nu}(t) = \exp [i\omega_{\mu\nu} t - G_{\mu\nu}(t)] \quad (3.67)$$

3.5. Supplement: Cumulant expansion

with the time-domain line-shape functions defined by

$$G_{\mu\nu}(t) = \frac{1}{2\pi} \int_{-\infty}^{\infty} \Gamma_{\mu\nu}(\omega') \frac{1 - i\omega't - \exp[-i\omega't]}{\omega'^2} d\omega'. \quad (3.68)$$

Here the function $\Gamma_{\mu\nu}(\omega')$ is exactly that given by Eq. 3.43. For the Debye spectral density in the high temperature limit (cf. Eq. 3.54) one obtains

$$G_{\mu\nu}(t) = 1 - \bar{\Gamma}_{\mu\nu}t - \frac{\bar{\Gamma}_{\mu\nu}}{\omega_D} \exp[-\omega_D t], \quad (3.69)$$

which in the Markov limit ($\omega_D \gg \bar{\Gamma}_{10}$) results in $G_{\mu\nu}(t) \approx \bar{\Gamma}_{\mu\nu}t$, reproducing the phenomenological frequency domain Green's function given by Eq. 2.20. In the limit $\bar{\Gamma}_{\mu\nu} \gg \omega_D$ one obtains approximately

$$G_{\mu\nu}(t) \approx -\frac{1}{2}\bar{\Gamma}_{\mu\nu}\omega_D t^2 \quad (3.70)$$

which results by Fourier-transformation in the frequency domain Green's function

$$\tilde{\mathcal{G}}_{\mu\nu,\mu\nu}(\omega) = \frac{1}{\sqrt{2\pi}\bar{\Gamma}_{\mu\nu}\omega_D} \exp\left[-\frac{(\omega - \omega_{\mu\nu})^2}{2\bar{\Gamma}_{\mu\nu}\omega_D}\right]. \quad (3.71)$$

This represents a Gaussian line-shape. In the inhomogeneous dephasing limit $\bar{\Gamma}_{\mu\nu} \gg \omega_D \gg \gamma_{\mu\mu} + \gamma_{\nu\nu}$ the Fourier-transformed Greens function represents a complex Voigt-profile as given by Eq. 3.63, due to the time-domain line-shape function being

$$G_{\mu\nu}(t) \approx \frac{1}{2}(\gamma_{\mu\mu} + \gamma_{\nu\nu})t - \frac{1}{2}\bar{\Gamma}_{\mu\nu}\omega_D t^2. \quad (3.72)$$

In the inhomogeneous limit, i.e. $\bar{\Gamma}_{\mu\nu}, \gamma_{\mu\mu} + \gamma_{\nu\nu} \gg \omega_D$, further considerations are necessary, due to the non-Markovian energy relaxation, which will be shown in the next section.

The cross-section of pumping $\sigma(\omega_p, \omega_p)$ as well as the probing functions $\zeta_{\mu\nu}(\omega)$, as they result from Eq. 3.71, are quite different from those obtained by the Eqs. 3.14 and 3.16, respectively, if one use the frequency dependent dephasing rates $\Gamma_{\mu\nu}^{(\nu)}(\omega)$ given as in Eq. 3.43 (see Fig. ??). The reason for this difference is that in Eq. 3.7, which the deduction of Eq. 3.43 based on, only the term linear in $\mathcal{R}(\omega)$ has been considered. The cumulant expansion, however, counts for all orders of $\mathcal{R}(\tau)$. Nevertheless, it is possible to deduce a frequency dependent dephasing rate $\Gamma_{\mu\nu}^{(\nu)}(\omega)$ from the cumulant expansion, which can be applied to the Eqs. 3.14 and 3.16. For Eq. 3.69 applied on Eq. 3.67 the Fourier-transformed Greens function $\tilde{\mathcal{G}}_{\mu\nu,\mu\nu}(\omega)$ can be expanded into a continued fraction [Mukamel, 1995], which compared with the first term in Eq. 3.9 results in the frequency dependent dephasing rate

$$\Gamma_{\mu\nu}^{(\nu)}(\omega) = \frac{\bar{\Gamma}_{\mu\nu}\omega_D}{\omega_D - i\left(\omega - \tilde{\omega}_{\mu\nu}^{(\nu)}\right) + \frac{\bar{\Gamma}_{\mu\nu}\omega_D}{2\bar{\Gamma}_{\mu\nu}\omega_D}} \quad (3.73)$$

$$= \frac{\bar{\Gamma}_{\mu\nu}\omega_D}{\omega_D - i\left(\omega - \tilde{\omega}_{\mu\nu}^{(\nu)}\right) + \frac{3\bar{\Gamma}_{\mu\nu}\omega_D}{3\omega_D - i\frac{\omega - \tilde{\omega}_{\mu\nu}^{(\nu)}}{\omega_D}} + \dots}$$

for the renormalized complex transition frequency

$$\tilde{\omega}_{\mu\nu}^{(\nu)} := \omega_{\mu\nu} - \frac{1}{2}(S_{\mu\mu} + i\gamma_{\mu\mu} + i\gamma_{\nu\nu}). \quad (3.74)$$

For a Markovian energy relaxation here the diagonal rates $\gamma_{\mu\mu}$ and $\gamma_{\nu\nu}$ have been supposed to be frequency independent (cf. sections 3.1.3 and 3.3.1). One can see that the result from second order perturbation theory as given by Eq. 3.60 represents a first approximation to the continued fraction in Eq. 3.73 for small $\bar{\Gamma}_{\mu\nu}$. In the center of the T_2 -peak where $|\omega - \omega_{\mu\nu}| \sim \bar{\Gamma}_{\mu\nu}$ this might be a good approximation. The outer wings, however, decay Gaussian-like, as results from Eq. 3.73 in the limit $|\omega - \omega_{\mu\nu}| \gg \omega_D$ (cf. Fig. 3.3).

3.5.2 Cumulant expansion for the NLPF-line-shape function

In order to calculate the NLPF line-shape function in the inhomogeneous limit (see section 3.1.3) one has to carry out the average over the reservoir degrees of freedom for the whole NLPF-line-shape function $s(\omega_t, \omega_p)$ (cf. Eq. 3.18). Analogously, in time domain one has to average over the whole third order response function as $\langle S(t_1, t_2, t_3) \rangle_R$ (see Eq. 2.44). Using the cumulant expansion for the two-level system (cf. [Mukamel, 1995]) this results in

$$\begin{aligned} \langle S(t_1, t_2, t_3) \rangle_R = \frac{1}{15} & \{ \zeta_{10}(t_3) \beta_{1010}(t_1, t_2, t_3) \zeta_{10}(t_1) \\ & + \zeta_{01}(t_3) \beta_{0110}(t_1, t_2, t_3) \zeta_{10}(t_1) \\ & + \zeta_{10}(t_3) \beta_{1001}(t_1, t_2, t_3) \zeta_{01}(t_1) \\ & + \zeta_{01}(t_3) \beta_{0101}(t_1, t_2, t_3) \zeta_{01}(t_1) \} (n_1 - n_0) \end{aligned} \quad (3.75)$$

using the time-propagation function for pumping and probing

$$\zeta_{\mu\nu}(t) = \frac{|\mu_{10}|^2}{\hbar \varepsilon_0 n c} \exp [i\omega_{\mu\nu} t - G_{\mu\nu}(t)] \quad (3.76)$$

and the triple time-correlation function given by

$$\begin{aligned} \beta_{\mu\nu\kappa\lambda}(t_1, t_2, t_3) & = \exp [-\gamma_{01} t_2] \times \exp [G_{\mu\nu}(t_2 + t_3) G_{\mu\nu}(t_2)] \\ & \times \exp [G_{\kappa\lambda}(t_1 + t_2) + G_{\kappa\lambda}(t_1 + t_2 + t_3)] \end{aligned} \quad (3.77)$$

Here the energy relaxation rate γ_{01} has again been supposed to be frequency independent and much larger than the backwards rate γ_{10} (cf. section 3.3.1). In general (cf. [Mukamel, 1995]) one obtains the NLPF-line-shape function as

$$\begin{aligned} s(\omega_t, \omega_p) = \frac{1}{15} \frac{|\mu_{10}|^4 \omega_t \omega_p}{(\hbar \omega_D \varepsilon_0 n c)^2} \sum_{n=0}^{\infty} & \left\{ \frac{Z_n(\tilde{\omega}_{10} - \omega_t) 2\Re \{ Z_n(\tilde{\omega}_{10} - \omega_p) \}}{n\omega_D + \gamma_{01}} \right. \\ & \left. + \frac{Z_n(\tilde{\omega}_{10} - \omega_t) \{ Z_n(\tilde{\omega}_{10} - \omega_t) + Z_n^*(\tilde{\omega}_{10} - \omega_p) \}}{n\omega_D + \gamma_{01} + i(\omega_p - \omega_t)} \right\} \end{aligned} \quad (3.78)$$

3.5. Supplement: Cumulant expansion

with the auxiliary (confluent hypergeometric) functions⁹

$$Z_n(\omega) = \sum_{m=0}^{\infty} \frac{n!}{m!} \frac{\left(\frac{\bar{\Gamma}_{10}}{\omega_D}\right)^m (n+1)_m}{\left(\frac{\bar{\Gamma}_{10}}{\omega_D} - i\frac{\omega}{\omega_D} + n + 1\right)_m \left(\frac{\bar{\Gamma}_{10}}{\omega_D} - i\frac{\omega}{\omega_D}\right)_{n+1}}. \quad (3.79)$$

For energy relaxations slower than the reservoir reorganization, i.e. $\omega_D \gg \gamma_{01}$ (cf. section 3.1.3), all addends in Eq. 3.78 but that for $n = 0$ can be neglected. In this case there exists no correlation between the probe- and pump-frequency dependence of the T_2 -peak, which result from the probing functions and the cross-section of pumping given by

$$\zeta_{10}(\omega) = \frac{|\mu_{10}|^2 \omega}{\hbar \varepsilon_0 n c} Z_0(\tilde{\omega}_{10}^{(0)} - \omega) \quad (3.80)$$

$$\zeta_{01}(\omega) = \frac{|\mu_{10}|^2 \omega}{\hbar \varepsilon_0 n c} Z_0(\tilde{\omega}_{10}^{(1)} - \omega) \quad (3.81)$$

$$\sigma_{10}(\omega, \omega') = \frac{|\mu_{10}|^2 \omega'}{\hbar \varepsilon_0 n c} \left(Z_0(\tilde{\omega}_{10}^{(0)} - \omega) + Z_0^*(\tilde{\omega}_{10}^{(0)} - \omega') \right), \quad (3.82)$$

respectively. The NLPF-line-shape function $s(\omega_t, \omega_p)$ yields as in Eq. 3.17 by using these functions.

In the Markov limit ($\bar{\Gamma}_{10}, \gamma_{01} \ll \omega_D$) the auxiliary function is given by

$$Z_0(\omega) = \frac{1}{i(\omega - \omega_{10}) + \bar{\Gamma}_{10}} \quad (3.83)$$

and the line-shape function is the same as for the phenomenological model Eq. 2.41, as expected. More interesting is the inhomogeneous dephasing limit ($\bar{\Gamma}_{10} \gg \omega_D \gg \gamma_{01}$) where the NLPF-line-shape function $s(\omega_t, \omega_p)$ for the T_2 -peak still factorize in a probe- and a pump-frequency dependence, the relevant auxiliary function $Z_0(\omega)$, however, is given by

$$Z_0(\omega) = \frac{i}{\sqrt{2\pi\bar{\Gamma}_{10}\omega_D}} \int_{-\infty}^{\infty} \exp\left[-\left(\frac{\omega'}{2\bar{\Gamma}_{10}\omega_D}\right)^2\right] \frac{d\omega'}{\omega' - \omega}. \quad (3.84)$$

This results in the probing function $\zeta_{10}(\omega_t)$ as given by Eq. 3.63 and a Voigt-profile for the cross-section of pumping $\sigma_{10}(\omega_p, \omega_p)$. Finally, for extreme slow reorganization of the reservoir compared to the energy relaxation in the ‘real’ inhomogeneous limit $\gamma_{01} \gg \omega_D$ the sum over n in Eq. 3.78 converges badly. Consequently, the probe- and pump-frequency dependence of the NLPF-line-shape function $s(\omega_t, \omega_p)$ are highly correlated. In this case it is preferable to use the alternative method of averaging the ‘homogeneous’ NLPF-line-shape function (considering the fast reorganizing part of the reservoir) over a distribution of transition frequencies as mentioned in section 3.1.3 and demonstrated in chapter 5.

⁹ $(x)_m = \begin{cases} 1 & \text{for } x = 0 \\ x(x+1)\dots(x+m-1) & \end{cases}$

Chapter 4

NLPF-spectra of multi-level systems

The NLPF-spectra as any spectra of molecular and supramolecular systems show a band structure, which represents the convolution of a discrete structure with different types of line-broadening. The former reflects the transitions between the different energy levels of the relevant system which can be e.g. displayed by a term scheme. The latter results from the interaction of the relevant system with a reservoir of modes as discussed previously (cf. chapter 3). In absorption spectroscopy only the distribution of the transition frequencies and the corresponding oscillator strengths determine the discrete structure of the spectrum. For NLPF as a combination of pump-probe and polarization spectroscopy additionally the energy relaxation path and the transition dipole orientations are important. To reveal both is the purpose for the analysis of the two-dimensional NLPF-spectrum. In order to do this, one can use the correlation between the probe- and pump-dependence of the T_2 -peaks and additionally the line shape of the T_1 -peak. The T_2 -peak correlations results from the fact that the probe beam can only pass the crossed polarizer, if the respective transition has been bleached or enhanced by pumping. Thereby the pumped transition may not be identically with the probed one. In fact the correlations depend on the respective term scheme and the accompanying energy relaxation path.

A first move towards a theoretical description of NLPF-spectra for multi-level systems was made by Andrews and Hochstrasser [Andrews and Hochstrasser, 1980], who investigate a three-level system with two well separated transitions¹. For more than two subbands, especially if they overlap, their method of deduction is not really suitable, though generalized it would be provide the same as what will be demonstrated in what follows. Completely ignored was the T_1 -peak, though this shows the interesting feature of being asymmetric for overlapping subbands.

¹Beside they also considered the tunneling terms (cf. section), what will not be done in the present work by reasons given below.

4.1. Discrete spectral structures

Instead of the T_1 -peak, they considered one of the tunneling terms (cf. section 2.3.2), which in the present work will be ignored with reasons as shown below. It is also astonishing that Saikan and Sei did not register such an asymmetry, though it is clearly to see by their data for rhodamine-B [Saikan and Sei, 1983a]. Neef and Mory discussed the T_1 -peak asymmetry but only in the context of the spectral diffusion, not as a general property of the NLPF-spectrum of multi-level systems [Neef and Mory, 1991]. First considerations towards the heterogeneous substructure (cf. section 4.1.1) have been made by E. Neef and B. Voigt [unpublished]. In order to accomplish the theory of NLPF spectra at low pump intensities, in the present chapter the author ventured to deduce and classify models for kinds of discrete substructures starting from the basic equations given in chapter 2 (cf. Eq. 2.39). The main part of results presented in this chapter have already been published by the author in ref. [Beenken and Ehlert, 1998]. The results will be of particular interest in the problem of photo-isomerization in pinacyanol and will be also applied in the subsequent chapters.

4.1 Discrete spectral structures

In a NLPF-spectrum of a multilevel system the probe- and pump-frequency dependences are correlated. For limitation to third order perturbation theory in the external fields, i.e. low pump and trivially probe intensities, one obtains the NLPF-line-shape function $s(\omega_t, \omega_p)$ by Eqs. 2.24, 2.33, and 2.36 (see chapter 2). Using the Secular- and Markov-approximation in the high temperature limit, where dephasing is most likely dominated by the pure-dephasing term, i.e. $\Gamma_{\mu\nu} \gg \frac{1}{2}(\gamma_{\mu\mu} + \gamma_{\nu\nu})$ and negligible Stokes shifts (cf. Eqs. 3.60 and 3.61), one can neglect all tunneling terms and the two-photon peaks, which amplitudes are of the order $\Gamma_{\mu\nu}^{-1}$ (cf. sections 2.3.2 and 2.3.3, respectively), while the heights of T_1 and T_2 -peaks are of the order $\gamma_{\mu\mu}^{-1}$. In this limit, which for measurements at room temperature may be almost sufficient, the NLPF-line-shape function for multi-level system in general reduces to

$$s(\omega_t, \omega_p) \approx \sum_{\mu, \nu, \kappa, \lambda} \zeta_{\mu\nu}(\omega_t) \left(\beta_{\nu\kappa}(0) g_{\mu\nu\kappa\lambda} \sigma_{\kappa\lambda}(\omega_p, \omega_p) + \beta_{\nu\kappa}(\omega_t - \omega_p) g'_{\mu\nu\kappa\lambda} \sigma_{\kappa\lambda}(\omega_t, \omega_p) \right) n_\lambda. \quad (4.1)$$

Here the indices $\mu, \nu, \kappa, \lambda$ represent the molecular states independently whether they belong to one and the same or different molecules, respectively. In Markov approximation the cross-section of pumping the transition $\lambda \rightarrow \kappa$ (cf. Eqs. 2.25, 2.29, and 3.14) is given by

$$\sigma_{\kappa\lambda}(\omega, \omega') = \frac{|\mu_{\kappa\lambda}|^2}{\hbar \varepsilon_0 n c} \left(\frac{\omega'}{\Gamma_{\kappa\lambda} + i(\omega - \omega_{\kappa\lambda})} + \frac{\omega'}{\Gamma_{\kappa\lambda} - i(\omega' - \omega_{\kappa\lambda})} \right) \quad \text{for } \omega_{\kappa\lambda} > 0. \quad (4.2)$$

and analogously the probing function for the transition $\mu \rightarrow \nu$ (cf. Eqs. 2.28, 2.30 and 3.16) by

$$\zeta_{\mu\nu}(\omega) = \frac{|\mu_{\mu\nu}|^2}{\hbar\varepsilon_0 n c} \frac{\omega}{\Gamma_{\mu\nu} + i(\omega - \omega_{\mu\nu})} \quad \text{for } \omega_{\mu\nu} > 0. \quad (4.3)$$

In order to reduce the number of terms in Eq. 4.1 the diagonal functions

$$\zeta_{\mu\mu}(\omega) = - \sum_{\nu \neq \mu} \zeta_{\mu\nu}(\omega) \quad \text{and} \quad \sigma_{\kappa\kappa}(\omega, \omega') = - \sum_{\lambda \neq \kappa} \sigma_{\kappa\lambda}(\omega, \omega') \quad (4.4)$$

have been introduced by definitions which are much like that of the diagonal elements of the energy relaxation matrix $\gamma_{\mu\mu}$ (cf. Eq. 3.42).

The matrix of correlation functions $\beta_{\nu\kappa}(\omega)$ apparent in Eq. 4.1 results from the central Fourier transformed Greens functions $\mathcal{G}(\omega)$ in Eqs. 2.24 and 2.33. In accordance with Eqs. 3.10 and 3.11 they result from the system of equations

$$\sum_{\nu} (\gamma_{\mu\nu} + i\omega\delta_{\mu\nu}) \beta_{\nu\kappa}(\omega) = -\delta_{\mu\kappa} \quad (4.5)$$

$$\sum_{\nu} \beta_{\nu\kappa}(\omega) = 0. \quad (4.6)$$

The latter equation represents the additional constriction which is necessary due to the singularity of the energy relaxation matrix γ (cf. Eqs. 2.15 and 3.42, respectively). For higher degrees of singularity additional constrictions of the same kind have to be applied. The occupations n_λ for the field-free case can be obtained from the system of equations

$$\sum_{\mu} \gamma_{\mu\lambda} n_\lambda = 0 \quad \text{and} \quad \sum_{\mu} n_\lambda = 1. \quad (4.7)$$

As mentioned in chapter 2 the first term in Eq. 4.1 represents a series of T_2 -peaks, each centered at different combinations of probe and pump frequencies $(\omega_t, \omega_p) = (\omega_{\mu\nu}, \omega_{\kappa\lambda})$. These T_2 -peaks are correlated to each other by the correlation matrix $\beta(0)$. For non-overlapping T_2 -peaks this means that only their relative heights, but not their line shapes are dependent on the discrete spectral structure. In the case of overlapping T_2 -peaks, however, the line shapes will be affected too for the complex superposition in $|s(\omega_t, \omega_p)|^2$, which represents the normalized NLPF-spectrum.

The second term in Eq. 4.1 represents the T_1 -peak, centered around $\omega_t = \omega_p$. Its line shape depends directly on the matrix of correlation functions $\beta(\omega_t - \omega_p)$, but weighted with the functions $\zeta_{\mu\nu}(\omega_t)\sigma_{\kappa\lambda}(\omega_t, \omega_p)$. Usually, the latter can be simplified to a function depending only on $\omega_t = \omega_p$ due to the narrowness of the T_1 -peak (see premise $\gamma_{\mu\mu} \ll \Gamma_{\mu\nu}$ stated above).

4.1. Discrete spectral structures

To accomplish Eq. 4.1 the geometry factors $g_{\mu\nu\kappa\lambda}$ and $g'_{\mu\nu\kappa\lambda}$, which take into account the orientational averaging over the molecular orientations (cf. section 2.4) shall be deduced. According to 2.24 for the first term in Eq. 4.1 the orientation dependence is given by

$$g_{\mu\nu\kappa\lambda} = \frac{1}{8\pi^2} \int_0^\pi d\theta \sin\theta \int_0^{2\pi} d\phi \int_0^{2\pi} d\psi (\mu_{\mu\nu}^0 \mathbf{E}_s^0) (\mu_{\mu\nu}^0 \mathbf{E}_p^0) |\mu_{\kappa\lambda}^0 \mathbf{E}_t^0|^2 \quad (4.8)$$

and analogously for the second term (cf. 2.33) as

$$g'_{\mu\nu\kappa\lambda} = \frac{1}{8\pi^2} \int_0^\pi d\theta \sin\theta \int_0^{2\pi} d\phi \int_0^{2\pi} d\psi (\mu_{\mu\nu}^0 \mathbf{E}_s^0) (\mu_{\mu\nu}^0 \mathbf{E}_p^0) (\mu_{\kappa\lambda}^0 \mathbf{E}_t^0) (\mu_{\kappa\lambda}^0 \mathbf{E}_p^0). \quad (4.9)$$

By spherical trigonometry one can express the scalar products between the unit vectors of the transition dipoles $\mu_{\mu\nu}^0$ respective $\mu_{\kappa\lambda}^0$ on the one side and those for the field polarizations \mathbf{E}_s^0 , \mathbf{E}_p^0 , \mathbf{E}_t^0 on the other side by the Euler angles θ , ϕ , and ψ for the orientation of the molecule (cf. Eq. 2.37) and the fixed angles $\Phi_{\mu\nu\kappa\lambda}$ between the transition dipoles $\mu_{\mu\nu}$ and $\mu_{\kappa\lambda}$. After integration over all three Euler angles the geometry factors yield as

$$g_{\mu\nu\kappa\lambda} = \frac{1 + 3 \cos(2\Phi_{\mu\nu\kappa\lambda})}{60} \quad (4.10)$$

$$g'_{\mu\nu\kappa\lambda} = \frac{7 + \cos(2\Phi_{\mu\nu\kappa\lambda})}{120}, \quad (4.11)$$

respectively. Note that $g_{\mu\nu\kappa\lambda}$ vanishes for the ‘magic’ angle $\Phi_{\mu\nu\kappa\lambda} \simeq 54,74^\circ$, while $g'_{\mu\nu\kappa\lambda} > 0$ is finite in any case². If the transition dipoles $\mu_{\kappa\lambda}$ and $\mu_{\mu\nu}$ are parallel one obtains $g_{\mu\nu\kappa\lambda} = g'_{\mu\nu\kappa\lambda} = \frac{1}{15}$ as shown for the two-level system in chapter 2. For sake of simplicity w.l.o.g this case will be used for the general discussion of the different examples of discrete and contentious spectral structures in what follows.

Though the line-shape function $s(\omega_t, \omega_p)$ as given in Eq. 4.1 provides already a sufficient general description for the NLPF-spectra of any kind of multi-level system in the mentioned limitations, it is useful to study specific cases. Particularly, one may be interested how the correlation matrix $\beta(\omega)$ reflects the term scheme and the associated energy relaxation path. Furthermore one may be interested in a simplification of the systems of equations Eq. 4.5 and Eq. 4.6 for principal term schemes being already known.

Hence, according to the possible relationships between pumped and probed transitions, the discrete substructure are to specify to the following cases (cf. Fig. 4.1): **(a)** the heterogeneous substructure (section 4.1.1), **(b)** the incoherent energy transfer (section 4.1.2), **(c)** the homogeneous substructure (section 4.1.3), **(d)** the excited state absorption (section 4.1.4), and last but

²The geometry factor $g_{\mu\nu\kappa\lambda}$ concerning the T₂-peaks is the same as used to calculate the induced anisotropy of absorption in time-resolved pump-probe experiments with non-overlapping pulses [Chachisvilis and Sundström, 1996]. For the geometry factor $g'_{\mu\nu\kappa\lambda}$ of the T₁-peak such an equivalent does not exist.

not least **(e)** the ground-state progression (section 4.3). Fig. 4.1 shows the corresponding term schemes in the case of two transitions (either probed or pumped). The ground-state progression (cf. Fig. 4.1 **e**) will not be discussed in the present work in two different aspects. First in the case where the middle level is not occupied (section 4.1.4), secondly for the Λ -system with two thermally occupied ground states (section 4.3)

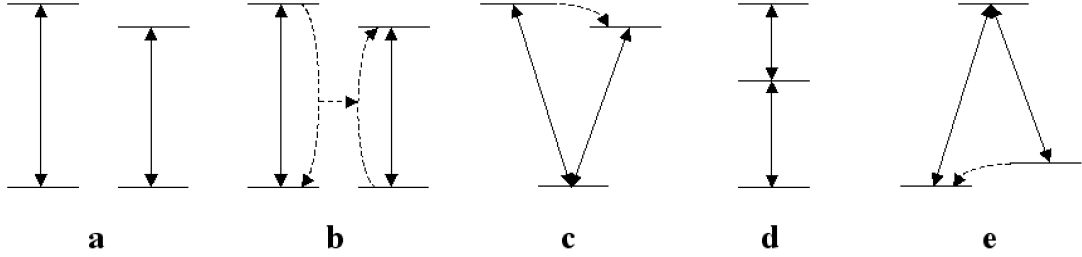


Figure 4.1: Term-schemes for different types of discrete spectral structures in the case of only two transitions: **a** heterogeneous substructure, **b** incoherent energy transfer, **c** homogeneous substructure (V-system), **d** excited state absorption (Ξ -system), and **e** ground-state progression (Λ -system). The solid double arrows represent the transitions (absorption and emission), each accompanied by an energy relaxation down hill (at least by fluorescence); the dashed lines the additional possible energy transfer and relaxation paths.

Finally for multi-level systems which do not contain a ground-state progression a more manageable definition of the correlation matrix function $\beta(\omega)$ can be found (section 4.2), combining the different types of substructures.

4.1.1 Heterogeneous substructure

The Heterogeneous substructure represents the case of independent transitions (cf. Fig. 4.1 panel **a**). These can be assigned to different species of non-interacting molecules mixed in the same sample. Each of them shall be describable by a two-level system with its own transition frequency $\omega_{\mu\mu'}$, dephasing rate $\Gamma_{\mu\mu'}$ and energy relaxation matrix γ_{μ} . In what follows the index μ represents the excited and the primed index μ' the ground state of the μ th two-level system. The energy relaxation matrix of this two-level system is given by

$$\gamma_{\mu} = \begin{pmatrix} -\gamma_{\mu'\mu} & \gamma_{\mu\mu'} \\ \gamma_{\mu'\mu} & -\gamma_{\mu\mu'} \end{pmatrix}. \quad (4.12)$$

The complete energy relaxation matrix γ yields as block-diagonal matrix containing one block γ_{μ} per spectral species. In order to obtain the correlation matrix $\beta(\omega)$ for the heterogeneous

4.1. Discrete spectral structures

substructure, this matrix has to be reduced to an equivalent matrix $\tilde{\gamma}$ which, however, is invertible (cf. Eqs. 4.5). For the singularity of the blocks γ_μ , each of them has to be substituted by the matrix element

$$\gamma_\mu = \gamma_{\mu'\mu} + \gamma_{\mu\mu'}, \quad (4.13)$$

Thus the reduced energy relaxation matrix $\tilde{\gamma}$, which takes only the excited states into account, is diagonal and can be easily inverted to the the correlation function matrix elements for the excited states given as

$$\beta_{\mu\nu}(\omega) = \frac{\delta_{\mu\nu}}{\gamma_\mu + i\omega}. \quad (4.14)$$

The missing matrix elements of the correlation matrix $\beta(\omega)$ are achievable from constrictions as given in Eq. 4.6 for each species separately, and yields as

$$\beta_{\mu'\nu'}(\omega) = -\beta_{\mu'\nu}(\omega) = -\beta_{\mu\nu'}(\omega) = \beta_{\mu\nu}(\omega). \quad (4.15)$$

By collecting identical terms one obtains the NLPF-line-shape function for the heterogeneous substructure as

$$s_{het}(\omega_t, \omega_p) = \frac{2}{15} \sum_{\mu} \zeta_{\mu\mu'}(\omega_t) \left(\frac{\sigma_{\mu\mu'}(\omega_p, \omega_p)}{\gamma_\mu} + \frac{\sigma_{\mu\mu'}(\omega_t, \omega_p)}{\gamma_\mu + i(\omega_t - \omega_p)} \right) n_{\mu'}. \quad (4.16)$$

The occupations $n_{\mu'}$ have to consider beside the thermal inversion of the two level system also the relative concentrations $n_{mol,\mu}$ of the molecular species μ , i.e. they are given by

$$n_{\mu'} = n_{mol,\mu} \tanh \left[\frac{\hbar\omega_{\mu\mu'}}{kT} \right]. \quad (4.17)$$

Note that Eq. 4.16 corresponds exactly to the sum over the NLPF-line-shape functions of different two-level system, weighted by the concentrations $n_{mol,\mu}$.

In Fig. 4.2 as an example the T_2 -peaks are shown for a NLPF-spectrum of a sample containing two different species of independent two-level systems (cf. Fig. 4.1 panel **a**).

Due to the diagonal structure of the correlation matrix $\beta(0)$ there occur only two T_2 -peaks at $(\omega_t, \omega_p) = (\omega_1, \omega_1)$ and (ω_2, ω_2) , respectively. This means that only if the same transition is pumped and probed one obtains a significant NLPF-signal, as to expect for independent transitions. The weak contributions at $(\omega_t, \omega_p) = (\omega_2, \omega_1)$ and (ω_1, ω_2) are not T_2 -peaks by their own but result from the finite overlap between the two diagonal T_2 -peaks.

Note that beside the determination of the transition frequencies $\omega_{\mu\mu'}$ and the dephasing rates $\Gamma_{\mu\mu'}$, the analysis of the T_2 -peaks provides only the quantity

$$x_{\mu\mu} = \frac{n_{\mu'} \mu_{\mu\mu'}^4}{\gamma_\mu} \quad (4.18)$$

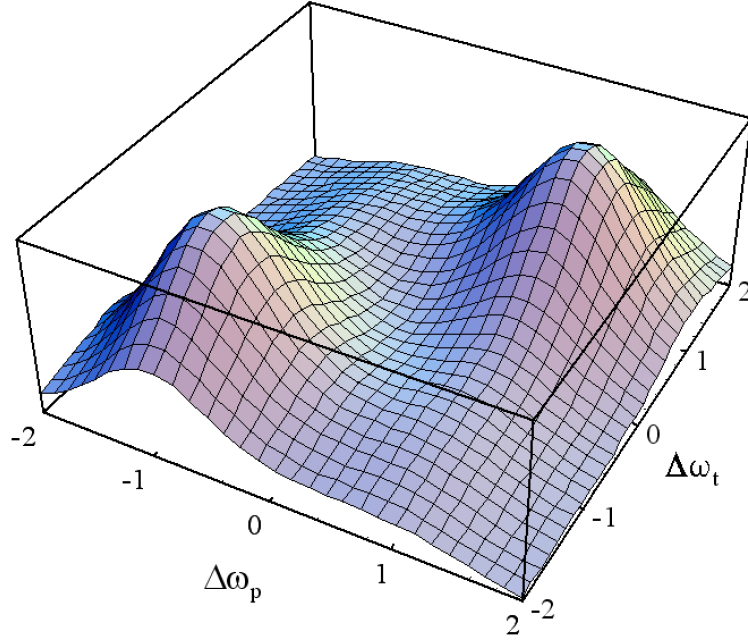


Figure 4.2: T_2 -peaks for a heterogeneous substructure of two independent two-level systems with $n_{1'} |\mu_{11'}|^2 / \gamma_1 = n_{2'} |\mu_{22'}|^2 / \gamma_2$ and $\Gamma_{11'} = \Gamma_{22'} = (\omega_2 - \omega_1) / 4$. Axes labels for $\Delta\omega_{p,t} = (2\omega_{p,t} - \omega_1 - \omega_2) / (\omega_2 - \omega_1)$.

, which is related to the height of the T_2 -peaks. Hence, in order to eliminate the factor $n_{\mu'} \mu_{\mu\mu'}^2$ for determination of the energy relaxation rates γ_μ , one needs e.g. the absorption spectrum, which according to Eq. 2.40 is given by

$$\sigma_{abs}(\omega) = \frac{1}{3} \sum_{\mu} \sigma_{\mu\mu'}(\omega, \omega) n_{\mu'}. \quad (4.19)$$

Another method is to determine $\sigma_{\mu\mu'}(\omega, \omega)$ independently from the concentration dependent $n_{\mu'}$ by strong-field NLPF as will be shown in chapter 6.

The appropriate method in NLPF for determination of the energy relaxation rates γ_μ is the T_1 -peak analysis. For $\gamma_\mu \ll \Gamma_{\mu\mu'}$, as supposed above, the T_1 -peak will be located in the vicinity of $\omega_t = \omega_p$. Hence, the line-shape function in Eq. 4.16 needed for the T_1 -peak analysis can be approximated by

$$s_{het}(\omega_t, \omega_p) \approx \sum_{\mu} c_{\mu\mu'}(\omega_t) \frac{2\gamma_{\mu\mu'} + i(\omega_t - \omega_p)}{\gamma_{\mu\mu'} + i(\omega_t - \omega_p)} \quad (4.20)$$

with a prefactors

$$c_{\mu\mu'}(\omega_{t,p}) = \frac{2}{15} \frac{\zeta_{\mu\mu'}(\omega_{t,p}) \sigma_{\mu\mu'}(\omega_{t,p}, \omega_{t,p})}{\gamma_\mu} n_{\mu'}, \quad (4.21)$$

4.1. Discrete spectral structures

dependent only on the probe- or pump-frequency for $\omega_t \approx \omega_p$, The prefactors can be easily determined from the T_2 -peak analysis. For energy relaxation rates γ_μ , which differs from each other, the maximum of the T_1 -peak is not exactly located at $\omega_p = \omega_t$ and the line-shape becomes asymmetric. In Fig. 4.3 both are shown, the symmetric T_1 -peak obtained for $\gamma_1 = \gamma_2$ and the extremely asymmetric T_1 -peak for $\gamma_1 = 100\gamma_2$. Note that both belong to the same pattern of T_2 -peaks as shown in Fig. 4.2.

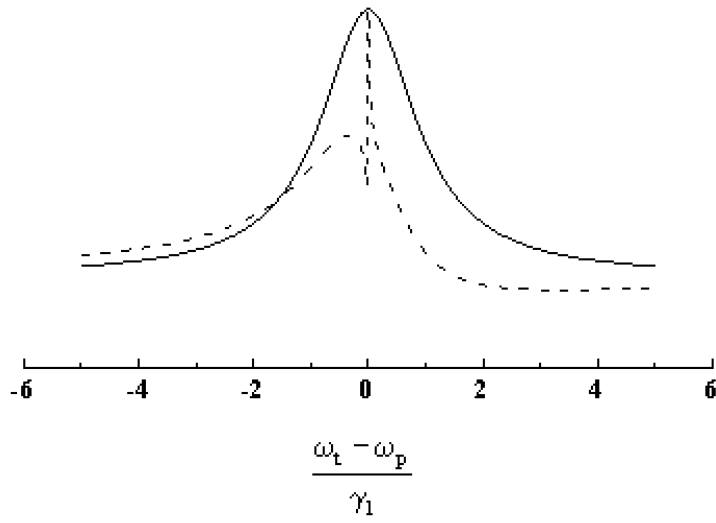


Figure 4.3: T_1 -peak at $\omega_t = (\omega_1 + \omega_2) / 2$ for two independent two level systems (heterogeneous substructure) with $\Gamma_{11'} = \Gamma_{22'}$ and $n_1 |\mu_{11'}|^2 / \gamma_1 = n_2 |\mu_{22'}|^2 / \gamma_2$. The solid line represents the symmetric case $\gamma_2 = \gamma_1$, the dashed the extrem asymmetric case $\gamma_2 = 0.01 \gamma_1$. For moderate case see Fig. 4.5.

In conclusion this means that highly resolved NLPF-spectra allow one to determine the relaxation rates γ_μ of different molecular species in the same sample by means of a combined T_2 - and T_1 -peak analysis. Even in cases where for limited frequency resolution the line shape of the T_1 -peak can not be resolved in detail, it is still possible to infer a spectral substructure by the overall asymmetry between the left and right wings of the T_1 -peak³. This has been achieved for pinacyanol, where an elsewhere hidden spectral substructure, apparent neither in

³The asymmetry of the T_1 -peak can be easily studied by using the asymmetry function

$$D(\omega_{pt}) = |s_{EET}(\omega_t, \omega_t + \omega_{pt})|^2 - |s_{EET}(\omega_t, \omega_t - \omega_{pt})|^2 \quad (4.22)$$

absorption nor in the pattern of the T_2 -peaks, has been revealed mainly by the asymmetry of the T_1 -peak [Voigt et al., 1997] (for details see summary).

4.1.2 Incoherent excitation energy transfer

In a supra-molecular aggregates between molecules, elsewhere describable as independent two-level systems, incoherent excitation energy transfer (EET) is often possible by e.g. dipole-dipole interaction [Förster, 1948]. In order to describe the hopping-like transfer of the excitation from one molecule to the other, one needs three relaxation matrix elements (cf. the three arrows in Fig. 4.1 panel b): First $\gamma_{\mu\nu}$ which describes jump of the excitation from the excited state of the donor $|\nu\rangle$ to the that of the acceptor $|\mu\rangle$, secondly $\gamma_{\mu'\nu} = -\gamma_{\mu\nu}$ which means the simultaneous depletion of the ground state $|\mu'\rangle$ of the acceptor, and finally $\gamma_{\nu'\nu} = \gamma_{\mu\nu} + \gamma_\mu$ for the transition of the donor from the excited state $|\nu\rangle$ to the ground state $|\nu'\rangle$, which may be caused either by energy transfer ($\gamma_{\mu\nu}$) or normal energy relaxation (γ_μ). Due to the coupling between the different two-level systems the combined energy relaxation and transfer matrix γ does not represent a block matrix any longer. Nevertheless it is still singular to a high degree. Again, it is necessary to change to a representation of the energy relaxation and transfer processes by a dimension-reduced energy relaxation matrix $\tilde{\gamma}$, which e.g. takes only the excited states into account. For the incoherent excitation energy transfer (but not for electron transfer) this is possible, since for each two-level systems, even if they are exchanging excitation energy, the depletion of the ground state follows exactly the occupation of the corresponding excited state for

$$\rho_{\mu\mu}^{(n_p, n_t)} + \rho_{\mu'\mu'}^{(n_p, n_t)} = \delta_{n_p 0} \delta_{n_t 0}. \quad (4.23)$$

The off-diagonal elements of the reduced energy relaxation matrix $\tilde{\gamma}_{\mu\nu}$ are just the energy transfer rates $\gamma_{\mu\nu} = -\gamma_{\mu'\nu}$, and the diagonal matrix elements are given by

$$\tilde{\gamma}_{\mu\mu} = -\gamma_\mu - \sum_{\nu \neq \mu} \tilde{\gamma}_{\nu\mu}, \quad (4.24)$$

which results in

$$D(\omega_{pt}) = 2 \sum_{\mu, \kappa \neq \mu} \Im \{ c_\mu^*(\omega_t) c_\kappa(\omega_t) \} \frac{(\gamma_\mu - \gamma_\kappa) (2\gamma_\mu \gamma_\kappa - \omega_{pt}^2) \omega_{pt}}{\gamma_\kappa \gamma_\mu (\gamma_\mu^2 + \omega_{pt}^2) (\gamma_\kappa^2 + \omega_{pt}^2)}$$

The asymptotic of $D(\omega_{pt})$ for $|\omega_{pt}| \gg \gamma_\mu, \gamma_\nu$ is given by

$$D(\omega_{pt}) \rightarrow 2 \sum_{\mu, \kappa \neq \mu} \frac{\Im \{ c_\mu^*(\omega_t) c_\kappa(\omega_t) \}}{\omega_{pt}} \left(\frac{1}{\gamma_\kappa} - \frac{1}{\gamma_\mu} \right)$$

which allows one the determination of the energy relaxation rates γ_μ but one.

4.1. Discrete spectral structures

which contains beside the effective energy relaxation rates γ_μ of the isolated two-level system (cf. Eq. 4.13) additionally the sum over the rates of all energy transfers starting from the donor μ . For the excited states the correlation function matrix elements $\beta_{\nu\kappa}(\omega)$ result from the inversion of the matrix $(\tilde{\gamma} - i\omega\mathbf{1})$ according to the system of equations given by

$$\sum_{\nu} (i\omega\delta_{\mu\nu} + \tilde{\gamma}_{\mu\nu}) \beta_{\nu\kappa}(\omega) = \delta_{\mu\kappa}. \quad (4.25)$$

which is equivalent to Eq.4.5. From Eq. 4.23 the remaining matrix elements yields as $\beta_{\mu'\nu'}(\omega) = -\beta_{\mu'\nu}(\omega) = -\beta_{\mu\nu'}(\omega) = \beta_{\mu\nu}(\omega)$. Thus the line-shape function for two-level systems coupled by incoherent energy transfer yields as

$$s_{EET}(\omega_t, \omega_p) = \frac{2}{15} \sum_{\mu, \nu} \zeta_{\mu\mu'}(\omega_t) \{ \beta_{\mu\nu}(0) \sigma_{\nu\nu'}(\omega_p, \omega_p) + \beta_{\mu\nu}(\omega_t - \omega_p) \sigma_{\nu\nu'}(\omega_t, \omega_p) \} n_{\nu'}. \quad (4.26)$$

For sake of simplicity, all transition dipole moments have been assumed to be parallel. In principle the factors $n_{\nu'}$ are given as in Eq. 4.17, however, here the concentration $n_{mol, \mu}$ of donors and acceptors are defined not by the spectral molecular properties but also by the site occupied in the aggregate for the extremely distance-dependent energy transfer.

The pattern of T₂-peaks results the first term in Eq.4.26. Compared to the heterogeneous substructure here ‘off-diagonal’ T₂-peaks occur due to the energy transfer from the pumped to the probed transition. This specific behavior shall be demonstrated on a system consisting of two two-level systems coupled by an irreversible incoherent energy transfer⁴ with rate $\gamma_{12} > 0$. Here, the index 2 assigns the donor, the index 1 the acceptor. According to Eq. 4.25 the correlation matrix elements yield as

$$\begin{aligned} \beta_{11}(\omega) &= \frac{1}{\gamma_1 + i\omega} \\ \beta_{12}(\omega) &= \frac{1}{\gamma_1 + i\omega} \frac{\gamma_{12}}{\gamma_2 + \gamma_{12} + i\omega} \\ \beta_{21}(\omega) &= 0 \\ \beta_{22}(\omega) &= \frac{1}{\gamma_2 + \gamma_{12} + i\omega}. \end{aligned} \quad (4.27)$$

Note that the elements $\beta_{11}(\omega)$ and $\beta_{12}(\omega)$ rule the line-shape function for probing the acceptor, $\beta_{22}(\omega_{pt})$ rules it for probing the donor. Inserting these elements in Eq. 4.26, the part of the

⁴Here the index 1 assign the acceptor and the index 2 the donor of the excitation energy.

NLPF-line-shape function which describes the T_2 -peaks is obtained as

$$\begin{aligned}
 s_{EET}(\omega_t, \omega_p) &\approx \frac{2}{15} \zeta_{11'}(\omega_t) \frac{1}{\gamma_1} \sigma_{11'}(\omega_p) n_{1'} \\
 &+ \frac{2}{15} \zeta_{22'}(\omega_t) \frac{1}{\gamma_2 + \gamma_{12}} \sigma_{22'}(\omega_p, \omega_p) n_{2'} \quad (4.28)
 \end{aligned}$$

$$+ \frac{2}{15} \zeta_{11'}(\omega_t) \frac{\gamma_{12}}{\gamma_1 (\gamma_2 + \gamma_{12})} \sigma_{22'}(\omega_p, \omega_p) n_{2'}. \quad (4.29)$$

An example for T_2 -peaks which result from a incoherent excitation energy transfer is shown in Fig. 4.4.

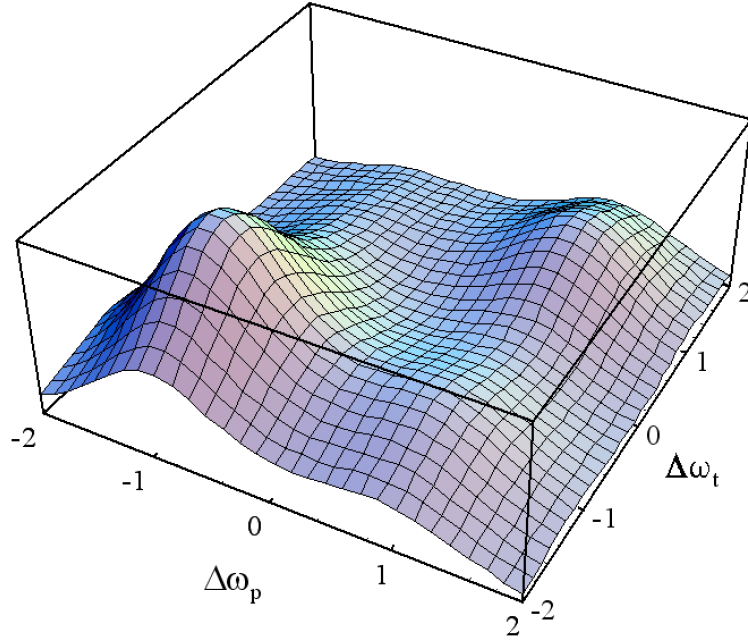


Figure 4.4: T_2 -peaks for donor acceptor pair with an excitation energy transfer with rate γ_{12} half the amount of the energy relaxation rates $\gamma_1 = \gamma_2$. The dephasing rates are given as $\Gamma_{11'} = \Gamma_{22'} = (\omega_2 - \omega_1) / 2$ and $n_{1'} |\mu_{11'}|^2 = n_{2'} |\mu_{22'}|^2$. Axis labels as in Fig. 4.2.

Compared to Fig. 4.2 two differences can be seen at once: First there occur an additional T_2 -peak at $(\omega_t, \omega_p) = (\omega_1, \omega_2)$, which represents the probing of the acceptor (1) when pumping the donor (2). This occurs because of the excitation energy transfer from the latter to the former. The second difference is an reduction of the height of the T_2 -peak at $(\omega_t, \omega_p) = (\omega_2, \omega_2)$, which results from the fact that the donor can lose excitation by two channels: the normal energy relaxation to the ground-state and the excitation energy transfer to the acceptor, as well (cf. the denominator $\gamma_2 + \gamma_{12}$ for $\beta_{22}(0)$ in Eq. 4.27). The height of the T_2 - peak representing the energy

4.1. Discrete spectral structures

transfer depends on two limiting factors (cf. $\beta_{12}(0)$ in Eq. 4.27). First it is proportional to the branching ratio between energy transfer and energy relaxation as given by $b_{12} = \gamma_{12}/(\gamma_2 + \gamma_{12})$. For fast normal energy relaxation of the donor ($\gamma_2 \gg \gamma_{12}$) there will not be time for sufficient transfer of occupation to the probed acceptor, and the off-diagonal T₂-peak will not appear. The life-time of the acceptor given by γ_1^{-1} limits the off-diagonal T₂-peak in the same way as it limits the diagonal T₂-peak at $(\omega_t, \omega_p) = (\omega_1, \omega_1)$.

In the case of incoherent energy transfer the T₂-peak analysis provides beside $\omega_{\mu\mu'}$ and $\Gamma_{\mu\mu'}$ the quantities

$$x_{\mu\nu} = n_{\nu'} |\mu_{\nu\nu'}|^2 |\mu_{\mu\mu'}|^2 \beta_{\mu\nu}(0). \quad (4.30)$$

Though the pattern of this x -matrix give already some hints to the structure of the excitation energy transfer path, for determination of the energy transfer and relaxation matrix $\tilde{\gamma}$ again the absorption spectrum is needed. However, the absorption spectrum can not distinguish between sites in a supramolecular aggregate which are only different in respect of the excitation energy transfer. In this case at least one matrix element $\tilde{\gamma}_{\mu\mu}$ has to be determined independently, for example by fluorescence decay measurement.

Alternatively, the line-shape analysis of the T₁-peak may solve this problem. To describe the T₁-peak for a system of several two-level systems connected by EET with $\tilde{\gamma}_{\mu\mu} \ll \Gamma_{\mu}$ the NLPF-line-shape function given by 4.26 can be approximated to

$$s_{EET}(\omega_t, \omega_p) \approx \sum_{\mu, \nu} c_{\mu\nu}(\omega_{p,t}) (\beta_{\mu\nu}(0) + \beta_{\mu\nu}(\omega_t - \omega_p)) \quad (4.31)$$

using the pump respectively probe frequency dependent prefactors

$$c_{\mu\nu}(\omega_{p,t}) = \frac{2}{15} \zeta_{\mu\mu'}(\omega_{p,t}) \sigma_{\nu\nu'}(\omega_{p,t}, \omega_{p,t}) n_{\nu'}. \quad (4.32)$$

In Fig. 4.5 the T₁-peak at $\omega_t = \omega_p = (\omega_1 + \omega_2)/2$ of the model donor–acceptor pair already used for displaying the T₂-peaks in Fig. 4.4 is shown .

One can see, that the T₁-peak of the donor–acceptor pair coupled by incoherent energy transfer (solid line) is only a little bit more asymmetric than that of the corresponding heterogeneous substructure (dotted line) for the same difference in the total life-times. Nevertheless, both kinds of peaks are distinguishable since their the maxima shift approximately about the same value, but the wings differ from each other significantly. For the special but reasonable case $|\omega_t - \omega_p| \sim \gamma_{12} \gg \gamma_2, \gamma_1$, one obtains the line-shape function of the single donor–acceptor pair approximately as

$$s_{EET}(\omega_t, \omega_p) \approx \frac{1}{\gamma_1} \left(c_{11}(\omega_t) + c_{12}(\omega_t) \left(1 + \frac{2\gamma_{12}}{i(\omega_t - \omega_p)(\gamma_{12} + i\omega_{pt})} \right) \right). \quad (4.33)$$

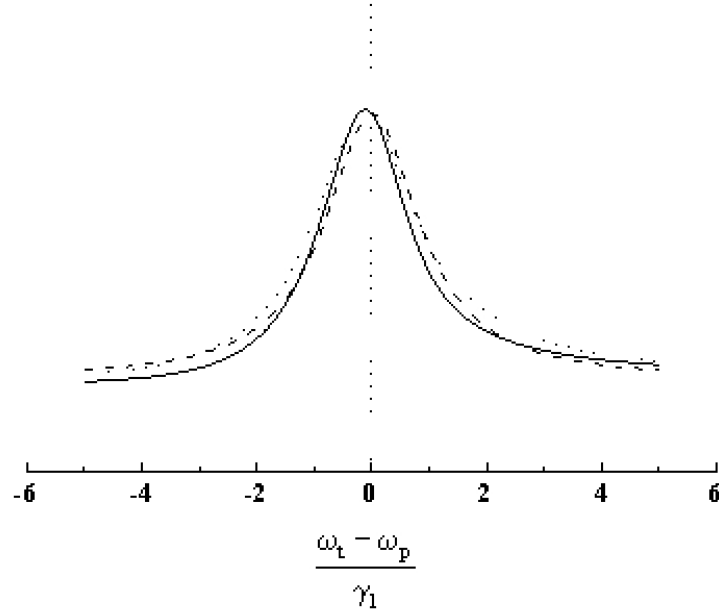


Figure 4.5: T_1 -peak for donor acceptor pair (solid line) with excitation energy transfer rate $\gamma_{12} = \gamma_2/2 = \gamma_1/2$ as in Fig. 4.4 at $\omega_t = (\omega_1 + \omega_2)/2$. For comparison the heterogeneous structures for $\gamma_2 = \gamma_1$ (dashed line) and $\gamma_2 = 1.5 \gamma_1$ (dotted line) are also shown.

Therefore it might be possible to reveal an incoherent excitation energy transfer even for overlapping transitions of donor and acceptor, which can not be revealed by analysis of the T_2 -peaks. However, the resulting effect on the T_1 -peak is very small and needs a extreme good signal to noise ratio. Furthermore in this case the approximation used for Eq. 4.31 may not hold. In this situation one should better use the original line-shape function $s_{EET}(\omega_t, \omega_p)$ as given by Eq. 4.26.

4.1.3 Homogeneous substructure

Homogenous substructure results from multilevel-systems with several excited states associated to one common ground state, here assigned with index 0 (cf. Fig. 4.1 panel c). For sake of simplicity it will assumed, that all transition dipoles $\mu_{\mu 0}$ are parallel. Even though the energy relaxation matrix γ is singular in a much lower degree, a reduction as described above is necessary. By eliminating the common ground state $|0\rangle$ the reduced energy relaxation matrix

4.1. Discrete spectral structures

yields as

$$\tilde{\gamma}_{\mu\nu} = \gamma_{\mu\nu} - \gamma_{\mu 0} \quad (4.34)$$

$$\tilde{\gamma}_{\mu\mu} = -\gamma_{\mu} - \sum_{\nu \neq \mu, 0} \gamma_{\nu\mu}. \quad (4.35)$$

where the effective energy relaxation to the ground state is given by $\gamma_{\mu} = \gamma_{0\mu}$ for neglecting back transfer from the ground state to the excited state $\gamma_{\mu 0}$, what is justified by $\hbar\omega_{\mu 0} \gg kT$. The correlation function matrix $\beta(\omega)$ is identical with that for the incoherent energy transfer given by Eq. 4.25, except of the matrix elements $\beta_{0\nu}(\omega)$ which yields as

$$\beta_{0\nu}(\omega) = - \sum_{\mu \neq 0} \beta_{\mu\nu}(\omega) \quad (4.36)$$

for Eq. 4.6. Thus one obtains the NLPF-line-shape function for the homogeneous substructure from Eq. 4.1 as

$$\begin{aligned} s_{hom}(\omega_t, \omega_p) &= \frac{1}{15} \sum_{\mu \neq 0} \left(\zeta_{\mu 0}(\omega_t) + \sum_{\kappa \neq 0} \zeta_{\kappa 0}(\omega_t) \right) \\ &\times \sum_{\nu \neq 0} (\beta_{\mu\nu}(0)\sigma_{\nu 0}(\omega_p) + \beta_{\mu\nu}(\omega_t - \omega_p)\sigma_{\nu 0}(\omega_t, \omega_p)) n_0. \end{aligned} \quad (4.37)$$

The term $\sum_{\kappa \neq 0} \zeta_{\kappa 0}(\omega_t)\beta_{\mu\nu}(0)$ describes the simultaneous bleaching of all transitions, when only one of the excited sates is occupied. This is the most significant feature of the homogeneous substructure, which allows one to distinguish homogeneous from heterogeneous substructure as well as from incoherent energy transfer, except in the case $\gamma_{\mu\nu} \sim \gamma_{\nu\mu}$. The other terms $\zeta_{0\mu}(\omega_t)\beta_{\mu\nu}(\dots)$, represent the stimulated emissions from the actually excited state $|\mu\rangle$ to the ground state $|0\rangle$.

In order to demonstrate the specific pattern of T_2 -peaks of a homogeneous substructure, a three-level system with energy relaxations from the upper to the lower excited state (γ_{12}) and from both to the ground state (γ_1, γ_2) will be discussed in what follows (cf. Fig. 4.1 panel c). The back-transfer is excluded ($\gamma_{21} = 0$). Note that all correlation function matrix elements $\beta_{\mu\nu}(\omega)$ needed in Eq. 4.1 are already given by Eq. 4.27. Thus the T_2 -peaks results from that part of the NLPF-line-shape function which is given by

$$\begin{aligned} s_{hom}(\omega_t, \omega_p) &\approx \frac{1}{15} \frac{2\zeta_{10}(\omega_t) + \zeta_{20}(\omega_t)}{\gamma_1} \sigma_{10}(\omega_p, \omega_p) \\ &+ \frac{1}{15} \frac{\zeta_{10}(\omega_t) + 2\zeta_{20}(\omega_t)}{\gamma_2 + \gamma_{12}} \sigma_{20}(\omega_p, \omega_p) \\ &+ \frac{1}{15} \frac{2\zeta_{10}(\omega_t) + \zeta_{20}(\omega_t)}{\gamma_2 + \gamma_{12}} \frac{\gamma_{12}}{\gamma_1} \sigma_{20}(\omega_p, \omega_p). \end{aligned} \quad (4.38)$$

The first term dominates for pumping the transition $|0\rangle \rightarrow |1\rangle$, the second the transition $|0\rangle \rightarrow |2\rangle$. According to the appearance of $\zeta_{10}(\omega_t) + \zeta_{20}(\omega_t)$ in all three terms, even for states not exchanging occupation (i.e. the third term disappears for $\gamma_{12} = 0$), four well pronounced T_2 -peaks will appear in the NLPF-spectrum regularly: Two for pumping and probing the same transition, and two for pumping another transition than the probed one. The latter two T_2 -peaks result from the bleaching of the common ground state as mentioned above. All four T_2 -peaks can be clearly seen in Fig. 4.6.

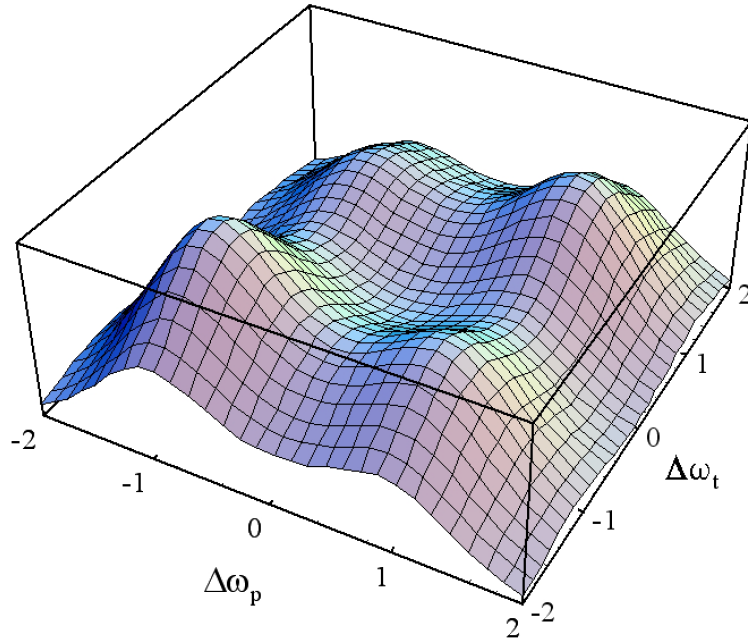


Figure 4.6: T_2 -peaks for a homogeneous substructure with $\gamma_{12} = \gamma_2/2 = \gamma_1/2$. The dephasing rates are given as $\Gamma_{10} = \Gamma_{20} = (\omega_2 - \omega_1)/2$ and $|\mu_{10}|^2 = |\mu_{20}|^2$. Axis labels as in Fig. 4.2.

The occurrence of four T_2 -peaks allows one to distinguish the homogeneous three-level system from two independent two-level systems very well. Also the case of irreversible energy transfer can be excluded easily, where only three T_2 -peaks occur (cf. Fig. 4.4).

If generally it can be assumed that $\forall \gamma_{\mu\nu} > 0 \Rightarrow \gamma_{\nu\mu} \approx 0$, the x -matrix (cf. Eq. 4.30) as determined by the T_2 -peak analysis has a special structure, dependent on the kind of substructure: For heterogeneous substructure it is diagonal, for inhomogeneous energy transfer trigonal, and for homogeneous substructure quadratic. For $\gamma_{\mu\nu} \approx \gamma_{\nu\mu}$, however, i.e. comparable back- and forward energy transfer and relaxation, respectively, this possibility to determine the principal term scheme is not given. By lowering the temperature, this may be to overcome.

The T_1 -peak of the homogeneous substructure is given by the same type of line-shape

4.1. Discrete spectral structures

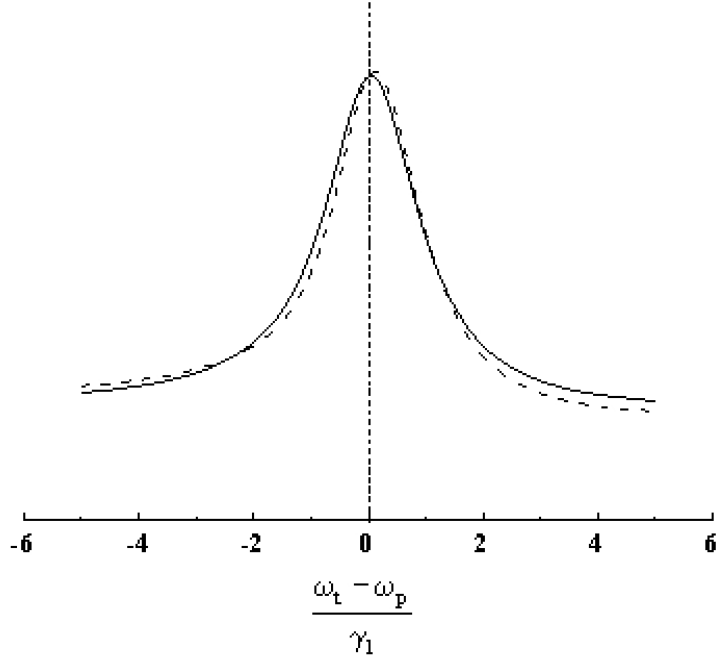


Figure 4.7: T_1 -peak for homogeneous substructure (solid line) with parameters as in Fig. 4.6 at $\omega_t = (\omega_1 + \omega_2)/2$. For comparison the T_1 -peak for the corresponding incoherent energy transfer (dashed line) with parameters as in Fig. 4.4 is also shown.

function as given in Eq. 4.31 since the functions $\beta_{\mu\nu}(\omega_t - \omega_p)$ for $\mu, \nu \neq 0$ are identical for both, homogeneous substructure and incoherent energy transfer. The homogeneous substructure differs only for the prefactors

$$\begin{aligned}
 c_{11}(\omega_{t,p}) &= \frac{1}{15} (2\zeta_{10}(\omega_{t,p}) + \zeta_{20}(\omega_{t,p})) \sigma_{10}(\omega_{t,p}, \omega_{t,p}) \\
 c_{12}(\omega_{t,p}) &= \frac{1}{15} (2\zeta_{10}(\omega_{t,p}) + \zeta_{20}(\omega_{t,p})) \sigma_{20}(\omega_{t,p}, \omega_{t,p}) \\
 c_{22}(\omega_{t,p}) &= \frac{1}{15} (\zeta_{10}(\omega_{t,p}) + 2\zeta_{20}(\omega_{t,p})) \sigma_{20}(\omega_{t,p}, \omega_{t,p}).
 \end{aligned} \tag{4.39}$$

as given by the underlying T_2 -peaks. Therefore the analysis of the T_1 -peak scarcely enables one to reveal a homogeneous substructure unequivocally, though for the same energy relaxation and transfer matrix γ the T_1 -peak for homogeneous substructure the T_1 -peak is usually less asymmetric than for incoherent energy transfer as shown in Fig. 4.7 displaying comparable T_1 -peak for both cases.

4.1.4 Excited-state absorption and stimulated emission

For the homogeneous substructure discussed above only the bleaching of and the stimulated emission to the ground state has been considered. However, there may exist also excited-state absorption and stimulated emission to other states than the ground state. For low pump intensity, these can not be pumped but only probed for the pumped excited states. This shall be demonstrated for the three-level system as shown in Fig. 4.1 panel **d**, where the frequencies of ground and excited state transition are similar, i.e. $\omega_{21} \sim \omega_{10}, \omega_{21}$. For this system the T_2 -peaks are given by the following terms of the NLPF-line-shape function:

$$\begin{aligned}
 s_{exc}(\omega_t, \omega_p) &\approx \frac{1}{15} \frac{2\zeta_{10}(\omega_t) + \zeta_{20}(\omega_t) - \zeta_{21}(\omega_t)}{\gamma_1} \sigma_{10}(\omega_p, \omega_p) \\
 &+ \frac{1}{15} \frac{\zeta_{10}(\omega_t) + 2\zeta_{20}(\omega_t) + \zeta_{12}(\omega_t)}{\gamma_2 + \gamma_{12}} \sigma_{20}(\omega_p, \omega_p) \\
 &+ \frac{1}{15} \frac{2\zeta_{10}(\omega_t) + \zeta_{20}(\omega_t) - \zeta_{21}(\omega_t)}{\gamma_2 + \gamma_{12}} \frac{\gamma_{12}}{\gamma_1} \sigma_{20}(\omega_p, \omega_p) + \dots
 \end{aligned} \quad (4.40)$$

If the molecule possess inversion symmetry, due to the parity selection rules for dipole transitions not all three terms can occur together. In this case $\mu_{21} \neq \mathbf{0}$ either μ_{10} or μ_{20} have to vanish.⁵ Both cases are realized in nature.

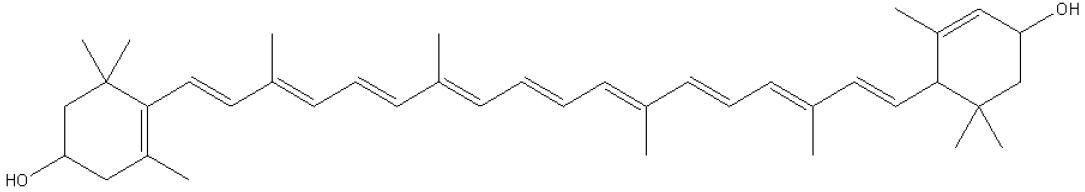


Figure 4.8: Chemical structure of the xanthophyll lutein. Though it is not completely inversion symmetric, the S_1 state is almost forbidden [Polivka et al., 1999].

For example in the most carotenoids and xanthophylls (e.g. lutein in Fig. 4.8) the lowest singlet excited state S_1 is forbidden, i.e. $\mu_{10} = \mathbf{0}$, while a higher excited state, named S_2 can be optically pumped from the ground state for $\mu_{20} \neq \mathbf{0}$. Between both excited states S_1 and S_2 transitions are allowed, i.e. $\mu_{21} \neq \mathbf{0}$. This means that pumping the higher excited state, the lower excited state may be detectable by probing the excited state absorption $S_1 \rightarrow S_2$ due to the fast energy relaxation from S_2 to S_1 ($\gamma_{12} \gg \gamma_2, \gamma_1$) [Polivka et al., 1999]. In NLPF this case is represented by the last of the three terms in Eq. 4.40, which yields approximately

$$s_{exc}(\omega_t, \omega_p) \approx \frac{1}{15} \frac{\zeta_{20}(\omega_t) - \zeta_{21}(\omega_t)}{\gamma_1} \sigma_{20}(\omega_p, \omega_p) \quad (4.41)$$

⁵Note that the case $\mu_{21} = \mathbf{0}$ results in the homogeneous substructure, which has been already discussed.

4.1. Discrete spectral structures

To the author's regret, this interesting experiment has not been achieved, yet. For $\omega_{21} \ll \omega_{20}$ in the case of lutein an additional T_2 -peaks at probe frequencies around 6000cm^{-1} are expected for pumping the S_2 -state around 19000cm^{-1} (cf. ref. [Polivka et al., 1999])

Note that due to the fact that the NLPF-spectrum is represented by $|s_{sem}(\omega_t, \omega_p)|^2$ in Eq. 4.41 the different signs of $\zeta_{20}(\omega_t)$, which represents probing of absorption from respectively emission to the ground -state, and $\zeta_{21}(\omega_t)$, would be only recognizable for overlapping T_2 -peaks.

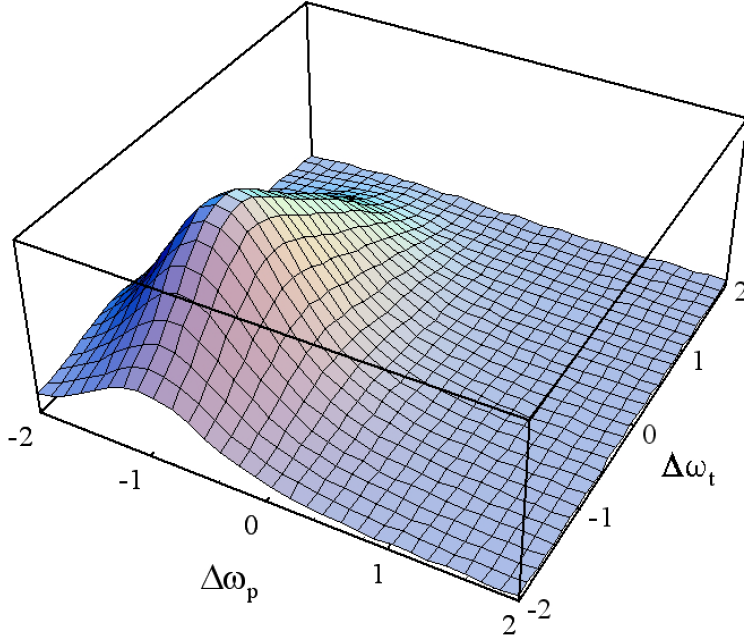


Figure 4.9: T_2 -peaks for a three level system in the case $\omega_{21} \sim \omega_{10}$ with $\mu_{21} = \mu_{10}$ pumped at $\omega_p = \omega_{10}$. Dephasing rates $\Gamma_{10} = \Gamma_{21} = \omega_{20}/4$. Axis labels $\Delta\omega_{p,t} = (2\omega_{p,t} - \omega_{10} - \omega_{21})/\omega_{20}$.

In Fig. 4.9 the T_2 -peaks are shown in the case where the lower excited state is pumped, i.e. and excited- and ground-state absorption are nearly degenerate, i.e. $\omega_{10} \sim \omega_{21}$. By section along the $\Delta\omega_p$ -axis one can see that the pump-frequency dependence is like that of the two-level system an quadratic Gaussian centered at ω_{10} . The probe-frequency dependence can be split off as factor $|2\zeta_{10}(\omega_t) - \zeta_{21}(\omega_t)|^2$. Due to the complex superposition of the functions $2\zeta_{10}(\omega_t)$ and $\zeta_{21}(\omega_t)$, the NLPF-spectrum shows instead of two clearly separate T_2 -peaks only a single but extremely asymmetric one. In Fig. 4.10 different probe-frequency dependences are shown for different ratios

$$r = -\frac{\mu_{12}^2}{2\mu_{10}^2}. \quad (4.42)$$

The effect of the stimulated emission $|2\rangle \rightarrow |1\rangle$, which appears for inhibited energy relaxation

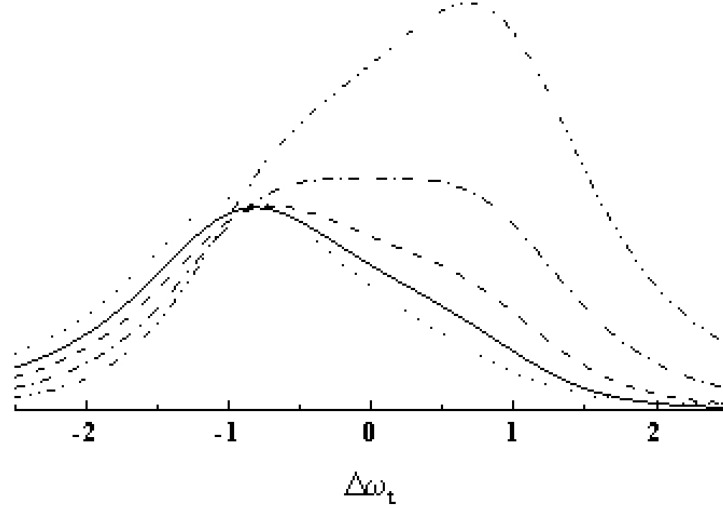


Figure 4.10: Probe-frequency dependence of the T_2 -peaks of three-level systems pumped at $\omega_p = \omega_{10}$ for ratios (see text) $r = -1$ (dot), -4 (solid line), -8 (dash), -16 (dash-dot), and -32 (dash-dot-dot) for the value of μ_{10} being fixed. Other parameters and axis as in Fig. 4.9.

between the state $|2\rangle$ and $|1\rangle$, i.e. for $\gamma_{12} \ll \gamma_{02}$ when pumping the transition $|0\rangle \rightarrow |2\rangle$, is determined by the second term in Eq. 4.40. Only in the case of ground-state progression, which will be discussed below in section 4.3, the corresponding probing function $\zeta_{12}(\omega_t)$ will interfere with $\zeta_{20}(\omega_t)$. The interference with $\zeta_{10}(\omega_t)$ is inhibited by the assumed slow energy relaxation γ_{12} . The resulting probe-frequency dependence are two separate T_2 -peaks at $\omega_t = \omega_{20}$ and $\omega_t = \omega_{21}$.

If the precondition $\gamma_{12} \ll \gamma_2$ has been dropped, for pumping the transition $|0\rangle \rightarrow |2\rangle$ one can write the probe-frequency dependence as

$$\left| \zeta_{10}(\omega_t) \left(1 + 2 \frac{\gamma_{12}}{\gamma_1} \right) + \zeta_{21}(\omega_t) \left(1 - \frac{\gamma_{12}}{\gamma_1} \right) \right|^2, \quad (4.43)$$

which is shown in Figs. 4.10 and 4.11 for ratios

$$r = \frac{\mu_{12}^2}{\mu_{10}^2} \times \frac{\gamma_1 - \gamma_{12}}{\gamma_1 + 2\gamma_{12}} \quad (4.44)$$

In the special case $\gamma_{12} = \gamma_1$, i.e. $r = 0$, the excited-state absorption and the stimulated emission between the first and the second excited state cancel each other, and only the stimulated emission and the bleaching of the transition $|0\rangle \leftrightarrow |1\rangle$ and $|0\rangle \leftrightarrow |2\rangle$ remain. This case, however, is fully covered by the homogeneous substructure.

4.1. Discrete spectral structures

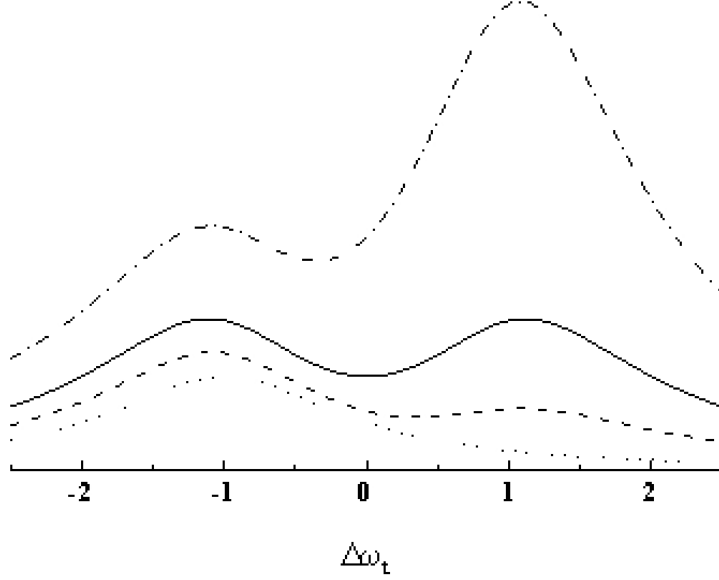


Figure 4.11: Probe-frequency dependence of the T_2 -peaks of a three-level system pumped at $\omega_p = \omega_{20}$ for $r = 1$ (solid line), $r = 0$ (dot), $r = 0.5$ (dash), and $r = 2$ (dash-dot) where μ_{10}/γ_1 has been fixed. Other parameters and axis as in Fig. 4.9.

A further interesting example for excited-state absorption in NLPF is probing the Triplet after inter-system crossing. In this case the state $|2\rangle$ represents the first excited singlet state, while the state $|1\rangle$ stands for the lowest triplet state. The probed excited triplet state is assigned as $|3\rangle$. Note that due to the selection rules $\mu_{32} = \mu_{30} = \mu_{21} = \mu_{10} = \mathbf{0}$. Thus the pump-frequency dependence of the T_2 -peaks results from the squared cross-section of pumping the singlet absorption $\sigma_{10}(\omega_p, \omega_p)^2$ and the probe-frequency dependence is given by

$$\left| \zeta_{20}(\omega_t) \left(2 + \frac{\gamma_{12}}{\gamma_1} \right) - \zeta_{31}(\omega_t) \frac{\gamma_{12}}{\gamma_1} \right|^2. \quad (4.45)$$

For overlapping triplet and singlet bands, this results in line shapes like those shown in Figs. 4.10 and 4.11 in dependence of the

$$r = -\frac{|\mu_{31}|^2}{|\mu_{20}|^2} \frac{\gamma_{12}}{2\gamma_1 + \gamma_{12}}. \quad (4.46)$$

Note that the ratio r is determined by the balance between triplet generation via inter-system crossing (γ_{12}) and the almost non-radiative triplet decay (γ_1). In the case that the former

process is much faster than the latter there occurs an accumulation of occupation in the lowest triplet state by pumping the singlet transition. In this case one obtains a saturation for both, triplet absorption and singlet bleaching, which is to be described in the framework of the strong field theory of NLPF (cf. chapter 6).

Though it is really of some interest to obtain information about higher excited states, the complex contributions of the excited-state absorption as well as stimulated emission to the probe-dependence of the NLPF-spectra complicates the analysis of the T_2 -peaks for determination of the substructure. Particularly, one has to be very cautious in using the simple relation $\sigma_{\mu\nu}(\omega_p, \omega_p) = \zeta_{\mu\nu}(\omega_p) - \zeta_{\mu\nu}^*(\omega_p)$ as constriction in fitting NLPF-spectra. Furthermore, non-overlapping excited-state absorption and stimulated emission can hardly be distinguished from each other by the T_2 -peaks. Finally it shall be noted that T_1 -peak analysis does not help to overcome these problems, since the line-shape of the T_1 -peak is influenced by excited-state absorption and stimulated emissions only in respect of different probe- respective pump-frequency dependent prefactors $c(\omega_{p,t})$, which has to correspond to the pattern of the underlying T_2 -peaks.

4.2 Mixed discrete substructures

For the T_2 -peak analysis of measured NLPF-spectra for arbitrary systems a generalized NLPF line-shape function is needed, which includes potentially all kinds of substructures but based on the observable transitions instead of states of an initially only tentative term scheme. All substructures discussed above, i.e. heterogeneous substructure, incoherent energy transfer, and homogeneous substructure, and excited state absorption, as well as combinations of them can be represented by the NLPF-line-shape function

$$s(\omega_t, \omega_p) = \sum_{\mu\nu} \zeta_{\mu}(\omega_t) \left\{ g_{\mu\nu} \tilde{\beta}_{\mu\nu}(0) \sigma_{\nu}(\omega_p, \omega_p) + g'_{\mu\nu} \tilde{\beta}_{\mu\nu}(\omega_p - \omega_t) \sigma_{\nu}(\omega_p, \omega_p) \right\} n_{\nu}. \quad (4.47)$$

where the indices μ and ν assign the transitions which populates them. $\sigma_{\nu}(\omega_p, \omega_p)$ and $\zeta_{\mu}(\omega_t)$ represents the corresponding cross-sections of pumping and probing functions, respectively. The generalized correlation matrix $\tilde{\beta}(0)$ is given by the system of equations

$$\sum_{\nu} \tilde{\beta}_{\mu\nu}(\omega) (\tilde{\gamma}_{\nu\kappa} + i\omega\delta_{\nu\kappa}) = d_{\mu\kappa}, \quad (4.48)$$

where the reduced energy relaxation matrix $\tilde{\gamma}$ is given as by Eqs. 4.34 and 4.35. Thereby the off-diagonal elements $\tilde{\gamma}_{\mu\nu}$ represent energy transfer and relaxation from the excited transition μ to ν , independently of the corresponding ground states, which can be identical or not. Also the diagonals $\tilde{\gamma}_{\mu\mu}$ given by the inverse life-time of the excited state the transition μ leads to (cf. Eq. 4.35) are independent of the respective ground state.

4.3. Ground state progression

The substructure determined elements in Eq. 4.48 is the matrix \mathbf{d} on the right side of equality. The diagonals for all transitions one of the respective ground states is involved yields as $d_{\mu\mu} = 2$. The off-diagonal elements $d_{\mu\kappa}$ depends on the kind of substructure. For both transitions, κ and ν belongs to a common ground state, i.e. are homogeneous to each other, one obtains $d_{\mu\kappa} = 1$, which follows from comparison of Eqs. 4.37 and 4.47 for the homogeneous substructure resulting in

$$\tilde{\beta}_{\mu\nu}(\omega) = \sum_{\kappa} (\delta_{\mu\kappa} + 1) \beta_{\kappa\nu}(\omega). \quad (4.49)$$

For the heterogeneous substructure and incoherent excitation energy transfer (cf. Eqs. 4.26 and 4.25) one obtains $\tilde{\beta}_{\mu\nu}(\omega) = \beta_{\mu\nu}(\omega)$ and consequently $d_{\mu\kappa} = 0$. In the case of excited state transitions μ'' associated with the transition μ (cf. section 4.1.4) the \mathbf{d} -matrix elements yields as $d_{\mu''\mu} = \pm 1$. Here the plus-sign means stimulated emission and the minus-sign excited state absorption. In both cases one has to set $\tilde{\gamma}_{\mu'\kappa} = \tilde{\gamma}_{\mu\kappa}$, $\tilde{\gamma}_{\kappa\mu'} = \tilde{\gamma}_{\kappa'\mu'} = 0$, and $n_{\mu'} = 0$. In principle, Eqs. 4.47 and 4.48 represent already the searched all-purpose theory for the discrete substructure of room-temperature NLPF spectra recorded at low pump intensities (cf. Introduction). Only the ground-state progression, could not have been included, since it needs a different treatment, as will be shown in the next section.

4.3 Ground state progression

Unfortunately a simple system of equations like Eq. 4.48 can not be used in cases where different ground states are connected to each other, either by common excited states (cf. Fig. 4.1 panel e). The reason is, that the ground states has been eliminated by constructing the reduced energy relaxation matrix $\tilde{\gamma}$, completely. Thus, in Eqs. 4.47 and 4.48 the transitions could be unequivocally assigned by the excited state they leads to. For transitions from different ground-states to a common excited state this assignment fails, at least if initially both ground-states can be occupied, e.g. by thermalization (otherwise see section 4.1.4). Therefore, the ground-state progression has to be to calculate for the initial definition of the correlation function matrix $\beta(\omega)$ (cf. Eq. 4.5) by use of the NLPF-line shape function as given in Eq. 4.1.

4.3.1 The Λ -system

In what follows, the results for the simplest case of a ground-state progression, the so-called Λ -system shall be featured. The Λ -system represents a three-level system with transition frequency $\omega_{10} \ll \omega_{20}$. Therefore, the state $|1\rangle$ may be thermally occupied for detailed balance (cf.

Eq. 3.44), i.e.

$$n_1 = n_0 \exp[-\hbar\omega_{10}/kT] > 0, \quad (4.50)$$

and can act for pumping as a second ground-state beside the state $|0\rangle$. Concatenating equivalent terms resulting from Eq. 4.1 the NLPF-line shape function for the T_2 -peaks of the Λ -system yields as

$$s_\Lambda(\omega_t, \omega_p) = \frac{1}{15} \left(\frac{\tilde{\zeta}_{prog}(\omega_t) \tilde{\sigma}_{abs}(\omega_p)}{\gamma_{02} + \gamma_{12}} + \frac{\tilde{\zeta}_\Lambda(\omega_t) \tilde{\sigma}_\Lambda(\omega_p, \omega_p)}{\gamma_{01} + \gamma_{10}} \right) + \dots \quad (4.51)$$

The first term containing the probing and pumping functions

$$\tilde{\zeta}_{prog}(\omega_t) = \zeta_{21}(\omega_t) (1 + n_1) + \zeta_{20}(\omega_t) (1 + n_0) \quad (4.52)$$

$$\tilde{\sigma}_{abs}(\omega_p) = \sigma_{21}(\omega_p, \omega_p) n_1 + \sigma_{20}(\omega_p, \omega_p) n_0 \quad (4.53)$$

is dominant in the homogeneous limit $\gamma_{01} + \gamma_{10} \gg \gamma_{02} + \gamma_{12}$, i.e. for fast equilibration between the two ground-states. The second term containing the effective probing and pumping functions as given by

$$\tilde{\zeta}_\Lambda(\omega_t) = \zeta_{21}(\omega_t) - \zeta_{20}(\omega_t) \quad (4.54)$$

$$\tilde{\sigma}_\Lambda(\omega_p) = b_{12} \sigma_{20}(\omega_p, \omega_p) n_0 - b_{02} \sigma_{21}(\omega_p, \omega_p) n_1, \quad (4.55)$$

for energy relaxation branching ratios

$$b_{02} = \frac{\gamma_{02}}{\gamma_{02} + \gamma_{12}} \quad \text{and} \quad b_{12} = \frac{\gamma_{12}}{\gamma_{02} + \gamma_{12}}. \quad (4.56)$$

represents what the author likes to call NLPF-‘hole-burning’.

In the ‘hole-burning’ limit $\gamma_{02} + \gamma_{12} \ll \gamma_{01} + \gamma_{10}$ the equilibration between the two ground-states is slow. By pumping the excited state $|2\rangle$ from only one ground-state, either $|1\rangle$ or $|0\rangle$, and by the subsequent fast energy relaxation, which is branched to both ground-states according to Eq. 4.56, occupation will be reshuffle from the pumped to the idle ground-state. This difference, will be only slowly equalized. Therefore probing both ground-state, for pumped ground state one obtains persistent bleaching, for the idle enhanced absorption.⁶ In standard hole-burning spectroscopy, the former represent the ‘hole’ and the latter the ‘anti-hole’ with opposite sign. In NLPF-spectra, however, the T_2 -peaks for both are similar in shape. The fact that T_2 -peaks representing ‘holes’ are located on the primary diagonal $\omega_t = \omega_p$, i.e. at $(\omega_p, \omega_t) = (\omega_{10}, \omega_{10})$ and $(\omega_{20}, \omega_{20})$, respectively, and those representing ‘anti-holes’ are located off-diagonal, i.e. at $(\omega_p, \omega_t) = (\omega_{10}, \omega_{20})$ and $(\omega_{20}, \omega_{10})$, respectively, does not help much. A quite similar pattern is obtained for the homogeneous substructure (cf. Fig. 4.6). Only for

⁶Stimulated emission is negligible due to the fast energy relaxation.

4.3. Ground state progression

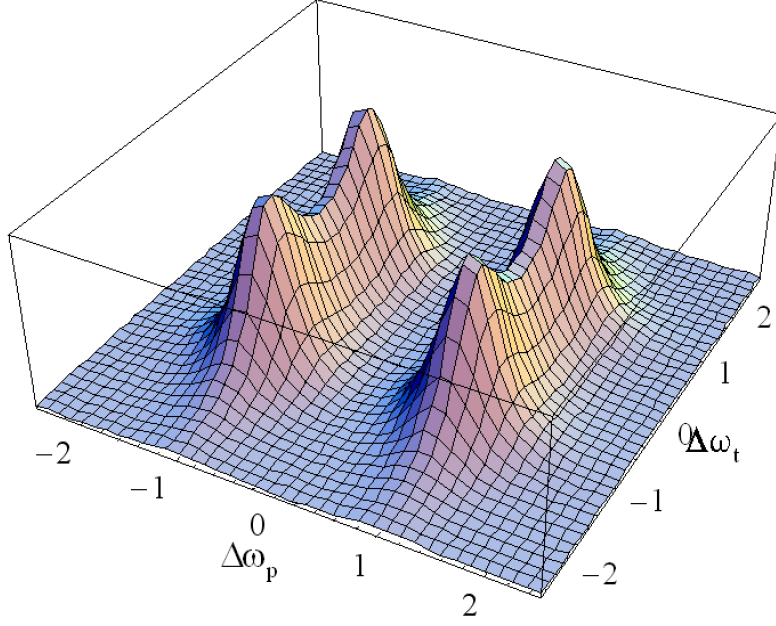


Figure 4.12: T_2 -peaks for a Λ -system in the ‘hole-burning’ limit $\gamma_{02} + \gamma_{12} \gg \gamma_{10} + \gamma_{01}$ with a branching ratios $b_{02} = b_{12} = 0.5$ at high temperature ($kT \gg \hbar\omega_{10} \Rightarrow n_0 = n_1 = 0.5$). The transition dipoles are equal as well as the depasing rates given by $\Gamma_{02} = \Gamma_{12} = \omega_{01}/4$. Axes are labeled for $\Delta\omega_{p,t} = 2\omega_{p,t}/(\omega_{12} + \omega_{02}) - 1$.

overlapping T_2 -peaks the opposite sign in the probing function for ‘holes’ and ‘anti-holes’ does effect (cf. Fig. 4.12). The resulting line shapes in respect of the probe-frequency dependence are quite similar to those obtained for excited state absorption (cf. section 4.1.4), but here four T_2 -peaks appear instead of only two. For ‘holes’ and ‘anti-holes’ which do not overlap, comparison with the absorption spectrum may reveal a ground state progression in the ‘hole-burning’ limit, but not in the homogeneous limit for $\tilde{\sigma}_{abs}(\omega_p) = 3\sigma_{abs}(\omega_p)$. Hence, in respect of the ground-state progressions, the T_2 -peak analysis calls for supporting information from other spectroscopic methods like Raman spectroscopy.

The T_1 -peak is in both limits quite similar to that for the two-level system, being approximately Lorentzian with a line width of $2(\gamma_{02} + \gamma_{12})$ in the homogenous and $2(\gamma_{01} + \gamma_{10})$ in the ‘hole-burning’ limit, respectively. For the intermediate case see Fig. 4.13

Note, that the asymptotic for the outer wings of the T_1 -peaks is independently of the branching ratios NLPF-line shape function given by

$$s_{\Lambda}(\omega_t, \omega_p) \xrightarrow{|\omega_p - \omega_t| \rightarrow \infty} \frac{2}{5} \tilde{\zeta}_{prog}(\omega_t) \left(\frac{\sigma_{abs}(\omega_p, \omega_p)}{\gamma_{02} + \gamma_{12}} + \frac{\sigma_{abs}(\omega_t, \omega_p)}{\gamma_{02} + \gamma_{12} + i(\omega_t - \omega_p)} \right). \quad (4.57)$$

This means there does not exist a long-reaching asymmetry between the left and right wing of

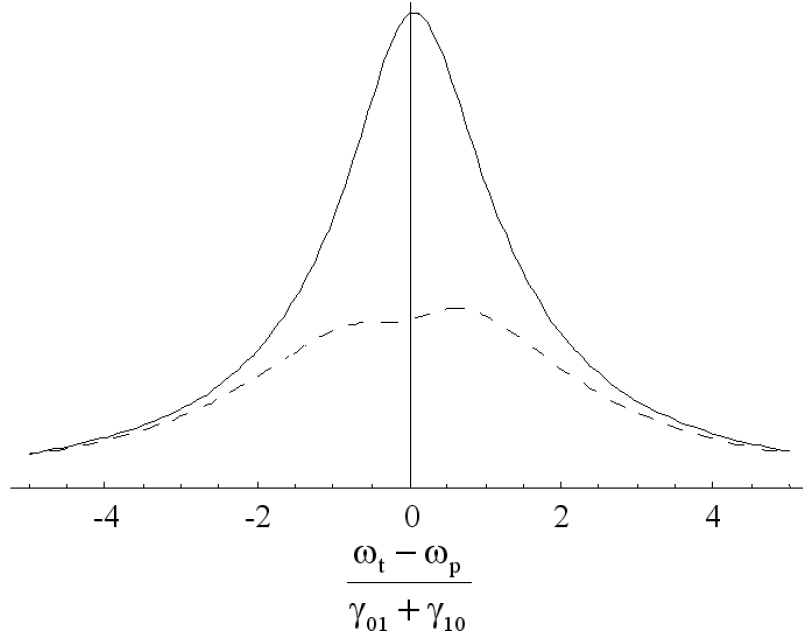


Figure 4.13: T_1 -peaks for a Λ -system with $\gamma_{02} = 4\gamma_{01} = 4\gamma_{10}$ and $\gamma_{12} = 0$ taken at $\omega_t = \omega_{12}$ (solid line) and $\omega_t = \omega_{02}$ (dashed line). Other parameters as in Fig. 4.12

the T_1 -peak, as it has been so significant for the other kinds of substructure (cf. Figs. 4.3, 4.5, and 4.7).

4.3.2 ‘Raman’-peaks

As mentioned in chapter 2 (cf. section 2.3.2) for multi-level systems tunneling terms may occur in the NLPF-line-shape function. In the previous sections, these have been neglected for dephasing rates $2\Gamma_{\mu\nu} \gg |\gamma_{\mu\mu} + \gamma_{\nu\nu}|$ (cf. section 4.1). For the ground-state progression in the ‘hole-burning’ limit this condition may not hold, while tunneling terms from the excite-state progression are usually negligible for

$$2\Gamma_{\mu\nu} \gtrsim \gamma_{\mu} + \gamma_{\nu} + \gamma_{\mu\nu} + \gamma_{\nu\mu} \gg \gamma_{\mu} + \gamma_{\nu} \text{ or } \gamma_{\mu\nu} + \gamma_{\nu\mu}. \quad (4.58)$$

In the special case of the Λ -system, as the simplest case of ground-state progression, one obtains two ‘Raman’-peaks (cf. Fig. 4.14) for the resonances of the Greens functions

$$\mathcal{G}_{1010}(\omega_t - \omega_p) = \frac{1}{\Gamma_{10} + i(\omega_t - \omega_p - \omega_{10})} \quad (4.59)$$

$$\mathcal{G}_{0101}(\omega_t - \omega_p) = \frac{1}{\Gamma_{01} + i(\omega_t - \omega_p + \omega_{10})} \quad (4.60)$$

4.4. Summary

at $|\omega_t - \omega_p| = \omega_{10}$. The respective terms in the NLPF-line-shape function are given as

$$s(\omega_t, \omega_p) = \dots + \frac{\zeta_{20}(\omega_t) (g \zeta_{20}(\omega_t) - \zeta_{21}^*(\omega_p))}{\Gamma_{10} + i(\omega_t - \omega_p - \omega_{10})} + \frac{\zeta_{21}(\omega_t) (g^{-1} \zeta_{21}(\omega_t) - \zeta_{20}^*(\omega_p))}{\Gamma_{01} + i(\omega_t - \omega_p + \omega_{10})}. \quad (4.61)$$

with $g = \mu_{21}^2 / \mu_{01}^2$ for parallel transition dipoles and rotating wave approximation (cf. section 2.3.2). Note that in the ‘hole-burning’ limit at least for $T \rightarrow 0\text{K}$ according to Eq. 3.45 the dephasing rate

$$\Gamma_{10} = \frac{\gamma_{01} + \gamma_{10}}{2} + \bar{\Gamma}_{10}, \quad (4.62)$$

where $\bar{\Gamma}_{10}$ represents the temperature dependent pure dephasing, may be of the same order of magnitude as the effective relaxation rate $\gamma_{01} + \gamma_{10}$, which is the relevant one for the height of T_1 - and T_2 -peaks (see above).⁷

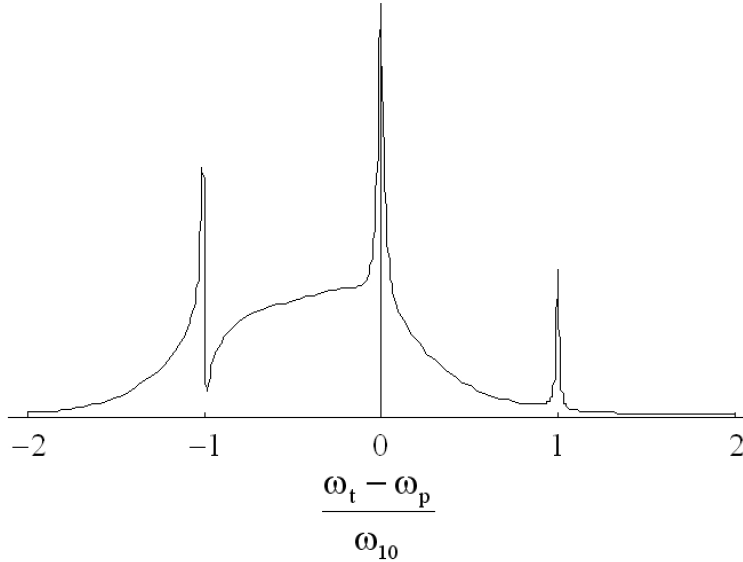


Figure 4.14: NLPF-spectrum with T_1 -peak (center) and two ‘Raman’-peaks for a three-level system with $\omega_{10} \ll \omega_{20}$ (Λ -System) at $T \rightarrow 0\text{K}$ ($2\Gamma_{10} = \gamma_{10} + \gamma_{01} = 0.1\omega_{10}$). The pump frequency has been fixed at $\omega_p = \omega_{20}$. The asymmetry of the left Raman-peak and the T_1 -peak result from interference with the underlying T_2 -peak being of ‘anti-hole’ type (see above).

4.4 Summary

NLPF at low pump intensities provides a deeper insight into the spectral structure of a molecular multi-level system, than absorption and fluorescence spectroscopy. This is possible due to

⁷For the homogeneous limit this can not be for $2\Gamma_{10} \gg \gamma_{02} + \gamma_{20}$.

the two-dimensionality of the NLPF-spectrum. By scanning the probe- and pump-frequency independently correlations between the T_2 -peaks can be revealed, which contain information about the type of the discrete spectral structure (homogeneous or heterogeneous), the energy relaxation and transfer path, and the relative orientations of the transition dipole. Furthermore, excited state absorption and stimulated emission from the pumped excited state can be probed. However, the fact that the NLPF-spectrum is given by $|s(\omega_t, \omega_p)|^2$ complicates the analysis of the NLPF-spectrum significantly. To the author's knowledge model functions for describing NLPF-spectra of systems with more than one ground-state level (section 4.3), have been deduced in the present work for the first time.

4.5 Supplement: Application of NLPF to subband analysis in praxi

Since a direct interpretation of the correlated pump and probe dependence of the T_2 -peaks and the T_1 -peaks is not possible, a fitting algorithm has to be applied to the NLPF-spectra. J. Ehlert and the author of the present work have developed a global fitting program [Ehlert and Beenken, 1998], which allows to fit absorption and NLPF-spectra to the line-shape function given in Eqs. 4.47 and 4.48, in order to reveal the term-scheme with associated energy relaxation path $\gamma_{\mu\nu}$, dephasing rates $\Gamma_{\mu\nu}$, transition frequencies $\omega_{\mu\nu}$ and transition dipoles $\mu_{\mu\nu}$, the latter in both respects, relative strengths as well as relative orientation as given by the angles $\Phi_{\mu\nu}$ (cf. Eq. 4.10). For the determination of absolute transition dipole strengths see chapter 6. By addition of a T_1 -peak analysis (cf. Eq. 4.31) this program provides theoretically an all-purpose tool for analysis of the relevant spectroscopic properties in molecules and supramolecular aggregates. Unfortunately the ground-state progression could not be implemented into the mentioned program, yet.

In praxi the author recommend strongly to search for additional information by other spectroscopic methods. In any case the absorption spectrum has to be included into the analysis with reasons (cf. Eq. 4.30). For multi-level systems with long ground-state-recovering times, where a sufficient resolution of the T_1 -peak can not be reached, necessary information about the energy relaxation could be provided by e.g. fluorescence-decay measurements. For energy relaxation and transfer process which are much faster than the lifetime of the final state, the correlation between the T_2 -peaks depends not significantly on the values of the respective rates. In this case the analysis of the T_2 -peaks can only provide global information about the energy relaxation and transfer, like answering the question, where the final state is located a certain excited state decays to, or whether bottle necks occur in the energy relaxation path. Hence,

4.5. Supplement: Application of NLPF to subband analysis in praxi

time-resolved pump-probe spectroscopy might be more useful than NLPF for tracking fast energy transfer in detail. Nevertheless, NLPF with its high spectral resolution represents an ideal complementary method, which allows one to assign the respective lifetimes even to overlapping spectral subbands.

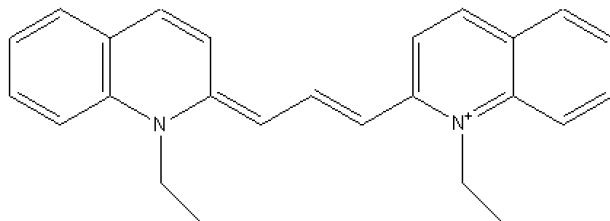


Figure 4.15: Structure formula of the pinacyanol (kation).

The first experimental studies [Voigt et al., 1997] global analysis of NLPF-spectra as described above has been applied to, was to pinacyanol (cf. Fig. 4.15). There heterogeneous substructure consisting of three subbands at 520nm, 565nm and 607nm has been clearly revealed. A fourth very weak subband at 556nm with lifetime of even 4.5ns, heterogeneous to the others as revealed by the subband analysis has been attributed to an impurity of the sample. Based on their nearly equal distances in the absorption spectrum, the three main subbands have been previously interpreted as part of one and the same vibrational progression. However, the analysis of the NLPF-spectra, especially of the asymmetry of the T_1 -peak (see Fig. 4.16) results in 13ps lifetime of the transitions at 520nm and 565nm but only 7ps lifetime of the transition at 607nm. From these results the conclusion is allowed that the subbands at 520nm and 565nm with nearly double the lifetime are *not* part of the vibrational progression to a basis-transition at 607nm, but in fact belong most probably to a different spectral species. This species is most probably an isomer of pinacyanol, though the measured NLPF-spectra have not provided any information whether this results from a photo-isomerization or not. This example should have shown how powerful NLPF is in order to reveal a spectral substructure, which is otherwise hidden in the broad absorption spectrum. For applications of the method to photosynthetic antennae see part two.

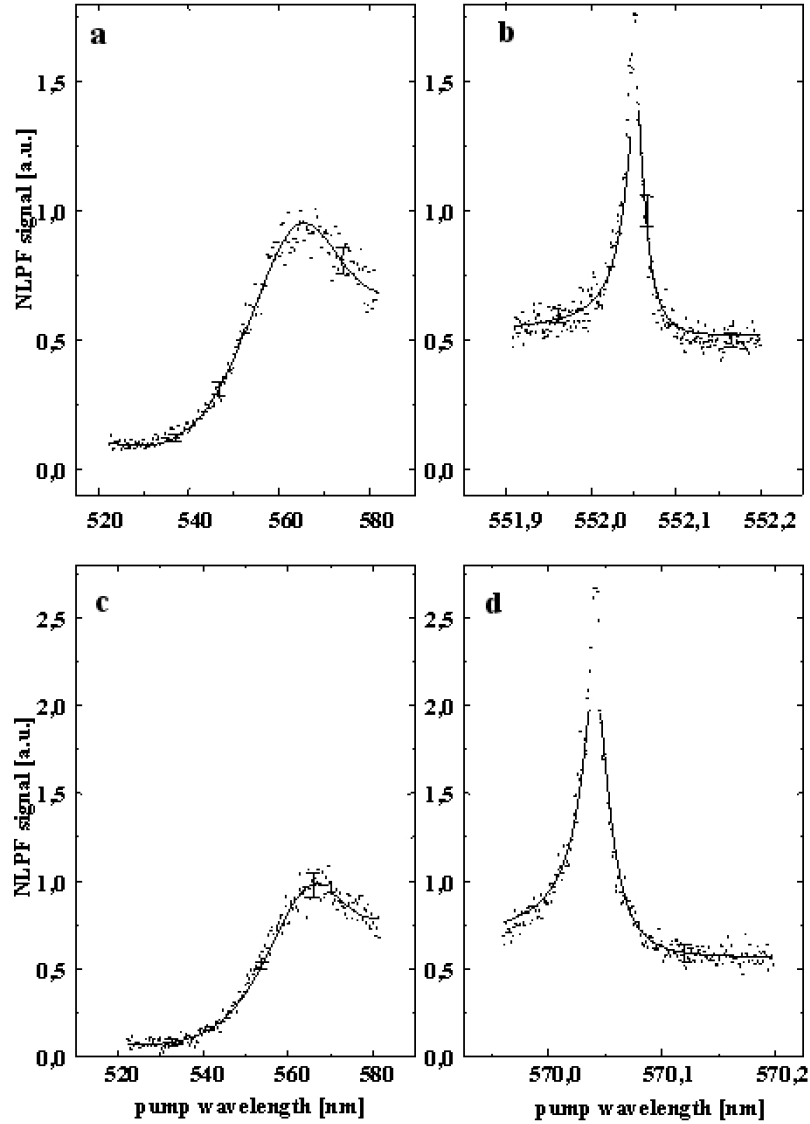


Figure 4.16: NLPF spectra of pinacyanol in low (panels **a,c**) and high (panels **b,d**) spectral resolution recorded over the pump wavelength at probe wavelengths $\lambda_t = 552.052$ nm (panels **a, b**) and $\lambda_t = 570.040$ nm (panels **c,d**). The solid curves represent the result of the best fit using the theoretical model as described in the text.

Chapter 5

Inhomogeneously broadened NLPF-spectra

In the previous chapter only the homogeneous broadening has been considered, though the line-broadening is to assume somewhere between the three limits presented in chapter 3: (i) the homogeneous broadening for Markovian dephasing, resulting in (quadratic) Lorentzian line shapes; (ii) the inhomogeneous dephasing limit with Gaussian line shapes for the T_2 -peaks due to Markovian energy relaxation but non-Markovian dephasing process; and (iii) the inhomogeneous broadening, where the energy relaxation is slow compared to the reservoir reorganization. In the case inhomogeneous dephasing the NLPF-line-shape function $s(\omega_t, \omega_p)$ can be easily obtained by substituting the Lorentzians in the functions $\zeta(\omega)$ and $\sigma(\omega, \omega')$ by Gaussians respective complex Voigt-profiles (cf. Eq. 3.63). The calculation of inhomogeneous broadening, however, turned out to be difficult in the framework of cumulant expansion (cf. supplement 3.5.2). Therefore, in what follows an alternative approach shall be established, based on the methods developed for the discrete spectral structures. This approach will enable one to describe inhomogeneous broadening, spectral diffusion, and orientational relaxation. The latter is not related to spectral line-broadening but can be described by the same approach as the spectral diffusion. It is a very important process, since it sets an upper limit for energy relaxation times that can be measured by NLPF.

The application of NLPF to determine inhomogeneous and homogenous line width has been studied experimentally and theoretically by numerous authors. Actually, the distinction of inhomogeneous and homogenous broadening was the reason for Song, Lee and Levenson to introduce NLPF as a method of molecular spectroscopy in condensed phase [Song et al., 1978]. In the following the differences in the line shapes between homogeneously and inhomogeneously broadened NLPF-spectra as well as spectral diffusion effects has been worked out [Marcano O

et al., 1990, Garcia-Golding, 1983, Neef and Mory, 1991]. All these previous studies concern mainly the relation between T_2 - and T_1 -peak. Astonishingly, the correlation between the pump- and probe-frequency dependences of the single T_2 -peak has not been emphasized, though it is included in the given formulas. To establish the T_2 -peak analysis as method to determine the type of line-broadening will be the main objective of the present chapter. Though, the significant differences in the NLPF-spectrum at fixed probe frequency, as pointed out in the mentioned previous works, has enabled determination of the homogeneous line widths even in complex pigment-protein aggregates like photosynthetic antennas [Leupold et al., 1993, Leupold et al., 1994, Lokstein et al., 1995], the approach presented in what follows may provide quantitatively more precise results. In particular it provides the inhomogeneous line width explicitly (cf. chapters 8).

5.1 Inhomogeneous broadening

In principle the inhomogeneous broadening represents the continuous limit of the heterogeneous substructure¹ (cf. section 4.1.1). This means simply that in Eq. 4.16 the sum $\sum_{\mu} \dots$ has to be substituted by an integral $\int \dots d\omega$ and the weighting factors n_{μ} by the distribution function $n_{10}(\omega)$, which describe the probability to find a two-level systems with transition frequency ω within the frequency range $d\omega$. Consequently, the NLPF-line-shape function of an inhomogeneously broadened two-level system is given by

$$s_{inh}(\omega_t, \omega_p) = \int s(\omega_t - \omega, \omega_p - \omega) n_{10}(\omega) d\omega, \quad (5.1)$$

where $s(\omega_p - \omega, \omega_t - \omega)$ is the normalized two-level line-shape function as given in Eq. 2.41 [Marcano O et al., 1990]. This definition is in full agreement with Eq. 3.18 for $\langle s(\omega_t, \omega_p) \rangle_R$ as given in section 3.1.3. Usually, in the transition-frequencies are assumed to be normal distributed, i.e.

$$n_{10}(\omega) = \frac{1}{\sqrt{2\pi}\Delta_{10}} \exp\left[-\frac{\omega^2}{2\Delta_{10}^2}\right] \quad (5.2)$$

with the inhomogeneous line-width parameter Δ_{10} .

In contrast to the only homogeneously broadened, the inhomogeneously broadened T_2 -peak shows a positive correlation between pump and probe frequency dependence (see Fig. 5.1). This can be explained by the typical properties of the correlation matrix $\beta(\mathbf{0})$ for a heterogeneous substructure containing only diagonal elements (cf. Eq. 4.14). For finite homogeneous line $2\Gamma_{10}$

¹Etymologically the word ‘inhomogeneous’ means the same as ‘heterogeneous’. In the present context however the term heterogeneous shall be reserved for discrete spectral substructures, while the term inhomogeneous shall be used for the corresponding continuous substructure.

5.1. Inhomogeneous broadening

width this strong correlation is to convolute with the distribution $n_0(\omega)$. However, note that neither the probe- nor the pump-frequency dependence of the T_2 -peak represents a Voigt-profile as in the inhomogeneous dephasing limit (cf. Eq. 3.63).

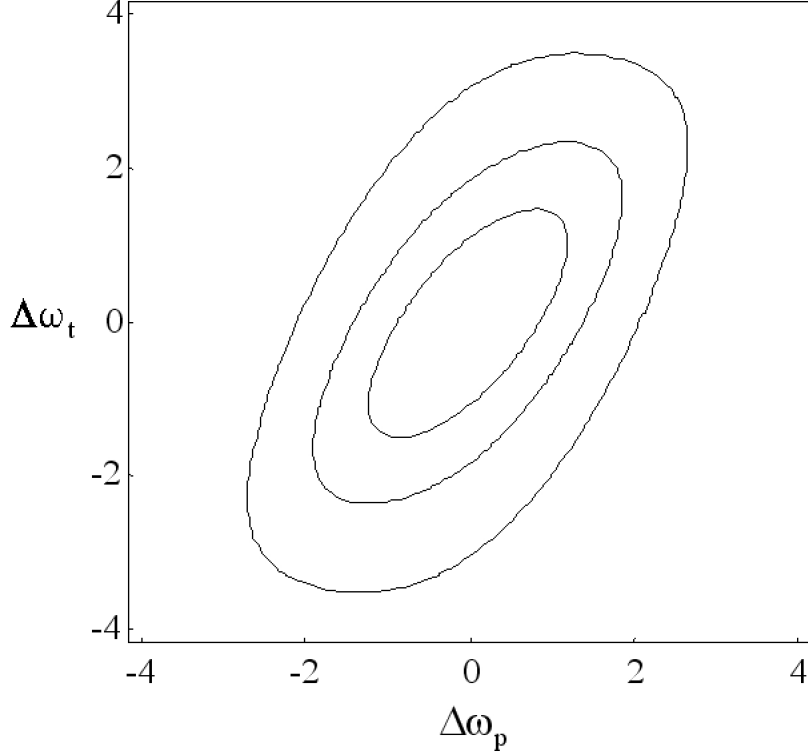


Figure 5.1: T_2 -peak for a inhomogeneous broadened two-level system with a inhomogeneous width $\Delta = 2\Gamma$. Contourlines shown for 25%, 50% and 75% of the peak maximum. Axes are labeled as $\Delta\omega_{p,t} = (\omega_{p,t} - \omega_{10}) / \Gamma$.

For inhomogeneously broadened multi-level systems, which means an assemble of discrete homogeneous substructure with normal-distributed transition frequencies, the convolution is more complicated than that in Eq. 5.1. due to the fact that one part of the pump-probe correlation caused by the discrete spectral structure, the other by the inhomogeneous broadening. The easiest way is to calculate first the discrete system as described above (see section 4.1) and averaged the resulting NLPF-line-shape functions $s(\omega_t, \omega_p, \{\omega_{\mu\nu}\})$, which depends on the set of transition frequencies $\omega_{\mu\nu}$, over the distributions of transition frequencies $n(\{\omega_{\mu\nu}\})$ as

$$s_{inh}(\omega_t, \omega_p) = \int \cdots \int s(\omega_t, \omega_p, \{\omega_{\mu\nu}\}) n(\{\omega_{\mu\nu}\}) d^N \omega_{\mu\nu}. \quad (5.3)$$

For statistically independent transition frequencies $\omega_{\mu\nu}$ one can factorize the distribution func-

tion as

$$n(\{\omega_{\mu\nu}\}) = \prod_{\mu\nu} n_{\mu\nu}(\Omega). \quad (5.4)$$

If furthermore the discrete correlation matrix elements $\beta_{\mu\nu,\kappa\lambda}(\omega)$ are independent of the transition frequencies $\omega_{\mu\nu}$, Eq. 5.3 results in

$$\begin{aligned} s_{inh}(\omega_t, \omega_p) &= \frac{1}{15} \sum_{\mu\nu} \left\{ \beta_{\mu\nu,\mu\nu}(0) \tilde{\zeta}_{\mu\nu}(\omega_t, \omega_p, \omega_p) + \beta_{\mu\nu,\mu\nu}(\omega_t - \omega_p) \tilde{\xi}_{\mu\nu}(\omega_t, \omega_t, \omega_p) \right\} \\ &+ \frac{1}{15} \sum_{\mu\nu \neq \kappa\lambda} \tilde{\zeta}_{\mu\nu}(\omega_t) \left\{ \beta_{\mu\nu,\kappa\lambda}(0) \tilde{\sigma}_{\kappa\lambda}(\omega_p, \omega_p) + \beta_{\mu\nu,\kappa\lambda}(\omega_t - \omega_p) \tilde{\sigma}_{\kappa\lambda}(\omega_t, \omega_p) \right\} \end{aligned} \quad (5.5)$$

using the functions

$$\tilde{\zeta}_{\mu\nu}(\omega) = \int (\zeta_{\mu\nu}(\omega - \Omega) + \zeta_{\nu\mu}(\omega - \Omega)) n_{\mu\nu}(\Omega) d\Omega \quad (5.6)$$

$$\tilde{\sigma}_{\kappa\lambda}(\omega, \omega') = \int \sigma_{\kappa\lambda}(\omega - \Omega, \omega' - \Omega) n_{\kappa\lambda}(\Omega) d\Omega \quad (5.7)$$

$$\tilde{\zeta}_{\mu\nu}(\omega, \omega', \omega'') = \int d\omega (\zeta_{\mu\nu}(\omega - \Omega) + \zeta_{\nu\mu}(\omega - \Omega)) \sigma_{\mu\nu}(\omega' - \Omega, \omega'' - \Omega) n_{\mu\nu}(\Omega) d\Omega. \quad (5.8)$$

The latter function $\tilde{\zeta}_{\mu\nu}(\omega_t, \omega_p)$ takes into account that for probing the bleaching and the stimulated emission of the pumped transition ($\mu \leftrightarrow \nu$) the probing functions $\zeta_{\mu\nu}(\omega - \Omega)$ and $\zeta_{\nu\mu}(\omega - \Omega)$ can only refer to the cross-section of pumping $\sigma_{\mu\nu}(\omega' - \Omega, \omega'' - \Omega)$ for the same molecule. Consequently they are distributed as a whole. Note that for normal distributed transition frequencies only the cross-section of pumping $\tilde{\sigma}_{\kappa\lambda}(\omega, \omega)$ results in the typical Voigt-profile of an inhomogeneously broadened absorption band.

5.2 Förster transfer for inhomogeneously broadened donors and acceptors

The approach given by Eqs. 5.5-5.8 holds for all kinds of substructures except of the case where energy relaxation and transfer rates depends on the frequencies of the pumped and probed transitions. A very important example of such an exception is the Förster-transfer, where the energy transfer rates $\gamma_{\mu\mu',\nu\nu'}$ depend on the spectral overlap between donor emission and acceptor absorption. For a donor-acceptor pair (d, a) with identical (Lorentzian) homogeneous broadening ($\Gamma_d = \Gamma_a = \Gamma$) one obtains the energy transfer rates approximately as

$$\gamma_{ad}(\omega - \omega') = \frac{\bar{\gamma}_{ad}}{2\pi} \frac{4\Gamma}{4\Gamma^2 + (\omega_{da} + \omega' - \omega)^2} \quad (5.9)$$

$$\gamma_{da}(\omega - \omega') = \frac{\bar{\gamma}_{ad}}{2\pi} \frac{4\Gamma}{4\Gamma^2 + (\omega_{ad} + \omega - \omega')^2} \quad (5.10)$$

5.2. Förster transfer for inhomogeneously broadened donors and acceptors

where ω_{da} is the difference between the mean emission frequency of the donor and absorption frequency of the acceptor and vice versa ω_{ad} for the back-transfer. The latter is generally larger than the (negative) value of the former due to the Stokes-shift. $\bar{\gamma}_{ad}$ represents the over-all Förster transfer rate in the case of a extreme inhomogeneous broadening ($\Delta_a, \Delta_d \rightarrow \infty$). Note that in the present model the energy transfer rates depend only on the difference between the actual transition frequencies of donor and acceptor molecule $\omega_{da} - \omega' - \omega$. In general, energy transfer rates depend in a more complicated way on the actual acceptor and donor frequencies. Furthermore, it has to be note that for a more precise description of the overlap integral non-Markovian line shapes as given in section 3.3.3 are to use. Only these guarantee the detailed balance between the energy transfer rates $\gamma_{ad}(\omega, \omega')$ and $\gamma_{da}(\omega, \omega')$ (cf. Eq. 3.44). Nevertheless, for the more qualitative discussion the Förster transfer in what follows the simplifications made above are acceptable.

The terms of the NLPF-line-shape function describing the T_2 -peaks obtained for the inhomogeneously broadened donor-acceptor system connected by Förster transfer as described above yield as

$$\begin{aligned}
s_{ft}(\omega_t, \omega_p) = \frac{1}{15} & \iint \left\{ \zeta_a(\omega_t - \omega) \frac{\gamma_d + \gamma_{ad}(\omega - \omega')}{F(\omega - \omega')} \sigma_a(\omega_p - \omega, \omega_p - \omega) \right. \\
& + \zeta_d(\omega_t - \omega') \frac{\gamma_{da}(\omega - \omega')}{F(\omega - \omega')} \sigma_a(\omega_p - \omega, \omega_p - \omega) \\
& + \zeta_a(\omega_t - \omega) \frac{\gamma_{ad}(\omega - \omega')}{F(\omega - \omega')} \sigma_d(\omega_p - \omega', \omega_p - \omega') \\
& \left. + \zeta_d(\omega_t - \omega') \frac{\gamma_d + \gamma_{da}(\omega - \omega')}{F(\omega - \omega')} \sigma_d(\omega_p - \omega', \omega_p - \omega') \right\} \\
& \times n_a(\omega) n_d(\omega') d\omega d\omega'. \tag{5.11}
\end{aligned}$$

with

$$F(\omega) = \gamma_a \gamma_d + \gamma_a \gamma_{ad}(\omega) + \gamma_d \gamma_{da}(\omega) \tag{5.12}$$

(cf. Eq. 5.3 as well as Eqs.4.26 and 4.25). The energy relaxation rates of the isolated acceptor and donor are assigned as γ_a and γ_d , respectively. According to the incoherent nature of the Förster transfer the probing functions $\zeta_a(\omega_t)$ and $\zeta_d(\omega_t)$ contain always both, the bleaching and emission of the respective molecule (cf. section 4.1.2). The second and third term in Eq. 5.11 represent the energy transfer, while the other terms describes the NLPF signal caused by the excitation remaining on the pumped species.

Fig. 5.2 shows the NLPF-spectrum (without T_1 -peak) for a donor-acceptor system where the mean emission frequency ω_d of the donor equals the mean absorption frequency ω_a of the acceptor. Due to the very low back-transfer rate γ_{da} there occur only five T_2 -peaks. Three

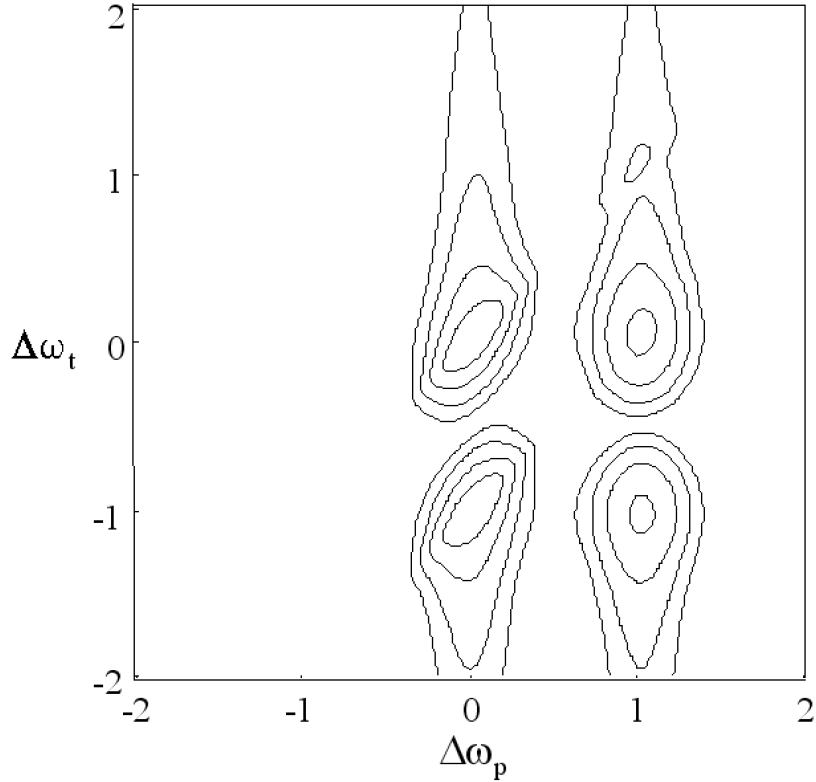


Figure 5.2: T_2 -peaks for a donor acceptor pair with $\omega_{da} = 0$. Contourlines are shown for $1/16$, $1/8$, $1/4$ and $1/2$ of the maximum value. Axes are labeled as $\Delta\omega_{p,t} = (\omega_{p,t} - \omega_a)/S$, where ω_a is the absorption frequency of the acceptor and S the Stokes shift equal for acceptor and donor. The homogeneous and inhomogeneous linewidths are equal and given by $\Delta = 2\Gamma = S/5$. Energy relaxation and transfer rates are related to each other by $\gamma_a = \gamma_d = 0.01 \bar{\gamma}_{ad}$.

of them are shaped like in Fig. 5.1. These represent the cases where the excitation remains on the acceptor ($\Delta\omega_p = 0$) or on the donor ($\Delta\omega_t, \Delta\omega_p = 1$) to be probed either by bleaching or stimulated emission, respectively (cf. Eq. 5.11 first and last term within the brackets). The latter peak attributed to the donor is rather low due to the fact that the lifetimes of the donor is significantly shortened by the resonant energy transfer. The remaining two T_2 -peaks are clearly related to the energy transfer – in particular that at $(\Delta\omega_p, \Delta\omega_p) = (-1, 1)$, which represents the probing of the stimulated emission of the acceptors for pumping the donors. Due to the persistently resonant energy-transfer this T_2 -peak is symmetric in respect of the pump-frequency dependence. The T_2 -peak at $(\Delta\omega_p, \Delta\omega_p) = (0, 1)$ is not completely symmetric in this respect, since it represents a mixture of probing the stimulated emission of the donor and the bleaching of the acceptor induced by the energy transfer. The former results in the

5.2. Förster transfer for inhomogeneously broadened donors and acceptors

correlation like the absorption of the donor (see above). For faster energy relaxation from the donor to their ground state $\gamma_d \gg \gamma_{ad}$ (cf. Fig. 5.3) the T_2 -peak at $(\Delta\omega_p, \Delta\omega_t) = (0, 1)$ is correlated as the other three peaks related to the donor. Thus the dependence of the energy transfer on the actual frequency is only reflected by the T_2 -peak at $(\Delta\omega_p, \Delta\omega_t) = (-1, 1)$, which is slightly correlated. The correlation causes from the fact that for donor-acceptor pairs being off-resonant, i.e. the actual frequency difference is $\Delta\omega \not\approx 0$, the lowered energy transfer rate can not compete with the energy relaxation rates, what it might do better for resonant pairs ($\Delta\omega \approx 0$). This means that for the referred T_2 -peak the difference between probe and pump frequency is to be the Stokes shift of the acceptor for maximum NLPF-signal. In the previously described case this effect was not important, since the energy transfer was the dominant decay channel for all donor-acceptor pairs, even for the off-resonant ones. A similar behavior but more pronounced is obtained in the case where the mean frequency of the donor emission is higher than that of the acceptor absorption, i.e. in the case $\omega_{da} > 0$.

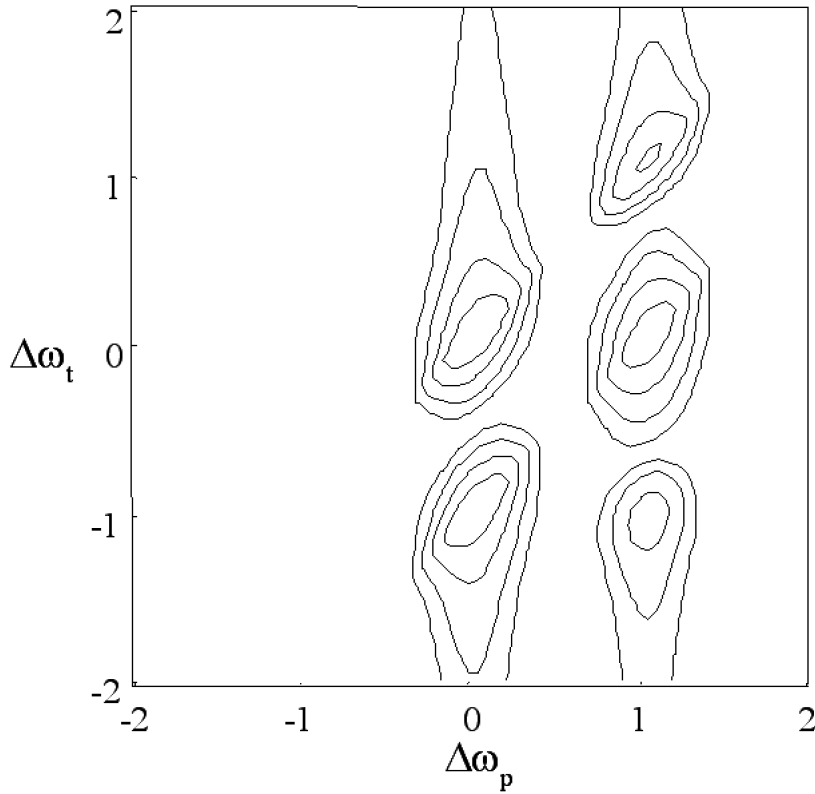


Figure 5.3: T_2 -peaks for the same donor-acceptor pair as in Fig. 5.2 but with energy relaxation rates are given as $\gamma_a = \gamma_d = \bar{\gamma}_{ad}/2$. Other parameters and axes see Fig. 5.2.

In the opposite case where the mean frequency of the donor emission is lower than that

of the acceptor absorption, i.e. $\omega_{da} < 0$, one obtains a negative correlation for the probe- and pump frequency dependence for probing the stimulated emission of the acceptors when pumping the donors. However this negative correlation is not as clearly pronounced as the positive one in the case $\omega_{da} \geq 0$. This causes from the fact that the Lorentzian resulting from the overlap which determines $\gamma_{ad}(\Omega)$ has more extended wings than the Gaussian representing the distribution function $n_a(\Omega)$. The four other T_2 -peaks are positively correlated anyway (cf. Fig. 5.4).

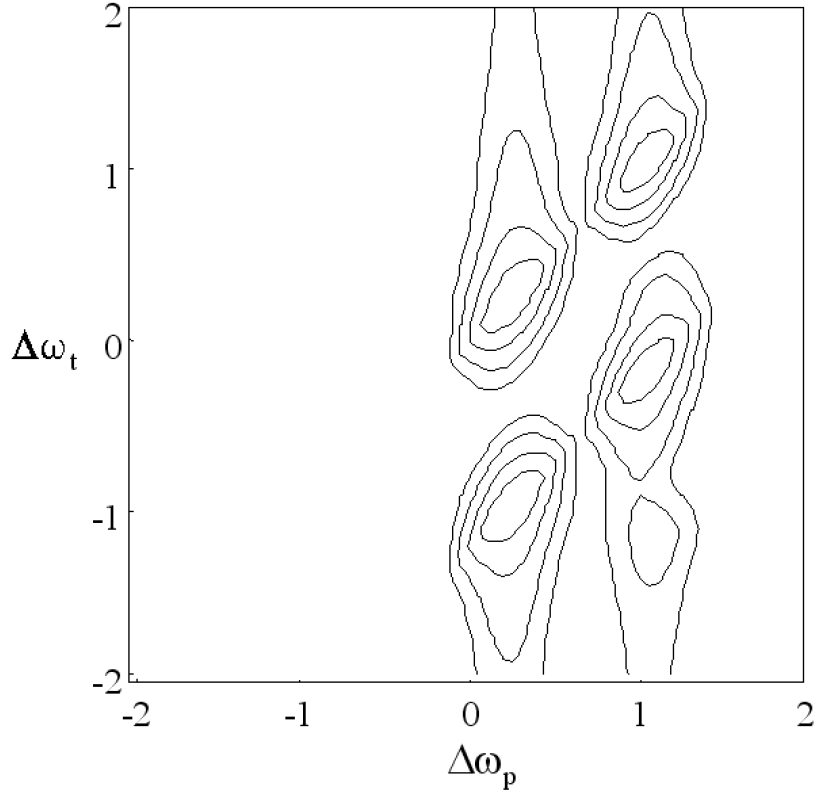


Figure 5.4: T_2 -peaks for the same donor-acceptor pair as in Fig. 5.3 but with $\omega_{da} = -\Delta$. Other parameters see Figs. 5.3 and 5.2.

5.3 Spectral diffusion

The inhomogeneous broadening discussed in the pervious sections represents the static disorder limit for a dynamics of the reservoir being infinitely slow compared to the relaxation processes for the relevant system. This dynamics includes not only the reorganization of the surrounding

5.3. Spectral diffusion

in response of a change of state of the relevant system, but also stochastic fluctuations of the reservoir itself. According to the dissipation-fluctuation theorem these fluctuations can not be avoided (cf. ref. [Mukamel, 1995]). One result of such stochastic fluctuations will be spectral diffusion. Note that even at $T \rightarrow 0\text{K}$ there will exist some fluctuations due to the quantum-mechanical zero-point motion of the reservoir modes.

In the present section the spectral diffusion will be modelled by excitation energy transfer between two-level systems representing a continuum of normal distributed transition frequencies. The rate for a change of the transition frequency from a value ω to a value ω' is given by $\gamma_{sd}(\omega', \omega)$. For the calculation one solves the discrete energy transfer problem for a high number N of two-level systems (for multi-level systems see below) connected by a energy transfer matrix γ_{sd} (cf. section 4.1.2). Then one applies the continuous limit

$$\sum_{\nu=1}^N \dots \rightarrow \int \dots n(\omega) d\omega \quad (5.13)$$

as in section 5.1. For frequency-independent spectral diffusion rates, i.e. $\gamma_{sd}(\omega', \omega) d\omega' = \gamma_{sd}$, one obtains the T_2 -peaks from the part of the NLPF-line-shape function terms which is given by

$$s_{sd}(\omega_t, \omega_p) = \frac{1}{\gamma_{\mu'\mu} + \gamma_{sd}} \left(\tilde{\zeta}_{\mu\mu'}(\omega_t, \omega_p, \omega_p) + \tilde{\zeta}_{\mu\mu'}(\omega_t) \frac{\gamma_{sd}}{\gamma_{\mu'\mu}} \tilde{\sigma}_{\mu\mu'}(\omega_p, \omega_p) \right) + \dots \quad (5.14)$$

for probing and pumping functions as defined in Eqs. 5.6-5.8. Here $\gamma_{\mu'\mu}$ represents the inverse lifetime of the excitation assumed to be independent of the current transition frequency. Before one applies this approach to the case of independent molecules with fluctuating transition frequency some considerations are to be made. In the present model the time-correlation function for the fluctuating transition frequency is given by

$$\langle \omega_{\mu\mu'}(t), \omega_{\mu\mu'}(0) \rangle = \langle \omega_{\mu\mu'} \rangle^2 + \Delta_{\mu\mu'}^2 \exp[-\gamma_{sd}t]. \quad (5.15)$$

This correlation function has to be compared with the correlation function of the reservoir in the harmonic oscillator model (cf. section 3.2 and ref. [Mukamel, 1995]). For a Debye spectral density in the high temperature limit one can identify

$$\Delta_{\mu\mu'}^2 = \frac{S_{\mu\mu'} kT}{\hbar} \quad \text{and} \quad \gamma_{sd} = \omega_D. \quad (5.16)$$

This is in full accordance with the result of the cumulant expansion (cf. section 3.5). In the inhomogeneous dephasing limit $\gamma_{sd} \gg \gamma_{\mu'\mu}$ Eq. 5.14 factorize in the probe-frequency dependence as given by 3.63 and the corresponding cross-section representing a Voigt profile. In the opposite limit $\gamma_{\mu'\mu} \gg \gamma_{sd}$ one obtains static inhomogeneous broadening for

$$s_{inh}(\omega_t, \omega_p) = \tilde{\zeta}_{\mu\mu'}(\omega_t, \omega_p, \omega_p) \gamma_{\mu'\mu}^{-1} \quad (5.17)$$

(cf. Eqs. 5.1 and 5.8). The intermediate case $\gamma_{\mu'\mu} = \gamma_{sd}$ is shown in Fig. 5.5, where pump- and probe-frequency dependences of the T_2 -peak are still correlated but weaker than in the case without spectral diffusion (cf. Fig. 5.1).

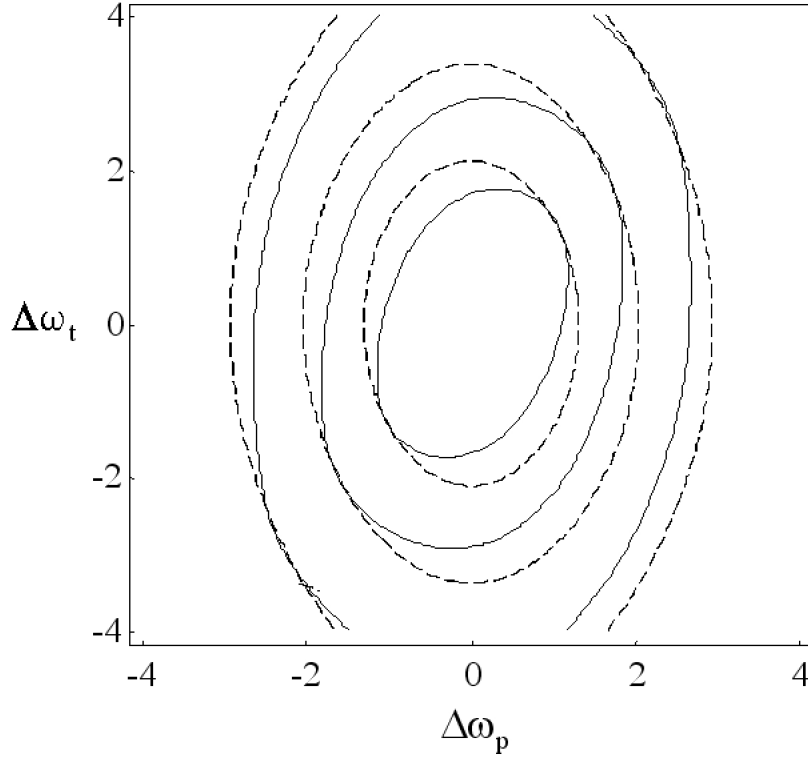


Figure 5.5: T_2 -peak for spectral diffusion: Contours for $\gamma_{sd} = \gamma_{\mu'\mu}$ (solid) and $\gamma_{sd} \gg \gamma_{\mu'\mu}$ (dashed). For the case $\gamma_{sd} \ll \gamma_{\mu'\mu}$ see Fig. 5.1. All other parameters and axes as in Fig. 5.1.

In all three limits the T_1 -peaks are approximately the same as for the two-level system, i.e. they represent almost Lorentzians centered at $\omega_p = \omega_t$ with line width $2\gamma_{\mu'\mu}$. Only in the intermediate cases between the three limits slight deviations from the Lorentzian line shape may occur in the wings of the T_1 -peak. Note, however, that the approach described here is only approximately valid. For a more precise description the cumulant expansion may be the better, but even more complicated method (cf. Eq. 3.78).

For an inhomogeneously broadened multilevel-system the NLPF-line-shape function is given

5.4. Orientational relaxation

as

$$\begin{aligned}
s_{sd}(\omega_t, \omega_p) &= \frac{1}{15} \sum_{\mu\nu} \left\{ \beta_{\mu\nu, \mu\nu}^{(s)}(0) \tilde{\zeta}_{\mu\nu}(\omega_t, \omega_p, \omega_p) + \beta_{\mu\nu, \mu\nu}^{(s)}(\omega_t - \omega_p) \tilde{\xi}_{\mu\nu}(\omega_t, \omega_t, \omega_p) \right\} \\
&+ \frac{1}{15} \sum_{\mu\nu} \tilde{\zeta}_{\mu\nu}(\omega_t) \left\{ \beta_{\mu\nu, \mu\nu}^{(s)}(0) \tilde{\sigma}_{\mu\nu}(\omega_p, \omega_p) + \beta_{\mu\nu, \mu\nu}^{(s)}(\omega_t - \omega_p) \tilde{\sigma}_{\mu\nu}(\omega_t, \omega_p) \right\} \\
&+ \frac{1}{15} \sum_{\mu\nu, \kappa\lambda} \tilde{\zeta}_{\mu\nu}(\omega_t) \left\{ \beta_{\mu\nu, \kappa\lambda}^{(s)}(0) \tilde{\sigma}_{\kappa\lambda}(\omega_p, \omega_p) + \beta_{\mu\nu, \kappa\lambda}^{(s)}(\omega_t - \omega_p) \tilde{\sigma}_{\kappa\lambda}(\omega_t, \omega_p) \right\}. \quad (5.18)
\end{aligned}$$

The probing and pumping functions are given as in Eqs. 5.6-5.8. The correlation function matrix $\beta^{(s)}(\omega)$ is obtained from $\beta(\omega)$ by substituting $\gamma_{\mu\mu} \rightarrow \gamma_{\mu\mu} + \gamma_{sd}$. Note that this substitution affects only the T_2 -peaks on the diagonal of the two-dimensional NLPF-spectrum, i.e. those centered at $\omega_t = \omega_p = \omega_{\mu\nu}$. In the limit $\gamma_{sd} \rightarrow 0$ Eq. 5.18 is transferred to Eq. 5.5 for the static inhomogeneous broadening (cf. Fig. 5.1). The opposite limit $\gamma_{sd} \gg \gamma_{\mu\mu}$ results in $\beta^{(s)}(\omega) \rightarrow \mathbf{0}$. Consequently, the T_2 -peaks are correlated to each other by the discrete spectral structure (cf. chapter 4) but not in respect of their own pump- and probe-frequency dependence. Hence, their line shapes are axially symmetric (cf. Fig. 5.5 dashed lines). The intermediate cases for finite ratios $\gamma_s : \gamma_{\mu\mu}$ result in T_2 -peaks on the diagonal much the same as obtained for the two-level system (cf. Fig. 5.5).

5.4 Orientational relaxation

The orientational relaxation of the NLPF signal results from a stochastic motion changing the orientation of the molecular transition dipole. The turning the transition dipole $\mu_{\mu\nu}$ about an angle Φ in the period of time between pumping and probing affects a correlation between pump and probe-frequency dependence of the T_2 - and T_1 -peaks according to the now dynamic geometry factors $\mathbf{g}(\Phi)$ and $\mathbf{g}'(\Phi)$, respectively (cf. Eq. 4.10 and 4.11). For low-pump intensities the time dependent geometry factors given by

$$g_{\mu\nu\kappa\lambda}^{(r)}(t) = g_{\mu\nu\kappa\lambda}^{(r)}(0) \exp[-\gamma_{\Phi} t], \quad (5.19)$$

with γ_{Φ} as the rate of changing the dipole orientation [Hackbarth and Röder, 2000]. This means that the NLPF-signal decays not only by energy relaxation with a rate γ_{μ} but also by orientational relaxation with the rate γ_{Φ} . This approach is valid for Note that this orientational diffusion process will finally erase the anisotropy created initially by the pump field, which means a lower limit for energy relaxation rates γ_{μ} , which can be determined by NLPF.

Like the spectral diffusion, the orientational relaxation can be modeled by an excitation energy transfer among multi-level systems with different but equally distributed orientations of

the transition dipole. For the two-level system with wobbling transition dipole moment one obtains the NLPF-line-shape function as

$$s(\omega_t, \omega_p) = \frac{2}{15} \zeta_{10}(\omega_t) \left(\frac{\sigma_{10}(\omega_p, \omega_p)}{\gamma_{01} + \gamma_{\Phi}} + \frac{\sigma_{10}(\omega_p, \omega_t)}{\gamma_{01} + \gamma_{\Phi} + i(\omega_t - \omega_p)} \right) \quad (5.20)$$

The unedifying consequence of the orientational relaxation that energy relaxation rates $\gamma_{\mu\nu}$ much smaller than the orientational relaxation rate γ_{Φ} can not be detected by NLPF is clearly to see for the denominators contain γ_{Φ} . One way to circumvent this limitation is to dilute the dye molecules of interest in a highly viscous solvent or to immobilize them in a solid matrix like a glass². On the other hand this reduces the use of NLPF e.g. for studying solvation dynamics.

5.5 Summary

Even though it is the oldest field of application of NLPF [Song et al., 1978, Marcano O et al., 1990, Neef and Mory, 1991] in the work presented the analysis of the homogeneous and inhomogeneous broadening by NLPF could be significantly improved. Particularly, the previously neglected correlation between probe- and pump-frequency dependence for the T₂-peak has been elaborated as an important criterion for detecting and quantifying inhomogeneous broadening. This method is superior to all kinds of line-shape analysis of absorption bands. In particular it allows distinction between static inhomogeneous broadening and inhomogeneous dephasing. The spectral-diffusion, which interpolates between both has been described in a model much simpler than the cumulant expansion, but not much less accurate. Both approaches, provide identical results in the inhomogeneous dephasing limit as well as for the static inhomogeneous broadening. For the intermediate case of spectral diffusion the results of the approach to spectral diffusion demonstrated in section 5.3 may be more questionable, but in this region even the cumulant expansion shows up a lot of difficulties (cf. Eq. 3.78). At least the spectral diffusion approach interpolates quite well between inhomogeneous broadening and inhomogeneous dephasing limit. For the transition from inhomogeneous dephasing to homogeneous broadening the cumulant expansion provides certainly the more accurate line shapes (cf. Fig. 3.3).

In Fig. 5.6 a schematic overview of the different kinds of broadening is displayed. The methods to calculate the corresponding NLPF for the two-level system spectra in the high temperature limit ($kT \gg \hbar\omega_D$, cf. Eq. 3.54) most suitable are for

- (I) homogeneous broadening the Eqs. 2.41 and 3.61 (cf. Fig. 2.3);
- (II) inhomogeneous dephasing the Eqs. 3.17 and 3.63 with $\sigma_{10}(\omega, \omega') = \zeta_{01}(\omega) + \zeta_{10}^*(-\omega')$;

²In this case one has to avoid any birefringence induced by the matrix.

5.5. Summary

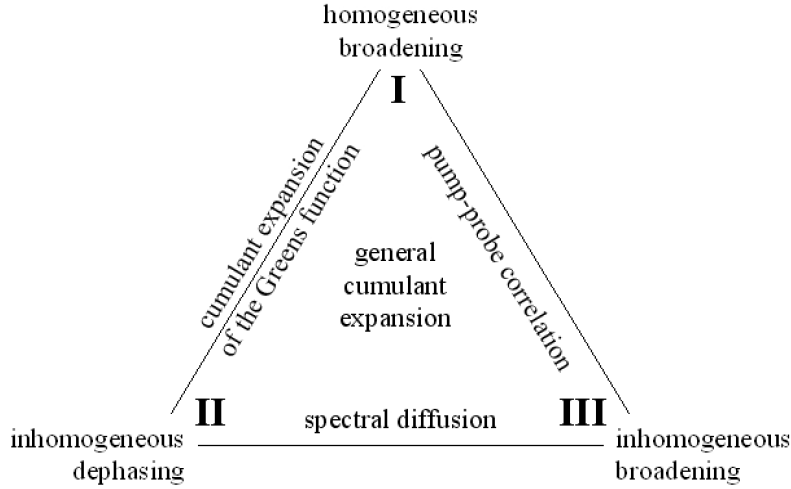


Figure 5.6: Scheme for different kinds of broadening at high temperatures ($kT \gg \hbar\omega_D$, cf. Eq. 3.54). For explanation see text

(III) inhomogeneous broadening Eqs. 5.1 for $s(\omega_t, \omega_p) \approx \delta(\omega_t - \omega_p)$.

and between the limits

(I) and (II) the cumulant expansion of the Greens function as described in supplement 3.5.1;

(I) and (III) the partially correlated pump- and probe-frequency dependences as given by Eqs. 5.5-5.8

(II) and (III) the spectral diffusion according to Eqs. 5.18 and 5.6-5.8.

For the most general case of broadening the cumulant expansion is to be apply as given by Eqs. 3.78 and 3.79.

The global fitting program developed by J. Ehlert and the author of the work be presented [Ehlert and Beenken, 1998] includes beside the analysis of the discrete substructure (cf. chapter 4) the possibility to analyze the T_2 -peaks of a multi-level system in respect of homogeneous and inhomogeneous broadening (I \leftrightarrow III), as well as spectral diffusion (I \leftrightarrow III). The cumulant expansion of the Greens function covering the whole region between homogeneous and inhomogeneous dephasing (I \leftrightarrow II) will be included in a future revision of the program. Thus, the theory of low-intensity NLPF is almost accomplished also in respect of the different kinds of broadening. In the present work this will pay off in particular for the analysis of the spectroscopic properties of the bacterial photosynthetic antennae LH2 (see chapter 8).

Of more general interest is the model for orientational relaxation, which has been established in this chapter. It is quite similar to that for spectral diffusion and has proven the already presumed fact that the orientational relaxation rate γ_Φ (cf. Eq. 5.19) represents a lower bound

Chapter 5. Inhomogeneously broadened NLPF-spectra

for the determination of energy relaxation rates by using NLPF. Another limitation causes from the incoherence between pump and probe laser. The latter, however, can be almost avoided technically, without changing the surroundings of the molecular system to be studied.

Chapter 6

Strong field theory of NLPF

In the previous chapters 3-5 probe as well as pump intensities were assumed to be as low as necessary for the use of perturbation theory of lowest orders, namely first order in the probe field and second order in the pump field. In what follows, this limitation in respect of the pump intensity will be dropped. Therefore, saturation of the NLPF-signal will occur for the pumping rate exceeding the ground state recovering rate. A similar effect is used in nonlinear absorption (NLA). However the saturation of the NLPF-signal is more sophisticated due to the fact that the NLPF-spectrum contains at least two different spectral features the T_1 - and the T_2 -peaks, which may be affected by the saturation differently. Secondly, NLA measures the change of the transmission independent of the polarization, while NLPF based on a pump induced anisotropy. The saturation behavior of these two quantities is quite different as will be seen in what follows. Interesting for pump-intensity-dependent NLPF one obtains a much more clearly defined saturation intensity as from NLA. Since the saturation intensity depends on the absolute cross-section of ground- and excited-state absorption as well as stimulated emission, pump-intensity-dependent NLPF like NLA may provide useful information about the oscillator strength of a transition, without knowing the concentration of dye molecules. A precise determination of the oscillator strength of a single transition can be used for example to determine the exciton delocalization in supra-molecular aggregates by superradiant enhancement of the transition dipole moment [Spano and Mukamel, 1989]. In chapters 8 and 9 the application of pump-intensity-dependent NLPF to photosynthetic antennae for this purpose will be presented.

6.1 General description of the NLPF-signal at high pump intensities

In chapter 2 it has been stated, that in principle for high pump intensities the system of equations for Fourier components of the statistical operator $\rho^{(n_p, n_t)}$ (see Eq. 2.23 and 2.32) can be solved in a self-consistent way. This shall be demonstrated in what follows explicitly. Thereby, the probe field will be still assumed to be weak. For sake of simplicity as in chapter 4 the dephasing is supposed to be faster than the energy relaxation, i.e. $\Gamma_{\mu\nu} \gg \frac{1}{2} |\gamma_{\mu\mu} + \gamma_{\nu\nu}|$. This means tunneling terms need not be considered in general, even the two-photon peak (cf. section 2.3.3). Hence, one has only to construct the self-consistent equation for the Fourier components $\rho_{\mu\mu}^{(0,0)}$ and $\rho_{\mu\mu}^{(-1,1)}$. As mentioned in section 2.3.2, the latter has to be recurred to the former, since only for the state-occupations which $\rho_{\mu\mu}^{(0,0)}$ represents (cf. section 3.12) one obtains a break-off point of the recursion.

Despite of the possibility that the reorganization of the reservoir (cf. section 3.1.3) may be different under high and low pump-intensity conditions, in what follows it will be assumed that all relevant quantities as there are transition frequencies and dipoles, as well as, dephasing and energy relaxation rates are the same as for low-intensities. Furthermore, Markovian reservoir-dynamics will be supposed in what follows, what implies absence of inhomogeneous broadening. Here may be also referred to effects like thermal grating and lensing, photochemical hole-burning, etc. which can influence the NLPF-signal at high pump intensities as well. All these effects shall be not considered in what follows. Only a Stokes shift between absorption and stimulated emission may be admitted.

6.1.1 Self-consistent equation for occupation

From the recursion formula for the occupations $\rho_{\nu\nu}^{(0,0)}$ (cf. Eq. 2.23) one can directly deduce the self-consistent system of equations

$$\sum_{\nu} (\gamma_{\mu\nu} + \sigma_{\mu\nu}(\omega_p, \omega_p) I_p \cos^2 \phi_{\mu\nu} \sin^2 \theta_{\mu\nu}) (\rho_{\nu\nu}^{(0,0)} - \rho_{\nu\nu}^{eq}) = 0, \quad (6.1)$$

which under the conditions mentioned above is valid for arbitrary pump intensities I_p . Terms containing Fourier components $\rho_{\mu\mu}^{(n,0)}$ with $n \neq 0$ could be neglected in Eq. 6.1 for $|\gamma_{\mu\mu} \pm i n \omega_p| \gg \gamma_{\mu\mu} \implies |\rho_{\mu\mu}^{(n,0)}| \ll \rho_{\mu\mu}^{(0,0)}$ and for weakness of the probe field $\rho_{\nu\nu}^{(0,0)}$ can not be traced back to Fourier components $\rho_{\mu\mu}^{(-n,n)}$ with $n \neq 0$, as well (cf. section 2.3.1). The energy relaxation matrix γ is defined as usual with diagonal elements $\gamma_{\mu\mu}$ given by Eq. 3.42. Analogously, for the cross-sections of pumping the diagonal elements $\sigma_{\mu\mu}(\omega_p, \omega_p)$ have been defined as in Eq. 4.4.

6.1. General description of the NLPF-signal at high pump intensities

Note that $\sigma_{\mu\nu}(\omega_p, \omega_p)$ may represent the cross-sections of pumping ground- and excited-state absorption ($\omega_{\mu\nu} > 0$) as well as stimulated emission ($\omega_{\mu\nu} < 0$). Due to the definitions of the diagonal elements the combined matrix $\gamma + \sigma(\omega_p, \omega_p)I_p$ is singular. As described in chapter 4 this problem can be overcome by including the constriction

$$\sum_{\nu} \rho_{\nu\nu}^{(0,0)} = 1 \quad (6.2)$$

into the system of equations given by Eq. 6.1.

For the Fourier components $\rho_{\nu\nu}^{(-1,1)}$, which describe the T_1 -peak (cf. section 2.3.2), from Eq. 2.32 one obtains the system of equations

$$\begin{aligned} \sum_{\nu} (i(\omega_p - \omega_t) \delta_{\mu\nu} + \gamma_{\mu\nu} + \{\sigma_{\mu\nu}(\omega_p, \omega_p) + \sigma_{\mu\nu}(\omega_t, 2\omega_p - \omega_t)\} I_p \sin^2 \theta_{\mu\nu} \cos^2 \phi_{\mu\nu}) \rho_{\nu\nu}^{(-1,1)} = \\ - \sum_{\nu} \sigma_{\mu\nu}(\omega_t, \omega_p) I_p \frac{E_t}{E_p} \sin^2 \theta_{\mu\nu} \cos 2\phi_{\mu\nu} \rho_{\nu\nu}^{(0,0)}. \end{aligned} \quad (6.3)$$

Terms containing $\rho_{\mu\mu}^{n,1}$ for $n \neq -1$ as well as tunneling terms corresponding to $\rho_{\mu\nu}^{(-1,1)}$ or $\rho_{\mu\nu}^{(1,1)}$ have been neglected with reasons mentioned above for $\rho_{\mu\mu}^{0,0}$. As one can see of the equality the matrix elements $\rho_{\nu\nu}^{(-1,1)}$ are traced back to the Fourier components $\rho_{\nu\nu}^{(0,0)}$ at the right side, which are already self-consistent solutions by their own for Eq. 6.1 being independent of $\rho_{\mu\mu}^{-1,1}$.

Using the self-consistent solutions of both systems of equations, Eqs.6.1 and 6.3, the pump-intensity-dependent NLPF-line-shape function yields as

$$\begin{aligned} S(\omega_t, \omega_p, I_p) \approx \frac{1}{4\pi} \int_0^\pi \sin \theta d\theta \int_0^{2\pi} d\phi \sum_{\mu\nu\kappa} \zeta_{\mu\nu}(\omega_t) \sin^2 \theta_{\mu\nu} \\ ((\rho_{\mu\mu}^{(0,0)} - \rho_{\nu\nu}^{(0,0)}) \cos 2\phi_{\mu\nu} + (\rho_{\mu\mu}^{(-1,1)} - \rho_{\nu\nu}^{(-1,1)}) \cos^2 \phi_{\mu\nu}). \end{aligned} \quad (6.4)$$

Then the pump-intensity-dependent NLPF-signal is given by $|S(\omega_t, \omega_p, I_p)|^2$. The outstanding integration over the angles θ and ϕ (cf. section 2.4) is rather complicated, not to say impossible, due to the fact that the solutions of Eqs. 6.1 and 6.3 $\rho_{\mu\mu}^{(0,0)}$ and $\rho_{\mu\mu}^{(-1,1)}$, respectively, depend on the angles $\theta_{\mu\nu}$ and $\phi_{\mu\nu}$ in a non-trivial way.

6.1.2 Two-level system

Fortunately, for the two-level system after determination of the self-consistent solutions $\rho_{11}^{(0,0)}$ and $\rho_{11}^{(-1,1)}$ from Eqs. 6.1 and 6.3 the integration over the two Euler angles θ and ϕ in Eq. 6.4 can be done analytically, and one obtains

$$\begin{aligned} S(\omega_t, \omega_p, I_p) \approx \zeta(\omega_t) F[\xi(\omega_p, \omega_p) I_p] \\ + \zeta(\omega_t) \frac{F[\xi'(\omega_t, \omega_p) I_p] - F[\xi(\omega_p, \omega_p) I_p]}{\xi'(\omega_t, \omega_p) - \xi(\omega_p, \omega_p)} \xi(\omega_t, \omega_p) \end{aligned} \quad (6.5)$$

for the saturation function

$$F[x] = \left(1 + \frac{3}{x}\right) \frac{\arctan[\sqrt{x}]}{\sqrt{x}} - \frac{3}{x} \quad (6.6)$$

as shown in Fig. 6.1.

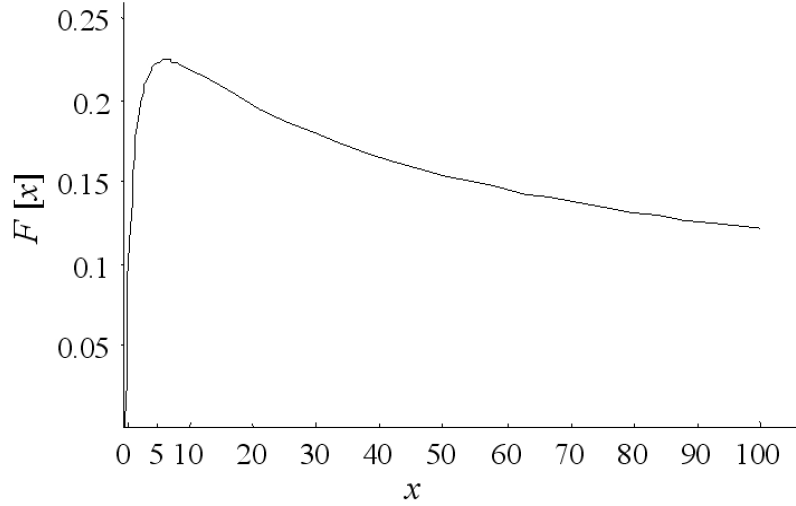


Figure 6.1: Saturation function $F[x]$ according to Eq. 6.6.

In Eq. 6.5 two different dimensionless arguments of $F[x]$ occur, which consists of the pump intensity I_p times one of the saturation parameters

$$\xi(\omega, \omega') = \frac{\sigma_{10}(\omega, \omega') + \sigma_{01}(\omega, \omega')}{\gamma + i(\omega - \omega')} \quad (6.7)$$

$$\xi'(\omega, \omega') = \frac{\sigma_{10}(\omega, 2\omega' - \omega) + \sigma_{01}(\omega, 2\omega' - \omega)}{\gamma + i(\omega - \omega')}. \quad (6.8)$$

From the saturation parameter $\xi(\omega_p, \omega_p)$ the sum of the absolute cross-sections of absorption and stimulated emission can be determined for known energy relaxation rate γ . The latter can be determined by either fluorescence decay or T_1 -peak analysis at low pump intensities (cf. section 2.3.2). Note that $F[\xi(\omega_p, \omega_p)I_p]$ becomes maximum for $\xi(\omega_p, \omega_p)I_p \approx 6.4$. This is caused by the fact that the NLPF-signal results from the difference of bleaching of (and stimulated emission for) transitions with dipoles enclose an angle θ with the pump field in the range $0^\circ < \theta < 45^\circ$ on the one side and those with dipole orientations in the range $45^\circ < \theta < 90^\circ$ on the other side (cf. chapter 2). For increasing pump intensity first the transitions with dipoles more parallel to the pump field will saturate, while the bleaching of the others will increase linearly further on. Therefore, the NLPF-signal will stagnate quite similar to the saturation

6.1. General description of the NLPF-signal at high pump intensities

behavior in NLA. However, for increasing the pump intensity further on also the transitions with dipoles in the range $45^\circ < \theta < 90^\circ$ will be saturated, and the pump-induced anisotropy, NLPF based on will be diminished (cf. also ref. [Hackbarth and Röder, 2000]). From the maximum saturation parameter ξ_{\max} one can define the global saturation intensity, which the whole NLPF-spectrum depends characteristically on (see Fig. 6.2 panel **a-f**), as

$$I_{sat} \approx \frac{6.4}{\xi_{\max}} \approx 1.6 \frac{\hbar \varepsilon_0 n c \Gamma_{10} \gamma_{10}}{\mu_{10}^2 \omega_{10}} \quad (6.9)$$

The second saturation parameter $\xi'(\omega_p, \omega_p)$ is related to the optical Stark effect. According to Eq. 6.3 the matrix element $\rho_{11}^{(-1,1)}$ will get maximum for minima of $|1 + \xi(\omega_t, 2\omega_p - \omega_t) I_p \sin^2 \theta \cos^2 \phi|$. Assuming negligible small energy relaxation and dephasing rates γ and Γ respectively, these are equivalent to resonance poles at probe frequencies

$$\omega_t^\pm = \omega_p \pm \sqrt{(\omega_p - \omega_0)^2 + 4 \frac{|\mu|^2 \sin^2 \theta \cos^2 \phi}{\hbar \varepsilon_0 n c} I_p}. \quad (6.10)$$

as known for optical Stark effect [Zimmermann, 1990]. Note, however, that in NLPF the averaging over the molecular orientations (θ, ϕ) is different from that in absorption. Therefore, also the optical Stark-effect may affect the probed spectrum in absorption differently from that in NLPF in respect of the split.

Fig. 6.2 shows the pump-intensity dependence of the NLPF-spectrum for the two-level system according to $|S(\omega_t, \omega_p; I_p)|^2$ from Eq. 6.5. As expected for low pump intensities (panel **a**) the NLPF-spectrum is the same as deduced in third order perturbation theory (cf. Fig. 2.3). For slightly increased pump-intensity the only recognizable effect is a broadening of the T_2 -peak in respect of its pump-frequency dependence, which results from the fact that due to earlier saturation the center parts of the T_2 -peak increases less than the wings. This effect, called power-broadening, has been previously described in ref. [Marcano O and Garcia-Golding, 1985]. The general rule is: the higher the pump intensity the broader the T_2 -peak in respect of the pump-frequency dependence (panel **b-d**). For moderate pump-intensities $I_p \lesssim I_{sat}$ (panel **b-c**), the corresponding line width of the T_2 -peak (full width at quarter maximum) is approximately given by

$$FWQM_p \approx 2\Gamma \left(1 + \frac{I_p}{I_{sat}} \right). \quad (6.11)$$

Note that according to Eq. 6.9 the additional line width caused by power-broadening is independent of the dephasing rate Γ , but depends on the oscillator strength and the energy relaxation rate. Only for the lowest pump intensity (panel **a**) shown the T_1 -peak appears as a crest set on the broader T_2 -peak along the diagonal $\omega_p = \omega_t$. Already for pump intensities

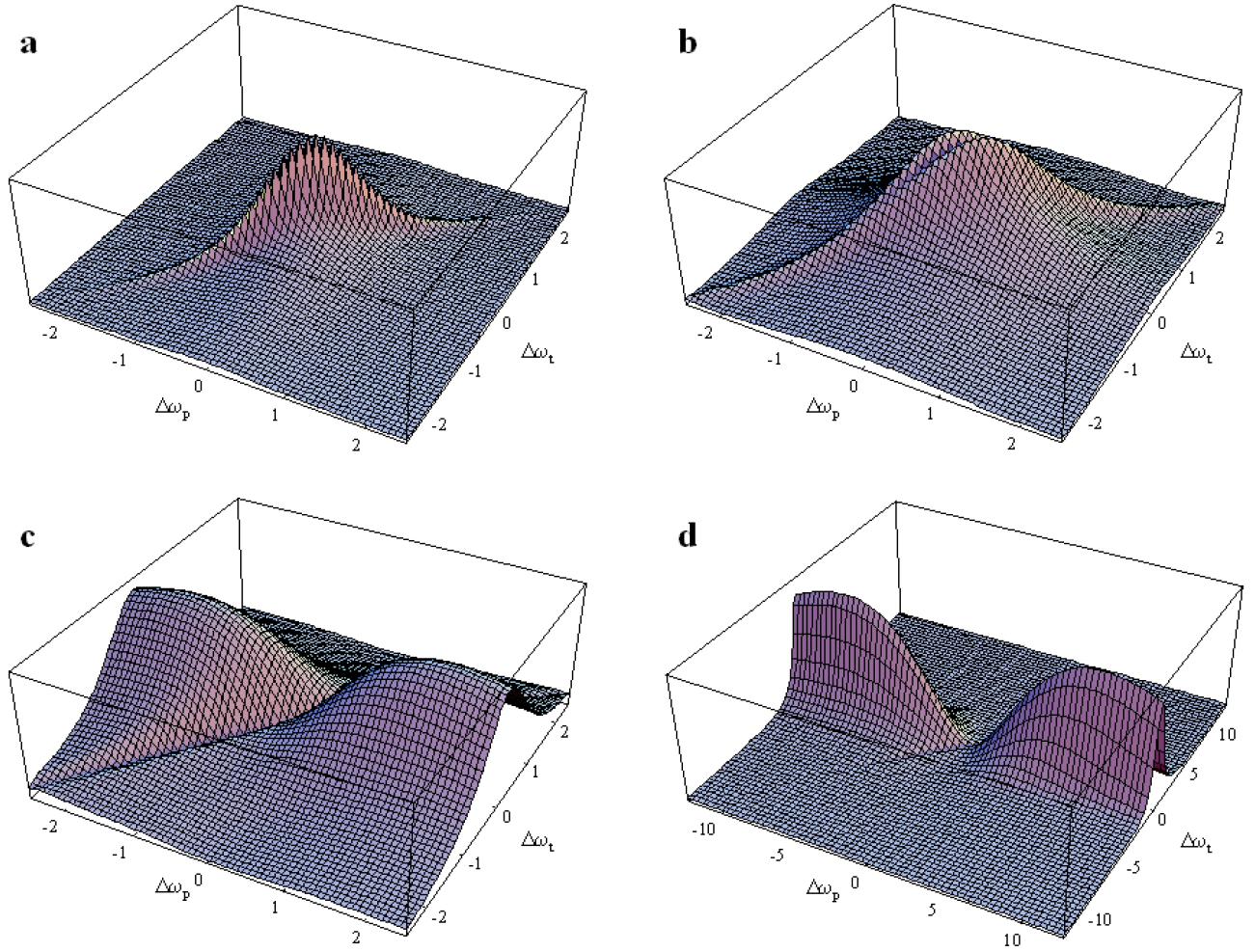


Figure 6.2: NLPF-spectra of a two-level system with $\gamma = 0.1\Gamma$ for pump intensity $I_p = 0.05I_{sat}$ (a), $0.5I_{sat}$ (b), $5I_s$ (c), and $50I_{sat}$ (d). Axes labeled as $\Delta\omega_{p,t} = (\omega_{p,t} - \omega_0) / \Gamma$.

$I_p > 0.23I_{sat}$, that means far below the saturation point, at the top of the T_2 -peak this crest changes to a cleft (panel **b**). It will deepen with increasing pump intensity but does not broaden much (panel **c**). For pump intensities beyond the saturation point ($I_p > I_{sat}$) the T_2 -peak itself get a hollow at $\omega_p = \omega_0$ (panel **c**). This hollow corresponds to the Lamb dip in absorption and results directly from the decrease of the saturation function $F[\xi(\omega_p, \omega_p)I_p]$ (cf. Fig. 6.1 and Eq. 6.5). At highest pump intensities (panel **d**) both effects, Lamb-dip and the T_1 -cleft, result in a notch around $\omega_t, \omega_p = \omega_0$ parting the T_2 -peak into two asymmetric peaks which are quite extended in respect of the pump-frequency dependence (note the changed frequency scale in panel **d**). The probe-frequency dependence of the two peaks is also asymmetric due to a shift of the maxima apart from ω_0 (see Fig. 6.3), but not much more broadened than for

6.2. Multi-level systems at high pump intensities

lower intensities. Note, that even the crest results from the optical Stark effect, the maxima of the NLPF-spectrum at highest pump intensities are not directly related the frequencies ω_t^\pm (cf. Eq. 6.10) due to the complicated orientational averaging.

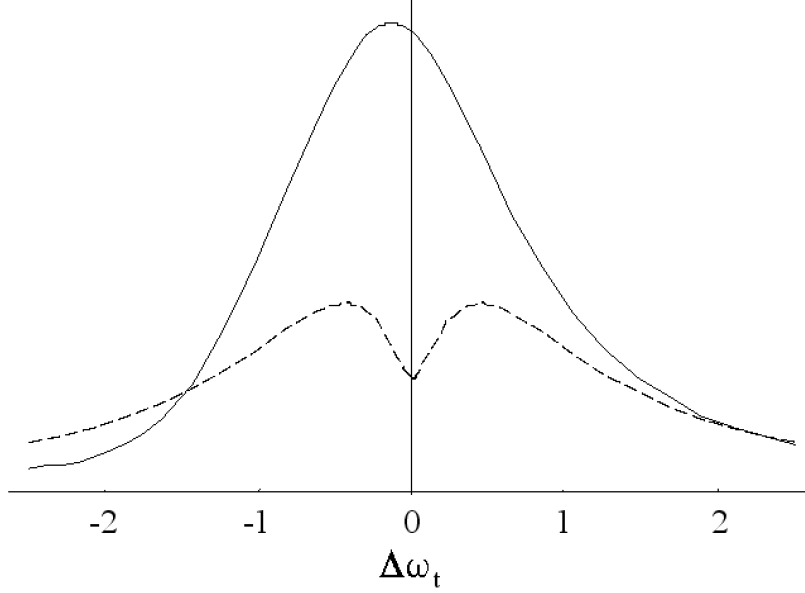


Figure 6.3: Probe dependency of the NLPF-spectrum for $I_p = 50I_s$ at $\omega_p = \omega_0$ (dashed line) and at the maximum $\omega_p \approx 9\omega_0$ (solid line $\times 10$). For other parameters and axes see Fig. 6.2 panel d.

6.2 Multi-level systems at high pump intensities

As mentioned above, for multi-level systems in general the orientational average in Eq. 6.5 can not be performed analytically. However, for some special cases it is possible to reduce the multi-level system problem to the solution for the two-level system as given in Eq. 6.5. Two of these cases, shall be featured in what follows. For sake of simplicity, but without loss of generality, only the saturation of the T_2 -peak will be calculated. The T_1 -peak can be calculated analogously.

6.2.1 Fast intra- and inter-band relaxation

For a multi-level system where the energy relaxation among the excited states is much faster than the ground state recovering and where up-hill transfers can be excluded (i.e. $\gamma_\mu, \gamma_\nu, \gamma_{\nu\mu} \ll$

$\gamma_{\mu\nu}$ for $\omega_{\nu\mu} > 0$ and $\mu, \nu \neq 0$) all excitation will accumulate in the lowest excited state, independently of the state they have been pumped to. Consequently, the cross-section of pumping contains stimulated emission and excited-state absorption only for the lowest excited state, but all possible absorptions from the ground state. Fig. 6.4 shows an exemplary four-level system with the relevant excitation and relaxation channels, except the slow energy relaxations to the ground state. Thereby it shall be distinguished between the manifold of the single excited states (here represented by $|1\rangle$ and $|2\rangle$) and the doubly excited states (here $|3\rangle$). For the energy relaxation within one manifold (band) the intra-band relaxation rate is defined as γ_{intra} , while the energy relaxation between the doubly and singly excited states are given by the inter-band relaxation rate γ_{inter} . In the present case both are assumed to be much higher than the ground-state recovering rate γ_{gsr} . Thus the distinction in intra- and inter-band relaxation seems to be needless. However, in the next section for treating the incoherent excitation transfer the advantage of such a distinction will become obvious.

In the case of the special multi-level systems presented in this section, the intensity-dependent NLPF-line-shape function for the T_2 -peaks is given as

$$S(\omega_t, \omega_p, I_p) \approx \eta(\omega_t, \omega_p) F[\xi(\omega_p, \omega_p) I_p] \quad (6.12)$$

with saturation parameter

$$\xi(\omega_p, \omega_p) = \frac{\sigma_{abs}(\omega_p, \omega_p) + \sigma_{em}(\omega_p, \omega_p) + \sigma_{exc}(\omega_p, \omega_p)}{\gamma_{gsr}} \quad (6.13)$$

and a probe- and pump-frequency dependent prefactor

$$\eta(\omega_t, \omega_p) = \frac{\zeta_{abs}(\omega_t) + \zeta_{em}(\omega_t) - \zeta_{exc}(\omega_t)}{\sigma_{abs}(\omega_p, \omega_p) + \sigma_{em}(\omega_p, \omega_p) + \sigma_{exc}(\omega_p, \omega_p)} \sigma_{abs}(\omega_p, \omega_p). \quad (6.14)$$

The probing functions $\zeta_x(\omega_t)$ are defined in analogy to the cross-sections $\sigma_x(\omega_p, \omega_p)$. The pump-frequency dependence of $\xi(\omega_p, \omega_p)$ represents what the author has named the ξ -spectrum. Multiplied with the ground-state recovering time γ_1^{-1} this provides the absolute cross-section of absorption, emission, and excited state absorption, summarized. For decomposition, one can use the standard absorption, fluorescence and transient spectra. Another possibility is to use the prefactor $\eta(\omega_t, \omega_p)$. This works out, since by its pump frequency-dependences $|\eta(\omega_t, \omega_p)|^2$ does not only relate the saturation parameter $\xi(\omega_p, \omega_p)$ to the absorption spectrum for $\sigma_{abs}(\omega_p, \omega_p) = 3\sigma_{abs}(\omega_p)$, but it enables one also to separate the excited state absorption from the stimulated emission by its different dependence on the probe-frequency. The main disadvantage of this method is that recording and evaluating of a now three-dimensional NLPF-spectrum with variables ω_t , ω_p , and I_p means quite an effort.

6.2. Multi-level systems at high pump intensities

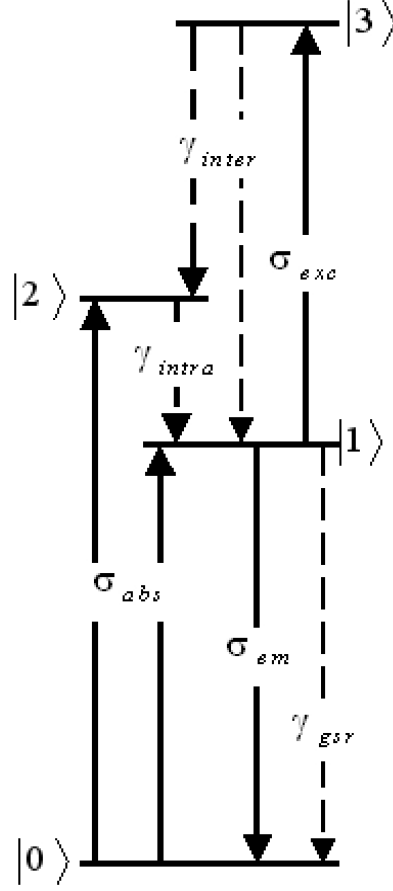


Figure 6.4: Term scheme for the model system containing fast intra- and inter-band relaxation. The excited states $|1\rangle$ and $|2\rangle$ are single excitation band, while the state $|3\rangle$ is doubly excited. The relevant pumping and relaxation rates are shown. Assignments see text.

Even for fast intra-band relaxation the NLPF-signal resulting from the higher excited states can not to be neglected. This is linear in pump intensity even at higher intensities. There it can exceed the NLPF-signal caused by the already saturated transition to the lowest excited state. In order to take this into account, the pump-intensity-dependent NLPF-line-shape function $S(\omega_t, \omega_p, I_p)$ in Eqs. 6.12 has to be extended by adding the term $s_{lc}(\omega_t, \omega_p)I_p$. For the exemplary system shown in Fig. 6.4 this term yields as

$$s_{lc}(\omega_t, \omega_p)I_p = \{\zeta_{abs}(\omega_t) + \zeta_{02}(\omega_t) - \zeta_{32}(\omega_t)\} \frac{\sigma_{20}(\omega_p, \omega_p)}{\gamma_{intra}} I_p. \quad (6.15)$$

This linear continuation of the pump-intensity dependence of the NLPF-signal occurs only for probing the whole absorption spectrum, but not for probing only the emission from the saturated, lowest excited state, which spectrum is almost identical with the fluorescence spectrum

of the whole system. Instead of this the emission of the higher excited states can be probed (cf. $\zeta_{02}(\omega_t)$ in Eq. 6.15), which otherwise is quenched for the fast energy transfer. Similar effects applies to probing the excited state absorption.

6.2.2 Fast energy transfer and excitation annihilation

For a pair of two-level systems acting as donor and acceptor of a fast incoherent energy transfer, the homogeneous model can not be applied directly. However, the status of occupation in a donor-acceptor pair can be mapped to the four-level system shown in Fig. 6.4 as follows:

$$\begin{aligned} \text{Neither donor nor acceptor are excited} &\rightarrow |0\rangle. \\ \text{Only the acceptor is excited} &\rightarrow |1\rangle. \\ \text{Only the donor is excited} &\rightarrow |2\rangle. \\ \text{Both, donor and acceptor are excited} &\rightarrow |3\rangle. \end{aligned}$$

Next the cross-sections and the energy relaxation rates in Fig. 6.4 are to redefine according to this mapping: For the absorption to the single excited band one obtains $\sigma_{abs}(\omega_p, \omega_p) := \sigma_A(\omega_p, \omega_p) + \sigma_D(\omega_p, \omega_p)$, where $\sigma_A(\omega_p, \omega_p)$ and $\sigma_D(\omega_p, \omega_p)$ represent the cross-section of pumping the absorption of acceptor and donor respectively, while $\sigma_{em}(\omega_p, \omega_p)$ stand for the stimulated emission of the acceptor $\sigma_{A'}(\omega_p, \omega_p)$. The excited state absorption means now excitation of the donor when the acceptor is already excited. Therefore one set $\sigma_{exc}(\omega_p, \omega_p) := \sigma_D(\omega_p, \omega_p)$. The energy transfer from donor to acceptor is represented by the intra-band relaxation rate as $\gamma_{intra} := \gamma_{AD}$, while the energy relaxation to the ground state is given by γ_A , for $\gamma_{AD} \gg \gamma_D$. The relaxation of the doubly excited state represented by γ_{inter} , however, a similar relation does not exist for the donor and acceptor being two-level systems. The reason is that according to the mapping the inter-band relaxation represents either that of the donor γ_D or that of the acceptor γ_A . Both channels can be summed up, since in the case the acceptor relaxes first, the donor will immediately transfer its energy to the acceptor for $\gamma_{AD} \gg \gamma_D, \gamma_A$. Consequently, one obtains $\gamma_{inter} = \gamma_A + \gamma_D$. This means the inter-band relaxation is slow compared to the intra-band relaxation, and approximately of the same speed as the ground-state recovering. Therefore, accumulation of excitation may not only occur in the state $|1\rangle$ but also in the state $|3\rangle$. A system where this can happen is not to solve by the method demonstrated above.

However, for acceptors being multi-level systems, one can get rid of this problem for excitation annihilation. In Fig. 6.5 this process is outlined. Bottom line it is only important, that when the acceptor is already excited, additional excitation from the donor will be annihilated on a time scale comparable to the fast energy transfer. Though excitation annihilation seems to be a rather special case, it is quite often realized e.g. for chlorophylls in photosynthetic antennae (see chapters 8 and 9).

6.2. Multi-level systems at high pump intensities

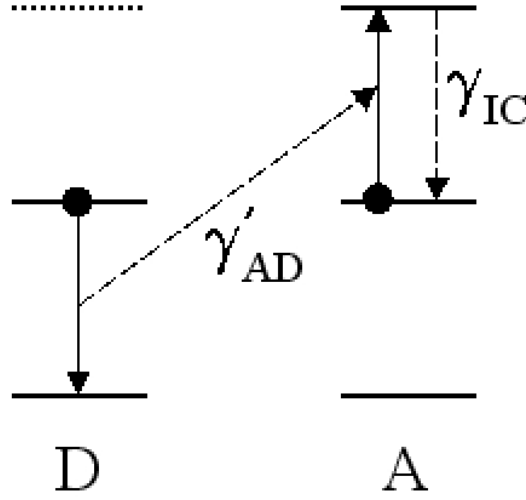


Figure 6.5: Scheme of the annihilation process. Initially both donor (D) and acceptor (A) are in the lower excited state (dots). Then the donor transfers its excitation energy to the acceptor with a rate γ'_{AD} . Thereby the donor returns to its ground state, while the acceptor switches to the higher excited state. From there by internal conversion the excitation will return to the first excited state of the acceptor with the rate γ_{IC} . Thus the acceptor is in the initial state, and the excitation on the donor is annihilated.

By identifying the fast energy transfer and the likewise fast excitation annihilation with the inter- and inter-band relaxation, respectively, one has the donor–acceptor pair exactly mapped to the previously solved homogeneous system. Thus, the pump-intensity-dependent NLPF-line-shape function results from Eq. 6.12 for saturation parameter and prefactor as given by Eqs. 6.13 and 6.14, respectively. Expressed in terms of the cross-sections of pumping absorption and emission of donor and acceptor these yield as

$$\xi(\omega_p, \omega_p) = \frac{\sigma_A(\omega_p, \omega_p) + \sigma_{A'}(\omega_p, \omega_p) + \sigma_D(\omega_p, \omega_p)}{\gamma_A} \quad (6.16)$$

$$\eta(\omega_t, \omega_p) = (\zeta_A(\omega_t) + \zeta_{A'}(\omega_t)) \frac{\sigma_A(\omega_p, \omega_p) + \sigma_D(\omega_p, \omega_p)}{\sigma_A(\omega_p, \omega_p) + \sigma_{A'}(\omega_p, \omega_p) + \sigma_D(\omega_p, \omega_p)}. \quad (6.17)$$

The probe-frequency dependence of $\eta(\omega_t, \omega_p)$ demonstrates that the saturation of the NLPF-signal is only observed for probing the acceptor. This is easily to understand, since excitations will reside on the acceptor due to the slow energy relaxation to the ground state, while on the donor they will be immediately transferred to the acceptor (γ_{AD}) or annihilated (γ'_{AD}). Bleaching of the donor by the acceptor is not possible for $\gamma_{DA} \ll \gamma_{AD}$. For probing the donor at higher intensities, where the acceptor is already saturated, one obtains the linear continuation

(cf. Eq. 6.15) as

$$s_{lc}(\omega_t, \omega_p) I_p = \{\zeta_D(\omega_t) + \zeta_{D'}(\omega_t)\} \frac{\sigma_D(\omega_p, \omega_p)}{\gamma'_{AD}} I_p. \quad (6.18)$$

Note that here the probing functions for bleaching and excited state absorption cancel out due to the mapping $\zeta_{32}(\omega_t) = \zeta_{10}(\omega_t) = \zeta_A(\omega_t)$. Hence, for saturated absorber the donor contributes to the NLPF-signal like other heterogeneous admixtures (cf. section 4.1.1).

For a multitude of donors one just sums up the cross-sections for pumping absorption. For a multitude of acceptors one has to consider the branching ratios (cf. Eq. 4.56 in section 4.3). In the case of two acceptors 1 and 2 with ultrafast but balanced energy transfer between them ($\gamma_{12} \sim \gamma_{21} \gg \gamma_1, \gamma_2$)¹ one obtains the saturation parameter as

$$\xi(\omega_p, \omega_p) = \frac{\sigma_{abs}(\omega_p, \omega_p) + w_1 \sigma_{em1}(\omega_p, \omega_p) + w_2 \sigma_{em2}(\omega_p, \omega_p)}{w_1 \gamma_1 + w_2 \gamma_2} \quad (6.19)$$

where $\sigma_{em1}(\omega_p, \omega_p)$ and $\sigma_{em2}(\omega_p, \omega_p)$ represents the cross-sections of pumping the emission of the respective acceptor 1 and 2, weighted by factors

$$w_1 = \frac{1}{1 + \exp[\omega_{12}/kT]} \quad \text{and} \quad w_2 = \frac{1}{1 + \exp[\omega_{21}/kT]} \quad (6.20)$$

according to the detailed balance (cf. Eq. 3.44). The cross-sections for pumping the absorption $\sigma_{abs}(\omega_p, \omega_p)$ is the sum of those for donors and acceptors in equal measures.

The case where the acceptors are not connected by energy transfer can be solved for pumping either donors or acceptor, i.e. in spectral regions where both do not overlap. In this case one obtains the pump-intensity-dependent NLPF-line-shape function as

$$S_D(\omega_t, \omega_p, I_p) = \sum_A \zeta_A(\omega_t) F[\xi_D(\omega_p, \omega_p) I_p] \quad (6.21)$$

with the saturation parameter given by

$$\xi_D(\omega_p, \omega_p) = \frac{b_{AD} \sigma_D(\omega_p, \omega_p) + \sigma_A(\omega_p, \omega_p) + \sigma_{A'}(\omega_p, \omega_p)}{\gamma_A}. \quad (6.22)$$

The parameters b_{AD} represent the branching ratios for the energy transfer from the pumped donor D to the probed acceptor A . For systems with only one donor but a multitude of acceptors they are given as

$$b_{AD} = \frac{\gamma_{AD}}{\sum_A \gamma_{AD}}. \quad (6.23)$$

For a multitude of donors, one has to construct a model of the energy path and to calculate b_{AD} quite similar as the correlation matrix $\beta(0)$ in chapter 4. For probing and pumping only one acceptor one obtains the same pump-intensity dependence of the NLPF-signal as if the respective

¹ γ_1 and γ_2 are the rates of energy relaxation to the ground state of the respective acceptor 1 and 2.

6.3. Summary

accepter would be an isolated two-level system. Unfortunately, for the pump-frequency range of the branching, where donors and acceptors overlap, a mapping to an equivalent two-level systems as for the other spectral regions is not possible. Therefore, for this spectral region the ξ -spectrum will provide a reliable absolute cross-section of pumping for neither the donors nor the acceptors.

6.3 Summary

In the presented chapter it has been shown that the intensity dependence of the NLPF-signal provides additional information about the spectroscopic properties of a molecule. Namely, it is rather suitable for the determination absolute values of the cross-sections of absorption and emission. These can be in principle also determined by e.g. nonlinear absorption (NLA). However, in special cases the saturation intensity obtained by pump-intensity dependent NLPF is quite better to defined. For the two-level system it corresponds to the pump-intensity at maximum NLPF-signal (cf. Fig. 6.1), while in NLA no maximum appears. For moderate pump intensities T_2 -peak features the already known power broadening [Marcano O and Garcia-Golding, 1985]. At highest pump-intensities an effect analogous to the optical Stark effect splits the T_2 -peak. Whether this effect is usable or more unedifying for complicating the evaluation of a NLPF-spectra remains questionable. The results for the two-level system have been already published by the author in ref. [Beenken and May, 1997].

The pump intensity dependence of the NLPF-signal of a multi-level systems can be also evaluated. However, due to the complicated orientational averaging this is almost limited to special cases. Two have been demonstrated, here for the first time. It has turned out that for a homogeneous substructure with fast energy transfer among the excited states the saturation behavior is much the same as for a two-level system. The resulting ξ -spectrum, which describe the pump-frequency dependence of the saturation for the NLPF-signal (cf. Eqs. 6.6, 6.7 and 6.13), provides the absolute cross-section of absorption and emission for known ground-state recovering time. The main difference to the two-level case is that for pump-intensities beyond the first saturation the NLPF signal continues to rise linearly with the pump-intensity again (linear continuation). The second system where the pump-intensity dependence of the NLPF-spectrum has been studied is a donor–acceptor pair with fast incoherent energy transfer and excitation annihilation . It could be shown that it is also possible to map this case to the two-level system. In this special, but quite often realized case of energy transfer (e.g. in chapters 8 and 9), the ξ -spectrum provides the absolute cross-section of pumping for the summarized absorption and emission spectrum of the pair. Since the linear continuation gives the absorption spectrum of only the donor, a decomposition of the ξ -spectrum into the three cross-sections

for absorption of the donor, absorption of the acceptor, and emission of the acceptor may be achievable without external information. An interesting field for application of the strong-field NLPF is the determination of molecular aggregation. For application of the method to photosynthetic antennae see chapters [8](#) and [9](#).

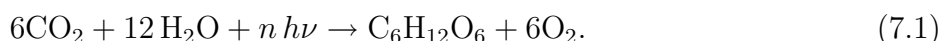
Part II

Application of NLPF to photosynthetic antennae

Chapter 7

Short introduction to photosynthesis

Photosynthesis is one of the most fundamental process for life. Therefore it is of essential interest to understand the processes which enables plants, cyanobacteria, green and purple bacteria, as well as several other bacteria to convert light into chemical energy e.g. for the glucose synthesis in higher plants according to the reaction



for a number of photons $n \sim 100$. This summarized reaction is separated into two major reaction complexes: The primary conversion of light and water into oxygen, protons, and electrons (light reactions). The latter will be bound to electron carriers, either NAD^+ or NADP^+ , which by their reduced forms NADH and NADPH , respectively, act as hydrogenators for the mentioned conversion of carbon dioxide into glucose in the second reaction complexes (Calvin-cycle) and other secondary reactions like nitrogen fixation, isoprene synthesis, etc. – all together often subsumed under the term ‘dark reactions’ [Blankenship, 2001, Alberts et al., 2002, Berg et al., 2002]. In the present context only the light reactions is of interest, where photo-excitations are directly involved. These are very well accessible to direct investigations by means of spectroscopic methods [Amesz and Hoff (eds), 1996].

Except of some archea (e.g. *Halobacterium halobium*), where photosynthesis is based on Bacteriorhodopsin being quite similar to the retinal in the human eye [Alberts et al., 2002], all other known photosynthetic organisms contains either chlorophyll (Chl) or bacteriochlorophyll (Bchl) in different forms. Fig. 7.1 shows the three molecules which are of interest in the following chapters.

chlorophylls are found in the higher plants and in cyanobacteria in mainly two modifications (see Fig.7.1), while bacteriochlorophylls are the constituents of the purple bacterial photosynthetic apparatus. For bacteriochlorophyll in green bacteria see ref. [Scheer, 1991].

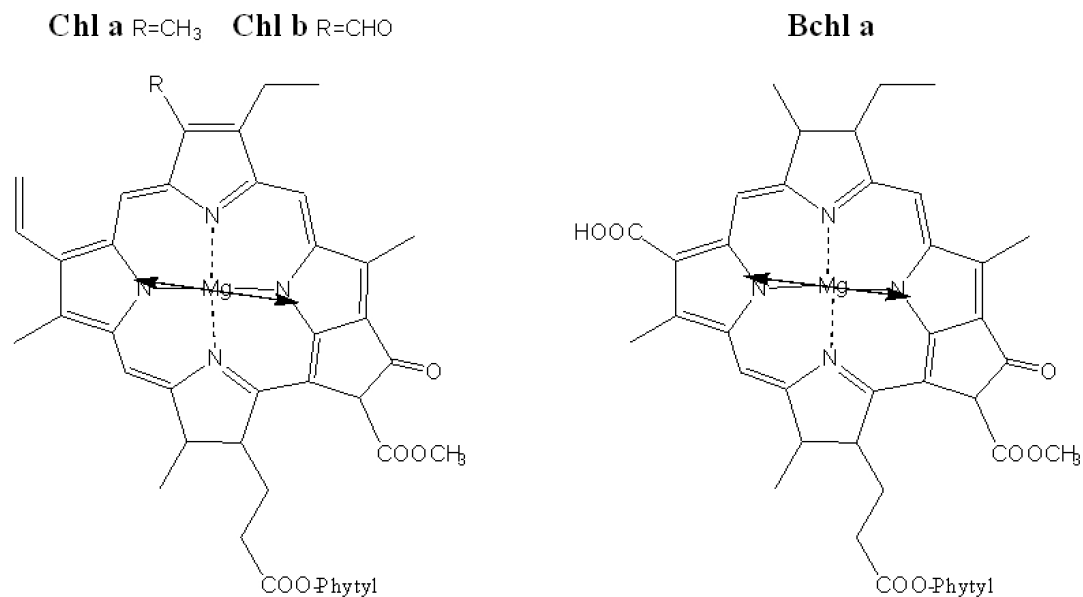


Figure 7.1: Structure formulas of chlorophyll a and b (Chl a, Chl b) as well as of bacteriochlorophyll a (Bchl a) according to [Scheer, 1991]. Shown are the tetrapyrrole rings with attached side groups, but not the full phytyl chain. The approximative orientations of the Q_y -transition dipoles are assigned by the double-arrows [Scherz et al., 1991, Fuchs et al., 2003].

Except of chlorosomes in green photosynthetic bacteria, which are attached to protein-lipid layers [Pearlstein, 1991, Blankenship et al., 1995b] both, Chls and Bchls are regularly embedded in transmembrane proteins forming different complexes. The most important of these complexes is of course the reaction center (RC), where the mentioned conversion of light energy into chemical energy happens. For higher plants these are located specific organelles, the chloroplasts, which contains the multiply folded lipidic thylakoid membrane all Chl-protein complexes are built in. Chloroplasts as well as cyanobacteria possess two photosystems (PS I and PS II) with different RC acting in series (see Fig. 7.2). This is necessary to overcome the electrochemical potential needed to reduce water to oxygen and two protons. The resulting pH gradient, enhanced by additional proton transport via intra-membrane (plasto)quinones as driven by the electron transport from PS II as well as PS I to the Cytochrome b_6f complex, across the thylakoid membrane is used by ATPase to synthesize ATP from ADP, which is the universal energy carrier for all kinds of metabolism. The photo-excited electrons pass the two reaction center and redox chains containing several cytochromes (e.g. cytochrome b_6f complex cf. Fig. 7.2) in order reduce to finally $NADP^+$ to NADPH which is the likewise universal hydrogenator in plants as mentioned above [Blankenship, 2001, Alberts et al., 2002, Berg et al., 2002]. Purple

bacteria possess mainly one type of RC, which are Purple and green bacteria work with H_2S or organic compounds instead of H_2O as electron donor. Therefore, a single type of RC located in the bacterial membrane is sufficient for them [Blankenship et al., 1995a].

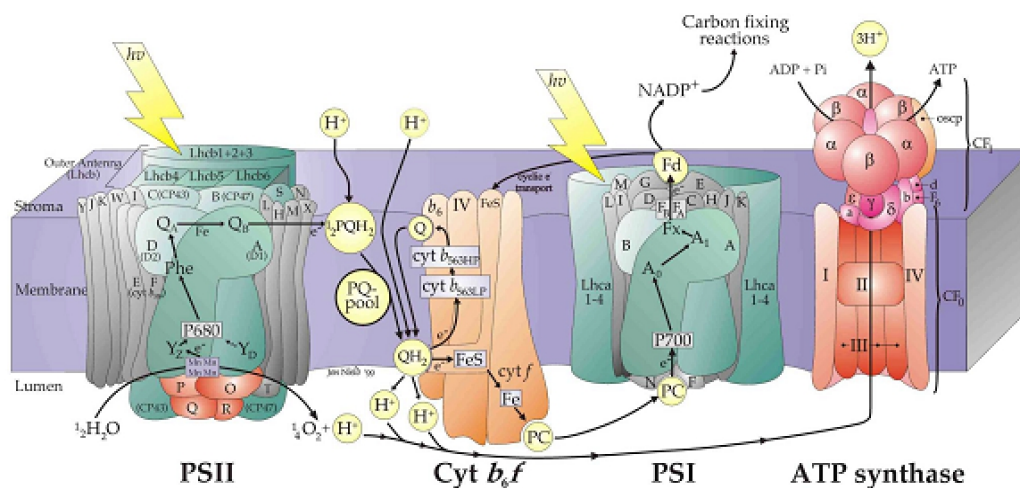


Figure 7.2: Artistic illustration (by Joe Nield, 1999) of the thylakoid membrane with embedded photosystems PS I and PS II, associated antennae complexes, cytochrome- b_6f complex and ATPase. Electron and proton transport paths are indicated. For description see text.

The major fraction of Chls as well as of Bchl, however, is not contained in the respective reaction centers, but in antennae complexes surrounding them. These antennae collect the incident light and funnel it to the reaction centers. Thereby, they do not only extend the geometrical cross-section per reaction center but also the spectral range of light that can be accepted. Antennae complexes has been investigated by a biochemical, crystallographic [Deisenhofer et al., 1984, Kühlbrandt et al., 1994, McDermott et al., 1995, Karrasch et al., 1995, Koepke et al., 1996, Camara-Artigas et al., 2003], and spectroscopic methods, which are numbers [Amesz and Hoff (eds), 1996]. In the following chapters studies will be demonstrated, how NLPF has been applied to the peripheral light harvesting antenna (LH2) of different purple bacteria as well as to two different light harvesting complexes (CP29 and LHC II) of higher plants, in order to reveal the nature of coupling between the constituent Bchls and Chl, respectively. Thereby the T_2 - and T_1 -peak analysis (cf. chapter 4) as well as the pump-intensity-dependent NLPF (cf. chapter 6) will show there potentials quite well.

Chapter 8

The B850-band of the peripheral light harvesting antenna (LH2) of purple bacteria

In photosynthetic active purple bacteria the reaction center (RC), where light energy is converted into chemical energy, is supplied with photo-excitations by two light harvesting antennae, the core antenna LH1 and peripheral antennae LH2. For all three components, RC, LH1, and LH2 exist crystallographic structures. As first of all the X-ray structure of the reaction center has been revealed [Deisenhofer et al., 1984]. This is surrounded by the core light harvesting antenna complex LH1 which consists of some tens of bacteriochlorophyll molecules (Bchl a cf. Fig 7.1) arranged in a wide ring [Karrasch et al., 1995]. The peripheral light harvesting antenna complexes LH2 are also ring-shaped but smaller in diameter than LH1. They adjoin edge to edge to each other and to the LH1 (cf. Fig. 8.1). The highly resolved X-ray structures of the LH2 of *Rhodospseudomonas (Rps.) acidophila* [McDermott et al., 1995] as well as of *Rhodospirillum (Rs.) molischianum* [Koepke et al., 1996] have stimulated both, theoretical calculations and experimental investigations to their structure–function relation [Blankenship et al., 1995a, Sundström et al., 1999, van Amerongen et al., 2000].

8.1 Structure and absorption spectrum of LH2

The LH2 of *Rs. molischianum* contains 24 Bchl a, which are arranged in two rings stacked one on the other (cf. Fig. 8.2). Both ring systems have nearly the same diameter. The one ring, named B800, contains 8 Bchl a (Bchl-B800) with shortest Mg–Mg distances of 22.0Å. Their tetrapyrrole planes are turned out of the ring plane about 38°. The other ring, named B850, contains 16

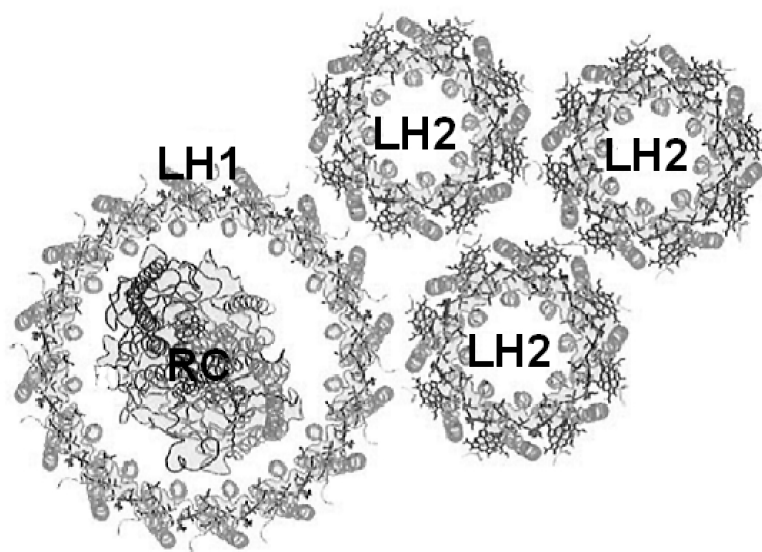


Figure 8.1: Artistic illustration of the photosynthetic reaction center (RC), the core antenna (LH1) and several peripheral antennae (LH2) of the purple bacterium *Rhodospirillum (Rs.) molischianum* [Hu et al., 1997] (based on the X-ray crystal structure [Koepeke et al., 1996]) Shown are pigments and protein backbones.

Bchl a (Bchl-B850) with alternating Mg–Mg distances of 8.9\AA and of 9.2\AA . Consequently the B850 system has the same C_8 -symmetry as the whole aggregate. The tetrapyrrole planes of the Bchl-B850 are nearly perpendicular to the ring plane, forming a densely packed water-wheel like structure. The detailed X-ray structure analysis shows, furthermore, that two neighboring Bchl-B850 are oriented to each other up-side down and their Q_y -transition dipoles are slightly turned to each other and out of the ring-plane. The shortest Mg–Mg distance between Bchl-B800 and Bchl-B850 is 19.1\AA . Additionally LH2 contains eight carotenoids (lycopene), which span both rings (not shown in Fig. 8.2) [Koepeke et al., 1996].

The absorption spectrum of the LH2 of *Rs. molischianum* (see Fig. 8.3) shows two Q_y -absorption bands at 798nm and 847nm, the Q_x -band at 580nm and a broad Soret band between 300 and 400nm attributed to Bchls as well as several subbands between 430 and 530nm of the lycopenes. In the present context its the Q_y -absorption in the near-infrared (NIR) which is of interest. The split of the Q_y -absorption band, which for isolated Bchl a in solution would be located at 773nm [Hoff and Amesz, 1991], into two bands has been related to the two different kinds of Bchl sites.

The band at 798nm has been attributed to the Bchl-B800, by the assumption that they

8.2. Theoretical model for the B850 band

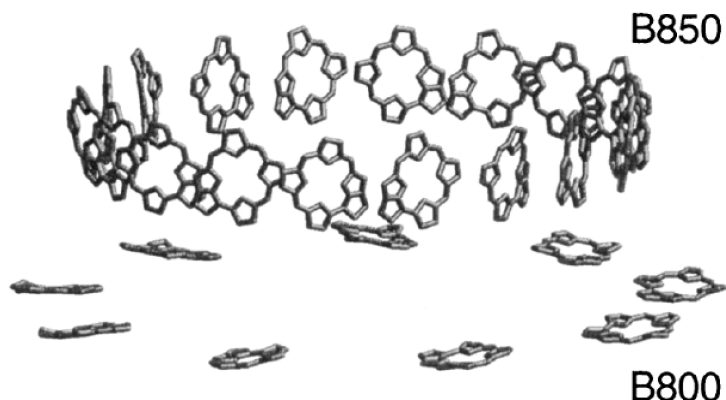


Figure 8.2: Arrangement of the BChls in the peripheral antenna complex LH2 of *Rps. acidophila* as results from the X-ray crystall structure data [McDermott et al., 1995].

interact with the protein environment but not between each other.¹ For the closer packed Bchl-B850, however, a strong dipole-dipole interactions between the Bchls has been assumed to be responsible for the redshift of the Q_y -absorption to 847nm. However, the relation between the dipole-dipole coupling strengths and the static as well as dynamic disorder among the Bchl-B850 is discussed controversially [Hu et al., 1997, Bakalis et al., 1999, Linnanto et al., 1999, Kimura et al., 2000, Dahlbom et al., 2001, van Amerongen et al., 2000].

Though there does not exist a X-ray crystallography for the LH2 of *Rhodobacter (Rb.) sphaeroides*, yet, the structure has been assumed to be quite similar to the LH2 of *Rs. molischianum* due to the nearly identical absorption spectra. For both species one obtains absorption bands at 800nm and 850nm. For *Rps. acidophila* the X-ray crystal structure reveals a C_9 -symmetry of the aggregate [McDermott et al., 1995] in accordance to the content of 27 Bchl. These are also arranged in two stacked rings, one with 9 Bchl, the other with 18 Bchl. The NIR absorption spectrum shows two Q_y -bands at 801nm and 859nm (cf. Fig. 8.4) [Cogdell et al., 1997]. Despite of a different spectral position the latter band is also named B850.

8.2 Theoretical model for the B850 band

Theoretical calculations for the B850 excitation of *Rs. molischianum* [Hu et al., 1997] show that for negligible energetic and structural disorder of the circular B850 aggregate the excited state split into 16 partially degenerate exciton states (see Fig. 8.5). The sum of oscillator

¹Of course, historically, the X-ray structures have followed the already known absorption spectra – so the naming of the B800 and B850 ring.

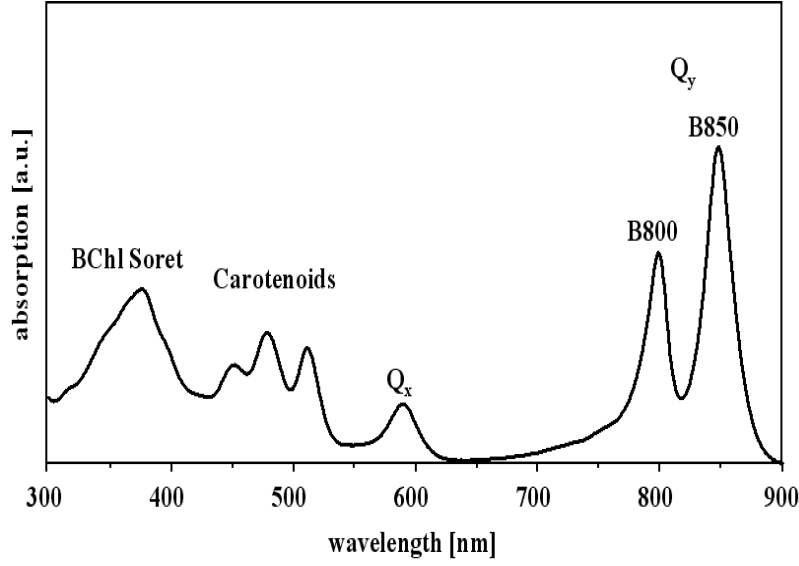


Figure 8.3: Absorption spectrum for the peripheral light harvesting antenna (LH2) of *R. molischianum* [Voigt, unpublished]. Band assignments see text

strengths of the 16 Bchl-B850, however, is redistributed to only some of these states – mainly into the two degenerate exciton states $|1_{\parallel}\rangle$ and $|1_{\perp}\rangle$ energetically being the lowest but one (cf. supplement 8.6). In this model the 50nm shift of the B850-band in respect to the B800-band is explained by only the strong dipole-dipole interaction [Atkins, 1998] between the Bchl-B850 molecules given by

$$V_{ij} = \frac{1}{4\pi n\epsilon_0} \left(\frac{\mu_i \mu_j}{R_{ij}^3} - 3 \frac{(\mu_i \mathbf{R}_{ij})(\mu_j \mathbf{R}_{ij})}{R_{ij}^5} \right). \quad (8.1)$$

Note that due to the R_{ij}^{-3} dependence the dipole-dipole interaction of the Bchl-B800 is one order of magnitude smaller than that between Bchl-B850. For the latter, however, the dipole-dipole interaction might be too correct for the distance being in the same order of magnitude as the molecular size [Krueger et al., 1998, Scholes, 1999]. For small elliptical deformation of the B850-ring the degeneration of the exciton states $|1_{\parallel}\rangle$ and $|1_{\perp}\rangle$ will break. In this case the B850-band splits to two subbands (cf. supplement 8.6). Since the Q_y -transition dipoles of the Bchl-B850 are slightly out of plane, the energetically lowest exciton state $|1_0\rangle$ will also share a small amount of oscillator strength. The three energetically highest exciton states will get an even smaller part due to the fact that the basic cell contains two instead of only one Bchl-B850 [Hu et al., 1997, Koepke et al., 1996].

For increasing static disorder in respect of site energies and structure of the B850-ring, one expects that the oscillator strength will be distributed over more than the mentioned two

8.2. Theoretical model for the B850 band

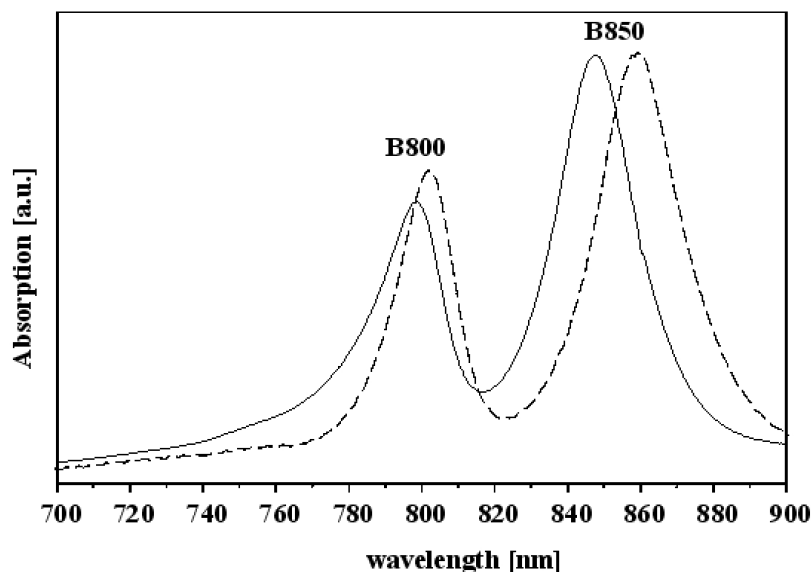


Figure 8.4: NIR-absorption spectra for the peripheral light harvesting antennae (LH2) of *Rb. sphaeroides* (solid line) and *Rps. acidophila* (dashed line) [Nowak, 1999]. For band assignments see text

exciton states [Knoester, 1993]. Furthermore, the energy splitting of the excitonic states will become equally spaced. X. Hu *et al.* have calculated the exciton band for normal distributed site energies with standard deviation $\sigma = 170\text{cm}^{-1}$ [Hu et al., 1997]. This has resulted in a Gaussian-shaped B850-band with line-width parameter $\Delta = 60\text{cm}^{-1}$, which is in agreement to the inhomogeneous line width obtained by hole burning measurements for the B850-band of *Rb. sphaeroides* at 4K [Reddy et al., 1991]. As mentioned above *Rhodobacter (Rb.) sphaeroides* and *Rs. molischianum* are assumed to be very similar in structure and spectra. In principal the exciton band model for *Rps. acidophila* is comparable to that of *Rs. molischianum*, but due to the C_9 -symmetry the two exciton states in the middle of the exciton-band are now doubly degenerate (cf. Fig. 8.5 and ref. [Sauer et al., 1996]). It may be assumed that the different structure may be responsible for the more red-shifted B850-band of *Rps. acidophila* at 859nm (cf. Eq. 8.4).

It has to be mentioned, that the theoretical model of the B850-band by [Hu et al., 1997], as presented above, is not unchallenged. There exists a long-standing debate of the nature of the excitations on the B850 aggregate as already indicated above [Chachisvilis et al., 1997, Sundström et al., 1999, van Amerongen et al., 2000, Dahlbom et al., 2001]. The interpretations of the results reach from the assumption of molecular excitations localized by static or dynamic disorder to only a Bchl-B850 dimer [Jimenez et al., 1996] up to delocalized Frenkel-excitons

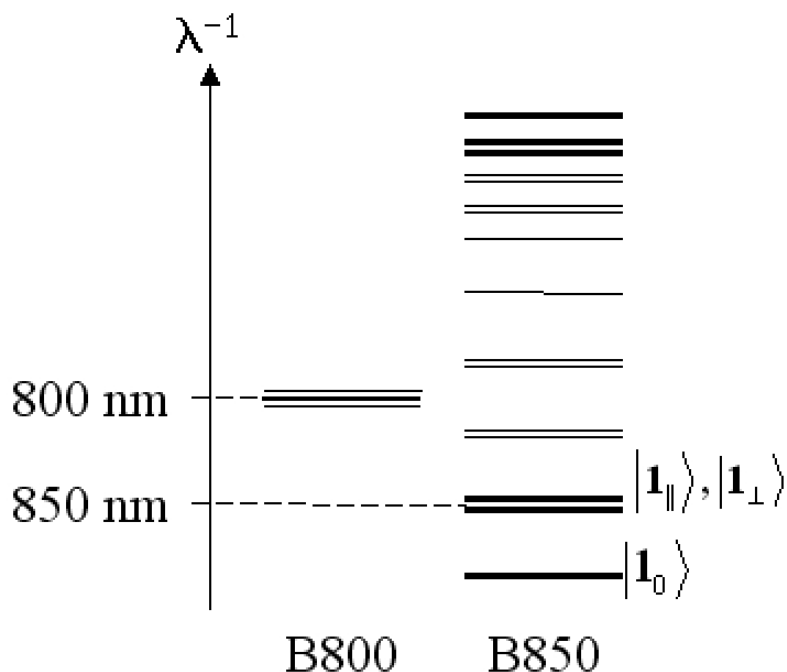


Figure 8.5: Theoretically predicted exciton bands for the LH2 of *Rb. molischianum* [Hu et al., 1997]. The thick lines assign exciton states which can carry some oscillator strength. The B800 band consists of eight energy levels which are quite close. The B850 band mainly of two degenerate exciton states lowest but one.

over nearly the entire B850 ring [Novoderezhkin et al., 1999, Leupold et al., 1996, Leupold et al., 1999]. In the former model one assume the localized excitation hops from one Bchl-B850 dimer to the next on a one-dimensional random walk. Thereby the initial orientation of the associated transition dipole is lost due the circular arrangement of them in the plane of the B850 ring. This would explain the observed depolarization of the excitation on a time-scale of some 100fs by a Förster-like transfer [Jimenez et al., 1996]. The totally delocalized excitons excited at 850nm were the two, degenerate in energy with transition dipole moments perpendicular to each other, mentioned above. The actual polarization of the excited exciton, however, is represented by a coherent superposition of these two transition dipoles (cf. supplement 8.6). Since the exciton states are degenerate, slightest fluctuations of the molecular structure give rise to the transition dipole to rotate in the B850 plane randomly. Being thermally driven by molecular vibrations of the Bchls themselves as well as the surrounding protein, a 100fs time-scale for this kind of exciton dynamics is not unreasonable [Kühn et al., 2002]. Recently, theoretical studies have shown that the conflict between both pictures can be solved by studying

8.3. Low-intensity NLPF-spectra of the B850-band

the dynamics resulting from the exciton-phonon interaction in detail [Dahlbom et al., 2000, Dahlbom et al., 2001, Dahlbom et al., 2002]. In particular this has been demonstrated for the B850 aggregate. In these models the initially delocalized exciton will be start to localized mainly after relaxation to the lowest exciton state by a feed-back process for exciton-phonon interaction, analogously to polaron formation. The extend of the finally reached delocalization length of the exciton depends significantly on temperature, static disorder, and the coupling to the vibrational modes. The stronger the exciton-phonon and the larger the static disorder, the shorter is the delocalization-length and the more incoherent is the exciton motion. The latter depends also on the spectral density of phonon modes. In the extreme case the excitation can be trapped to a single site [?, Kühn et al., 2002, Beenken et al., 2002, Dahlbohm, 2002].

From excitation annihilation experiments on *Rb. sphaeroides* it has been concluded that the coherence length of the exciton is $N_{coh} = 2.8 \pm 0.4$, i.e. the exciton is delocalized over approximately three Bchl-B850 [Trinkunas et al., 2001]. This is in contradiction to conclusions from nonlinear absorption (NLA) measurements stating that the observed enhancement of the cross-section of absorption results from the redistribution of oscillator strength according to excitons delocalized nearly over the entire B850 ring [Leupold et al., 1996, Leupold et al., 1999]. In the cited works already results from NLPF by F. Nowak [Nowak, 1999] concerning the determination of inhomogeneous and homogeneous line widths have been used [Leupold et al., 1993, Leupold et al., 1994, Leupold, 1995, Leupold et al., 2000].

8.3 Low-intensity NLPF-spectra of the B850-band

In the work be presented the enhancement of the oscillator strength in the B850-band will be determined by only using NLPF, i.e. a combination of T_2 -peak analysis for low-intensity NLPF-spectra in order to determine the homogeneous line width, and pump-intensity-dependent NLPF for extracting the absolute cross-section of absorption at a certain wavelength. Thereby T_1 -peak analysis at low pump-intensities will provide the necessary information about the ground-state-recovering time (cf. chapters 4 and 6). One will see that this combination of nearly all methods receiving information from NLPF, demonstrated in the previous chapters, allows one to determine the enhancement of oscillator strength in the B850 quite well, and to distinguish between the two models presented in the previous section.

8.3.1 T_2 -peaks

In order to determine the inhomogeneous and homogeneous line width at room temperature NLPF spectra of LH2 for *Rs. molischianum* and *Rb. sphaeroides* have been measured by

B. Voigt (partly published in [Leupold et al., 2000]), those for *Rps. acidophila* by F. R. Nowak [Nowak, 1999] (sample preparation by B. Ücker and M. Bandilla, respectively).

For *Rs. molischianum* (Fig. 8.6 panel a) no shifts of the T₂-peak centered at 850.0 ± 0.2nm have been observed for moving the probe frequency from 840 to 860nm. This means that here the B850-band represents a single transition at 850nm. T₂-peak analysis determines the homogeneous line width to 474 ± 10cm⁻¹ and limits the inhomogeneous line-width parameter Δ to an upper bound of 60cm⁻¹ (cf. section 5.1). The latter value is in good agreement to that obtained for *Rb. sphaeroides* by the hole-burning measurements at 4K [Reddy et al., 1991]. In the NLPF-spectra for *Rps. acidophila* probed from 840 to 860nm. shifts of the T₂-peak are absent as well (cf. Fig. 8.6 panel b). Nevertheless, there may exist a substructure due to the fact that the maximum of the T₂-peak occurs at 853 ± 1nm, while the absorption spectrum is maximum at 860nm.

Only for *Rb. sphaeroides* (Fig. 8.6 panel c) a shift of the T₂-peak maximum is clearly apparent, particularly, for moving the probe wavelength from 850 to 860nm. By global fitting of all four spectra (λ_t = 830, 840, 850, 860nm) using the methods mentioned in chapters 4 and 5 as implemented in ref. [Ehlert and Beenken, 1998], two subbands at 843 ± 1 and 852 ± 1nm has been identified within the B850-band. The ratio of their strengths is approximately 10 : 1 as obtained from the simultaneous fit of the absorption spectrum (cf. Fig. 8.7). The remaining small differences have been attributed to the B800-band, which has not been considered for the fit. With 470 ± 10cm⁻¹ the homogeneous line width of the main subband at 843nm is comparable to that of the B850-band in *Rs. molischianum*. The inhomogeneous line-width parameter, however, is limited to Δ ≤ 50cm⁻¹, what is 20% less than the value obtained by the hole-burning measurements at 4K [Reddy et al., 1991] (see above). Both subbands seems to be heterogeneous to each other (cf. section 4.1.1). This means that they may belong to two different kinds of aggregates, may be due to a slightly different structure. Due to the similarity between the main subband is comparable to the B850 band of *Rs. molischianum*, the structures of the LH2 seems to be comparable for both species, at least at room temperature.

At low temperatures, however, the NLPF-spectra of the LH2 of *Rb. sphaeroides* change significantly, though the absorption spectrum remains nearly unchanged. At 20K the NLPF-spectrum probed at 830nm reveals clearly two distinct subbands located at 838nm and 860nm (cf. Fig. 8.6, panel d). Now the 860nm subband is the stronger one, even though the probe wavelength is in the range of the subband at 838nm, what hints to a homogeneous substructure (cf. section 4.1.3). The appearance of two homogeneous subbands for *Rb. sphaeroides* is quite surprising, since the absorption spectrum of the isolated LH2 does not show any indication of spectral substructure within the B850-band – not even at 4K [Wu et al., 1996].

The reason of the split of the B850 band for *Rb. sphaeroides* is still unknown. The lowest

8.3. Low-intensity NLPF-spectra of the B850-band

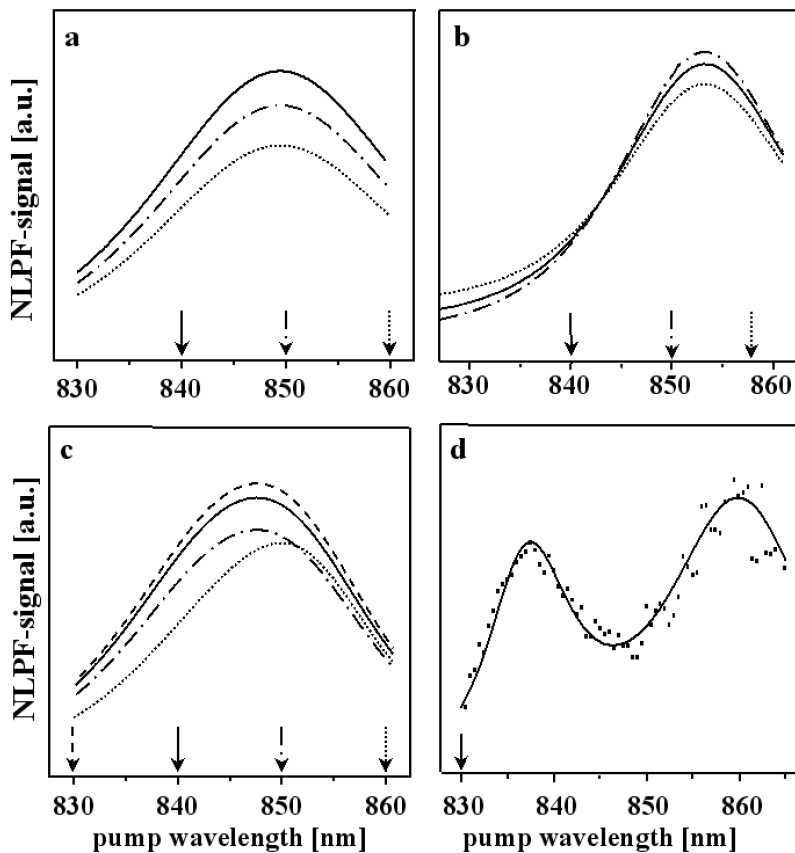


Figure 8.6: Fitted NLPF-spectra (B850-band) of the light harvesting antenna LH2 of the purple bacteria *Rs. molischianum* (a), *Rps. acidophila* (b), and *Rb. sphaeroides* (c) at room temperature. The latter has been also investigated at 20K (d). All NLPF-spectra recorded over the pump wavelength for fix probe wavelengths (arrows) Fits based on data (shown for d as dots) by B. Voigt (partly published in [Leupold et al., 2000]) and F. R. Nowak [Nowak, 1999].

exciton state, which can carry some oscillator strength (see above) can be excluded to be responsible, since the corresponding transition is to expect around 870nm [Hu et al., 1997]. A recently reported polaron state detected in fluorescence for the LH2 of a mutant of *Rb. sphaeroides* at 880nm free of LH1 [Polivka et al., 2000] should not appear in absorption due to the fact that it is formed after excitation and relaxation of the B850 exciton band. To attribute the splitting to an elliptical deformation of the cylindric LH2 aggregate does not hold as explanation either. Though this geometrical defect will split the doubly degenerate exciton levels (see above) including the two which carry the main oscillator strength, the perpendicular transition dipoles, which are now pinned to the main axes of the elliptical deformation, should

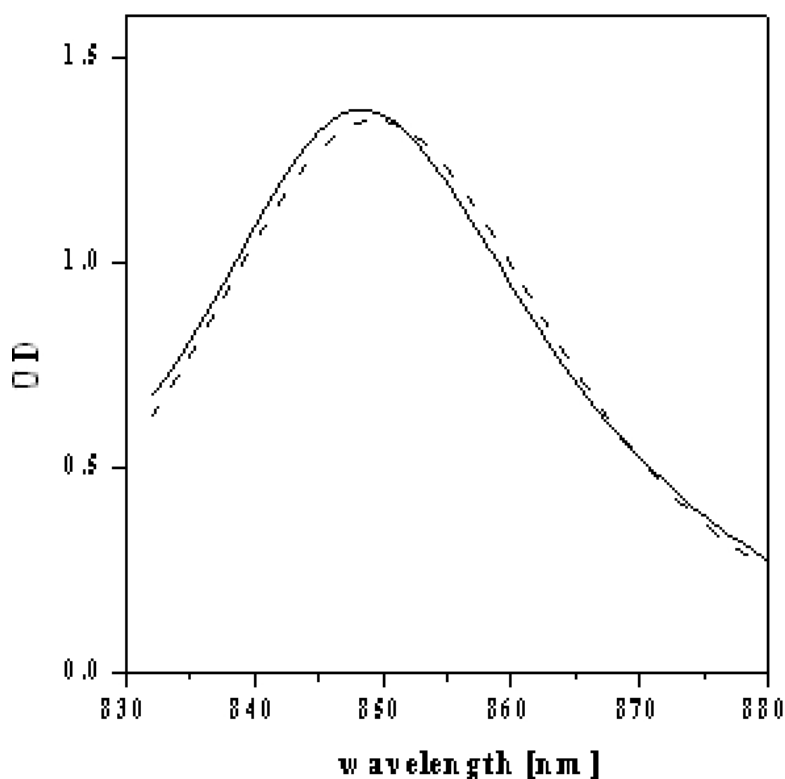


Figure 8.7: Room-temperature absorption spectrum of the LH2 of *Rb. sphaeroides* (solid line) and fit (dashed line) according to the two subbands at 843 and 852nm found by NLPF.

be of nearly the same strength. Considering the geometry factor (cf. Eq. 4.10) for perpendicular dipoles, this means that for probing the subband at 838nm, in respect of the pump-wavelength dependence, the heights of the two subbands at 838 and 860nm should yield a ratio 2 : 1. Obviously, the opposite is the case (cf. Fig. 8.6 panel **d**). As last explanation the static energy disorder reported as about $\sigma = 170\text{cm}^{-1}$ (see above [Hu et al., 1997]) is to reject, as well. Though it causes a split of the observed order of magnitude, this will also result in a symmetric redistribution of the oscillator strength to the two subbands. Thus the B850 band for *Rb. sphaeroides* is still an interesting object for further spectroscopic investigations and theoretical studies.

8.3.2 T_1 -peak

Beside the information about the substructure of the B850-band, the NLPF-spectra contains also information about the lifetime of the B850 excitation. This could be obtained by the T_1 -

8.4. Pump-intensity dependence of the NLPF-signal in the B850 band

peak, which could not be displayed in Fig. 8.6 for its narrowness. In Fig. 8.8 a NLPF-spectrum of the B850 band of *Rs. molischianum* for probe wavelength $\lambda_t = 840.011\text{nm}$ (11904.61cm^{-1}) highly resolved in frequency is shown. Since the T_1 -peak is quite symmetric, the fit could be performed as for the two-level system (cf. Eq. 2.41). It results in a energy relaxation rate of $\gamma = 0.0275 \pm 0.002\text{cm}^{-1}$, which corresponds to $T_1 = 1.2 \pm 0.1\text{ns}$. This lifetime is in agreement with those usually found for purple bacteria, e.g. *Rb. sphaeroides* $T_1 \sim 1\text{ns}$ [Monshouwer et al., 1997].

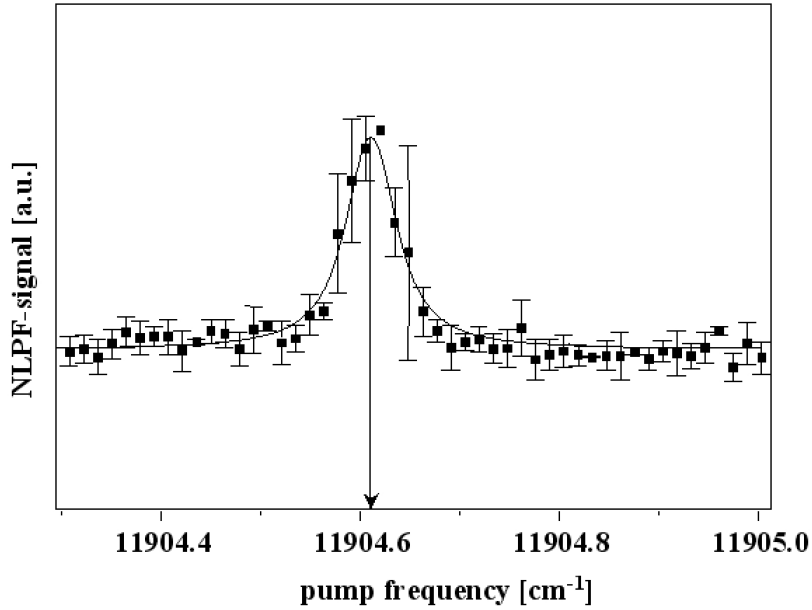


Figure 8.8: T_1 -peak for LH2 of *Rs. molischianum* probed at 11904.61cm^{-1} (arrow), i.e. $\lambda_t = 840.011\text{nm}$. Experimental data (squares) by B. Voigt (unpublished). Fit for $\gamma = 0.055 \pm 0.003\text{cm}^{-1}$ (solid line) according to Eq. 2.41.

8.4 Pump-intensity dependence of the NLPF-signal in the B850 band

Beside information about homogeneous and inhomogeneous broadening one may be also interested in the absolute cross-section $\sigma_{B850}(\omega)$ of the B850 absorption. This information can be obtained by the pump-intensity dependence of the NLPF-signal according to Eqs. 6.5-6.7 for known lifetime of the excitation. Note that this is not the lifetime of the initially excited B850 exciton, which may be much shorter by exciton thermalization, but the ground-state recovering

time, which is exactly the quantity determined from T_1 -peak analysis. In Fig. 8.9 the intensity dependence of the NLPF-signal pumped at $\lambda_p = 850\text{nm}$ and probed at $\lambda_t = 840\text{nm}$ is shown for isolated LH2 of *Rs. molischianum*.

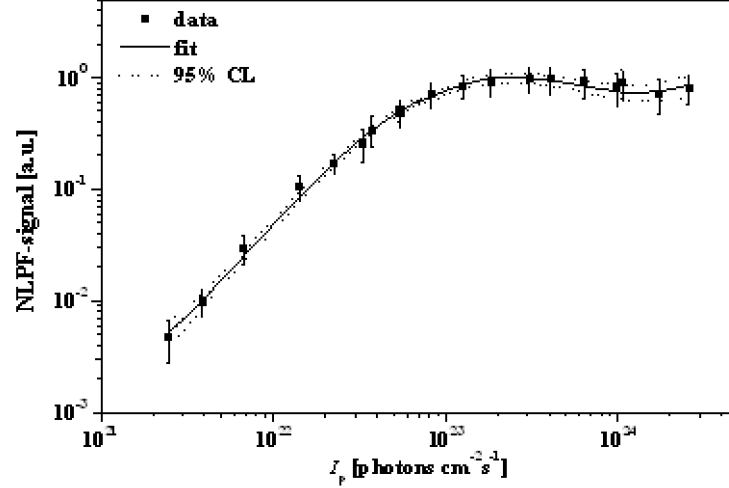


Figure 8.9: Pump-intensity dependence of the NLPF signal for LH2 of *Rs. molischianum* pumped at 850 nm and probed at 840 nm. Experimental data (squares) by B. Voigt (unpublished). Fit (solid line) according to Eqs. 6.12, 8.2, and 6.15 results in saturation parameter $\xi(850\text{nm}) = (1.01 \pm 0.07) \times 10^{-23}\text{cm}^2\text{s}$. Margins for confidence level 95% are shown (dotted lines).

In order to interpret the results of the previous section it is useful to treat the two possible models – the delocalized exciton model and the incoherent hopping transfer model – as presented in section 8.2, separately.

8.4.1 Delocalization length of an assumed B850-exciton

In the exciton model used above [Hu et al., 1997], the transitions to the two exciton states $|1_{\parallel}\rangle$ and $|1_{\perp}\rangle$, carry the major part of the oscillator strength. The corresponding transition dipoles μ_{\parallel} and μ_{\perp} are lying in the B850 plane perpendicularly to each other. For modelling the pump-intensity dependence of the NLPF-signal beside the two degenerate exciton states $|1_{\parallel}\rangle$ and $|1_{\perp}\rangle$ also the lowest non-degenerate exciton state $|1_0\rangle$ has to be taken into account. As mentioned above this is connected with a transition with only tiny oscillator strength. For sake of simplicity, it will be assumed to be ‘dark’ in what follows, i.e. $\mu_0 \approx 0$. The intra-

8.4. Pump-intensity dependence of the NLPF-signal in the B850 band

band relaxation to the lowest exciton state as well as the exciton–exciton annihilation can be assumed to be quite fast compared to the ground-state recovering, which is about 1.2ns (see section 8.3.2). Note that in the exciton picture, the excitation annihilation is to be described as inter-band relaxation from the two- to the one-exciton band [Brüggemann et al., 2001]. According to the excitation annihilation measurements for *Rb. sphaeroides* the inter-band relaxation happens within 600fs [Trinkunas et al., 2001].

Hence, fulfilling the preconditions the B850 system band can be described by the model given in section 6.2.1, in principle. Only an adaptation to the orientational averaging for circular aggregates is to be made (see supplement 8.6). This results in the specific saturation function

$$F[x] = 2x^{-1} \left(3 + (2 + 3x^{-1}) \frac{\operatorname{arccoth}[\sqrt{1+x^{-1}}]}{\sqrt{1+x^{-1}}} \right) \quad \text{for } x = \xi_{B850}(\omega_p, \omega_p) I_p. \quad (8.2)$$

to be used in Eq. 6.12 for argument $x = \xi_{B850}(\omega_p, \omega_p) I_p$. In complete analogy to Eq. 6.13 the saturation parameter is given by

$$\xi_{B850}(\omega_p, \omega_p) = \frac{\sigma_{0 \rightarrow 1}(\omega_p, \omega_p) + \sigma_{1 \rightarrow 2}(\omega_p, \omega_p) + \sigma_{em}(\omega_p, \omega_p)}{\gamma_{gsr}}, \quad (8.3)$$

where $\sigma_{0 \rightarrow 1}(\omega_p, \omega_p)$ represents the cross-section of pumping the one-exciton states $|1_{\pm}\rangle$ from the ground-state $|0\rangle$, and $\sigma_{1 \rightarrow 2}(\omega_p, \omega_p)$ that of pumping the two-exciton states from the relaxed one exciton state $|1_0\rangle$. For non-interacting excitons the spectrum of $\sigma_{1 \rightarrow 2}(\omega_p, \omega_p)$ is usually blue-shifted compared to that of $\sigma_{0 \rightarrow 1}(\omega_p, \omega_p)$ [Spano, 1992]. The cross-section $\sigma_{em}(\omega_p, \omega_p)$ representing the emission from the lowest exciton state is assumed to be quite small (see above).

Fitting the experimental data results in a saturation parameter $\xi(850\text{nm}) = (1.01 \pm 0.07) \times 10^{-23} \text{cm}^2 \text{s}$. For the linear continuation (cf. Fig. 8.9 for $I_p \gtrsim 10^{24} \text{cm}^{-2} \text{s}^{-1}$) an real value of $s_{lc}(840\text{nm}, 850\text{nm}) = (4 \pm 2) \times 10^{-26} \text{cm}^2 \text{s}$ has been found, but no significant imaginary part. For the decomposition of the saturation parameter in terms of ground- and excited-state absorption, here transient absorption spectra for *Rb. sphaeroides* as shown in Fig. 8.10 will be used [Leupold et al., 1996], resulting in $\sigma_{0 \rightarrow 1}(850\text{nm}) \approx (1.7 \pm 0.2) \times \sigma_{1 \rightarrow 2}(850\text{nm}) \approx (11 \pm 1) \times \sigma_{em}(850\text{nm})$. With the lifetime $T_1 = 1.2 \pm 0.1 \text{ns}$ as results from the T_1 -peak (see above) the cross-section of pumping the one-exciton band of *Rs. molischianum* yields at 850nm as $\sigma_{0 \rightarrow 1}(850\text{nm}) = 5.0 \pm 0.6 \times 10^{-15} \text{cm}^2$. Note that, using a definition different from Eq. 2.40 due to the specific orientational averaging for the circular B850-aggregate (cf. supplement 8.6), the absolute cross-section of the B850-absorption of *Rs. molischianum* is given as

$$\sigma_{B850}(850\text{nm}) = \frac{2}{3} \sigma_{0 \rightarrow 1}(850\text{nm}) = (3.3 \pm 0.4) \times 10^{-15} \text{cm}^2. \quad (8.4)$$

This value found by pump-intensity-dependent NLPF is quite high, but even higher values have been calculated from NLA measurements: for *Rb. sphaeroides* $\sigma_{0 \rightarrow 1}(848\text{nm}) \approx 7.5 \times 10^{-15}\text{cm}^2$ [Leupold et al., 1996] and for B800-depleted *Rps. acidophila* $\sigma_{0 \rightarrow 1}(858\text{nm}) = 5.8 \pm 0.8 \times 10^{-15}\text{cm}^2$ [Leupold et al., 1999], respectively.

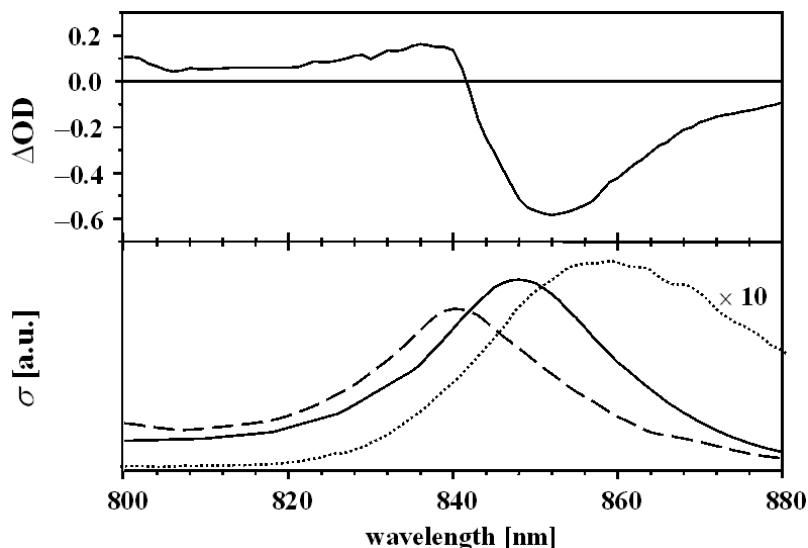


Figure 8.10: Transient absorption spectrum of the for *Rb. sphaeroides* (top) with decomposition (bottom) into crosssections for pumping absorption ($\sigma_{0 \rightarrow 1}$, solid line), excited-state absorption ($\sigma_{1 \rightarrow 2}$, dashes), and stimulated emission (σ_{em}) in arbitrary units [Leupold et al., 1996].

Of more interest than the cross-section of absorption at a single wavelength is the transition dipole moment of the B850-absorption. Compared to the single Bchl_a, this should provide the number of molecules forming the exciton state in terms of the superradiant delocalization length [Dahlbom et al., 2001] as

$$L_1 = 2 \frac{|\mu_{B850}|^2}{|\mu_{Bchl a}|^2}. \quad (8.5)$$

The factor two results again from the orientational averaging. The transition dipole can be determined from the cross-section $\sigma_{0 \rightarrow 1}(\omega_p, \omega_p)$ for known homogeneous line shape of the B850-band (cf. Eq. 4.2). Using $474 \pm 10\text{cm}^{-1}$ homogeneous line width of the B850-band as results from T_2 -peak analysis (see above), the transition dipole moment turns out to be $\mu_{B850} = 11 \pm 1 \text{ D}$.² For the transition dipole of the single Bchl_a being 6.3 D [Shipman, 1977], this corresponds to an exciton delocalization over 3 – 4 Bchl-B850. A similar value has been found in *Rb. sphaeroides* by means of exciton–exciton annihilation [Trinkunas et al., 2001]. Not in agreement

²1D = 1Debye = $3.335 \times 10^{-30}\text{Cm}$

8.4. Pump-intensity dependence of the NLPF-signal in the B850 band

is the presented result from pump-intensity-dependent NLPF with delocalization over 6 – 7 Bchl, as has been found for *Rb. sphaeroides* by relative difference absorption spectroscopy [Novoderezhkin et al., 1999]. Consequently, a completely delocalized exciton is to deny as well.

8.4.2 Fast hopping transfer

Since the previous section showed that the B850-exciton is not completely delocalized, some of the assumptions made for the evaluation of the pump-intensity dependence of the NLPF-signal may be to revise. As shown in the supplement 8.6, however, the most crucial point, the specific orientational averaging has not to be changed. Hence, the saturation function $F[\xi_{B850}(\omega_p, \omega_p) I_p]$ is given as in Eq. 8.2. The assumption that the hopping transfer among the 16 Bchl-B850, which can be mapped to the intra-band relaxation rate γ_{intra} (cf. section 6.2.2), is much higher than the ground-state recovering rate γ_{gsr} holds, too [Jimenez et al., 1996]. Hence, for the fast hopping transfer model (cf. Eq. 6.16) one obtains the saturation parameter as

$$\xi_{B850}(\omega_p, \omega_p) = \frac{16 \sigma_{Bchl}(\omega_p, \omega_p) + \sigma_{Bchl^*}(\omega_p, \omega_p)}{2\gamma_{gsr}}. \quad (8.6)$$

Here $\sigma_{Bchl}(\omega_p, \omega_p)$ represents the cross-section of pumping the absorption and $\sigma_{Bchl^*}(\omega_p, \omega_p)$ that of pumping the emission plus the excited state absorption of a single Bchl-B850 molecule, respectively. The factor two in the denominator Eq. 8.6 differs from 6.16 results again from the averaging over the different orientations of Q_y -transition dipoles (cf. supplement). This is easily to understand, since only half the Bchl-B850 can have the right orientation in respect of the pump field. The cross-section of emission and excited state absorption occurs in Eq. 8.6 $\sigma_{Bchl^*}(\omega_p, \omega_p)$ only once due to the excitation annihilation in the B850-aggregate [Trinkunas et al., 2001], which allows only one excitation per B850-ring.

In the present model, one has to assume that the homogeneous line width of the B850-band represents also that for the absorption of the single Bchl-B850, since motional narrowing does not occur as for the excitonic system [Knapp, 1984]. Thus, from the transition dipole moment of Bchl a, which is given as $\mu_{Bchl} = 6.3 \text{ D}$ [Shipman, 1977], one can calculate a theoretical value of the saturation parameter ξ_{B850} . It turns out that this has to be larger than $1.5 \pm 0.2 \times 10^{-23} \text{ cm}^2\text{s}$ as lower bound obtained for ignoring the additional contributions by emission and excited state absorption completely. This value is definitely too high for resembling the experimental result $(1.01 \pm 0.07) \times 10^{-23} \text{ cm}^2\text{s}$ (see above). Hence, the model of hopping excitations localized to a single Bchl-B850 is not a appropriate description of the excitation dynamics in the B850 aggregate.

The reason why the exciton model still fits better to the measured saturation parameters is to find in the mentioned blue-shift of the spectrum $\sigma_{1 \rightarrow 2}(\omega_p, \omega_p)$ in Eq. 8.3 for the transitions

from the one- to the two-exciton band [Spano, 1992, Leupold et al., 1996]. Note, that a mapping from the scheme shown in Fig. 6.4 as shown in section 6.2.2 back to the incoherent energy transfer model fail in this case. In fact, the observed excited state absorption different from the absorption spectrum is to interpret as an addition to $\sigma_{Bchl^*}(\omega_p, \omega_p)$ in Eq. 8.6. This would increase the theoretical value for $\xi_{B850}(\omega_p, \omega_p)$ as given in Eq. 8.6 even more. For the partial delocalized exciton no limitations by mapping exist, since here the two-exciton state is already more than only the simple summation of two one-exciton states [Spano, 1992].

8.5 Summary

For the B850-band of the LH2 of three different species of purple bacteria – *Rs. molischianum*, *Rb. sphaeroides*, and *Rps. acidophila* – T₂-peak analysis of the NLPF-spectra could reveal inhomogeneous and homogeneous line width with good accuracy. For *Rb. sphaeroides* two subbands within the B850-band could be revealed, which were in absorption spectra hidden. In the case of *Rps. acidophila* a similar substructure may exist due to the fact that the T₂-peak is blue-shifted compared to the absorption band, but could not be revealed. The NLPF-spectra for *Rs. molischianum* have not given any hints to a spectral substructure. In the latter case the homogeneous line width of the single B850-band turned out to be $474 \pm 10 \text{cm}^{-1}$ and the inhomogeneous to be smaller than 120cm^{-1} . Additional T₁-peak analysis results in a ground-state recovering time for B850-excitation in *Rs. molischianum* of $1.2 \pm 0.1 \text{ns}$.

By the pump-intensity dependence of the NLPF-signal for the absolute cross-section of B850-absorption for *Rs. molischianum* at 850nm a value of $(3.3 \pm 0.4) \times 10^{-15} \text{cm}^2$ has been found. In combination with the homogeneous width for an assumable Lorentzian line shape the corresponding transition dipole moment could be determined to $11 \pm 1 \text{D}$. The significant enhancement of the dipole strength compared to Bchl a in solution has been interpreted as result of exciton delocalization over 3 – 4 Bchl molecules, what is in good agreement with results from exciton–exciton annihilation in *Rb. sphaeroides* [Trinkunas et al., 2001]. Neither the model of the excitations localized to a single Bchl-B850 nor of a completely delocalized exciton were able to reproduce this result. Therefore, the delocalization of the B850-excitation is to assume to be just in the middle between these two extreme cases [Dahlbom et al., 2001].

8.6 Supplement: Orientation-averaging for the circular B850-aggregate

The three lowest exciton states of a circular aggregate are given in the site representation [Knapp, 1984] by

$$|1_0\rangle = \frac{1}{\sqrt{16}} \sum_{j=1}^{16} |j\rangle \quad (8.7)$$

$$|1_{\parallel}\rangle = \frac{1}{\sqrt{16}} \sum_{j=1}^{16} \cos\left(\frac{2\pi}{18}j - \psi\right) |j\rangle \quad (8.8)$$

$$|1_{\perp}\rangle = \frac{1}{\sqrt{16}} \sum_{j=1}^{16} \sin\left(\frac{2\pi}{18}j - \psi\right) |j\rangle. \quad (8.9)$$

Here $|j\rangle$ assigns the state where the j th site (here occupied by Bchl a) is excited. The lowest exciton state $|1_0\rangle$ is fully symmetric for rotation around the axis of symmetry of the aggregate. Therefore he can only provide a transition dipole parallel to this axis, which is given by the very small components of the molecular transition dipoles μ_j pointing out of the B850-ring plane. The next higher exciton states, $|1_{\parallel}\rangle$ and $|1_{\perp}\rangle$, are degenerate in energy. Therefore, any the exciton state which represents a superposition of them is equivalent. In other words, one can choose the definition of the Euler angle ψ , which represents the orientation of the transition dipoles μ_{\parallel} and μ_{\perp} in the B850 plane, freely. The most proper choice is that where the scalar products with the external fields important for the orientational averaging (cf. Eq. 2.37) yields as

$$\mu_{\parallel}\mathbf{E}_p = \sqrt{16}\mu_{Bchl}E_p \sin\theta \quad \text{and} \quad \mu_{\perp}\mathbf{E}_p = 0. \quad (8.10)$$

This choice has the advantage that the coherent exciton dynamics, which have to include the off-diagonal reduced density matrix element $\rho_{\parallel\perp}$, are not needed to be calculated for the excitation process. Note that due to the degeneration of the exciton states $|1_{\parallel}\rangle$ and $|1_{\perp}\rangle$ the secular approximation may not be valid (cf. Eq. 3.9). For calculations of the depolarization and energy relaxation dynamics of the B850 aggregate in the framework of Redfield-theory see ref. [Kühn and Sundström, 1997b, Kühn and Sundström, 1997a, Kühn et al., 2002].

According to Eq. 8.10 for averaging the pumping only the Euler angle θ is important, which is given by the angle between the direction of the probe beam and the axis of symmetry of the B850-aggregate. Note that this definition is different from that has been used in Eq. 2.37, but more appropriate for the present problem. The rate of pumping the transition $|0\rangle \rightarrow |1_{\parallel}\rangle$ yields as $\sigma_{0\rightarrow 1}(\omega_p, \omega_p) I_p \sin^2\theta$, while all other one-exciton states are ‘dark’. In the same way one proceeds for the excited state transition $|1_0\rangle \rightarrow |2_{\parallel}\rangle$, which yields $\sigma_{0\rightarrow 1}(\omega_p, \omega_p) I_p \sin^2\theta$.

This is possible, since the one-exciton state $|1_0\rangle$, which is the mainly populated within the one-exciton band due to the fast intra-band relaxation, is fully symmetric in respect of rotations around the symmetry axis of the B850-aggregate [Hu et al., 1997].

Since μ_0 , i.e. the transition dipole of the transition $|0\rangle \rightarrow |1_0\rangle$, is assumed to be negligible and the energy relaxation $|1_{\pm}\rangle \rightarrow |1_0\rangle$ to be fast, one will probe mainly the bleaching of the ground state $|0\rangle$. For averaging the probing functions

$$\zeta_{\parallel}(\omega_t) = \zeta_{B850}(\omega_t) (\sin^2 \theta + \cos^2 \theta \cos^2 \phi) \quad (8.11)$$

$$\zeta_{\perp}(\omega_t) = -\zeta_{B850}(\omega_t) \cos^2 \phi, \quad (8.12)$$

over the second Euler angle ϕ one obtains

$$S(\omega_t, \omega_p, I_p) = \zeta_{B850}(\omega_t) \int_0^{\pi} (1 - 3 \cos^2 \theta) \frac{x \sin^3 \theta}{1 + x \sin^2 \theta} d\theta \quad (8.13)$$

introducing the saturation parameter as given by Eq. 8.3. Integration over the angle θ results in Eq. 6.12 for the saturation function $F[x]$ is given as in 8.2 with argument $x = \xi_{B850}(\omega_p) I_p$. Analogously the cross-section of absorption $\sigma_{B850}(\omega_p)$ is given by

$$\sigma_{B850}(\omega_p) = \frac{1}{4\pi} \int_0^{\pi} \sigma_{0 \rightarrow 1}(\omega_p, \omega_p) \sin^3 \theta d\theta = \frac{2}{3} \sigma_{0 \rightarrow 1}(\omega_p, \omega_p). \quad (8.14)$$

By elliptic deformation of the B850-ring, the degeneration may break down and the transition dipoles μ_{\parallel} and μ_{\perp} will be pinned to the semi-major and semi-minor axes, respectively. In this case an additional dependence on the second Euler angle ϕ will appear in Eq. 8.13, dependent of the remaining overlap of the two subbands for $|1_{\parallel}\rangle$ and $|1_{\perp}\rangle$.

For energetically and structurally disordered aggregates all exciton states will mix up, what results in a reduced delocalization length of the excitation [Hu et al., 1997, Dahlbom et al., 2001, Dahlbom et al., 2002]. From a certain extend of disorder the coherent exciton picture may not be the proper way to describe the dynamics in the excited state of the B850 aggregate.

This leads directly to the incoherent hopping transfer model³, where the orientation-average has to consider the circular arrangement of the Bchl-B850 with Q_y -transition dipoles within the B850 plane as well. Here, the relevant scalar products for pumping the Bchl-B850 are given by

$$\mu_j \mathbf{E}_p = \mu_{Bchl} E_p \cos \left(\frac{j}{16} + \psi \right) \sin \theta, \quad (8.15)$$

for j numbering the Bchl-B850 sites from 1 to 16 in the case of *Rs. molischianum*. The Euler angle θ is defined as above while ψ describes the rotation of the aggregate around the axis of

³In principle the exciton-model is also able to describe hopping transfers as recently has been demonstrated in the case of exciton-exciton annihilation [Brüggemann et al., 2001].

8.6. Supplement: Orientation-averaging for the circular B850-aggregate

symmetry. By summing up the cross-sections of all Bchl-B850 due to the fast hopping transfer (cf. Eq. 6.16) one obtains the same dependence on only the Euler angle θ as for the exciton model, but for different saturation parameter ξ_{B850} (cf. Eq. 8.6). Since the excitations will be distributed within approximately 100fs over all 16 Bchl-B850 sites [Jimenez et al., 1996], this is true for absorption, emission, and excited state absorption.

Chapter 9

Excitonic coupling of chlorophylls in the light-harvesting complex II of higher plants

As mentioned above higher plants possess two different photosystems (PS I and PS II) located in the thylakoid membrane of the chloroplasts. Each photosystem is surrounded by a specific light-harvesting antenna system containing antenna complexes, for enhancement and regulation of the photo-energy flux towards the reaction center. The bulk antennae is the light-harvesting complex II (LHC II), which binds about half of the total amount of chlorophyll (Chl a and b) in higher plants. Already this fact demonstrates its important role in photosynthesis [Blankenship, 2001, Alberts et al., 2002, Berg et al., 2002].

9.1 Structure of LHC II

The structure of trimeric LHC II has been modeled on the basis of electron crystallography to a resolution of about 3.4Å [Kühlbrandt et al., 1994]. As shown in Fig. 9.1 the known pigment content of 7 Chl a and 5 Chl b is embedded into the protein on specific Chl binding sites. Unfortunately, the resolution has not been sufficient to enable a distinction between Chl a and Chl b, which differs only by one residual group being either methyl or formyl (cf. Fig. 7.1). Therefore, the assignment of the Chl binding sites Chl a1-a7 and Chl b1-b6 (no b4) to Chl a and Chl b, respectively, is only tentative [Kühlbrandt et al., 1994]. Nevertheless it is well motivated by the presence of two luteins (L1 and L2 in Fig. 9.1; for structure formula see Fig. 4.8). Due to the difference in energy of the Q_y -absorption between Chl a and b the excitation energy (cf. Fig. 9.2) absorbed by LHC II will be accumulated to the Chl a. This increases the

9.1. Structure of LHC II

danger of inter-system crossing to triplet states for Chl a, which in presence of oxygen forming singlet oxygen can cause a lot of photo-damage. Chl b get rid off the problem by the fast by the energy transfer to Chl a. Therefore, the binding sites for Chl a should be close to the two luteins, which like other carotenoids act as triplet quencher [Young, 1991]. In the meanwhile, the occupation of some Chl binding sites has been verified by site-directed mutagenesis [Remelli et al., 1999, Rogl and Kühlbrandt, 1999, Rogl et al., 2002].

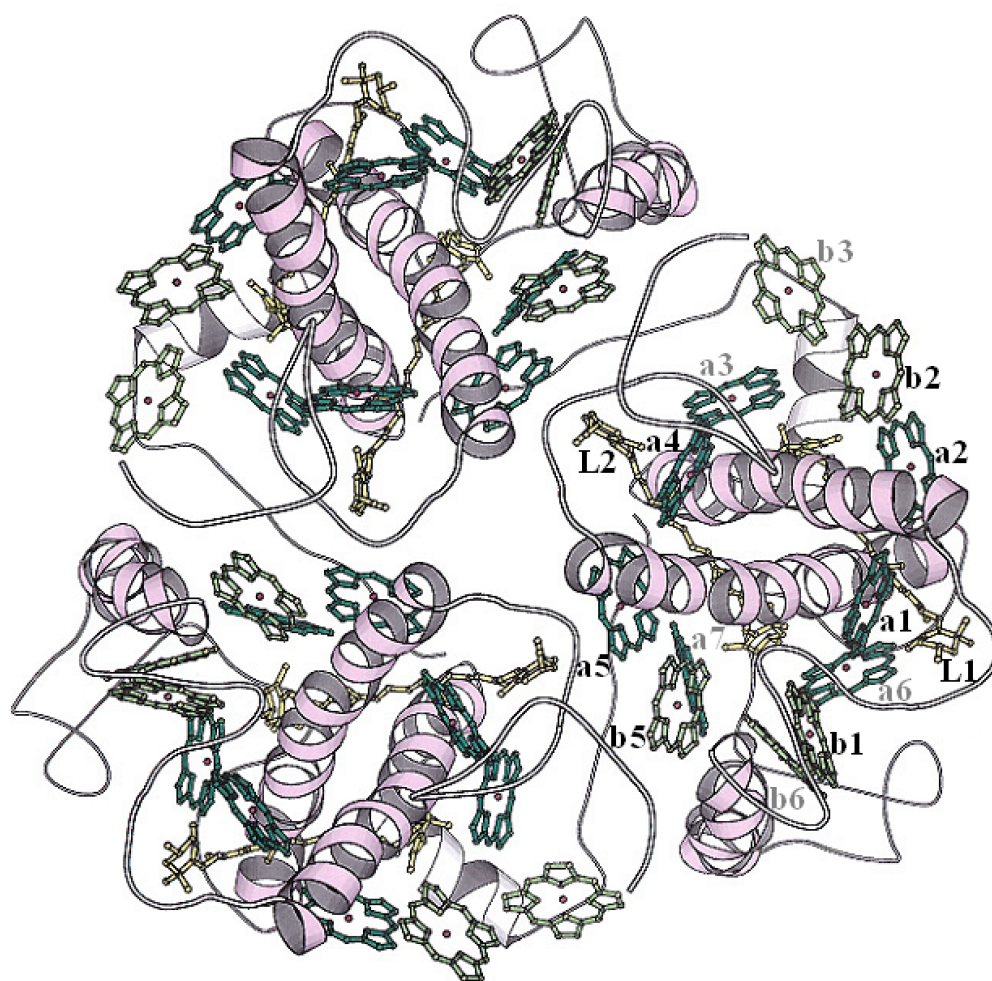


Figure 9.1: Structure of the trimeric LHC II (top-view) according to electron crystallography data [Kühlbrandt et al., 1994]. Shown are the protein helices and connecting backbones, the chlorophylls (a1-a7, b1-b6), and two lycopenes (L1, L2). Strong and light strike of the assignment means that the respective chlorophyll is arranged in the top and bottom layer, respectively. The two lycopenes span both layers.

The absorption spectrum of LHC II shows the typical band structure of Chl binding proteins. The Soret bands of Chl a and b not well separated from the absorption of xanthophylls are located between 400 and 535nm, peaking at 437nm for Chl a and 474nm for Chl b and xanthophylls. The Q_x -band approximately between 558 and 630nm is unstructured broad and contain certainly vibrational bands of the Q_y -band, which continues the spectrum between 630 till 720nm. The latter, which is of particular interest in the present work present two peaks at 651nm for Chl b and 676nm for Chl a. however, the spectral region between the two peaks contains several subbands as well (cf. ref. [Nussberger et al., 1994]). This could be shown very well by low temperature NLPF-spectra [Schubert et al., 1997] as well as by site directed mutagenesis [Rogl et al., 2002]. Notably, the fluorescence spectrum is much narrower than the absorption. This is caused by energy transfer from the spectral forms at shorter wavelength to the red-most terminal emitter on a time scale between 175fs to 170ps [Connelly et al., 1997], which is fast compared to the overall excitation life time of approximately 3.6ns.

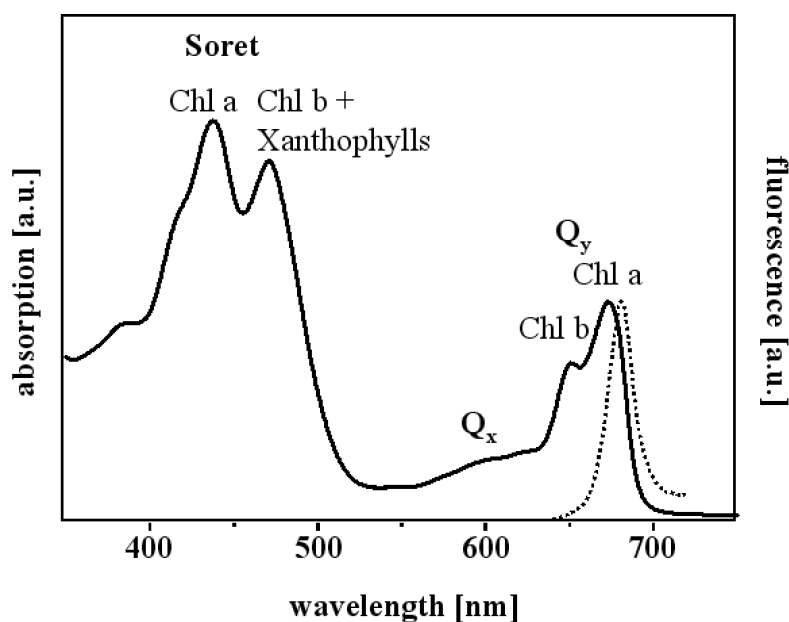


Figure 9.2: Absorption (solid line) and fluorescence spectrum of trimeric LHCII (data by A.Schubert). For explanation of the assignments of the bands see text.

9.2 Excitonic coupling in LHC II

Quite interesting the structure data provide shortest Mg–Mg distances between Chls in a range from 8 to 14Å. These distances are quite comparable to those found in bacterial antennae (cf.

9.2. Excitonic coupling in LHC II

chapter 8). Therefore the question came up whether dipole-dipole interaction might be strong enough to give rise for a delocalization of the excitation at least over Chl dimers [van Amerongen and van Grondelle, 2001]. However, due to the resolution being low, only the molecular planes of the Chls are approximately determined, while the orientations of the Q_y -transition dipoles can not unambiguously be determined. Hence, theoretical estimations for the dipole-dipole coupling (cf. Eq. 8.1) based on the available structure data for LHC II are not very reliable. Nevertheless, the couplings between the Chls in LHC II are crucial for understanding the mechanism of excitation transfer, which is the main task of a photosynthetic antenna system like LHC II. For strong interaction the excitation may be delocalized over most probably two Chls forming a dimer. This phenomenon would not only increase the coherent energy transfer within the Chl dimer [van Grondelle, 1985], but also the rates for Förster-transfer [Förster, 1948] from the respective dimer to other sites due to enhancement of the Q_y -transition dipole by redistribution of oscillator strength (see below).

9.2.1 Excitonic coupling for the Chl a2/b2 dimer

As an example, which of course is chosen on purpose as one will see below, the effects of excitonic coupling may be demonstrated for the Chl a2/b2 dimer (cf. Fig. 9.1). With approximately 8.3Å the Mg-Mg distance between Chl a2 and Chl b2 is the shortest in LHC II. The tetrapyrrole planes are nearly parallel oriented and tilted to the Mg-Mg distance vector by an angle of only 23°. Therefore, the Chl a2/b2 dimer most probably represents the dimer with the strongest dipole-dipole interaction, at least in the case the transition dipoles are oriented nearly in-line.

Assuming that the tentative assignment by Kühlbrandt (cf. Fig. 9.1) reflects the occupation of the binding sites with Chl a and b correctly, for transition dipoles oriented in a nearly in-line configuration one obtains $V_{a2b2} \approx 180\text{cm}^{-1}$ (cf. Eq. 8.1). This is comparable to the difference of transition frequency between monomeric Chl a and b of approximately 470cm^{-1} . Despite of this strong coupling the results are only tiny shifts of the Q_y -absorption bands from 668 to 672nm for Chl a2 and from 644 to 640nm for Chl b2, respectively (for calculation method cf. supplement 9.5). However, as mentioned above, the assignment is only tentative. For assuming that both binding sites, Chl a2 and Chl b2, are occupied by only Chl a one would obtain $V_{a2b2} \approx 220\text{cm}^{-1}$. This results in a split of the Q_y -absorption band of Chl a2 into two subbands at 661 and 678nm, respectively.

It has to be mentioned that the for the dipole-dipole interaction for the Chl a2/b2 (hetero)dimer with in-line arrangement of the transition dipoles as given here yields higher value than known from literature, e.g. $V_{a2b2} \approx 121.6\text{cm}^{-1}$ ref. [van Amerongen and van Grondelle, 2001]. This differences might result from several factors: The structure data let some freedom

in the choice of the direction of the transition dipoles. In the present work this freedom has been used excessively to get the most in-line arrangement compatible with the roughly defined tetrapyrrole planes for Chl a2 and Chl b2. Secondly there exists some uncertainty about the transition dipole strength of Chl a and b. Here averaged values of $\mu_{Chl a}^2 = 17 D^2$ and $\mu_{Chl b}^2 = 14 D^2$, respectively¹, has been taken from ref. [Sauer et al., 1966, Shipman, 1977]. This uncertainty regarding the strength of the transition dipoles is closely related to the third problem, the screening of the dipole–dipole interaction by the surrounding protein, as pointed out by the broad discussion in the literature [van Amerongen and van Grondelle, 2001, Cinque et al., 2000b]. The author of the present work is of the opinion that only using the microscopic distribution of charges, dipoles, and polarizabilities in the protein matrix can solve this problem satisfactorily. Therefore, in the presented calculations refractive index and local field correction factor has been set to one. The decisive argument for proceeding in this way is the fact that the space between Chl a2 and Chl b2 is not filled by protein and the cavity around the Chl a2/b2 is quite difficult to define for Chls on the outer edge of the trimeric LHC II (cf. Fig. 9.1). Finally, a more correct calculation of the excitonic interaction for the Chl a2/b2 dimer should go beyond the dipole–dipole interaction, due to the fact that the distance between the molecules is of their size [Krueger et al., 1998, Scholes, 1999]. In the present work the exact strength of the dipole-dipole interaction V_{a2b2} is of minor importance but the transition dipole strengths will be crucial (see below).

The the formation of a delocalized exciton affects not only the spectral position of the Q_y -absorption band of the Chl a2/b2 dimer, but also redistribute the oscillator strength between them (cf. supplement 9.5 and ref. [Cantor and Schimmel, 1980]). In the nearly in-line configuration of the transition dipoles this means that the oscillator strength for the band at 672nm is about an factor 1.6 enhanced compared to monomeric Chl a, while for the band at 640nm one obtains less than half of the oscillator strength of monomeric Chl b in solution. For the assumption that both binding sites contain Chl a one obtains an even stronger redistribution of oscillator strength. For the subband at 678nm this yields a 1.8 fold enhancement, while on the subband at 661nm remains only 20% of the oscillator strength of monomeric Chl a.

9.2.2 Alternative arrangements

Unfortunately, the orientation of Chl a2 and Chl b2 is still rather undetermined [Gradinaru et al., 1998b]. Therefore, also the results of excitonic coupling for three other principally different possible arrangements of transition dipoles has to be checked. In both cases where the transition dipoles of Chl a2 and Chl b2 are not parallel to each other, the dipole–dipole inter-

¹1D = 1Debye = 3.335×10^{-30} Cm

9.2. Excitonic coupling in LHC II

action is negligible ($V_{a2b2} \approx 5\text{cm}^{-1}$). Therefore, in these arrangements neither spectral shifts nor redistributions of oscillator strength do occur. For the ‘sandwich’ arrangement, where the transition dipoles are nearly parallel to each other, but perpendicular to the Mg–Mg distance vector, the dipole-dipole interaction yields only $V_{a2b2} \approx 95\text{cm}^{-1}$ for the original assignment. The oscillator strength of the Chl b subband scarcely shifted to 644nm is enhanced by factor 1.4 compared to Chl b in solution. Consequently, for the Chl a subband at 669nm only 68% of the Chl a oscillator strength remains. If both binding sites, Chl a2 and Chl b2, are occupied by Chl a, one obtains subbands at 673nm and 662nm, where the latter, shorter in wavelength, carries nearly the entire oscillator strength of both Chl a. Nevertheless, independently of the Chl assignment, a ‘sandwich’-arrangement of the transition dipoles in the Chl a2/b2 dimer contradicts clearly the results from site-directed mutagenesis, which have given evidence, that at least Chl a2 is related to a strong subband at 676nm – most likely the red-most one of all spectral forms [Rogl et al., 2002].

In order to extend the model further on, one may consider a Chl a2/a1 dimer, where the Mg–Mg distance is approximately 12.3Å. Here, however, the dipole-dipole interaction amounts to only 31cm^{-1} . Therefore, exciton delocalization over a Chl a1/a2 dimer or an Chl a1/a2/b2 trimer is more than questionable, though the latter would provide an 2.1 fold size enhancement of the Chl a band even for the binding site Chl b2 being occupied by Chl b.

9.2.3 Limitation of delocalization by exciton–phonon coupling

The theoretical description of delocalization has also to consider the coupling of the excitons to molecular vibrations and protein phonons [Meier et al., 1997, Bakalis and Knoester, 1999, Kimura et al., 2000, Beenken et al., 2002]. One common criterion in use compares the dipole-dipole interaction V_{ab} with the homogeneous line width of the observed subbands [Bakalis et al., 1999, Kimura et al., 2000]. In the case of a homodimer, one obtains partial delocalization just for $2V_{ab} > \Gamma$. Here the dephasing rate Γ represents the half homogeneous line width. In a previous study to trimeric LHC II by NLPF [Lokstein et al., 1995] the dephasing rate Γ of the red-most subband at 684nm has been determined to $\Gamma \approx 260\text{cm}^{-1}$. For the subband next to it at 677nm an even larger value of $\Gamma \approx 425\text{cm}^{-1}$ has been found. Though these values has to be taken with some reservation due to the outstanding consistent global analysis of NLPF spectra [Schubert, 2003], the dipole–dipole interaction is sufficient for prevailing delocalization of the excitation. For the Chl a2/b2 (hetero)dimers in the original assignment even in the in-line arrangement a similar condition, which considers the transition frequency difference of about 470cm^{-1} between monomeric Chl a and b, is clearly not fulfilled [Kimura et al., 2000].

Recently, by using a different theoretical approach, which considers the effects of exciton-

vibration coupling more directly, it has been shown that the lower exciton state in a dimer always tends more towards localization on one site, whereas the higher exciton state tends more towards delocalization, compared to the ideal case without exciton-vibration coupling [Beenken et al., 2002]. For a homo-dimer, the degree of these tendencies depends mainly on the ratio between excitonic coupling V_{ab} and monomeric Stokes-shift S , resulting in the criterion $2V_{ab} > S$, quite similar to that found above by using the dephasing rate Γ instead of the Stokes-shift². Fortunately, the crucial Stokes-shift of the main emitter of LHC II has been determined by fluorescence site selection measurements [Peterman et al., 1997] to be 400cm^{-1} . This means that in accordance to both theoretical approaches for the Chl a2/b2 homodimer, where both binding sites are occupied by Chl a, the excitation may be prevalingly delocalized over both binding sites. On the other hand, both approaches deny delocalization of the excitation in the case of the original assignment, i.e. for a Chl a2/b2 heterodimer, due to the high difference of transition frequency between Chl a and Chl b. Consequently, in this case redistribution of the oscillator strength should not occur. As one can see, experimental evidence for exciton formation in LHC II provides also severe impact to the theoretical models for pigment location as well as pigment–pigment and pigment–protein interaction in LHC II.

9.2.4 Experimental tests for spectral shifts and redistribution of oscillator strength in LHC II

Strong excitonic coupling between Chl in LHC II should be result in spectral shifts and oscillator strength redistribution between Chl subbands in the absorption spectrum, as well as in specific circular dichroism [Cantor and Schimmel, 1980, Somsen et al., 1996]. The Q_y -subbands as observed in the absorption spectrum of LHC II (cf. Fig. 9.2) are significantly shifted compared to Chl a and b in diethyl-ether, where they are located at 662nm and 644nm, respectively [Hoff and Amesz, 1991]. Nevertheless, these shifts are not unequivocally to relate only to dipole–dipole interaction between Chls forming dimers. In fact, the interactions of monomeric Chl with the protein environment as well as with xanthophylls are of the same order of magnitude [Nishigaki et al., 2001]. For the previous calculation of the subbands of the Chl a2/b2 dimer these shifts have been only roughly considered by an shift of 6nm for monomeric Chl a in protein compared to Chl a in solution.³ This was motivated by the position of the Q_y -absorption band at 668nm in the Peridinin-chlorophyll-a protein (PCP) [Kleima et al., 2000], where dipole–dipole inter-

²Note that Γ and S are connected to each other for Eq. 3.60 as shown in chapter 3. The conditions presented in ref. [Beenken et al., 2002] have been deduced for temperatures low compared to the oscillator energy $\hbar\omega$ of the respective vibrational mode, though the remain qualitatively valid for higher temperatures, too.

³For Chl b no environment shift has been applied.

9.2. Excitonic coupling in LHC II

action between the two Chl a can be neglected due to their distance of 17.4Å [Hofmann et al., 1996], while the interaction between Peridinin and Chl a is assumed to be limited to an energy transfer [Zigmantas et al., 2002]. Nevertheless the assumption that the shift of Chl a in PCP is only caused by the interaction protein environment remains questionable⁴. The moreover, the shifts by Chl–protein interaction may not to be uniform for the general heterogeneity of proteins containing different polar and nonpolar amino-acid residues. Due to these difficulties, it is not astonishing, that a consistent understanding of the LHC II absorption spectrum, which contains at least ten subbands, in an overall substructure model – including possible excitonic and environmental effects – has not been reached, yet [Nussberger et al., 1994, van Amerongen et al., 1994, Zucchelli et al., 1996, Cinque et al., 2000a]. By its ability to resolve substructures even hidden in the absorption spectrum (cf. supplement 4.5) NLPF may help to overcome the crucial problems associated with subband analysis of the LHC II absorption and CD-spectra. However, after promising beginnings [Lokstein et al., 1995, Schubert et al., 1997], the T₂-peak analysis of the Q_y-bands is stuck due to the multitude of parameters, in particular the necessary consideration of the geometry factors (cf. Eq. 4.10). Nevertheless, a step-by-step approach is in progress to render the NLPF-spectra of the Q_y-region of LHC II by a theoretical subband model, which considers explicitly the limitations for the orientation of the transition dipoles as given by the structure model [Schubert, 2003].

The redistributions of oscillator strength between subbands may provide an better experimental indication to delocalized excitations in LHC II. If this redistribution affects also the stimulated emission, it can be revealed by pump-intensity-dependent NLPF (cf. chapter 6) as will be demonstrated in section 9.3. Therefore, it is quite suitable that Chl a₂ seems to be at least part of the terminus of the energy transfer chain in monomeric LHC II as supported by site-directed mutagenesis [Rogl et al., 2002].

In circular dichroism spectra of LHC II the rotational strengths of some bands may hardly be explained without considering excitonic interaction between Chl dimers [Hemelrijk et al., 1992, Ruban et al., 1997, Gülen et al., 1997]. However, also a complete analysis of the circular dichroism spectrum of LHC II considering non-conservative contributions has not been accomplished, yet (cf. absorption spectrum above). For the theory of circular dichroism in excitonically coupled dimer the author may refer to ref. [Cantor and Schimmel, 1980]. At last it has to be mentioned that the CD-signal has not distort the NLPF-measurements for being almost compensated by the method described in section 2.1.1.

⁴For example, there has been observed a quite unusual blue-shifting of the Q_y-absorption maximum for Chl a when lowering the temperature [Kleima et al., 2000].

9.2.5 Homogeneous substructure for excitonically coupled Chl a/b dimers

Another approach to detect excitonic coupling in particular between Chl a and Chl b, where the assignment of excitonic shifts is quite difficult, using only T_2 -peak analysis (cf. chapter 4) will be shown in chapter 10. This method bases on the fact that for Chl a/b heterodimer pumping the Chl a Q_y -absorption band results in bleaching of both, Chl a and Chl b bands. The reason is that for an uncoupled Chl a/b dimer excitation of the one monomer does not influence the transition of the other, neither in spectral position nor in oscillator strength. This means that the substructure revealed by T_2 -peak analysis is heterogeneous (cf. section 4.1.1). This picture does not change for an ultra-fast energy transfer from Chl b to Chl a, if the back transfer is inhibited and one is pumping only the Q_y transition of Chl a (cf. section 4.1.2). For the same experiment a completely different result is obtained for the excitonically coupled Chl a/b dimer. In this case, the transitions from the ground state to the one-exciton states possess different transition dipole moments than the corresponding transitions from the one-exciton states to the two-exciton state (cf. supplement 9.5). Therefore, the excited-state absorption does not compensate the bleaching of the ground-state absorption completely, as it would do in the case of uncoupled Chls according to the mapping as given in section 6.2.2. Some previous studies of the exciton dynamics for Chl a/b dimers by means of pump-probe spectroscopy based also on this effect [?, Renger et al., 1994, Connelly et al., 1997]. Compared to fs pump-probe spectroscopy, which provides a better time resolution for the ultra-fast part of the exciton dynamics, the T_2 -peak analysis of NLPF-spectra has the advantage to be spectrally more selective by principle. On the other hand NLPF is mainly limited to such spectral Chl forms representing either the terminus or bottlenecks in the energy transfer chain, since the T_2 -peaks for probing long-living states are dominating the NLPF spectrum (cf. chapter 4). By fs-spectroscopy one can also under-run the life-time of intermediate states in the energy transfer chain. Thus both methods complement one another (cf. summary to chapter 2). A direct access to the coherence of the excitonic energy transfer should be enabled by three-pulse photon-echo experiments ???. Notably, there the results could be completely explained in the framework of almost incoherent energy transfer processes between Chl b and a.

For Chl a/a (homo)dimers⁵ the detection of excitonic coupling by bleaching of the Soret fails due to the unknown assignments of the Chl a subbands in LHC II (see above). The only significant hints to strongly excitonically coupled Chl a/a homodimers by means of simultaneous bleaching, is the occurrence of satellite holes in non-photochemical hole-burning experiments at 4K [Reddy et al., 1994]. Beside of the fact that this experiment has been performed at

⁵According to the structure data Chl b/b homodimers do not very likely occur (see above).

9.3. Pump-intensity-dependent NLPF-spectra for LHC II

temperatures which are physiologically of less relevance – the dephasing at room-temperature may change the result completely (cf. section 8.2 and Eq. 3.45) – this effect can also result from alterations in the protein by the hole-burning process, i.e. reversible photochemical hole-burning. Also absorption spectra of site-directed mutants of LHC II give some hints to excitonic coupling by simultaneous changes in different Q_y -subbands for mutagenesis of only one site [Rogl et al., 2002]. Here, however, alterations in the protein structure are much less under control.

9.3 Pump-intensity-dependent NLPF-spectra for LHC II

As mentioned above for the terminal Chlsites in the energy transfer chain pump-intensity-dependent NLPF-spectra can reveal an enhancement of the oscillator strength as caused by exciton delocalization. The limitation to terminal acceptors results from the fact that for coherent as well as incoherent energy transfer the cross-section of pumping absorption in the saturation parameter $\xi(\omega_p, \omega_p)$ (cf. Eq. 6.16 and 6.13) counts for all donors. In this way an enhancement would not be unequivocally to relate to a coherent exciton delocalized over donor and acceptor, but may represent only the incoherent sum of the cross-sections $\sigma_{abs}(\omega_p, \omega_p)$ according to Eq. 6.16. On the other hand as shown in chapter 6 the saturation parameter contains also the cross-section of stimulating emission $\sigma_{em}(\omega_p, \omega_p)$. In the case of incoherent energy transfer this counts only for one acceptor (cf. Eq. 6.16). In the case of a branching to several acceptors $\xi(\omega_p, \omega_p)$ will be even lower than for only one acceptor (cf. Eq. 6.22). Consequently, an enhancement of those parts of the ξ -spectrum, which represent the stimulated emission only, may originate exclusively from an enhancement of the transition dipole moment itself. This would be a strong indicator for a delocalized exciton.

9.3.1 ξ -spectrum of trimeric LHC II

NLPF-spectra of trimeric LHC II ⁶ have been recorded for fixed probe wavelength at 685nm, which is close to maximum fluorescence of LHC II, and different pump intensities (cf. Fig. 9.3). The pump wavelength λ_p has been varied from 645 to 690nm over the overlapping Q_y -absorption and emission regions.

In Fig. 9.4 a section through the spectra at $\lambda_p = 678$ nm is shown, illustrating the pump-intensity dependence. By fitting such curves for all pump wavelengths according to Eqs. 6.6

⁶LHCII sample preparation, measurements, and basic fits by A. Schubert; for experimental details see ref. [Schubert et al., 2002]

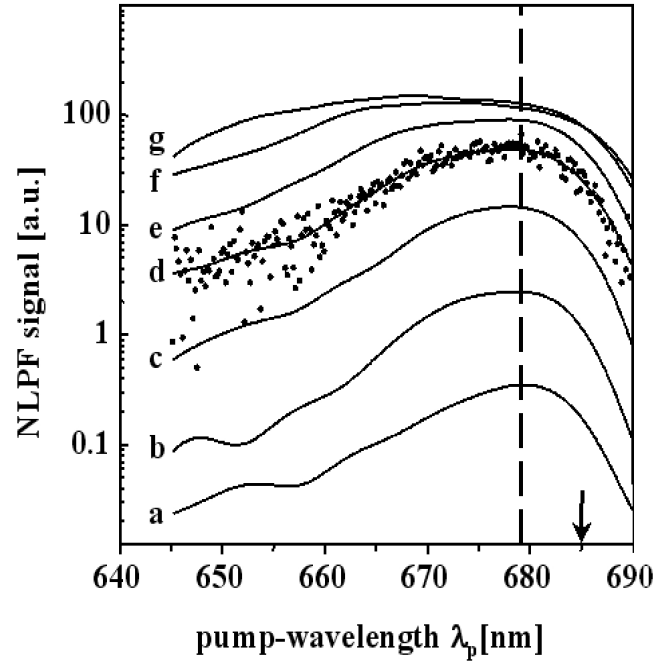


Figure 9.3: NLPF spectra of trimeric LHC II probed at $\lambda_p = 685\text{nm}$ (arrow) for pump intensities [photons $\text{cm}^{-2}\text{s}^{-1}$]: 5.7×10^{21} (a), 2.3×10^{22} (b), 8×10^{22} (c), 2.1×10^{23} (d), 4.3×10^{24} (e), 1.4×10^{22} (f), and 4.3×10^{22} (g). For case (d) original measurement data set is shown. Curves are averaged and smoothed [Schubert et al., 2002]. The dashed line at 678nm signifies the section for demonstrating the pump-intensity dependence in Fig. 9.4. Note that though the NLPF-signal is given in arbitrary units, the relative intensities are correctly rendered.

and 6.12 the ξ -spectrum has been determined as shown in Fig.9.5. For the pump-intensity curve in Fig. 9.4 the fit yields the $\xi(678\text{nm}, 678\text{nm}) = 8.4 \times 10^{-24}\text{cm}^2\text{s}$. A linear continuation $s(\lambda_t, \lambda_p) I_p$ has to be considered (cf. Eq. 6.15) and yields for the mentioned pump wavelength as $s(685\text{nm}, 678\text{nm}) = 2.7 \times 10^{-26}\text{cm}^2\text{s}$ with negligible imaginary part.

In order to analyze the ξ -spectrum, first one has to multiply it by the ground-state-recovering rate $\gamma_{gsr} \approx (3.6\text{ns})^{-1}$ to get the total cross-sections of pumping in dependence of the pump wavelength $\sigma_{tot}(\lambda_p, \lambda_p)$ (cf. Fig. 9.5, right scale). The latter is to decompose into the contributions of absorption $\sigma_{abs}(\lambda_p, \lambda_p)$, emission $\sigma_{em}(\lambda_p, \lambda_p)$, and excited-state absorption $\sigma_{exc}(\lambda_p, \lambda_p)$. For this decomposition being accomplishable (cf. section 6.2) some constrictions are to be fulfilled. Already the low values for the linear continuation parameter $s(\lambda_t, \lambda_p)$ indicate that the intra-band relaxation (cf. γ_{intra} in Fig. 6.4) is much faster than the ground-state recovering here approximated by the fluorescence decay rate as $\gamma_{gsr} \approx (3.6\text{ns})^{-1}$ [Connelly et al., 1997]. Accord-

9.3. Pump-intensity-dependent NLPF-spectra for LHC II

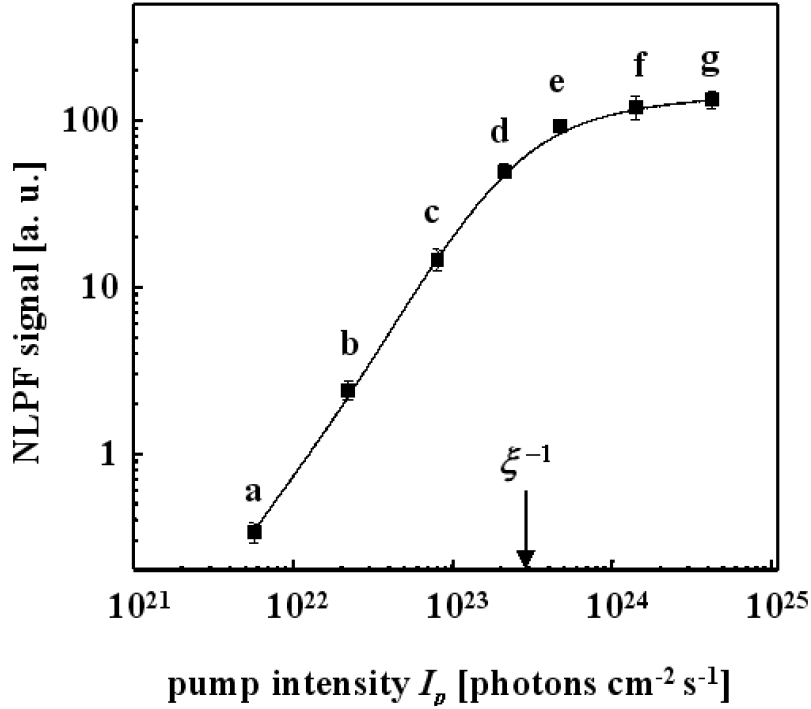


Figure 9.4: Pump-intensity dependence of the NLPF-signal probed and pumped at $\lambda_t = 685\text{nm}$ and $\lambda_p = 678\text{nm}$, respectively. Squares assigns measurement data the spectra shown in Fig. 9.3. Solid line shows the fit according to Eqs. 6.12 and 6.6 for saturation parameter $\xi = 8.4 \times 10^{-24}\text{cm}^2\text{s}$ (arrow) and linear continuation with $s(685\text{nm}, 678\text{nm}) = 2.7 \times 10^{-26}\text{cm}^2\text{s}$.

ing to the mapping demonstrated in section 6.2.2 the intra-band relaxation can be identified with the energy transfer within the LHC II complex. The corresponding transfer times have been determined by time-resolved spectroscopy to be in a range from 270fs to 24ps [Gradinaru et al., 1998b, Agarwal et al., 2000]. Also an ultra-fast excitation annihilation has been already observed for LHC II [Barzda et al., 2001]. For the present model (cf. Fig. 6.4) this means an fast inter-band relaxation rate⁷ of $\gamma_{inter} \approx (24\text{ps})^{-1}$. This means that in dependence of the used model either Eqs. 6.13, 6.16, 6.19, or 6.22 are to be used for decomposition. Thereby one may suppose that $\sigma_{abs}(\lambda_p, \lambda_p)$ follows the absorption spectrum and $\sigma_{em}(\lambda_p, \lambda_p)$ the fluorescence spectrum of LHC II. It turns out that this supposition does not hold for using Eqs. 6.13 or 6.16 in accordance with the model of a single energy relaxation or transfer chain with only one terminus. In the fast energy transfer model using Eq. 6.16 for fitting the absorption

⁷Note that here, differently from the usual definition as in ref. [Agarwal et al., 2000], γ_{inter} does not mean the transfer rate for Chl b to Chl a, which is included in γ_{intra} , but the annihilation rate. For the latter also the internal conversion from the Soret to the Q_y -band is to consider.

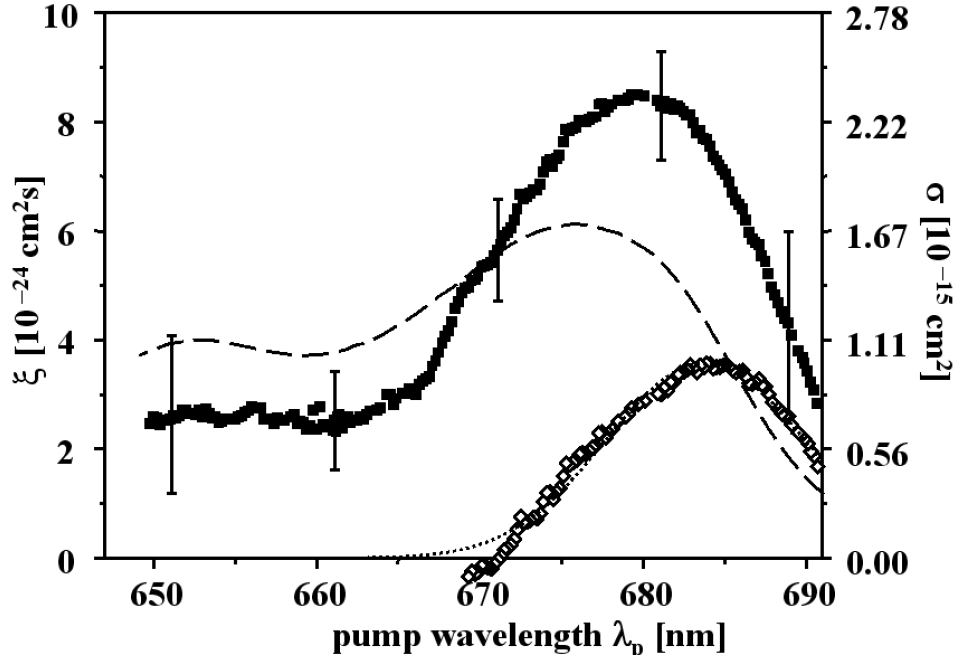


Figure 9.5: ξ -spectrum of the Q_y -band of trimeric LHC II (filled squares, left scale). The right scale gives the corresponding total cross-section of pumping for $\gamma_{gsr} = (3.6\text{ns})^{-1}$. For decomposition according to Eq. 6.13 the scaled absorption spectrum (dashed line) has been subtracted from the ξ -spectrum resulting in the cross-section of stimulated emission $\sigma_{em}(\lambda_p, \lambda_p)$ (open diamonds). For comparison the best fit to a Gaussian centered at 683nm with $FWHM = 260\text{cm}^{-1}$ (dotted line). For the discrepancy between rescaled absorption and ξ -spectrum at pump wavelengths $\lambda_p < 670\text{nm}$ see text.

spectrum to $\sigma_{tot}(\lambda_p, \lambda_p)$ for $\lambda_p < 670\text{nm}$, the residual values of $\sigma_{em}(\lambda_p, \lambda_p)$ are unreasonably high. Furthermore, they would not fit to the shape of the fluorescence spectrum at the red-side wing, anyhow. Last but not least the cross-section of pumping absorption $\sigma_{abs}(\lambda_p, \lambda_p)$ would not fulfill the condition that the area under the entire Q_y -absorption band of LHC II has to fit to the summarized transition dipole strength of 7 Chl a and 5 Chl b, i.e.

$$\frac{1}{2\pi} \int \frac{\sigma_{abs}(\lambda_p, \lambda_p)}{\lambda_p} d\lambda_p = \frac{7\mu_{Chl a}^2 + 5\mu_{Chl b}^2}{\hbar\epsilon_0 cn}. \quad (9.1)$$

This condition follows immediately from the sum over the cross-sections of all donors in Eq. 6.16. For the transition-dipole strengths of Chl a and Chl b averaged values of $\mu_{Chl a}^2 = 17 \pm 2 \text{D}^2$ [Shipman, 1977] and $\mu_{Chl b}^2 = 14 \pm 2 \text{D}^2$ [Sauer et al., 1966] will be used.⁸ Thus by rescaling the

⁸1D = 1Debye = $3.335 \times 10^{-30}\text{Cm}$

9.3. Pump-intensity-dependent NLPF-spectra for LHC II

absorption spectrum one obtains the cross-section of pumping the absorption $\sigma_{abs}(\lambda_p, \lambda_p)$ as given in Fig. 9.5 (dashed line). The maximum value of $(1.7 \pm 0.3) \times 10^{-15} \text{cm}^2$ is reached at $\lambda_p = 674 \text{nm}$. At least for $\lambda_p \geq 670 \text{nm}$ this results in a much more reasonable decomposition of the ξ -spectrum. The values of the cross-sections for pumping the emission $\sigma_{em}(\lambda_p, \lambda_p)$ (cf. Fig. 9.5, open diamonds) are now in the same order of magnitude as those for pumping the absorption. Nevertheless, it has to be noted that the resulting wavelength dependence of $\sigma_{em}(\lambda_p, \lambda_p)$ still does not fit to the fluorescence spectrum, but is significantly narrower. In fact it represents a Gaussian with a maximum value of $1.0 \pm 0.3 \times 10^{-15} \text{cm}^2$ at $\lambda_p = 683 \pm 1 \text{nm}$ and a line-width $FWHM = 260 \pm 30 \text{nm}$ (cf. Fig. 9.5, dotted line). By integration over $\sigma_{em}(\lambda_p, \lambda_p) / \lambda_p$ one obtains the dipole strength for the terminal emitter as

$$|\mu_{683}^{em}|^2 = 33 \pm 8 \text{D}^2. \quad (9.2)$$

This means a (1.9 ± 0.5) -fold enhancement of the oscillator strength for the terminal emitter in LHC II compared to monomeric Chl a in solution. Assuming that the terminal emitter is the Chl a2/b2 dimer, the lower error bar (enhancement ≥ 1.4 fold) would just include the theoretical value of 1.6 fold enhancement as obtained for tentative assignment by Kühlbrandt where the binding site Chl b2 is really occupied by Chl b. Much more confident, however, would be the assumption that both sites Chl a2 and b2 are occupied by only Chl a, which results in a 1.8 fold enhancement (see section 9.2.1). The latter case is particularly to prefer, since the delocalization of a homo-dimer persists even in a dynamic model including exciton-phonon interaction as mentioned above [Kimura et al., 2000, Beenken et al., 2002]. By the same reasons an extension of the exciton delocalization over a Chl a1/a2/b2 trimer is more than questionable, though the ideally resulting 2.1 fold size enhancement of the oscillator strength in the Chl a band fit quite well – in particular for the fact that in this trimer the binding site Chl b2 is actually occupied by Chl b.

For the correct interpretation of the results there remains three serious questions to be answered: (i) why is the spectrum of the cross-section of emission obtained by decomposition of the ξ -spectrum narrower than the fluorescence spectrum; (ii) how can the discrepancy between absorption and ξ -spectrum for $\lambda_p < 670 \text{nm}$ be explained; and (iii) is the result also cogent for the other possible models? One will see that the answers for the first and the second question are related to each other and lead directly to that of the third question.

9.3.2 Decomposition of the fluorescence band

The simplest explanation for the narrower emission band as obtained by decomposition of the ξ -spectrum is a substructure within fluorescence spectrum. This means more than one

emitting species for the LHC II. In fact, the fluorescence spectrum of LHC II has neither Gaussian nor Lorentzian line shape. Decomposition of the fluorescence spectrum by subtracting the Gaussian subband as obtained from the ξ -spectrum, which may not be inhomogeneously broadened (but indicates probably inhomogeneous dephasing, cf. summary to chapter 5 and ref. [Knapp, 1984]) produces an additional Lorentzian sub-band centered at $672 \pm 3\text{nm}$ with line width $FWHM = 260 \pm 30\text{cm}^{-1}$ (cf. Fig. 9.6). As one can see further subbands in the respective region are not needed. The maximum cross-section of pumping the additional emission band is formally $\sigma_{em}(672\text{nm}, 672\text{nm}) = 0.35 \pm 0.1 \times 10^{-15}\text{cm}^2$, which means that this band contributes less than 20% to the total fluorescence yield. Due to its absence in the ξ -spectrum the additional subband can not belong to the same emitter as the main subband at 683nm and the quantum yields can differ. Hence the cross-sections of the two emission subbands are not directly comparable.

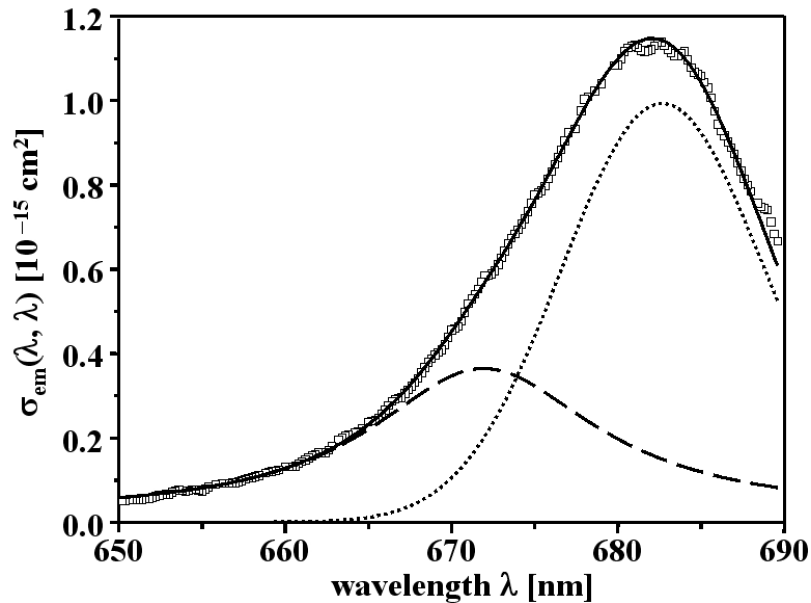


Figure 9.6: Decomposition of the measured fluorescence spectrum of LHCII (open squares) into the Gaussian subband of emission from the ξ -spectrum (dotted line; cf. Fig. 9.5) and an additional Lorentzian subband centered at 672nm with $FWHM = 260\text{cm}^{-1}$ (dashed line). For comparison the recomposed fluorescence spectrum is shown (solid line).

Nevertheless, the additional emitter at 672nm may influence the ξ -spectrum otherwise. Notably, the position of the additional subband fits quite well to the wavelength where the ξ -spectrum breaks off towards shorter wavelength (cf. Fig. 9.5). This already suggests that there exists a branching in the energy transfer path somewhere between 665nm and 670nm.

9.3. Pump-intensity-dependent NLPF-spectra for LHC II

In chapter 6 also cases of energy transfer chains with more than one emitter have been discussed (cf. section 6.2.2). First the case of fast energy transfer between the two emitters (cf. Eqs. 6.19 and 6.20) shall be discussed for the present problem. According to the difference in transition frequency between the two subbands of approximately 280cm^{-1} at room temperature (300K) one obtains as weights $w_{672} = 20\%$ and $w_{683} = 80\%$. These values fit quite well to the distribution of the total fluorescence yield on the two respective subbands as results from the decomposition of the fluorescence spectrum. This would mean that the two emitters are thermally equilibrated. Then, however, according to Eq. 6.19 the ξ -spectrum should also *contain* exactly that subband at 672nm which has been found by being *missed* in the ξ -spectrum (see above). For this contradiction, the model with fast excitation exchange between the two subbands has to be abandoned. Nevertheless, the calculation has shown at least that parallel emitter which are not strongly excitonically coupled but exchange excitation via Förster-type transfer can not explain the enhancement of the oscillator strength in emission.

For branching to two acceptors, which can not exchange excitation between each other, only the contribution of the probed acceptor appears in the ξ -spectrum (cf. Eqs. 6.22 and 6.23), as observed in Fig. 9.5. In the present case for probing at 685nm, the probed acceptor is clearly related to the subband at 683nm. This kind of branching in the energy transfer path is also able to explain the break off of the ξ -spectrum for pump wavelength $\lambda_p < 670\text{nm}$, which is in the spectral range for pumping the donors. According to Eq. 6.22 two different saturation parameters occur: One for the probed acceptor at 685nm given by

$$\xi_{685}(\lambda_p < 670\text{nm}) = \frac{\sigma_{abs}(\lambda_p < 670\text{nm})}{\gamma_{eff}}, \quad (9.3)$$

with an effective ground-state recovering rate $\gamma_{eff} = \gamma_{683}/b_{683}$ obviously higher than that of the probed acceptor itself (γ_{683}) for the branching ratio being $b_{683} < 1$ (cf. Eq. 6.23). The other ξ -spectrum for probing the acceptor emitting at 672nm has not been determined. Though this would in principle allow one to determine the branching ratio $b_{672} : b_{683}$, in the present case the results were more than questionable. Firstly, the acceptor subband at 672nm reaches into the spectral region of the donors for $\lambda_p < 670\text{nm}$ (cf. Fig. 9.6). Secondly, different orientations of the transition dipoles of the acceptors and donors will change the ξ -spectrum for this region in an unpredictable way. Therefore, even the value of γ_{eff} is rather arbitrary, and Eq. 9.3 is of more qualitative character in order to explain the break off of the ξ -spectrum. For the contributions by absorption and emission of the probed acceptor (emission subband at 683nm), however, one could confidently assume that the transition dipoles are parallel. Therefore, the quantitative results obtained from the ξ -spectrum for $\lambda_p > 670\text{nm}$ are reliable.

9.4 Summary

The ξ -spectrum obtained from the pump-intensity-dependent of the NLPF-spectra of LHC II has revealed a (1.9 ± 0.5) -fold enhancement of oscillator strength in an Gaussian-shaped emission subband centered at 683nm. By site-directed mutageneses the red-most subbands in absorption has been previously assigned to the Chl a2 binding site of LHC II [Rogl et al., 2002]. The resulting enhancement of the emission dipole-strength is most probably originated by strong excitonic coupling between the chlorophyll binding sites a2 and b2. Thereby, it is an open question whether the original, tentative assignment of these binding sites [Kühlbrandt et al., 1994] to Chl a and Chl b can be uphold. In fact, there is some evidence from the result be presented as well as from theoretical considerations [Beenken et al., 2002] that the Chl b2 binding site may be occupied by Chl a instead of Chl b.

Furthermore, the analysis of ξ -spectrum in combination with a decomposition of the fluorescence spectrum reveals two emission bands: A Gaussian subband at 683nm has been found in the ξ -spectrum, the other Lorentzian-shaped at 673nm, which provides only 20% to the total fluorescence yield, is missed in the ξ -spectrum. This fact leads to the assumption of a branching in the energy transfer path around 670nm to two different termini, which is also in good agreement with a break off for the ξ -spectrum in absorption for pump-wavelength $\lambda_p < 670$ nm. Due to an apparent thermalization for the oscillator strengths of the two emission subbands energy transfer between the two emitters could not be completely ruled out, but at least it has to be much slower than that from binding sites located at $\lambda_p < 670$ nm. Most probably they are more spacially than energetically separated. The existence of two subbands may not be in contradiction to a recent study on the bleaching behavior and fluorescence polarization of single complexes [Tietz et al., 2001]. The observed unique polarization of emission for each of the three subunits in trimeric LHC II may result from parallel oriented transition dipoles for the two subbands. By reasons of symmetry this means that the second emitter belongs to the same LHC II monomer, and that the branching is inside this monomer [A. Schubert, personal communication].

9.5 Supplement: Calculation of excitonic coupling in the Chl a2/b2 dimer

Due to the dipole–dipole interaction

$$V_{ab} = \frac{1}{4\pi\epsilon_0} \left(\frac{\mu_a\mu_b}{R_{ab}^3} - 3 \frac{(\mu_a\mathbf{R}_{ab})(\mu_b\mathbf{R}_{ab})}{R_{ab}^5} \right) \quad (9.4)$$

9.5. Supplement: Calculation of excitonic coupling in the Chl a2/b2 dimer

between the monomeric transition dipoles μ_a and μ_b separated by a distance vector \mathbf{R}_{ab} (cf. Eq. 8.1, and ref. [Cantor and Schimmel, 1980, Atkins, 1998]) the supramolecular Hamiltonian for the dimer yields as

$$H_{ab} = \begin{pmatrix} \varepsilon_a & V_{ab} \\ V_{ab} & \varepsilon_b \end{pmatrix}. \quad (9.5)$$

By diagonalization one obtains the eigen-frequencies by

$$\hbar\omega_{\pm} = \frac{\varepsilon_a + \varepsilon_b}{2} \pm \sqrt{\left(\frac{\varepsilon_b - \varepsilon_a}{2}\right)^2 + V_{ab}^2} \quad (9.6)$$

with associated eigenvectors

$$c_{\pm,a} = -\sqrt{\frac{\hbar\omega_{\pm} - \varepsilon_b}{2\hbar\omega_{\pm} - \varepsilon_a - \varepsilon_b}} \quad \text{and} \quad c_{\pm,b} = +\sqrt{\frac{\hbar\omega_{\pm} - \varepsilon_a}{2\hbar\omega_{\pm} - \varepsilon_a - \varepsilon_b}}. \quad (9.7)$$

Therefore, the transition dipole moments of the two subbands at ω_+ and ω_- are superpositions as given by

$$\mu_{\pm} = c_{\pm,a}\mu_a + c_{\pm,b}\mu_b, \quad (9.8)$$

and the corresponding transition dipole strengths yield as

$$|\mu_{\pm}|^2 = \frac{|\hbar\omega_{\pm} - \varepsilon_b|\mu_a^2 + |\hbar\omega_{\pm} - \varepsilon_a|\mu_b^2 - 2\sqrt{(1\hbar\omega_{\pm} - \varepsilon_b)(1\hbar\omega_{\pm} - \varepsilon_a)}\mu_a\mu_b \cos \phi_{ab}}{|2\hbar\omega_{\pm} - \varepsilon_a - \varepsilon_b|}, \quad (9.9)$$

where $\phi_{a_1a_2}$ is the angle between the monomeric transition dipoles μ_a and μ_b . The resulting transition dipoles μ_+ and μ_- of the dimer will be differently oriented [Cantor and Schimmel, 1980].

The dipoles for transitions from the one-exciton states $|+\rangle$ and $|-\rangle$ to the two-exciton state $|ab\rangle$ yields as

$$\mu_{ab,\pm} = c_{\pm,a}\mu_b + c_{\pm,b}\mu_a. \quad (9.10)$$

These are completely different from the dipoles μ_{\pm} for the transition between ground- to one-exciton states. Only for the case $c_{-,a} = c_{+,b} = 1$ and $c_{+,a} = c_{-,b} = 0$, which occurs in the case of no interaction between the monomers, i.e. $V_{ab} = 0$ one obtains $\mu_{ab,\pm} = \mu_{\mp}$. This corresponds exactly to the mapping for the incoherent energy transfer as given in section 6.2.2.

Chapter 10

Spectral substructure and excitonic interactions in the minor Photosystem II antenna complex CP29

The minor antenna complex CP29 is definitely attached to PS II. More precisely it is located between LHC II and the core antenna CP47 of PS 2 [Simpson and Knoetzel, 1996]. Therefore, it has been assumed to play a regulatory role in the excitation energy funneling from the bulk antennae LHC II towards the reaction center but may be also only a geometrically adapted docking station for the trimeric LHC II to the core antenna CP47. As minor antenna complex CP29 binds only 6 Chl a and 2 Chl b. Beside of chlorophylls CP29 contains also several xanthophylls, namely lutein, neoxanthin, and violaxanthin. Though there does not exist structure data from crystallography, iCP29 is assumed to be quite similar to a fraction of the LHC II monomer. Accordingly, the assignment of the Chl binding sites takes place as for the known LHC II structure leaving out those sites which are not to apparent in CP29 due to the lower Chl content [Cinque et al., 2000b, Simonetto et al., 1999]. Of course in this case the assignment of Chl a and b is even more tentative than it has been for LHC II .

All the more, it is interesting to study the interaction between the Chls in CP29 by spectroscopic methods. The absorption spectrum of CP29 at room temperature is shown in Fig. 10.1. As usual for Chl binding protein complexes the spectrum contains with three rather broad bands: the Q_y -absorption band is located between 660 and 680nm with the major peak at 676.5nm assigned to Chl a, and a much minor peak at approximately 650nm, assigned to Chl b. There exists a decomposition the Q_y -band into subbands assigned to the assumable binding sites in CP29 [Giuffra et al., 1997]. The Q_x -bands are broad and quite unspecific but definitely beyond 550nm. The Soret region of Chl a in CP29 is assumed to be located between

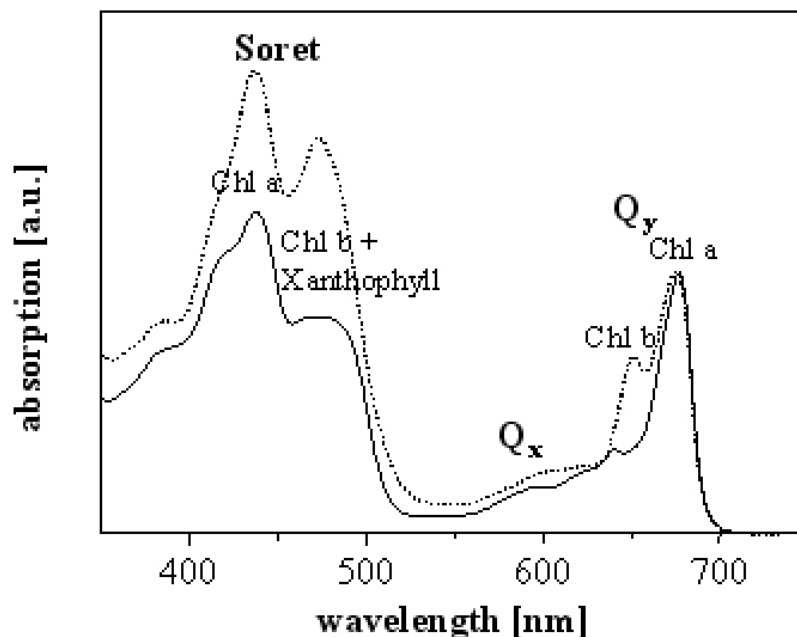


Figure 10.1: Absorption spectrum of CP29 (solid line) and for comparison that of LHC II (dots, normaliyed to Q_y -band) [Voigt et al., 2002]

400 and 460nm peaking at 440nm (B_x -band) and with a shoulder at 420nm (B_y -band), while the Soret of Chl b overlaps completely with the absorption of the xanthophylls in the region between 460 and 520nm [Giuffra et al., 1997, Pascal et al., 1999]. For low temperatures down to 13K, in the latter region three peaks become apparent. One at 464nm has been attributed to Chl b, the others at 483 and 496nm to the xanthophylls [Pascal et al., 1999]. Notably, the peaks in the Soret of Chl a are nearly unchanged. A deconvolution of the Soret absorption of CP29 at room temperature predicts clearly that the contributions by Chl a and b are well distinguishable [Gradinaru et al., 1998a], though there exists quantum chemical calculations predicting weak contributions from Chl a in the respective spectral range [Parusel and Grimme, 2000, Sundholm, 2000]. Nevertheless, in what follows it will be assumed that between 460 and 550nm absorption by Chl a is negligible. Time resolved pump-probe spectroscopy has already revealed also the kinetics between the subbands in the Q_y -band with energy transfer rates between 350fs and 13ps. Nevertheless subband analysis by means of NLPF may provide additional information about this spectral region. Due to the lower number of bound Chls in CP29 the T_2 -peak analysis might be not as difficult as it turns out to be for LHC II.

A possible excitonic coupling between Chl a and b is of particular interest. There exists some hints to a mixing of Chl a and b states by the appearance of a weak fluorescence in a

spectral region, which has been assigned to the Soret of Chl b, after two-photon excitation at 670nm, which should be in the spectral region of Q_y -absorption for Chl a only [Leupold et al., 2002]. In the work be presented [Voigt et al., 2002], a similar effect is searched for by pumping the Q_y -absorption and probing in the Soret in NLPF. Compared to the T_1 -peak analysis for only the Q_y -band, this approach has the great advantage that the effect to be observed is much less interfered by the energy transfer from Chl b to Chl a.

10.1 T_2 -peak analysis within the Q_y -band of CP29

In order to get information about the substructure of the Q_y -band of CP29, first the standard T_2 -peak analysis where probe and pump cover the same spectral region, here the Q_y -band will be applied (cf. Figs. 4.2, 4.4, and 4.6 in chapter 4).

NLPF-spectra¹ of CP29 have been recorded for pump wavelengths from 635 to 700nm, i.e. over nearly the entire Q_y -absorption band for fixed probe wavelengths moved from 640 to 690nm in steps of 10nm (see Fig. 10.2). The T_2 -peak analysis according to the methods described in section 4.2 has revealed three subbands at 660, and 670, and 681nm. For this spectral region Chl a is assumed to absorb. While the subband at 681nm is clearly heterogeneous to the other two (cf. Eq. 4.48), the nature of the substructure between the subbands at 660 and 670nm could not be clarified unequivocally. Most probably they constitute a homogeneous substructure.

Surprisingly, the T_2 -peak maximum shifted back from 665 to 670nm for moving the probe wavelength from 650 to 640nm. This accounts for a subband around 640nm which is associated to the subband at 670nm either by homogeneous substructure or excited state absorption. This can not be the excited state absorption from Q_{ya} to B_{xb} (cf. Fig. 10.3 arrow 1), which is located in the infrared around 1280nm, but should be one to an higher excited state around 330nm. However, the fact, that the respective transition appears clearly in the probe- but not the pump-wavelength dependence, typical for excited state absorption (cf. Fig. 4.9 in section 4.1.4), is not a sufficient argument against a homogeneous substructure in the present case. In fact the existence of subbands in the region around 640nm, where the Q_y -absorption of Chl b is expected, could be neither proven nor excluded due to the high signal to noise ratio in the region for pump wavelengths $\lambda_p < 645$ nm. However, even much more accurate NLPF-spectra will not help to reveal the spectral substructure in the Q_y -region of the Chl b, unequivocally. Due to the quadratic dependence of the NLPF-signal on the cross-section of pumping, the peaks representing the Q_y -absorption of Chl b, which are already tiny in the absorption spectrum (cf.

¹CP29 isolation and sample preparation by K.-D. Irrgang, NLPF-spectra by B. Voigt, Fits by J. Ehlert and B. Voigt using the software package NLPF 8.3 based on ref. [Ehlert and Beenken, 1998].

10.2. T_2 -peaks of CP29 for pumping the Q_y -band and probing the Soret

absorption spectrum, Fig. 10.1), the corresponding T_2 -peak would be vanishing small in any case, even for a homogeneous substructure.

10.2 T_2 -peaks of CP29 for pumping the Q_y -band and probing the Soret

As mentioned in the previous chapter (cf. section 9.2.5) excitonic coupling in particular between Chl a and Chl b can be found by T_2 -peak analysis due to the different redistribution of oscillator strength for ground- and excited-state transitions (cf. supplement 9.5). This effect may work also for pumping the Q_y -band and probing in the Soret. For a in-line arrangement of the Q_y -transition dipoles of the two Chl, the B_x -transition dipoles are necessarily in ‘sandwich’-configuration, i.e. parallel to each other but perpendicular to the distance vector (cf. section 9.2.1). In an ideal in-line Chl homodimer, where the redistribution of the oscillator strengths is maximum, the transitions from the one-exciton state $|Q_{y-}\rangle$ to the two-exciton state $|Q_{y-}+B_{x-}\rangle$ (cf. Fig. 10.3 arrow **3**) is allowed but not the corresponding transitions from ground-state $|0\rangle$ to the one-exciton state $|B_{x-}\rangle$ (cf. Eqs. 9.8 and 9.10). This difference results in an observable NLPF-signal for probing the B_{x-} -band and pumping Q_{y-} -band. The corresponding term of the NLPF-line-shape function is given as

$$s(\omega_t, \omega_p) = (\zeta_2(\omega_t) - \zeta_3(\omega_t)) \frac{1}{\gamma_{gsr}} \sigma_1(\omega_p, \omega_p) + \dots, \quad (10.1)$$

(indices according to Fig. 10.3). This holds even if one considers that the Q_y - and B_x -transition dipoles are not exactly perpendicular to each other [Scherz et al., 1991, Fuchs et al., 2003] and that the Chls may be of different kind, since only the uncoupled dimer without any redistribution of oscillator strength would result in $\zeta_2(\omega_t) - \zeta_3(\omega_t) = 0$, i.e. no NLPF-signal (cf. supplement 9.5).

NLPF-spectra of CP29 probed in the Soret region at 450, 460, 470, and 485nm has been recorded for pump wavelengths from 630 to 690nm, i.e. in the Q_y -region (see Fig. 10.2). For probing at 450 and 460nm the Soret of Chl a (see above) the pump-frequency dependence of the NLPF spectrum shows clearly two Q_y -subbands, one around 630nm, which represents Chl b, and a much larger one for Chl a at 670nm, which has been already seen in the NLPF-spectra probed and pumped in the Q_y -region (cf. Fig. 10.2). This result has been expected due to the energy transfer from Chl b to Chl a and a probable contamination of the Chl a B_x -band by the Chl b B_y -band, though not in such an extent (cf. previous section concerning Q_y -bands of Chl b).

Surprisingly, the NLPF-spectra do not change much when the probe wavelength is changed to 470 and 485nm, respectively, i.e. to the spectral region, where namely the B_x -band of Chl b but not the Soret of Chl a is assumed to be probed. One can still see the Q_y -subband at 670nm as the dominant one, while the Q_y -subband for Chl b around 630nm does not rise but gets only broader. These observations indicate strong influence of the excitation at 670nm, which is assigned to Chl a, on the Soret-band of Chl b or the xanthophylls (supposed the assignments for the previous decomposition of the absorption spectrum of CP29 [Gradinaru et al., 1998a] are correct). The most probable effect on the Soret-band of Chl b may be excitonic coupling between a Chl a/b pair in CP29 due to different redistribution of oscillator strength for the ground- and excited-state absorption, as described above. However, there exist other processes which provide similar effects. In particular for the bacterial antenna LH2 as well as for LHC II electrochromic shifts of the xanthophylls absorption for pumping the Q_y -band have been reported [Herek et al., 1998, Gradinaru et al., 2003]. In this case it is not the transition dipole, but the changed permanent charge distribution of Chl a in the excited state, which changes the transition frequency to the xanthophylls. Since they create the same difference between ground- and excited-state absorption as probed by NLPF (cf. $\zeta_2(\omega_t) - \zeta_3(\omega_t)$ in Eq. 10.1), electrochromic shifts can not be excluded as origin of the observed correlation between the Q_y -band at 670nm and the probing the spectral region between 470 and 485nm. If this explanation holds instead of the excitonic coupling, the correlation between the subband at 670nm and a band around 640nm (see above), which is hidden in the NLPF-spectrum, but for absorption clearly assigned to Chl b [Gradinaru et al., 1998a], has to be interpreted as excited state absorption to a higher excited state of Chl a.

Last but not least it has to be noted that the Q_y -subband at 681nm, found for probing the Q_y -region, is not apparent in all NLPF-spectra probed between 450 and 485nm. This means that the Soret band of the corresponding Chl a may be blue-shifted as the Q_y -band is red-shifted compared to the other subbands. The origin of this phenomenon could not be clarified on the basis of the available data. Stronger excitonic coupling as for the other subbands is not a sufficient explanation, since even for maximum redistribution of oscillator strength both bands B_{x+} and B_{x-} are detectable by NLPF, the one as ground-state absorption, the other as excited-state absorption, respectively (see above).

10.3 Summary

The T_2 -peak analysis of the NLPF-spectra of CP29 has revealed two distinct regions for the Chl a absorption in the Q_y -band. One represented by a single subband at 681nm, the other by two subbands at 660 and 670nm. This separation is reflected by the Soret region as well.

10.3. Summary

There exist strong correlation between the latter subbands and the Chl a Soret bands around 450 , which astonishingly is extended till 485nm, where the Soret of Chl b and the xanthophyll absorption are located. The previous interpretation [Voigt et al., 2002] of the latter correlation as clear indication for excitonic coupling between Chl a and b in CP29 might be to revise in favour of electrochromic shifts as have been found for LHC II, recently [Gradinaru et al., 2003]. Finally it has to be noted that similar results as presented here for CP29 have been also obtained for LHC II, except that in LHC II the red-most band seems to be fully involved in the correlation between Q_y -bands and the Chl b Soret and xanthophyll bands, respectively [Krikunova et al., 2002].

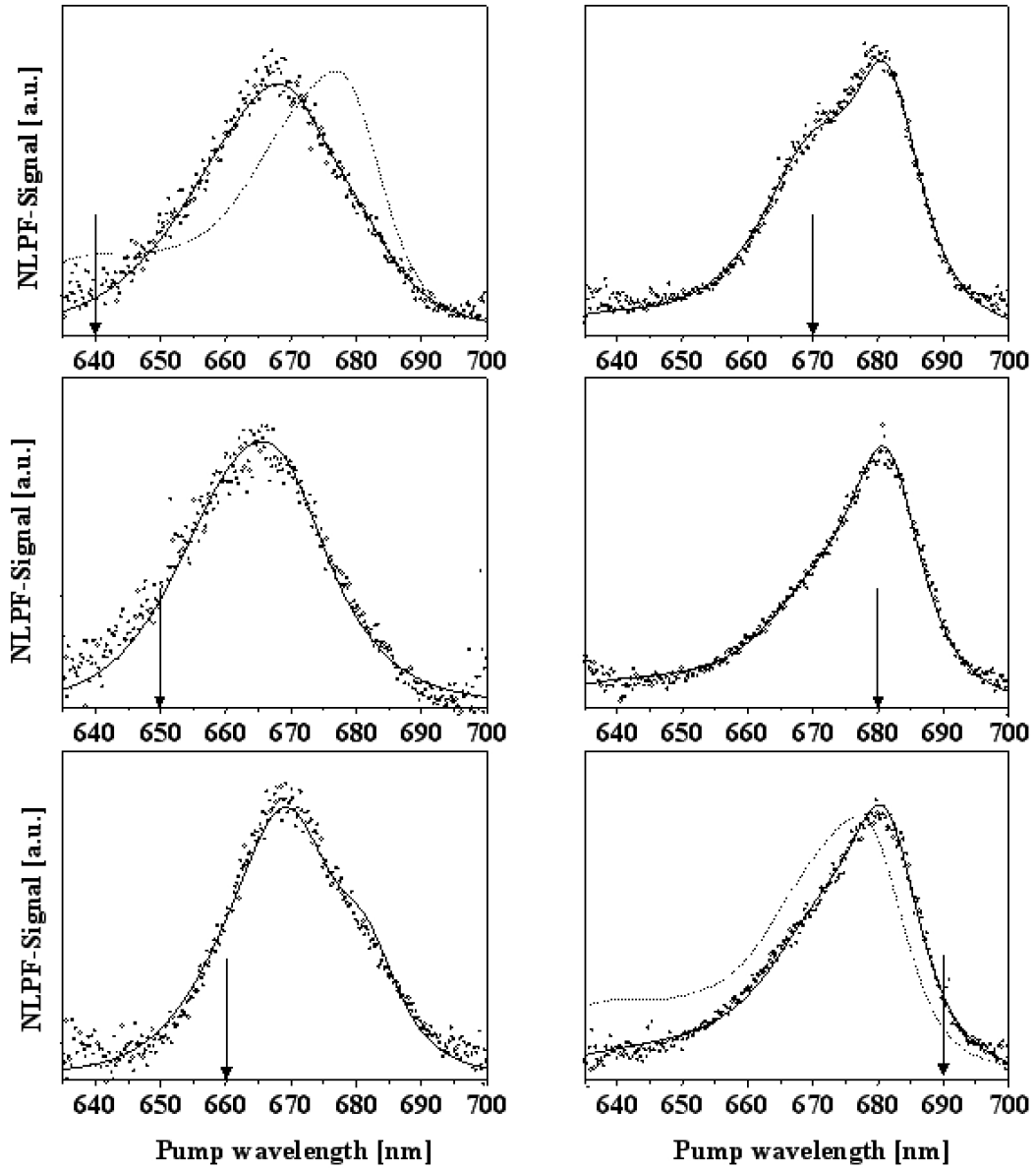


Figure 10.2: NLPF spectra for CP29 probed (arrows) and pumped in the Q_y -band (data: circles, fit: solid line). For comparison, the absorption spectrum is displayed for two panels (dotted line). [Voigt et al., 2002]

10.3. Summary

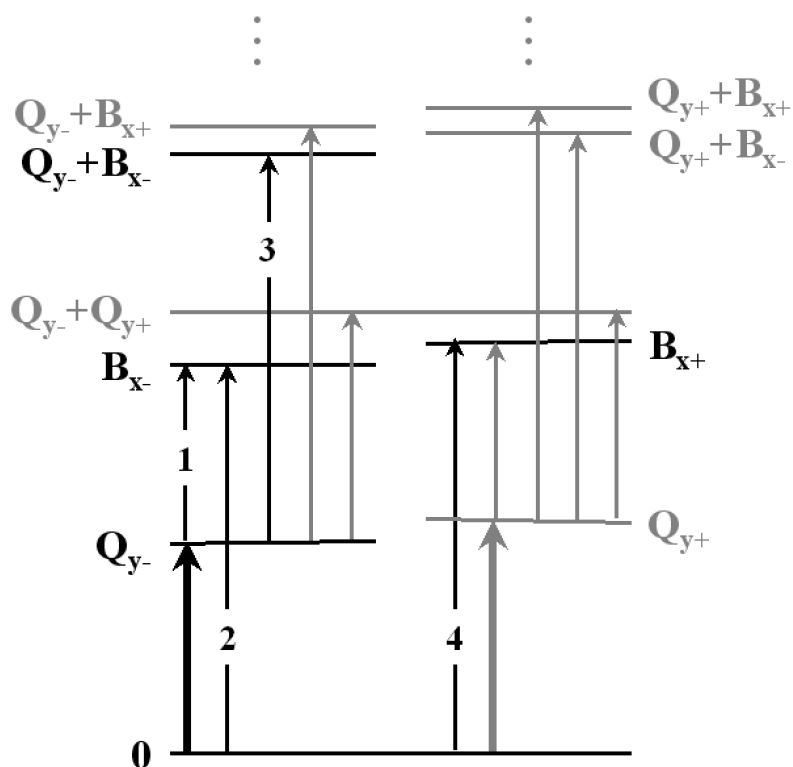


Figure 10.3: Term scheme for the Chl a/b dimer with excitonic coupling. The singly excited states are assigned due to their spectral position in the Q_{y-} -band and the Soret (B_x), respectively, and the sign according to Eq. 9.6. States corresponding to the Q_x and B_y bands are not shown. The doubly excited states are assigned by the sum of the respective excitation bands. Possible transitions between singly and doubly excited states are indicated by arrows, where states and transitions relevant for the NLPF measurements described in the text are emphasized by darker inking. The pumping is represented by a bold arrow. For numbering of the probed transitions see text.

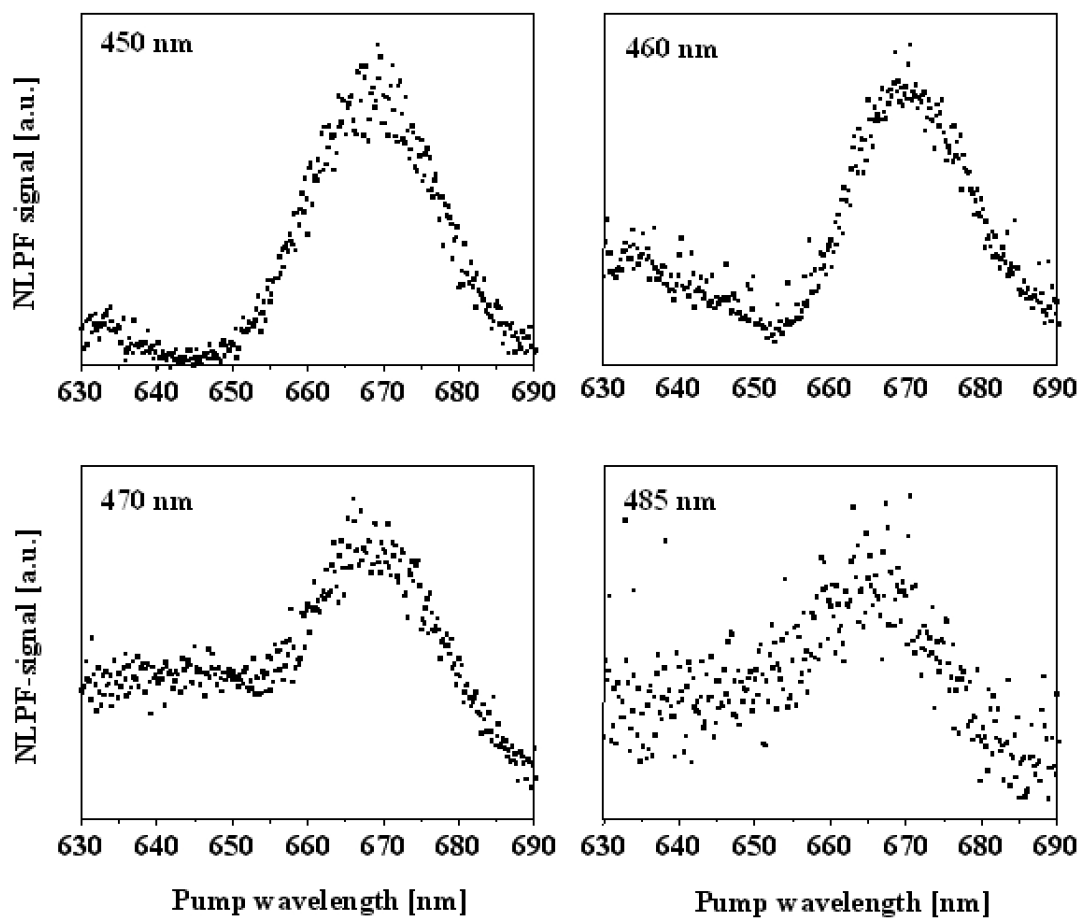


Figure 10.4: NLPF spectra for CP29 probed in the Soret region at 450, 460, 470 and 485nm (cf. panel assignment) for pumping the Q_y -band. [Voigt et al., 2002]

Chapter 11

Conclusion

In the work have been presented, starting from first principles a consistent, all-purpose theory for NLPF at low pump intensities could be established and more than first steps towards strong-field theory for NLPF have been achieved. In particular the theoretical description of NLPF-spectra for multi-level systems, combined with models for homogeneous and inhomogeneous broadening including also spectral diffusion, represents a break through for applicability of NLPF to complex molecular and supra-molecular systems. This has been demonstrated in particular for photosynthetic antennae (LH2 of purple bacteria and CP29 of higher plants). Beside these even previously studied mechanisms of broadening a general description in terms of non-Markovian dissipation processes has been presented.

Though being limited in praxi to the two-level system and special cases of multi-level systems, which can be mapped to it, the strong-field theory of NLPF developed here, has opened a complete new field of applications for NLPF. The pump-intensity dependence of the NLPF-spectra allows one to determine the absolute cross-sections of absorption, emission, and excited state absorption. This is of special interest for determination of molecular aggregation by size-enhancement of the absorption, and exciton delocalization by superradiant emission, independently of knowledge for the chromophore concentration.

Both techniques, low-intensity and strong-field NLPF, have been applied to photosynthetic antennae in order to determine the nature of their excited states. Thereby it turns out that the excitation on the circular B850-aggregate of the peripheral antenna LH2 of *Rb. molischianum* represents a exciton delocalized over 3-4 of the 16 bacteriochlorophylls. This supports the previous results from exciton–exciton annihilation [Trinkunas et al., 2001] in a long-standing debate. For the LH2 of *Rb. sphaeroides* surprisingly two subbands hidden in the B850 absorption band could be revealed by NLPF. In the higher-plant antenna complexes LHC II and CP29 evidence for excitonic coupling between chlorophylls could be provided at least for the

former case, by pump-intensity dependence of the NLPF-spectra. The attempt to CP29 using only low-intensity NLPF-spectra results unfortunately in an ambiguity between two interpretations: excitonic coupling between at least one Chl a and one Chl b or electrochromic shifts of xanthophylls induced by excitation of Chl a. Here further investigation, particularly probe frequency dependent NLPF spectra, may resolve this problem.

In the limited framework of the presented work, not to all experimental techniques resulting from the fundamental theory could be demonstrated. In particular the usage of so-called Raman-peaks in low-temperature NLPF is an interesting field for future applications. Also the strong-field theory of NLPF may be extendable.

Bibliography

- [Abramowitz and Stegun, 1972] Abramowitz, M. and Stegun, I. A. (1972). *Handbook of Mathematical Functions*. Dover Publications, Inc., New York, 9 edition.
- [Agarwal et al., 2000] Agarwal, R., Krueger, B. P., Scholes, G. D., Yang, M., Yom, J., Mets, L., and Fleming, G. R. (2000). Ultrafast energy transfer in lhci-ii revealed by three-pulse photon echo peak shift measurements. *J. Phys. Chem. B*, 104:2908–2918.
- [Alberts et al., 2002] Alberts, B., Bray, D., Lewis, J., Raff, M., Roberts, K., and Watson, J. D. (2002). *Molecular biology of the cell*. Garland Publ, 4 edition.
- [Amesz and Hoff (eds), 1996] Amesz, J. and Hoff (eds), A. (1996). *Biophysical techniques in photosynthesis*. Kluwer Academic Publishers, Dordrecht.
- [Andrews and Hochstrasser, 1980] Andrews, J. R. and Hochstrasser, R. M. (1980). Femtosecond relaxation of an iron porphyrin observed with polarization spectroscopy in a three-level system. *Proc. Natl. Acad. Sci.*, 77:3110–3114.
- [Atkins, 1998] Atkins, P. W. (1998). *Physical Chemistry*. Oxford University Press, Oxford, 6 edition.
- [Bakalis et al., 1999] Bakalis, L. D., Coca, M., and Knoester, J. (1999). Optical line shapes of dynamically disordered ring aggregates. *J. Chem. Phys.*, 110:2208–2218.
- [Bakalis and Knoester, 1999] Bakalis, L. D. and Knoester, J. (1999). Pump-probe spectroscopy and the exciton delocalization length in molecular aggregates. *J. Phys. Chem. B*, 103:6620–6628.
- [Barzda et al., 2001] Barzda, V., Gulbinas, V., Kananavicius, R., Cervinskis, V., van Amerongen, H., van Grondelle, R., and Valkunas, L. (2001). Singlet-singlet annihilation kinetics in aggregates and trimers of LHC II. *Biophys. J.*, 80:2409–2421.

- [Beenken and Ehlert, 1998] Beenken, W. and Ehlert, J. (1998). Subband analysis of molecular electronic transitions by nonlinear polarization spectroscopy in the frequency domain. *J. Chem. Phys.*, 109:10126–10137.
- [Beenken and May, 1997] Beenken, W. and May, V. (1997). Strong field theory of nonlinear polarization spectroscopy. fundamentals and the two-level system. *J. Opt. Soc. Am. B*, 14:2804–2810.
- [Beenken et al., 2002] Beenken, W. J. D., Dahlbom, M., Kjellberg, P., and Pullerits, T. (2002). Potential surfaces and delocalization of excitons in dimers. *J. Chem. Phys.*, 117:5810–5820.
- [Berg et al., 2002] Berg, J. M., Tymoczko, J. L., and Stryer, L. (2002). *Biochemistry*. W. H. Freeman, New York, 5 edition.
- [Biot, 1844] Biot, M. (1844). Sur l’emploi de la lumière polarisée pour étudier diverses questions de mécanique chimique. *Ann. Chim. Phys.*, 10:5–55.
- [Blankenship, 2001] Blankenship, R. E. (2001). *Molecular mechanisms of photosynthesis*. Blackwell Science, Malden, MA.
- [Blankenship et al., 1995a] Blankenship, R. E., Madigan, M. T., and Bauer (eds), C. E. (1995a). *Anoxygenic Photosynthetic Bacteria*. Kluwer Academic Publishers, Dordrecht.
- [Blankenship et al., 1995b] Blankenship, R. E., Olson, J. M., and Miller, M. (1995b). Antenna complexes from green photosynthetic bacteria. In Blankenship, R. E., Madigan, M. T., and Bauer, C. E., editors, *Anoxygenic Photosynthetic Bacteria*, chapter 20, pages 399–435. Kluwer Academic Publishers, Dordrecht.
- [Blum, 1981] Blum, K. (1981). *Density Matrix Theory and Applications*. Plenum Press, New York.
- [Brüggemann et al., 2001] Brüggemann, B., Herek, J. L., Sundström, V., Pullerits, T., and May, V. (2001). Microscopic theory of exciton annihilation: Application to the lh2 antenna system. *J. Phys. Chem. B*, 105:11391–11394.
- [Camara-Artigas et al., 2003] Camara-Artigas, A., Blankenship, R. E., and Allen, J. P. (2003). The structure of the FMO protein from *chlorobium tepidum* at 2.2 Å resolution. *Photosynth. Res.*, 75:49–55.
- [Cantor and Schimmel, 1980] Cantor, C. R. and Schimmel, P. R. (1980). *Biophysical Chemistry Part II: Techniques for the study of biological structure and function*. W. H. Freeman, New York.

Bibliography

- [Chachisvilis et al., 1997] Chachisvilis, M., Kühn, O., Pullerits, T., and Sundström, V. (1997). Excitons in photosynthetic purple bacteria: Wavelike motion or incoherent hopping? *J. Phys. Chem. B*, 101:7275–7283.
- [Chachisvilis and Sundström, 1996] Chachisvilis, M. and Sundström, V. (1996). The tunneling contributions to optical coherence in femtosecond pump-probe spectroscopy of a three level system. *J. Chem. Phys.*, 104:5734–5744.
- [Cinque et al., 2000a] Cinque, G., Croce, R., and Bassi, R. (2000a). Absorption spectra of chlorophyll a and b in lhcb protein environment. *Photosynth. Res.*, 64:233–242.
- [Cinque et al., 2000b] Cinque, G., Croce, R., Holzwarth, A. R., and Bassi, R. (2000b). Energy transfer among cp29 chlorophylls: Calculated förster rates and experimental transient absorption at room temperature. *Biophys. J.*, 79:1706–1717.
- [Cogdell et al., 1997] Cogdell, R. J., Isaacs, N. W., Freer, A. A., Arrelano, J., Howard, T. D., Papiz, M. Z., Hawthornthwaite-Lawless, A. M., and Prince, S. (1997). The structure and function of the LH2 (B800-B850) complex from the purple photosynthetic bacterium *rhodospseudomonas acidophila* strain 10050. *Prog. Biophys. molec. Biol.*, 68:1–27.
- [Cohen-Tannoudji et al., 1977] Cohen-Tannoudji, C., Diu, B., and Laloë, F. (1977). *Quantum mechanics*. Wiley-Interscience, New York.
- [Connelly et al., 1997] Connelly, J. P., Müller, M. G., Hucke, M., Gatzten, G., Mullineaux, C. W., Ruban, A. V., Horton, P., and Holzwarth, A. R. (1997). Ultrafast spectroscopy of trimeric light-harvesting complex ii from higher plants. *J. Phys. Chem. B*, 101:1902–1909.
- [Dahlbohm, 2002] Dahlbohm, M. (2002). *Collective Excitation Dynamics in Molecular Aggregates*. PhD thesis, Chemical physics, Lund University.
- [Dahlbom et al., 2002] Dahlbom, M., Beenken, W., Sundström, V., and Pullerits, T. (2002). Collective excitation dynamics and polaron formation in molecular aggregates. *Chem. Phys. Lett.*, 364:556–561.
- [Dahlbom et al., 2000] Dahlbom, M., Minami, T., Chernyak, V., Pullerits, T., Sundström, V., and Mukamel, S. (2000). Exciton-wave packet dynamics in molecular aggregates studied with pump-probe spectroscopy. *J. Phys. Chem. B*, 104:3976–3983.
- [Dahlbom et al., 2001] Dahlbom, M., Pullerits, T., Mukamel, S., and Sundström, V. (2001). Exciton delocalization in the b850 light-harvesting complex: Comparison of different measures. *J. Phys. Chem. B*, 105:5515–5524.

- [Deisenhofer et al., 1984] Deisenhofer, J., Epp, O., Miki, K., Huber, R., and Michel, H. (1984). X-ray structure analysis of a membrane protein complex. electron density map at 3 Å resolution and a model of the chromophores of the photosynthetic reaction center from *Rhodospirillum rubrum*. *J. Mol. Biol.*, 180:385–98.
- [DeLong and Trebino, 1994] DeLong, K. W. and Trebino, R. (1994). Improved ultrashort-pulse-retrieval algorithm for frequency-resolved optical gating. *J. Opt. Soc. Am. A*, 11:2429–2437.
- [Ehlert and Beenken, 1998] Ehlert, J. and Beenken, W. (1998). *NLFF 6.0 (Software)*. Max-Born-Institute, Berlin.
- [Feshbach, 1962] Feshbach, H. (1962). A unified theory of nuclear reactions 2. *Ann. Phys.*, 19:287–313.
- [Förster, 1948] Förster, T. (1948). Zwischemolekulare energiewanderung und fluoreszenz. *Ann. Phys.*, 6:55–75.
- [Fuchs et al., 2003] Fuchs, H., Zimmermann, J., and Röder, B. (2003). Experimental determination of the orientation of excited state transition dipoles in tetrapyrroles with different molecular symmetries. *Opt. Comm*, 220:119–127.
- [Garcia-Golding, 1983] Garcia-Golding, F. (1983). Spectral-diffusion effects in polarization spectroscopy. *J. Opt. Soc. Am. A*, 73:59–62.
- [Giuffra et al., 1997] Giuffra, E., Zucchelli, G., Sandonà, D., Croce, R., Cugini, D., Garlaschi, F. M., Bassi, R., and Jennings, R. C. (1997). Analysis of some optical properties of a native and reconstituted photosystem ii antenna complex, cp29: Pigment binding sites can be occupied by chlorophyll a or chlorophyll b and determine spectral forms. *Biochem.*, 36:12984–12993.
- [Gülen et al., 1997] Gülen, D., van Grondelle, R., and van Amerongen, H. (1997). Structural information on the light-harvesting complex ii of green plants that can be deciphered from polarized absorption characteristics. *J. Phys. Chem. B*, 101:7256–7261.
- [Gradinaru et al., 2003] Gradinaru, C., van Grondelle, R., and van Amerongen, H. (2003). Selective interaction between xanthophylls and chlorophylls in lhciii probed by femtosecond transient absorption spectroscopy. *J. Phys. Chem. B*, 107:3938–3943.

Bibliography

- [Gradinaru et al., 1998a] Gradinaru, C. C., Pascal, A. A., van Mourik, F., Robert, B., Horton, P., van Grondelle, R., and Amerongen, H. (1998a). Ultrafast evolution of the excited states in the chlorophyll a/b complex cp29 from green plants studied by energy-selective pump-probe spectroscopy. *Biochem.*, 37:1143–1149.
- [Gradinaru et al., 1998b] Gradinaru, C. C., Özdemir, S., Gülen, D., van Stokkum, I. H. M., van Grondelle, R., and van Amerongen, H. (1998b). The flow of excitation energy in lhci monomers: Implications for the structural model of the major plant antenna. *Biophys. J.*, 75:3064–3077.
- [Hackbarth and Röder, 2000] Hackbarth, S. and Röder, B. (2000). Anisotropy shape control via light quenching and ground state depletion. *Opt. Comm.*, 173:247–254.
- [Haken, 1989] Haken, H. (1989). *Licht und Materie, Bd. 1: Elemente der Quantenoptik*. BI-Wissenschaftsverlag, Mannheim, 2 edition.
- [Haken, 1994] Haken, H. (1994). *Licht und Materie, Bd. 2: Laser*. BI-Wissenschaftsverlag, Mannheim, 2 edition.
- [Hemelrijk et al., 1992] Hemelrijk, P. W., Kwa, S. L. S., van Grondelle, R., and Dekker, J. P. (1992). Spectroscopic properties of lhci-ii, the main light-harvesting chlorophyll a/b protein complex from chloroplast membranes. *Biochim. Biophys. A.*, 1098:159–166.
- [Herek et al., 1998] Herek, J. L., Polívka, T., Pullerits, T., Fowler, G. J. S., Hunter, C. N., Sundström, V., and (1998). Ultrafast carotenoid band shifts probe structure and dynamics in photosynthetic antenna complexes. *Biochem.*, 37:7057–7061.
- [Hoff and Amesz, 1991] Hoff, A. J. and Amesz, J. (1991). Visible absorption spectroscopy of chlorophylls. In Scheer, H., editor, *Chlorophylls*, chapter 4.1, pages 723–738. CRC Press, Boca Raton, FL.
- [Hofmann et al., 1996] Hofmann, E., Wrench, P. M., Sharples, F. P., Hiller, R. G., Welte, W., and Diederichs, K. (1996). Structural basis of light harvesting by carotenoids: Peridinin-chlorophyll-protein from *amphidinium carterae*. *Science*, 272:1788–1791.
- [Hu et al., 1997] Hu, X., Ritz, T., Damjanovic, A., and Schulten, K. (1997). Pigment organization and transfer of electronic excitation in the photosynthetic unit of purple bacteria. *J. Phys. Chem. B*, 101:3854–3871.

- [Jimenez et al., 1996] Jimenez, R., Dikshit, S. N., Bradforth, S. E., and Fleming, G. R. (1996). Electronic excitation transfer in the lh2 complex of rhodobacter sphaeroides. *J. Phys. Chem.*, 100:6825–6834.
- [Jänich, 1983] Jänich, K. (1983). *Analysis für Physiker und Ingenieure*. Springer Verlag, Heidelberg.
- [Kane and Trebino, 1993] Kane, D. J. and Trebino, R. (1993). Single-shot measurement of the intensity and phase of an arbitrary ultrashort pulse by using frequency-resolved optical gating. *Opt. Lett.*, 18:823–825.
- [Karrasch et al., 1995] Karrasch, S., Bullough, P. A., and Ghosh, R. (1995). The 8.5 Å projection map of the light-harvesting complex I from *rhodospirillum rubrum* reveals a ring composed of 16 subunits. *EMBO J.*, 14:631–638.
- [Kühlbrandt et al., 1994] Kühlbrandt, W., Wang, D. N., and Fujiyoshi, Y. (1994). Atomic model of plant light-harvesting complex by electron crystallography. *Nature*, 367:614–621.
- [Kühn and Sundström, 1997a] Kühn, O. and Sundström, V. (1997a). Energy transfer and relaxation dynamics in light harvesting antenna complexes of photosynthetic bacteria. *J. Phys. Chem. B*, 101:3432–3440.
- [Kühn and Sundström, 1997b] Kühn, O. and Sundström, V. (1997b). Pump-probe spectroscopy of dissipative energy transfer dynamics in photosynthetic antenna complexes: A density matrix approach. *J. Chem. Phys.*, 107:4154–4164.
- [Kühn et al., 2002] Kühn, O., Sundström, V., and Pullerits, T. (2002). Fluorescence depolarization dynamics in the b850 complex of purple bacteria. *Chem. Phys.*, 275:15–30.
- [Kimura et al., 2000] Kimura, A., Kakitani, T., and Yamato, T. (2000). Theory of excitation energy transfer in the intermediate coupling case. ii. criterion for intermediate coupling excitation energy transfer mechanism and application to the photosynthetic antenna system. *J. Phys. Chem. B*, 104:9276–9287.
- [Kleima et al., 2000] Kleima, F., Wendling, M., Hofmann, E., Peterman, E. J. G., van Gronnelle, R., and van Amerongen, H. (2000). Peridinin chlorophyll a protein: Relating structure and steady-state spectroscopy. *Biochem.*, 39:5184–5195.
- [Knapp, 1984] Knapp, E. W. (1984). Lineshapes of molecular aggregates - exchange narrowing and intersite correlation. *Chem. Phys.*, 85:73–82.

Bibliography

- [Knoester, 1993] Knoester, J. (1993). Third-order optical response of molecular aggregates. disorder and the breakdown of size-enhancement. *Chem. Phys. Lett.*, 203:371–377.
- [Koepke et al., 1996] Koepke, J., Hu, X., Muenke, C., Schulten, K., and Michel, H. (1996). The crystal structure of the light-harvesting complex ii (b800-850) from *rhodospirillum molischi-anum*. *Structure*, 4:581–597.
- [Krikunova et al., 2002] Krikunova, L., Voigt, B., and Lokstein, H. (2002). Direct evidence for excitonically coupled chlorophylls a and b in lhci of higher plants by nonlinear polarization spectroscopy in the frequency domain. *Biochim. Biophys. A.*, 1556:1–5.
- [Krueger et al., 1998] Krueger, B. P., Scholes, G. D., and Fleming, G. R. (1998). Calculation of couplings and energy-transfer pathways between the pigments of lh2 by the ab initio transition density cube method. *J. Phys. Chem. B*, 102:5378–5386.
- [Leupold, 1995] Leupold, D. (1995). Photobiological application of nonlinear visible/nir-spectroscopic techniques, exemplified by the primary processes of bacterial photosynthesis. *Photochem. Photobiol.*, 62:984–996.
- [Leupold et al., 1999] Leupold, D., Stiel, H., Ehlert, J., Nowak, F., Teuchner, K., Voigt, B., Bandilla, M., Ücker, B., and Scheer, H. (1999). Photophysical characterization of the b800-depleted light harvesting complex b850 of *rhodobacter sphaeroides*. *Chem. Phys. Lett.*, 301:537–545.
- [Leupold et al., 1996] Leupold, D., Stiel, H., Teuchner, K., Nowak, F., Sandner, W., Ücker, B., and Scheer, H. (1996). Size enhancement of transition dipoles to one- and two-exciton bands in a photosynthetic antenna. *Phys. Rev. Lett.*, 77:4675–4678.
- [Leupold et al., 2002] Leupold, D., Teuchner, K., Ehlert, J., Irrgang, K.-D., Renger, G., and Lokstein, H. (2002). Two-photon excited fluorescence from higher electronic states of chlorophylls in photosynthetic antenna complexes: A new approach to detect strong excitonic chlorophyll a/b coupling. *Biophys. J.*, 82:1580–1585.
- [Leupold et al., 2000] Leupold, D., Voigt, B., Beenken, W., and Stiel, H. (2000). Pigment-protein architecture in the light-harvesting antenna complexes of purple bacteria: does the crystal structure reflect the native pigment-protein arrangement? *FEBS Lett.*, 480:73–78.
- [Leupold et al., 1994] Leupold, D., Voigt, B., Nowak, F., Ehlert, J., Hirsch, J., Neef, E., Bandilla, M., and Scheer, H. (1994). Substructure analysis of the bacterial antenna lhii by nonlinear polarization spectroscopy. *Lietuvos fizikos zurnalas*, 34:339–343.

- [Leupold et al., 1993] Leupold, D., Voigt, B., Pfeiffer, M., Bandilla, M., and Scheer, H. (1993). Nonlinear polarization spectroscopy (frequency domain) studies of excited state processes: The b800-850 antenna of *rhodobacter sphaeroides*. *Photochem. Photobiol.*, 57:24–28.
- [Linnanto et al., 1999] Linnanto, J., Korppi-Tommola, J. E. I., and Helenius, V. M. (1999). Electronic states, absorption spectrum and circular dichroism spectrum of the photosynthetic bacterial lh2 antenna of *rhodospseudomonas acidophila* as predicted by exciton theory and semiempirical calculations. *J. Phys. Chem. B*, 103:8739–8750.
- [Lokstein et al., 1995] Lokstein, H., Leupold, D., Voigt, B., Nowak, F., Ehlert, J., Hoffmann, P., and Garab, G. (1995). Nonlinear polarization spectroscopy in the frequency domain of light-harvesting complex ii: absorption band substructure and exciton dynamics. *Biophys. J.*, 69:1536–1543.
- [Marcano O and Garcia-Golding, 1985] Marcano O, A. and Garcia-Golding, F. (1985). Power effects in polarization spectroscopy on a water solution of malachite green. *J. Chem. Phys.*, 82:1242–1245.
- [Marcano O et al., 1986] Marcano O, A., Garcia-Golding, F., and Rojas F, R. (1986). Pump-power dependences of thermal grating and electronic components of a polarization spectroscopy signal in dye solutions. *J. Opt. Soc. Am. B*, 3:3–7.
- [Marcano O et al., 1990] Marcano O, A., Marquez, L., Aranguren, L., and Salazar, M. (1990). Polarization spectra of homogeneously and inhomogeneously broadened two-level systems. *J. Opt. Soc. Am. B*, 7:2145–2149.
- [May and Kühn, 2000] May, V. and Kühn, O. (2000). *Charge and Energy Transfer Dynamics in Molecular Systems*. Wiley-VCH, Berlin.
- [McDermott et al., 1995] McDermott, G., Price, S. M., Freer, A. A., Hawthornthwaite-Lawless, A. M., Papiz, M. Z., Cogdell, R. J., and Isaacs, N. W. (1995). Crystal structure of an integral membrane light-harvesting complex from photosynthetic bacteria. *Nature*, 374:517–521.
- [Meier et al., 1997] Meier, T., Chernyak, V., and Mukamel, S. (1997). Multiple exciton coherence sizes in photosynthetic antenna complexes viewed by pump-probe spectroscopy. *J. Phys. Chem.*, 101:7332–7342.
- [Monshouwer et al., 1997] Monshouwer, R., Abrahamsson, M., van Mourik, F., and van Grondelle, R. (1997). Superradiance and exciton delocalization in bacterial photosynthetic light-harvesting systems. *J. Phys. Chem. B*, 101:7241–7248.

Bibliography

- [Mower, 1966] Mower, L. (1966). Decay theory of closely coupled unstable states. *Phys. Rev.*, 142:799–816.
- [Mukamel, 1995] Mukamel, S. (1995). *Nonlinear Optical Spectroscopy*. Oxford University Press, New York, 1st edition.
- [Nakajima, 1958] Nakajima, S. (1958). On quantum theory of transport phenomena steady diffusion. *Prog. theor. Phys.*, 20:948–959.
- [Neef and Mory, 1991] Neef, E. and Mory, S. (1991). Content of information of nonlinear polarization spectroscopy. *Exp. Techn. Phys.*, 39:385–388.
- [Nishigaki et al., 2001] Nishigaki, A., Ohshima, S., Nakayama, K., Okada, M., and Nagashima, U. (2001). Application of molecular orbital calculations to interpret the chlorophyll spectral forms in pea photosystem ii. *Photochem. Photobiol.*, 73:245–248.
- [Novoderezhkin et al., 1999] Novoderezhkin, V., Monshouwer, R., and van Grondelle, R. (1999). Exciton (de)localization in the lh2 antenna of rhodobacter sphaeroides as revealed by relative difference absorption measurements of the lh2 antenna and the b820 subunit. *J. Phys. Chem. B*, 103:10540–10548.
- [Nowak, 1999] Nowak, F. R. (1999). *Beiträge der Nichtlinearen Polarisationspektroskopie in der Frequenzdomäne zur Aufklärung ultraschneller Prozesse in photosynthetischen bakteriellen Pigment-Protein-Komplexen*. PhD thesis, Universität Potsdam.
- [Nussberger et al., 1994] Nussberger, S., Dekker, J. P., Kühlbrandt, W., van Bolhuis, B. M., van Grondelle, R., and van Amerongen, H. (1994). Spectroscopic characterization of three different monomeric forms of the main chlorophyll a/b binding protein from chloroplast membranes. *Biochem.*, 33:14775–14783.
- [Ogawa et al., 2002] Ogawa, K., Zhang, T., Yoshihara, K., and Kobuke, Y. (2002). Large third-order optical nonlinearity of self-assembled porphyrin oligomers. *J. Am. Chem. Soc.*, 124:22.
- [Parusel and Grimme, 2000] Parusel, A. B. J. and Grimme, S. (2000). A theoretical study of the excited states of chlorophyll a and pheophytin a. *J. Phys. Chem. B*, 104:5395–5398.
- [Pascal et al., 1999] Pascal, A., Gradinaru, C., Wacker, U., Peterman, E., Calkoen, F., Irrgang, K.-D., Horton, P., Renger, G., van Grondelle, R., Robert, B., and van Amerongen, H. (1999). Spectroscopic characterization of the spinach lhcb4 protein (cp29), a minor light-harvesting complex of photosystem II. *Eur. J. Biochem.*, 262:817–823.

- [Pearlstein, 1991] Pearlstein, R. M. (1991). Theoretical interpretation of antenna spectra. In Scheer, H., editor, *Chlorophylls*, chapter 4.11, pages 1074–1078. CRC Press, Boca Raton, FL.
- [Peterman et al., 1997] Peterman, E. J. G., Pullerits, T., van Grondelle, R., and van Amerongen, H. (1997). Electron-phonon coupling and vibronic fine structure of light-harvesting complex ii of green plants: Temperature dependent absorption and high-resolution fluorescence spectroscopy. *J. Phys. Chem. B*, 101:4448–4457.
- [Polivka et al., 1999] Polivka, T., Herek, J. L., Zigmantas, D., Åkerlund, H. E., and Sundström, V. (1999). Direct observation of the (forbidden) s_1 state in carotenoids. *Proc. Natl. Acad. Sci.*, 96:4914–4917.
- [Polivka et al., 2000] Polivka, T., Pullerits, T., Herek, J. L., and Sundström, V. (2000). Exciton relaxation and polaron formation in lh2 at low temperature. *J. Phys. Chem. B*, 104:1088–1096.
- [Pullerits et al., 1995] Pullerits, T., Monshouwer, R., van Mourik, F., and van Grondelle, R. (1995). Temperature-dependence of electron-vibronic spectra of photosynthetic systems - computer-simulations and comparison with experiment. *Chem. Phys.*, 194:395–407.
- [Reddy et al., 1991] Reddy, N. R. S., Small, G. J., Seibert, M., and Picorel, R. (1991). Energy transfer dynamics of the b800-850 antenna complex of rhodobacter sphaeroides: a hole burning study. *Chem. Phys. Lett.*, 181:391–399.
- [Reddy et al., 1994] Reddy, N. R. S., van Amerongen, H., Kwa, S. L. S., van Grondelle, R., and Small, G. J. (1994). Low-energy exciton level structure and dynamics in light harvesting complex ii trimers from the chl a/b antenna complex of photosystem ii. *J. Phys. Chem.*, 98:4729–4735.
- [Remelli et al., 1999] Remelli, R., Varotto, C., Sandonà, D., Croce, R., and Bassi, R. (1999). Chlorophyll binding to monomeric light-harvesting complex. *J. Biol. Chem.*, 274:33510–33521.
- [Renger et al., 1994] Renger, T., Voigt, J., May, V., and Kühn, O. (1994). Dissipative exciton motion in a chlorophyll a/b dimer of the light harvesting complex of photosystem ii: Simulation of pump-probe spectra. *J. Chem. Phys.*, 100:15654–15662.
- [Rogl and Kühlbrandt, 1999] Rogl, H. and Kühlbrandt, W. (1999). Mutant trimers of light-harvesting complex ii exhibit altered pigment content and spectroscopic features. *Biochem.*, 38:16214.

Bibliography

- [Rogl et al., 2002] Rogl, H., Schödel, R., Lokstein, H., Kühlbrandt, W., and Schubert, A. (2002). Assignment of spectral substructures to pigment-binding sites in higher plant light-harvesting complex lhc-ii. *Biochem.*, 41:2281–2287.
- [Ruban et al., 1997] Ruban, A. V., Calkoen, F., Kwa, S. L. S., van Grondelle, R., Horton, P., and Dekker, J. P. (1997). Characterisation of lhc ii in the aggregated state by linear and circular dichroism spectroscopy. *Biochim. Biophys. A.*, 1321:61–70.
- [Saikan and Sei, 1983a] Saikan, S. and Sei, J. (1983a). Experimental studies of polarization spectroscopy in dye solutions. *J. Chem. Phys.*, 79:4146–4153.
- [Saikan and Sei, 1983b] Saikan, S. and Sei, J. (1983b). Investigations of the conformational change in triphenylmethane dyes via polarization spectroscopy. *J. Chem. Phys.*, 79:4154–4157.
- [Sauer et al., 1996] Sauer, K., Cogdell, R. J., Prince, S. M., Freer, A., Isaacs, N. W., and Scheer, H. (1996). Structure-based calculations of the optical spectra of the LH2 bacteriochlorophyll-protein complex from *rhodospseudomonas acidophila*. *Photochem. Photobiol.*, 64:564–576.
- [Sauer et al., 1966] Sauer, K., Smith, J. R. L., and Schultz, A. J. (1966). The dimerization of chlorophyll a, chlorophyll b, and bacteriochlorophyll in solution. *J. Am. Chem. Soc.*, 88:2681–2688.
- [Scheer, 1991] Scheer, H. (1991). Structure and occurrence of chlorophylls. In Scheer, H., editor, *Chlorophylls*, chapter 1.1, pages 3–31. CRC Press, Boca Raton, FL.
- [Scherz et al., 1991] Scherz, A., Rosenbach-Belkin, V., and Fisher, J. R. E. (1991). Chlorophyll aggregates in aqueous solutions. In Scheer, H., editor, *Chlorophylls*, chapter 1.9, pages 237–268. CRC Press, Boca Raton, FL.
- [Scholes, 1999] Scholes, G. (1999). Theory of coupling in multichromophoric systems. In Andrews, D. L. and Demidov, A. A., editors, *Resonance Energy Transfer*, chapter 6, pages 213–242. John Wiley and Sons, New York.
- [Schubert, 2003] Schubert, A. (2003). *New approaches to refine the physical model of the higher plant light-harvesting complex LHC-II*. PhD thesis, Humboldt Universität zu Berlin (in preparation).
- [Schubert et al., 2002] Schubert, A., Beenken, W. J. D., Stiel, H., Voigt, B., Leupold, D., and Lokstein, H. (2002). Excitonic coupling of chlorophylls in the plant light-harvesting complex lhc-ii. *Biophys. J.*, 82:1030–1039.

- [Schubert et al., 1997] Schubert, A., Voigt, B., Leupold, D., Beenken, W., Ehlert, J., Hoffmann, P., and Lokstein, H. (1997). Direct observation of spectral substructure in the Q_y - absorption band of light harvesting complex II by nonlinear polarisation spectroscopy in the frequency domain at low temperature. *Biochim. Biophys. A.*, 1321:195–199.
- [Seke, 1991a] Seke, J. (1991a). Analysis of the projection-operator methode: inconsistencies and their removal. *J. Phys. A*, 24:2121–2129.
- [Seke, 1991b] Seke, J. (1991b). What is wrong with the projection operator method? removal of inconsistencies and a new self-consistent method for non-markovian treatment of atom-field interactions. *Il Nuovo Cimento D*, 13:1203–1219.
- [Shipman, 1977] Shipman, L. L. (1977). Oscillator and dipole strengths for chlorophylls and related molecules. *Photochem. Photobiol.*, 26:287–292.
- [Simonetto et al., 1999] Simonetto, R., Crimi, M., Sandona, D., Croce, R., Cinque, G., Breton, J., and Bassi, R. (1999). Orientation of chlorophyll transition moments in the higher-plant light-harvesting complex CP29. *Biochem.*, 38:12974–12983.
- [Simpson and Knoetzel, 1996] Simpson, D. J. and Knoetzel, J. (1996). Light harvesting complexes of plants and algae: Introduction, survey and nomenclature. In Ort, D. R. and Yocum, C. F., editors, *Oxygenic photosynthesis: the light reactions*, chapter 27, pages 493–506. Kluwer Academic Publishers, Dordrecht.
- [Somsen et al., 1996] Somsen, O. J. G., van Grondelle, R., and van Amerongen, H. (1996). Spectral broadening of interacting pigments: Polarized absorption by photosynthetic proteins. *Biophys. J.*, 71:1934–1951.
- [Song et al., 1978] Song, J. J., Lee, J. H., and Levinson, M. D. (1978). Picosecond relaxation measurements by polarization spectroscopy in condensed phases. *Phys. Rev. A*, 17:1439–1447.
- [Spano, 1992] Spano, F. C. (1992). Multiple-photon absorption and saturation in frenkel-exciton chains. *Phys. Rev. B*, 46:13017–13034.
- [Spano and Mukamel, 1989] Spano, F. C. and Mukamel, S. (1989). Superradiance in molecular aggregates. *J. Chem. Phys.*, 91:683–700.
- [Sundholm, 2000] Sundholm, D. (2000). Comparison of the electronic excitation spectra of chlorophyll a and pheophytin a calculated at density functional theory level,. *Chem. Phys. Lett.*, 317:545–552.

Bibliography

- [Sundström et al., 1999] Sundström, V., Pullerits, T., and van Grondelle, R. (1999). Photosynthetic light-harvesting: Reconciling dynamics and structure of purple bacterial lh2 reveals function of photosynthetic unit. *J. Phys. Chem. B*, 103:2327–2346.
- [Tietz et al., 2001] Tietz, C., Jelezko, F., Gerken, U., Schuler, S., Schubert, A., Rogl, H., and Wrachtrup, J. (2001). Single molecule spectroscopy on the light-harvesting complex ii of higher plants. *Biophys. J.*, 81:556–562.
- [Trebino et al., 1997] Trebino, R., DeLong, K. W., Fittinghoff, D. N., Sweetser, J. N., Krumbügel, M. A., Richman, B. A., and Kane, D. J. (1997). Measuring ultrashort laser pulses in the time-frequency domain using frequency-resolved optical gating. *Rev. Sci. Instrum.*, 68:3277–3295.
- [Trebino et al., 1996] Trebino, R., DeLong, K. W., Fittinghoff, D. N., Sweetser, J. N., Krumbügel, M., Bowie, J., Taft, G., Rundquidt, A., Murnane, M. M., and Kapteyn, H. C. (1996). Measurements of the intensity and phase of ultrashort pulses using frequency-resolved optical gating. In Svelto, O., De Silvestri, S., and Denardo, G., editors, *Ultrafast Processes in Spectroscopy*, chapter 134, pages 603–606. Plenum Press, New York.
- [Trinkunas et al., 2001] Trinkunas, G., Herek, J. L., Polivka, T., Sundström, V., and Pullerits, T. (2001). Exciton delocalization probed by excitation annihilation in the light-harvesting antenna lh2. *Phys. Rev. Lett.*, 86:4167–4170.
- [van Amerongen et al., 1994] van Amerongen, H., Kwa, S. L., van Bolhuis, B. M., and van Grondelle, R. (1994). Polarized fluorescence and absorption of macroscopically aligned light harvesting complex ii. *Biophys. J.*, 67:837–847.
- [van Amerongen et al., 2000] van Amerongen, H., Valkunas, L., and van Grondelle, R. (2000). *Photosynthetic Excitons*. World Scientific, River Edge, NJ.
- [van Amerongen and van Grondelle, 2001] van Amerongen, H. and van Grondelle, R. (2001). Understanding the energy transfer function of lhci, the major light-harvesting complex of green plants. *J. Phys. Chem. B*, 105:604–617.
- [van Grondelle, 1985] van Grondelle, R. (1985). Excitation transfer, trapping and annihilation in photosynthetic systems. *Biochim. Biophys. A.*, 811:147–195.
- [Voigt et al., 2002] Voigt, B., Irrgang, K.-D., Ehlert, J., Beenken, W., Renger, G., Leupold, D., and Lokstein, H. (2002). Spectral substructure and excitonic interactions in the minor

- photosystem ii antenna complex cp29 as revealed by nonlinear polarization spectroscopy in the frequency domain. *Biochem.*, 41:3049–3056.
- [Voigt et al., 1997] Voigt, B., Nowak, F., Ehlert, J., Beenken, W. J. D., Leupold, D., and Sandner, W. (1997). Substructures and different relaxation time within the first electronic transition of pinacyanol. *Chem. Phys. Lett.*, 222:380–390.
- [Voigt et al., 1999] Voigt, B., Nowak, F. R., and Beenken, W. (1999). A new set-up for nonlinear polarization spectroscopy in the frequency domain: experimental examples and theoretical background. *Meas. Sci. Technol.*, 10:N7–N11.
- [Weiss, 1999] Weiss, U. (1999). *Quantum dissipative systems*. World Scientific, Singapore, 2 edition.
- [Wieman and Hänsch, 1976] Wieman, C. and Hänsch, T. W. (1976). Doppler-free laser polarization spectroscopy. *Phys. Rev. Lett.*, 36:1170–1173.
- [Wu et al., 1996] Wu, H., Reddy, N. R. S., Cogdell, R. J., Muenke, C., Michel, H., and Small GJ, G. J. (1996). A comparison of the lh2 antenna complex of three purple bacteria by hole burning and absorption spectroscopies. *Mol. Cryst. Liq. Cryst. A*, 291:163–173.
- [Young, 1991] Young, A. J. (1991). The photoprotective role of carotenoids in higher plants. *Physiol. Plant.*, 83:702–708.
- [Zigmantas et al., 2002] Zigmantas, D., Hiller, R. G., Sundström, V., and Polívka, T. (2002). Carotenoid to chlorophyll energy transfer in the peridinin-chlorophyll-a-protein complex involves an intramolecular charge transfer stat. *Proc. Natl. Acad. Sci.*, 99:16760–16765.
- [Zimmermann, 1990] Zimmermann, R. (1990). The dynamical stark effect of excitons. *Festkörperprobleme*, 30:295–320.
- [Zucchelli et al., 1996] Zucchelli, G., Garlaschi, F. M., and Jennings, R. C. (1996). Thermal broadening analysis of the light harvesting complex ii absorption spectrum. *Biochem.*, 35:16247–16254.
- [Zwanzig, 1961] Zwanzig, R. (1961). Memory effects in irreversible thermodynamics. *Phys. Rev.*, 124:983–992.

Curriculum Vitae

- Name: Wichard Johann Daniel Beenken
- 14.10.1964 born in Munich, Germany 1970 - 1973 Primary school in Munich, Germany
- 1973 - 1983 Maximiliansgymnasium, humanistic secondary school in Munich, Germany
- 1983 - 1991 Study of physics at Faculty of Physics of Technical University Munich, Germany
- 24.10.1991 Graduation to Dipl. Physiker. Thesis about Quantum Chemical Calculations for Spectral Sensitizing of Silver-Halogenids at Chair for Theoretical Bio- and Molecular Physics under the supervision of Prof. Dr. Sighart Fischer and Dr. Philipp O. J. Scherer.
- 1991 - 1994 Study of economics at Faculty of Economics of Technical University Munich, Germany
- 4.3.1994 Graduation to Dipl. Wirtschaftsphysiker. Thesis about Self-Organization in Company at AIB under the supervision of Prof. Dr. Ralph Reichwald and Dr. Jürgen Weichselbaumer
- 1995 - 1999 PhD-student at the FemtoBiology group of Dr. Dieter Leupold at Max-Born-Institut, Berlin, Germany. Fields of Research: Theory of nonlinear polarization spectroscopy in the frequency Domain (NLPF) and photosynthetic antennae.
- 2000 - 2003 Scientific researcher in the Computational Chemical Physics group of associated professor Dr. Tõnu Pullerits at the Department of Chemical Physics of Lund University, Sweden. Fields of Research: Quantum chemical calculations of conjugated polymers (poly-thiophene) and exciton-polarons.

Selbständigkeitserklärung

Hiermit erkläre ich, die vorliegende Arbeit selbständig ohne fremde Hilfe verfaßt und nur die angegebene Literatur und Hilfsmittel verwendet zu haben.

Wichard Johann Daniel Beenken

15. Juli 2003